Cranfield University

School of Applied Sciences

Doctorial Thesis

M. W. Davies

Modelling Deposition Environments around Superheater Tubes

Supervisor: Dr N Simms, Dr S. Wu

November 2011

This thesis is submitted in partial fulfilment of the requirements for the Degree of Doctor of Philosophy.

Abstract

In an important initiative to reduce carbon dioxide emission from pulverized fuel boilers, coal is now co-fired with biomass. During the combustion process, however, chlorine and sulphur in chemical compounds associated with sodium and potassium are released in a form which can deposit onto and then corrode the steel heat exchanger tubes. The deposition and corrosion can have serious implications for the power generation industry because the corrosive damage on heat exchange tubes can shorten the operational life of the boilers and lead to significant economic penalties.

The deposition and corrosion processes have been widely studied but eliminating the deposits and corrosive materials is still a challenging problem. Computational fluid dynamics (CFD) has been used to model the deposition processes and it mainly focuses on experimentally deriving constants in the models that capture some aspects of the problem such as the motion behaviour of aerosols. However, using CFD has a limitation that results in periodic instability when solving the models with numerical computation.

Modelling deposition environments around superheater tubes is a complex problem as many aspects, such as particle motion, condensation of matter and continuous combustion of particles, should be considered.

This thesis has:

(1) developed a new mathematical approach that uses mesh-free methods to solve Hamilton's equations with a consideration of the total energy of the system, where the Hamilton's equation is scale independent;
(2) developed a model that can simulate the mass accumulation process based on graph and combinatorics theory;
(3) developed a model depicting the continuous combustion of particles in motion;
(4) developed a model depicting the behaviour of changing matter states;
(5) developed a model depicting the vapour phase deposition on particles; and
(6) verified the developed models with case studies.

This work shows the importance of homogenous and heterogeneous vapour depositions on binding particles onto superheater tubes.

Acknowledgements

I am very grateful for the invaluable help and guidance that I received from my academic supervisors Dr Nigel Simms and Dr Shaomin Wu throughout the duration of this project.

My special thanks also go to Professor John Oakey for providing useful comments and feedback throughout.

I would also like to take this opportunity to acknowledge other academic staff at Cranfield University who gave knowledge and expertise to carry out this piece of work.

Finally, I would like to thank the EPSRC Supergen consortium their financial support.

Nomenclature/List of Common Symbols

Statistical Quantum Mechanics

a' b'	Van der Walls Constant
k_B	Boltzmann constant
$\dot{m}$	Deposition rate
N	Number of molecules in a configuration
P	Pressure
R	Ideal Gas Constant
$r_{i,j}$	Molecular pair distances
α, a, b	Peng - Robinson Constants
$\dot{\beta}$	Mass Transfer Coefficient
$\mathcal{Z}$	Canonical Assembly
Z	Grand Canonical Assembly
ω	Accretion Factor

Fluid Dynamics

Nu	Nusselt Number
Kn	Knusden Number
Ma	Mach Number
Pe	Péclet Number

Constants

Boltzmann Constant	$k_B = 1.3806503 \times 10^{-23}$ m^2 kg s^{-2} K^{-1}
Universal Gas Constant	R=8.314472 J/Mol K
Karman Constant	$\kappa = 0.4187$

Contents

List of Figures

List of Tables

1 Introduction

1.1 Overview

A growing concern for energy consumption and climate change targets has led to social pressures on the way fossil fuels are used. The UK government has provided funding for research into the use of coal/biomass in operational power stations.

Burning biomass is not without problems since the by-products of combustion are potentially corrosive, particularly at higher temperature obtained on heat exchange surfaces on the 'fireside' of the boiler. The ash content can form deposit that reduces the overall efficiency of the energy conversion process as the ash is an insulator.

Potentially corrosive by-products take one of the forms: solid or semi-solid particles or condensing volatiles. The post-combustion by-products consist of compounds of chlorine, potassium, sodium and sulphur. In many instances these by-products can form a build up in the shape of a tapped cone of deposits or 'bridges' between the superheater tubes (Tomeczek, et al., 2004).

Deposit formation on superheater tubes is the result of many complex mechanisms that involve the integration of fine ash particles, gases and vapours that flow around these tubes. It's essential for the economic operation of power plants where the sources of deposition are correctly identified.

Through the research outlined within this thesis the subject has been critically reviewed. This thesis is the statement of the knowledge gained which will advance the understanding of the deposition of combustion products. The methods adopted throughout the thesis seek to promote a better understanding of this complex process regarding the deposition on PF (Pulverised Fuel) boilers superheater tubes, through the mathematical modelling techniques that encapsulate its pure chemical and physical science base.

1.2 Motivation for the present work

The present work was motivated by the fact that there is a wide variation in the performance in deposition models developed by other researchers. The models are principally built on meshed CFD (Computational Fluid Dynamics) which can be time consuming and the spatial

accuracy can be poor. The technology of CFD is moving forward and mesh-free systems are being adopted which make the bases of current research in fireside deposition obsolete. There is therefore need to advance the mathematical solution of the phenomena from which this study investigates and extends current knowledge. This might lead to new physical science and mathematical analytic approaches and improve the performance of prediction models of PF boilers failure.

To this end, this thesis will;

- embrace in the modelling, the complex array of physical, thermodynamic and chemical processes that result in the deposition of particles onto PF boilers heat exchanger tubes.
- design case studies that considering changes to geometry, and physical characteristics that affect the performance of modelling deposition of particles.
- develop a more integrated model.

In this power generation sector there is an expectation of improving the prediction of differing deposits types. Some examples of such expectations are predicting the type of chemical constitutes and mechanisms which particulates and vapours bond to superheater tubes. This will lead to advances to combat fireside corrosion. Since the study must consider the condensation of matter, which is a complex process; alternative approaches to modelling are required. A key motivation is to explore the numerical mesh-free methods to overcome the problems associated with mesh discontinuities and singularities usually experienced when modelling chaotic or quantum based systems.

The delivery of the model will use commercial packages (i.e. MS Excel) and bespoke software to develop a clearer insight into formation of deposits on superheater tubes. For example the thermodynamic system of condensation is broken down into a unit handled by MS Excel, while the calculations of the physical properties of the particles are handled by a unit written FORTRAN 2003. By using this configuration of commercial and bespoke applications, it can be demonstrated by sharing data using XML between units and applications; this approach offers the capability to solve a much wider class of problems than featured in this project.

1.3 Aims and Objectives

The overall aim is

To advance the study of particle and vapour behaviour around deposition on PF Boiler tubes through mathematical modelling.

The overall objectives of this thesis are:

- To improve the existing approach to modelling the movement of particles and vapour phase species around superheater tubes.
- To investigate the feasibility of using mesh-free solution to solve partial differential equations (PDE) to predict particle motion and thermodynamic properties.
- To combine models for both particles and vapour phase movement in the combustion gases.
- To extend and support the engineering (Newtonian/Gauss) models found in commercial CFD packages by applying statistical molecular mechanics.
- To validate model(s) with the confidence that model is close to the real world is gained by comparison with experimental data.

1.4 Thesis Structure

The thesis is structured as follows:

Chapter 2

- Conducts a literature review to review current 'state of art' and search for potential new ideas and lines of research.

Chapter 3

- Discusses the methods used to model coal/biomass combustion, where the rate of combustion of volatile particles is explored using the Arrhenius equation.
- Verifies the effectiveness of this approach against open literature
- Introduce the problems of non-deterministic period behaviour in solution of partial differential equation (PDE); and
- Demonstrates some strange effect of non-deterministic period behaviour, in the case of the importance of initial start values that ensure a PDE solver can converge to a solution.

Chapter 4

- Examines vapour deposition models, starting from initially review of current CFD models and their limitations.
- Examines if aerosol can model the properties of agglomeration and deposition. The chapter explores possible deficits in aerosol modelling of agglomeration and deposition where there are both high temperatures and the condensation of matter.
- Discusses the shortfalls of aerosol modelling of agglomeration and deposition at many scales of physics.
- Examines alternatives to aerosol modelling discovered by applying the physics of statistical mechanics.
- Develops a more complete model of vapour phase deposition using 'equations of state'.
- Develop a model designed using MS Excel can solve the vapour deposition rates using the 'equations of state and
- Illustrates the MS Excel model with a case study of the deposition of K_2SO_4 and the discussion of the results.

Chapter 5

- Considers current approaches to modelling particle impact deposition.
- Examines whether Stokes number is satisfactory measure of stopping distance of a particle to a characteristic dimension of the tube.
- Considers the main mechanisms in combustion devices which cause particle deposition are gravitational settling, inertial impaction, turbophoresis, thermophoresis and particle diffusion.
- Discusses whether the Stokes number and multi-scale physics can be compatible if so many different mechanisms are responsible for particle deposition.
- Considers the solution of partial differential equation of diffusion and interface the solution to the numerical method of SIMPLE algorithm used to solve the Navier-Stokes equation.
- Describe how partial differential equation involved in both vapour and particles are configured into one model by using the numerical solution of mesh-free method.

- Introduces the use of Mayer functions as the approach build layers of particle and vapours to form the characteristic bridge and deposit patterns found on superheater tubes.
- Discuss the inclusion of a wall turbulence model using k-ε is explained and the general track of particles in the wake of tube.
- Describes the vortex shedding model and use the Strouhal number to describe the oscillating flow mechanisms of deposition. The chapter explore the limits which Strouhal number can predict the oscillating flow mechanisms of deposition. The chapter examines if Strouhal approach to vortex shedding is compatible with multi-scale physics.
- A case study tests the validity using mesh-free method combined with the work of Mayer function. The chapter discusses of the effectiveness of the mesh-free method combined with the work of Mayer function and discussion of the results obtained in the case study tests.

Chapter 6

- Studies two cases where multi-scale physics is applied to different sizes (e.g. particles at micro scale to particles at molecular scale).
- Considers a new method of information storage of physics data that describes material and fluid flow properties using XML
- Uses case studies in this chapter to examine different configuration of tubes either inline or from staggered formation.
- Case studies in this chapter use of different fuels that evolve particles of different sizes.
- Reviews what happens to particles of different sizes by applying multi-scale physics to the deposition of vapour onto particles and the motion of particles in the combustion gas stream; and
- Summarises the reasons behind the behaviour of particles and gasses in the combustor.

Chapter 7,

- Examines results of the case studies in chapter 6 in more depth.
- Examines further extension of graph theory and many particle models.

- Discuses what degree all the models used in this thesis becomes numerically affected by pattern behaviour such as chaotic instability and the effects of truncation errors will also be examined.
- Examines how effective the edges of geometric boundary restored using L_2-Norm or L_∞- Norm after parametrically splitting the model form into vertex, inlets, outlets and moving stencils; and-
- Assess the effectiveness verification data used in chapter 5. Even though such data was not used to set the model's parameters in latter case studies it is important that a sensitivity analysis is valid, that the model will represent new data not presented in the validation study.

Chapter 8

Provide overall review to the work underpinning this thesis and bring together various aspects by drawing on important issue from the end of chapter summaries.

Chapter 9

Discuss future work which might advance this body of knowledge found in this thesis.

2 Literatures study

So far large progress has been made to understand the deposition mechanism on heat exchanger surfaces. Taking the overall view of coal combustion combined with mineral matter, one can summarised that computational modelling of this deposition mechanism has not been successful due to their.

- Low accuracy
- Unstable solutions and
- Poor generalizations of results.

Modelling of coal/biomass conversion to ash/vapour deposition has been followed as coal conversion to the respective ash/vapour deposition with the same issues.

The application of 3D (3 dimensional) codes that use software packages to plot the deposit is possible, but such codes do not usually have effective modules to deal with mineral mater transformations and inorganic vapours.

This review will show that existing modelling approaches have been from point of deposition growth; however they have limited capability to simulate the composition as well as the shape of the deposits (Adanez, et al., 2003). In considering the gaseous/solid phases, chemical reactions and subsequent condensation of Na_2SO_4 and K_2SO_4 are used to gain the overall view of this aspect (Adanez, et al., 2003)

2.1 Background

2.1.1 Systemic structure of biomass deposition

A systematic study of the power plant will identify those areas where deposition will build up and cause problems. Almost all coal and biomass mixture is pulverised in to a fine crumb and burned in a pulverised fuel (PF) boiler. While detailed design of PF boilers may vary, the overall design features are similar as illustrated in Figure 2-1.

Within a PF boiler the key areas of interest are the primary, secondary and tertiary superheater, which are highlighted in red in the Figure 2-1. The superheater tubes are the principle area where deposits collect and they are expensive and large components, one example is shown in Figure 2-2. The spaces between the tubes are very narrow, together with

the high bulk gas temperatures and the colder metal temperatures; particles can either directly impact or vapour condense onto the tube surfaces.

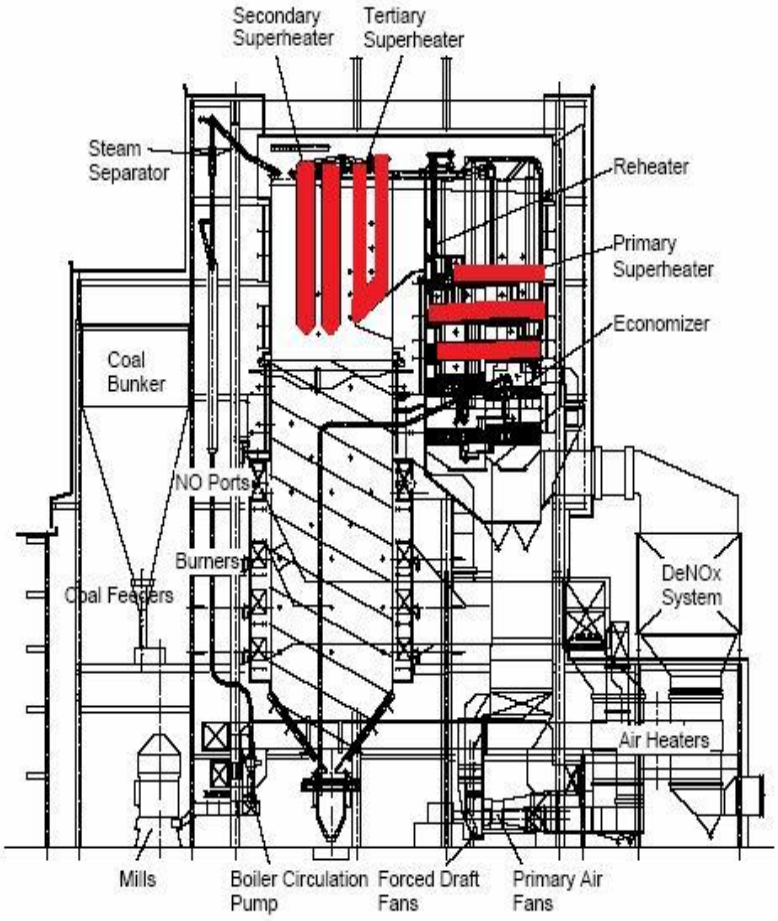

Figure 2-1. A cutaway pulverised fuel (PF) power generation boilers.

The type of process active in the gas stream or between the spaces between the superheater tubes are:

- process of direct impaction
- process of condensation of vapour

The path which particles track to the tubes can be split into three sub processes that are combustion, particle deposition and vapour deposition. In Figure 2-3 the relationships between each sub-process models and constructive element are illustrated.

A constitutive model is required to model the relationship between chemical or physical quantities that represent a specific behaviour. For example, the combustion constitutive

process model is represented by elements that consists a Large Eddy Simulation (LES) and a non premix Arrhenius law (Walas, 1994; Wang, 2008).

Figure 2-2. Banks of superheater tubes undergoing repair.

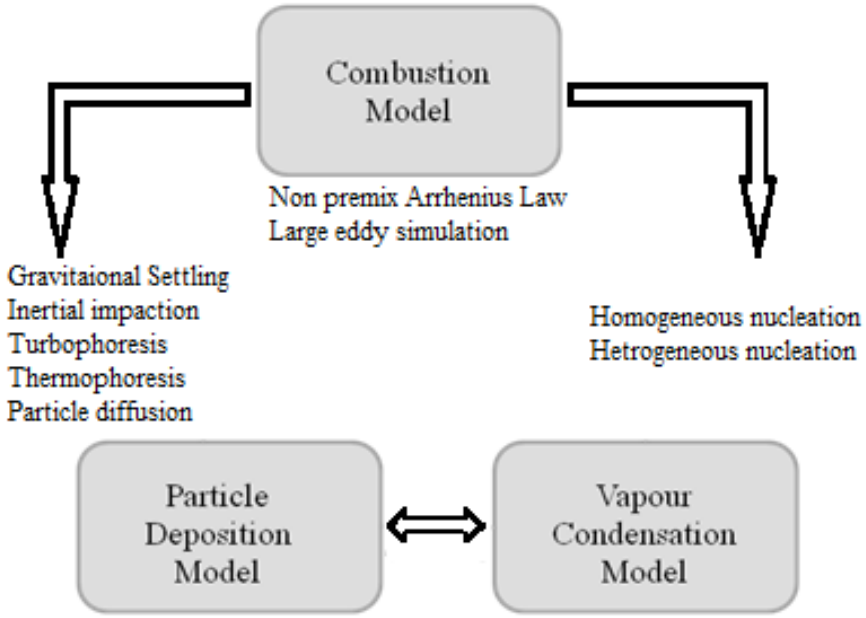

Figure 2-3. The schematic model of the fireside deposition processes.

Within the constitutive model that represents the chemical and physical behaviour within a PF boiler model, particle deposition and vapour condensation model are sub-process models

within this. In the case of particle deposition model, then these include ballistic impact of solid products and in the case of vapour deposition the nucleation of gas/vapour products near or onto the tubes surface.

2.1.2 **Definitions**

A combustion sub-process requires elements which will solve the partial differential equation that represents the numerical solution of the gas flow around the combustion process. The combustion sub-process is the function of the LES (Large Eddy Simulation) element of the model (Walas, 1994). The rate at which fuel and oxygen burn to produce by-products can be predicted using a non premixed Arrhenius law. The non-premixed Arrhenius law of combustion rate modelling is described in many papers (Versteeg & Malalasekera, 1995; Patankar, 1980) and widely used in CFD programmes.

The particle deposition sub-process has the following five elements.

1. The first element is the gravitational settling model which considers the opposing forces of gravity and drag on a falling particle.
2. An inertial impaction element replicates impact behaviour based on the velocity and size of the particle.
3. The turbophoresis model is the tendency for particles to migrate in the direction of decreasing turbulence level.
4. The thermophoresis model or the Ludwig-Soret effect models (Kaer, et al., 2006) is the phenomenon of the separation into thermal layers of two or more types of motile particles (particles able to move) by forces imparted by a temperature gradient.
5. The particle diffusion model or molecular diffusion model describes the net transport of molecules from a region of higher concentration onto one of lower concentration by random molecular motion.

The vapour deposition sub-process contains the following three elements.

- The first is homogeneous nucleation and is defined when a Van der Waals fluid (non-ideal gas/liquid with Van der Waals interactions) (Hein & Bemtgen, 1998) undergoes condensation of the liquid phase or evaporation of the liquid that is governed by the equation of state. For a fixed number density of atoms, changes in volume, pressure or temperature can drive the gas or liquid into an unstable state.

- The second element is heterogeneous nucleation when the initiator is a solid or semi-solid particle that seeds the condensation or evaporation on the wetted surface when the contact angles θ are less than 90 degrees as Figure 2-4 (Frank, 2001)
- The third element is direct condensation onto the colder superheater tubes, which is when hot gas meets colder metal and can no long retain its state as a gas and becomes a liquid.

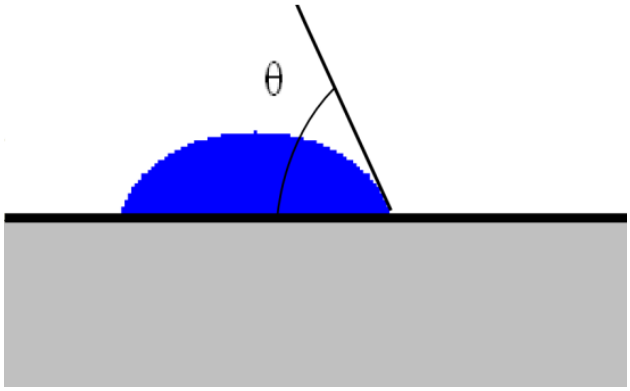

Figure 2-4. Contact angle θ of a liquid droplet wetted to a rigid solid surface

2.1.3 Partition of model space

If the mass of real particles is small and therefore offers small inertial forces, then collection of microscopic model systems in which these particles exists (i.e. pressure, temperature, chemical potential etc) can be put together to mirror the macroscopic state of a given physical system. It is assumed that the probability distribution (or density operator) D of given microscopic states *i* is constructed in such a way that the proportion of D_i/N of the members N of the assembly is proportional, over time, of finding a real world system.

In statistical thermodynamics, such configurations of microstates are a static collections of microscopic states that create a mirror of successive fluctuation of a macroscopic physical system being modelled (Hill, 1987).Within the physical system being modelled the grand canonical ensemble is an equilibrium with the external exchange of particles and energy with the environment. The chemical potential (which related closely to fugacity) is introduced to specify the fluctuation of the number particles in the assembly. The temperature is used to specify the fluctuation of energy within the assembly. This concept of statistical mechanics is used extensively to derive a numerical solution of vapour deposition on heat exchanger tubes. A more detailed description of the grand canonical assembly and its relationship with the

partition of model space is discussed later. The partition of model space is said to have has a one-to-one relationship with the grand canonical ensemble.

However, an important postulate leads to the concept of the canonical assembly and grand canonical assembly. The 'Postulate of maximum entropy' states:

> *Among all density operators consistent with the microstate constraint, the energy density operator* E *must give the maximum statistical entropy* S_{st} [E]. *At equilibrium, a microstate will therefore be represented by an energy density function.*

The canonical assembly has some important differences from the grand canonical assembly. The canonical assembly is defined as an ensemble of systems, each of which can share its energy with a large heat reservoir or heat bath. The system is allowed to exchange energy with the reservoir, and the heat capacity of the reservoir is assumed to be so large as to maintain a fixed temperature for the coupled system. The canonical assembly is not concerned with ensembles of particles, only the ensembles of energy in a reservoir.

2.1.4 **Real and potential flow**

A laminar flow of bulk gas around the cylinder can be defined by its streamlines or lines of similar properties. These streamlines can mathematically be predicted by the potential flow function, which is given by-

$$G(z) = z + \frac{1}{z} \tag{2-1}$$

where z relates to a potential function that describes a streamlines or flow sheet passing diametrically around the cylinder (Kreyszig, 2006).

This potential flow function only applies when the fluid is incompressible, inviscid and irrotational. This means that with the properties this fluid will obey the laws of conservation of mass and the conservation of momentum.

In real fluid flows, there is a separation of fluid flow from the cylinder caused by a mixture of pressure drag and skin friction drag. This separation of fluid flow is not described by the potential flow of fluids which assumes a smooth flow around the shape. Skin friction drag is the result of the interaction of the fluid with the surface and the effect of fluid viscosity

boundary layers. In general, for stationary bluff bodies such as cylinders then pressure drag is much greater than skin friction drag.

A potential flow or real fluids flow, as described by Euler's law, is scale variant and is therefore not applicable to the study of particles motion in the size that ranges from sub micro to millimetre size. It is not possible to determine the exact position of particles in respect to time in a fluid flow using Euler's law because the fluid is assumed to be a continuum. Some important principles that limit the study of fluid using potential flow mathematics are outlined in Appendix B.

2.1.5 Graph theory and the solution of perturbation series

Graph theory is a branch of mathematics that is connected to the study of planer graphs and their properties (Berge, 1962; Wilson & Beineke, 1979). A planer graph can be described as a graph that can be embedded in a plane and further explanation is available in Appendix C.

Perturbation theory consists of mathematical methods that are used to find approximations to problems that cannot be solved exactly. The mathematical method seeks to find an approximated solution by computing a series expansion from an exact solution of a similar problem. The solution of the position change of many-bodies in a fluid is one problem that is solvable using perturbation theory (Berge, 1962).

Graph theory and perturbation series has a mathematical link, since graph theory can assist in the simplification of perturbation series (Berge, 1962). How graph theory can simplify the solution of perturbation series is explained in Appendix D.

The following two graphs are examples of planer graphs

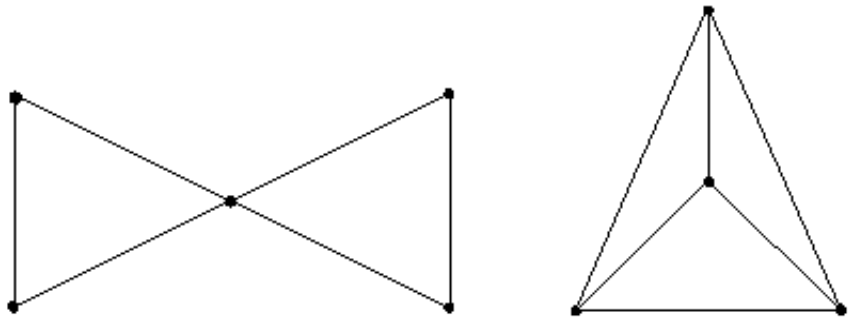

Figure 2-5. Examples of two planer graph, which are graphs that are embedded on a flat plane.

2.1.6 **Mayer functions**

Mayer's Functions are named after Joseph Edward Mayer and Maria Goeppert Mayer who investigated real gases and their molecular interactions (Mayer & Mayer, 1940).

In an 'ideal gas' molecular interactions between molecules do not occur, but for a 'real gas' they do. Mayer and Mayer developed a theoretical treatment of the virial coefficients in terms of cluster integrals. The term 'virial coefficients' refer to how far the real gas departs from the ideal gas; and the simplest model is two hard spheres molecules not bonded together; the proof is explained in greater depth in Appendix E.

2.1.7 **Meshed methods for the solution of partial differential equations**

The meshed method is a system for the numerical simulation of physical phenomena. In classical methods of solving elliptic partial differential equation leading to boundary value problems, a specific boundary condition is prescribed as one of Dirichlet, Neumann or mixed problems (Kreyszig, 2006). The solutions is obtained either by replacing the partial derivatives Laplace equation in the form of the velocity u for in the direction of vectors u_{xx} and $u_{yy,}$ as

$$\nabla^2 u = u_{xx} + u_{yy} = 0 \tag{2-2}$$

and for the Poisson equation in the form of eq.(2-2) as

$$\nabla^2 u = u_{xx} + u_{yy} = f(x, y) \tag{2-3}$$

with difference quotients.

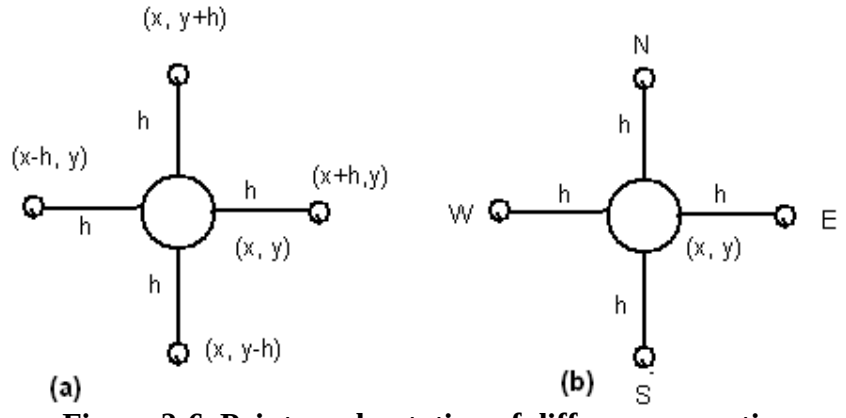

Figure 2-6. Points and notation of difference equation

In the example shown Figure 2-7, the approximation is taken around 5 points and together with the coefficient scheme is called a stencil and may be expressed graphically for Laplace

equation as $\begin{Bmatrix} & 1 & \\ 1 & -4 & 1 \\ & 1 & \end{Bmatrix}$ or for Poisson equation as $\begin{Bmatrix} & 1 & \\ 1 & -4 & 1 \\ & 1 & \end{Bmatrix} \boldsymbol{u} = h^2 f(x,y)$ using this stencil notation. The notational picture $\begin{Bmatrix} & 1 & \\ 1 & -4 & 1 \\ & 1 & \end{Bmatrix}$ is not a matrix but a stencil or a geometric arrangement of a nodal group that relate to the point of interest by using a numerical approximation routine.

At its simplest, a stencil is geometric arrangement of a nodal group that relates to the point of interest by using a numerical approximation routine. These stencils can be manipulated to solve the appropriate partial differential equation (ANSYS, 2001; Johnson, 1998; Versteeg & Malalasekera, 1995).

2.1.8 **Combustion of biofuels with coal**

The combustion of coal as a pulverised fuel has been practiced for over 100 years. In this operation, coal is converted to a fine dust and then blown into a PF boiler and once it is ignited, and further quantities of powdered coal keep the boiler operating. The boiler has varying temperature areas, near to the flame in excess of 1673K are recorded, while near the secondary and tertiary superheater temperatures in excess of 1173 K (Walsh, et al., 1990). The superheater consist of banks of approximately 40 mm diameter tubes through which a continuous supply of steam is fed. The surface temperature of these tubes can be up to 923K (Walsh, et al., 1990) and on contact with the hot surface the steam flowing internally becomes superheated. The steam is used to turn turbines and generate electricity through a generator set.

Energy crops biomass fuels are made more compact for easier transportation these types of biomass are cooked at atmospheric pressure in the absent of oxygen at a temperature of 400 to 520 K (Tumuluru, et al., 2011). This process is called torrefaction and after this process it can be densified, usually into briquettes or pellets using conventional densification equipment. Torrefaction also has the added benefit of reducing hydrogen volatiles and tars in the biomass fuel that can lead to pollution.

The combustion of coal and biomass mixtures can produce both depositions from fuel derived particulates or from the condensation of gaseous on all the combustor (fireside) surfaces. However, in the areas around the Ternary and Secondary superheater the temperature outside

the tubes can be in excess of 923 K. A schematic diagram of the path of the gas flow through a PF boiler is illustrated in Figure 2-7. As a consequence of the gas flow and the high temperature, in areas highlighted in blue and red in Figure 2-7 will be susceptible to potential damage from the corrosive constituents that make-up the bulk gas.

In the same areas around the superheater tubes there is likely to be very unstable gas flow with vortex flow patterns as the gas flow passes across the heat exchanger structures. As the consequence of this turbulent and vortex flow in these parts of the PF boiler will be an area where highest deposits are likely. In Figure 2-7 the red shaded areas is the location where the largest deposit yields will be found. In the areas in blue in Figure 2-7 are the areas of decreased but still significant yields of deposits can be found compared to the areas in red.

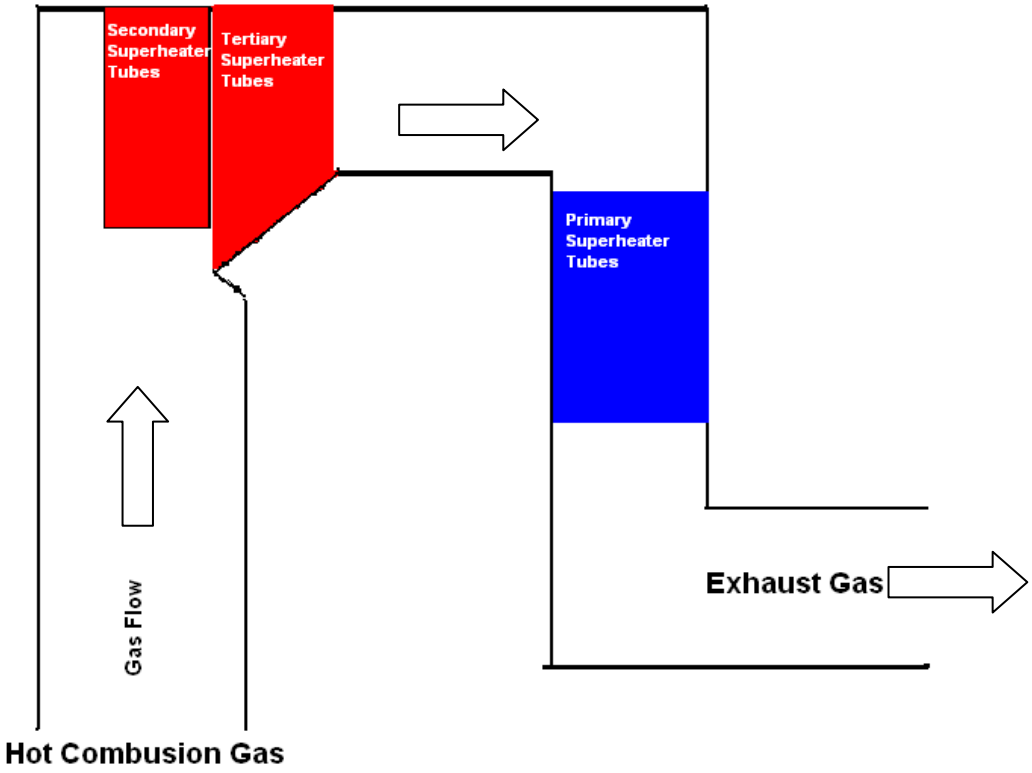

Figure 2-7. Gas flow through a PF boiler with the area shaded at which deposition occurs.

A debate has developed between researchers as to whether particulates are deposited from mechanism that centre on whether particle that impact directly on the tube (Jöller, et al., 2007) or mechanism of vapour deposition. The alternative hypothesis is that pressure increases because of aerodynamic effects a head of the tubes causes a vapour phase to come out of

solution (Baxter, 1998) of the gas flow. In the latter view of vapour deposition, the discussion is that particle form as droplets and transported to the tube surface by complex turbulent and vortex flows present around the tube bank. On impact with the tube the vapour particle combine with the silica-rich particles to form sticky agglomerates (Andersen, et al., 2000).

Current research has direct impact of particles onto tubes a more significant mechanism for the deposition of deposits onto tubes than thermophoresis (or Ludwig - Soret effect) (Hirota & Kimura, 1943), inertial impaction and eddy impaction (Andersen, et al., 2000). This proves an important point in that both particles dominate deposition and vapours dominate deposition are mixture of at least five mechanisms inertial impaction, thermophoresis, condensation, eddy impaction, and chemical reaction (Lokare, 2006). Which proportion of the 5 mechanisms are more significant, along with the approaches to modelling the predict biomass co-firing with pulverized coal has been reviewed in (Baxter, 1998; Baxter, 2004) these reviews make an appreciation of the physical size of particles, their potential sources and the temperature the particles experience within a PF boiler.

The use of biomass with coal is seen to be a significant step in the reduction of CO_2 (Energy Technologies Unit, 2007). Other emissions include SO_x and NO_x (Demirbaş, 2005) which are processed so as to remove them from the flue gas. Biomass is renewable and sustainable when the resource is managed and lately as much biomass is grown as the coal is extracted from mining sources. However, the use of biomass is more expensive than coal and therefore a subsidy is pay to the power generators.

2.2 Corrosive effects of co-firing biofuels on superheater tubes

Biomass comes from many sources, for example biomass such as sawdust, forest wood waste and straw or from fast growing crops like willow or Miscanthus grass (Energy Technologies Unit, 2007). The reactions that result from the combustion of biomass fuel are more sophisticated than the models concerning coal combustion alone. With biomass product the resulting gaseous and predicates will evolve or contain such elements as Si, K, Na, S, Cl, P, Ca, Mg, and Fe. These are much same products as those found in coal although biomass makes some of the unwanted products more available to develop corrosion problems in the plant (Srinivasachar, et al., 1990; Frandsen, et al., 1997; Robinson, et al., 1984). The principle corrosion constitutes Potassium and Chlorine is contained in the ‘char’ formed during

combustion. Char is formed partially through the combustion process while ash is formed after the combustion process. The mechanism for transportation from the combustor components to the heat transfer surfaces is by diffusion (for small particle), which directly impacts (large particles) or is with the high temperature associated in the process in a gaseous vapour (Walsh, et al., 1990; Basttisa, et al., 2000).

The effects of deposits can be radically reduced by co-firing with coal (Åmand, et al., 2006; Buhre, et al., 2007; Robinson, et al., 1984) or by inducing higher temperatures by Oxy-firing. Oxy-firing will reduce the corrosion from NaCl because the cadmium and magnesium in the biomass competes for chlorine with the sodium. In both instances the gas flow can enter a transition or turbulent flow regime range and have active unstable combustion reactions present (Magnussen & Hjertager, 1976), while some upstream reactions are corrosive to heat transfer surfaces. With other chemical reactors that involve cadmium and magnesium (Andersen, et al., 2000) are inhibiting to corrosion. The net result of the presence of cadmium and magnesium results is that these elements also compete with potassium, sodium any other chlorine holding compounds. The binding of cadmium and magnesium with chlorine reduces the potassium and sodium salt available to coat the tube fireside surfaces and this preventing further corrosion (Leckner, et al., 2004; Åmand, et al., 2006).

In short life and annual crops potassium is especially abundant (Davidsson, 2002) with sodium substituting in smaller amounts. In fast growing parts of the tree twigs and leaves the alkali content can be around 90% held in solution with water and is therefore readily vaporised. The release of alkali compounds causes formation of molten salts on the surface of the accessible tubes surface. In the process of combustion the silica sand is used in the fluidised bed, the silica and the alkali form low melting point eutectic mixtures. This alkali-silica mixture will form into agglomeration particle this can be a problem within the fluidised bed where it inhibits fluidisation.

In straw co-firing with coal there may be high chlorine content in the form of potassium chloride and sulphur chlorine (Mueller, et al., 2003); especially when burning bituminous coal. Through condensational and depositional process these give rise to deposits rich in potassium chloride and potassium sulphates on superheater components; which then gives rise to different degrees of accelerated corrosion. These potassium salts play a significant role in deposition because they can act as glue that bonds the individual fly ash particles together

(Srinivasachar, et al., 1990; Zhenga, et al., 2007). This makes it possible for silicon-rich ash particles to stick to the surface of the superheater forming a hard coating. This action is reported by the literature as temperature dependant with increasing temperature the silicon-rich coating will re-melt and form a harder surface coating.

Table 2-1. Principle Forms of Biomass and Coal Co-firing

Fuel Mixture	Fuel Description	Study/Pilot Plant	Positives	Detrimental	Ref.
Wood Waste/Coal	Sawdust/ US anthracite	Seward Station, USA	Low NO_x, SO_2 emissions	Unburned carbon in the bottom ash,	(Basttisa, et al., 2000; Leckner, et al., 2004; De & Assadib, 2009)
Fast grown Crops, non-wood plant waste /Coal	German Hard Coal Lignite/Straw	IVD Pilot Plant, Germany	Low initial investment cost CO2 reduction from existing coal-fired units Low NO_x emissions	Fuel handling. Emissions, ash deposits and corrosion through higher alkali release	(De & Assadib, 2009; Hein & Bemtgen, 1998; Jensen, et al., 1997) (De & Assadib, 2009; Hein & Bemtgen, 1998; Jensen, et al., 1997)
Waste/Coal	Chicken Litter/Low Rank US bituminous Coal	Laboratory-scale fluidised bed combustor Kentucky State University, USA	Easy to Handle	Increase of NO_x through higher N_2 volatiles emission Higher SO_2 emissions	(Li, et al., 2008)

In waste co-firing, corrosion and fouling is dependent on the fuel used. For example co-firing chicken litter with coal produces higher temperatures, increase CO emissions, the SO_2

emission are reduced; but higher NO_x emission (Li, et al., 2008). Other examples waste products and coal co-firing offer higher level of chlorine either as HCl or Cl_2, else in combination as salts with Na, K, Zn, Sn, Pb, (Becidan, et al., 2009; Albina, et al., 2004). In Table 2-1 the various options for biomass co-firing have been summarized based on specific pilot plant studies. There is normally a costs penalty in co-firing bio-mass with coal because of the loss of availability and efficiency which is reflected in the higher electricity unit costs.

To offset the higher energy price there are the economic incentives such as in carbon credits and/or lower pollution charges or taxes when there is a reduction in CO2 emissions. Carbon credits are a tradable commodity that permits the holder the right to emit one tonne of carbon dioxide or another greenhouse gas. It is important that the biofuel fuel cost is factored into the overall energy generation cost in such a way that the total fuel cost does not exceed the cost in burning coal without biomass. Hence 100% biofuel combustion is not normally undertaken and higher percentage values would also produce the unwanted effects of corrosion (Basttisa, et al., 2000; Obernbergera, et al., 2006). Studies have shown that 10-25% biomass is the optimum level for biomass – coal fuel ratio for many fuel/biomass combinations (Baxter, 2004).

2.3 Current deposition models using CFD and Finite Element Method

The use of Computation Fluid Dynamics (CFD) has been widely applied in many areas of deposition modelling, heat transfer and fluid flow (Magnussen & Hjertager, 1976; Patankar, 1980; Tomeczek, et al., 2004; Versteeg & Malalasekera, 1995; Wang, 2008). One key aim has been to understand experimental test on PF boilers by macro-scale numerical modelling. The overall objective in generalisation of experimental data sets by verifying the data sets validity against a numerical model is to widen the application of such data to physical circumstances that are similar, but not identical to the original experimental data sets. The data set is not normally produced from within a simulation, nor is the data set usually proceeded from any stochastic model approaches (Meneveau, et al., 1998) such as Monte Carlo analysis and very few published literature references make use of artificial intelligence (for example neural networks) (Makkonen, 1999).

Extensive research has been under taken to model fluidised beds in both coal only and coal/biomass co-combustion (Mueller, et al., 2003). This work has been exploited to generate

a complete numerical model of a fluidised bed boiler and generated a map of where deposits are prevalent in the fluidised bed boiler (Miltner, et al., 2008; Witt, et al., 1997). The findings of this research effort have been reported to have good qualitative agreement with real plant deposition patterns. Follow up work to this research output has driven a good representation of the deposition on banks of tubes (Kær & Rosendah, 2003; Tomeczek, et al., 2004; Tomeczek & Wacławiak, 2009). The considered approach is to use a commercial package (for example Fluent) to undertake the analysis using it as a stable framework to solve the turbulent fluid flow, gas and particle, combustion, heat transfer and particle transport.

If the standardised software packages offered commercially are not the capability to study a particular phenomenon, the short fall is substituted by a user defined function written in a script language or coded. These script codes will calculate deposition rate, thermo-chemical conversion and the 'stick fraction' of the fuel. Using this method the general result is a mechanistic departmentalisation of the combustion, transportation and deposition of the fuel mixture. It has enables the evaluation of the costs, availability and efficiency of coal/biomass co-combustion mixtures at an early stages and is widely use in the design of power plant. In simplifying the numerical models to fit the limit capabilities of applications these models will operate on, has been at the cost of accuracy and stability.

The detail science behind the attraction between particle, tube banks and sticking of the biomass onto tubes banks is often not considered in sufficient depth and wide approximation are made in the subsequent modelling analysis. One example of note in journal paper is the non-specific parameter such as 'stick probability' that represents the measure of probability that a particle will stick to tube surface. The computational science should expect a concise solution, but using this type of mechanistic approach locks in the user to using standard solution methods.

Another example, biased to software package standardisation, is when adopting a Lagrangian tracking model usually supplied with these commercial packages for particle motion in aerosols/fluids (Kosinski & Hoffmanna, 2005). This is perfectly acceptable for many applications, particularly if the flow regime is laminar. If the flow regime is turbulent this approach is not valid since the turbulence data set is not complete. The solution set of a turbulent flow will governed by the Navier - Stokes equation in which turbulent flow is not a closed solution. By a close solution it is meant that the solution has a finite set of data (Chow,

1999), but turbulence data set is chaotic quasi-periodicity and dynamical systems, therefore does not have a finite set of results. Without care in interpolation the turbulence data set will deliver a very unrealistic approximation.

To resolve these issues two methods are used, at low Reynolds numbers then direct numerical simulation (DNS). For higher Reynolds numbers the large eddy simulation (LES) is operated. The closure problem for LES is usually solved using an adaptive or Sub Grid Scale (SGS) models. An application of fractal interpolation to the Lagrangian tracking problem is an answer ((Salvetti, et al., 2006) this is not application offer in many commercial packages and so underlines the lag in application capability.

Closely examine the particle stick probability' and the mechanistic approach to capture of particle on tubes in more depth. Typically, the empirical data is applied to model the mass deposition rate using an equation that has following general form.

$$\dot{m} = BP_1P_2C_{p,m}w \tag{2-4}$$

where $\dot{m}$ = mass rate of deposition per unit surface area, kg/(m^2s)

B = constant (i.e. 6.2 x 10^{-5}).

P_1 = probabilities that the particles will impact the target surfaces.

P_2 = stick probability.

$C_{p,m}$ = concentrations of particles in the gas stream (kg/m^3)

w = gas velocity component perpendicular to local point of heat transfer surface (m/s)

This approach is has been reported by other researchers in this field (Richards, et al., 1984; Srinivasachar, et al., 1990; Srivastava, et al., 1997). They all offer the following method of obtaining P_1, P_2

$$\mathrm{P_1} = \frac{\mathrm{A_{duct}} - \mathrm{A_{free}}}{\mathrm{A_{duct}}} \tag{2-5}$$

where A_{duct} is the duct cross section and A_{free} is the cross section of the free path of the flue gas

$$\mathrm{P_2} = \frac{\eta_{\mathrm{ref}}}{\eta} \tag{2-6}$$

The speculation in these papers is the value of η_{ref} which each authors set as a different value with (Tomeczek, et al., 2004) siding with (Walsh, et al., 1990) and justifying their assertion with a call for further experimental work. The modelling is based on 2D modelling and does not consider secondary reaction in the gas flows; the latter aspect is acknowledged (Tomeczek & Wacławiak, 2009). The modelling of the 'stickiness' of particle in this mechanistic view has some drawbacks. The fundamental science behind the process that causes the particles to adhering to the surface of the tubes is overlooked. The phenomenon of deposition of particles on tubes can be better understood if the if the physics and chemistry of the problem is investigated. Latter in this thesis the modelling of particle deposition will be expanded with an alternative approach which allows for multi-body and multi-scale physics. Under a non-mechanistic or quantum system the 'stickiness' of particles becomes, in part, the probability of a particle undergoing a physical or chemical change.

The reactions in the combustion of biomass fuel, that is fuel containing plant material, is more sophisticated than the models concerning coal combustion with product such as Si, K, Na, S, Cl, P, Ca, Mg, Fe giving rise to ash fouling and 'slagging'. The principle corrosion constitutes Potassium and Chlorine is contained within the 'Char' formed after combustion. The mechanism for transportation from the combustor components to the heat transfer surfaces is by diffusion (for small particle) or direct impact (large particles). The effects of deposits can be radically reduced by Co-firing with coal (Buhre, et al., 2007; Åmand, et al., 2006; Robinson, et al., 1984) or inducing higher temperatures by Oxy-firing. In both instances gas flow rates after the combustion process can enter a transition or turbulent flow regime range and have active unstable combustion reactions present as (Brink, et al., 2001; Frandsen, et al., 1997; Magnussen & Hjertager, 1976; Miltner, et al., 2008; Spalding, 1976). While some upstream reactions are corrosive to heat transfer surfaces, other reactors such as Ca and Mg are inhibiting to corrosion (Mile, et al., 1994).

The basis for all the models presented here from other references, is marked on the formation of deposits derived from empirical results and not gaseous/solid multiphase's physics (Obernbergera, et al., 2006). The formation of a more complete model with gaseous/solid multiphase's physics and turbulent modelling using commercial CFD packages such as Fluent (ANSYS, 2001), as already stated usually, requires additional modules to cover the more complex chemistry after combustion. This includes coupling the transportation and reactor

rate models to the Fluent code (Magnussen & Hjertager, 1976). The prime solution model within commercial code is the use of SIMPLE type algorithms which are stable, provides good result and very robust (Versteeg & Malalasekera, 1995). However, the direct numerical simulation of turbulent is out of reach when applied to complex geometries and the solution is of 'accurate low order' (Di Mare, et al., 2004). This requires the flow regime and turbulence to be calculated before running the combustion and dispersion models simulation (Dudek, et al., 1991; Miltner, et al., 2008). The char particle interactions reactions often fall well below the resolution of the mesh which then affects the accuracy. The accuracy issues are then resolved by a dependency on non-continuum empirically derived models (Tomeczek, et al., 2004).

2.4 Mesh-free method of solving partial differential equations

The multi-scale aspects of deposition on superheat tubes are best implemented through a mesh-free approach (Li & Liu, 2002; Liu, et al., 1998; Melenk & Babuška, 1996). The mesh-free method is an approach that applies mathematical rigor and is based on a provable mathematical construct (Li & Liu, 2004). The mesh-free approach has been applied to combustion and fluid mechanics problems but not to the multi-scale problems of particle and vapour deposition. In this thesis this new method uses the interpolation of Partition of Unity to enable the solution Γ of the partial differential equation over a domain C* (Babuška & Melenk, 1997; Li, et al., 2008) as Figure 2-8.

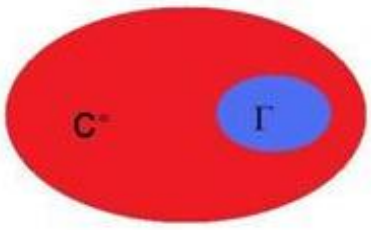

Figure 2-8. Partition of unity of the solution Γ of partial differential equation over domain C*

The association with the mesh-free method with finite difference method combine the strengths of both methods with higher order accuracy solution (Liszka & Orkisz, 1980). In brief outline of other workers progress in developing Least Square Finite Difference approach

LSFD, a solution space Γ is circumscribed an arbitrary series of points in geometric space as Figure 2-9.

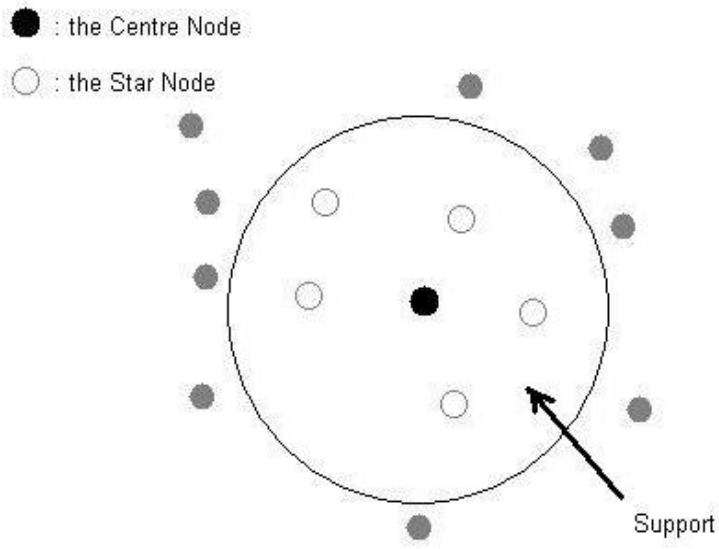

Figure 2-9. Least Squares Finite Difference Method with a selection of star nodes based local support at a centre node.

The centre node is positioned in the centre of the support circle with the Cartesian coordinates of (x_o, y_o). The area within the circumscribed circle that is labelled 'Support' in Figure 2-9 captures an arbitrary number star nodes that are referenced by a centre node. Together, the support area, the star node and the centre nodes provide a method of solving partial differential equations.

If the unknown solution to the differential equation is at a point (x_o, y_o) then the coordinate of each star node referenced to the local index to the centre node, (x_1, y_1), (x_2, y_2) … (x_m, y_m), becomes a Taylor series expansion that offers a solution method to the partial differential equation (Li & Liu, 2004).

Considering star node at (x_1, y_1), in Figure 2-9 if the collection of points of a scalar solution to the differential solution at the point (x_o, y_o) is represented as $f_0 = (x_o, y_0)$, the centre node then

$$f_i = f_0 + h_i \frac{\partial f_0}{\partial x} + k_i \frac{\partial f_0}{\partial y} + \frac{h_i^2}{2}\frac{\partial^2 f_0}{\partial x^2} + \frac{k_i^2}{2}\frac{\partial^2 f_0}{\partial y^2} + h_i k_i \frac{\partial^2 f_0}{\partial x \partial y} + \cdots \mathcal{O}(\Delta^3) \qquad (2\text{-}7)$$

$$l \leq i \leq m$$

here

$$h_i = x_i - x_0 \qquad (2\text{-}8)$$
$$k_i = y_i - y_0$$

Let

$$\{\delta f\}^T = \{f_1 - f_0, f_2 - f_0, \dots, f_m - f_0\} \qquad (2\text{-}9)$$

This follows that a series of linear algebraic equations will have a solution ($m \geq 5$)

$$[A]\{Df\} = \{\delta f\} \qquad (2\text{-}10)$$

With the non-square matrix taking the coefficients of the Taylor series expansion

$$[A] = \begin{bmatrix} h_1 & k_1 & h_1^2/2 & k_1^2/2 & h_1 k_1 \\ h_2 & \dots & \dots & \cdots & \dots \\ \vdots & \ddots & \dots & \dots & \dots \\ \vdots & \dots & \ddots & \dots & \dots \\ \vdots & \dots & \dots & \ddots & \dots \\ h_m & \dots & \dots & \dots & h_m k_m \end{bmatrix} \qquad (2\text{-}11)$$

Where the five unknown derivatives at point (x_0, y_0) are

$$\{DF\}^T = \left\{\frac{\partial f_0}{\partial x}, \frac{\partial f_0}{\partial y}, \frac{\partial^2 f_0}{\partial x^2}, \frac{\partial^2 f_0}{\partial y^2} \frac{\partial^2 f_0}{\partial x \partial y}\right\} \qquad (2\text{-}12)$$

The solution can be obtained from weighted least square minimisation (Golub & Van Loan, 1998) if applied to a uniform particle distribution then a five or nine point stencil can be used (Mohanty & Sigh, 2006; Press, et al., 1989). It is should be noted that the mesh-free approximation are more accurate than the standard finite difference model as Figure 2-10 demonstrated and this can increase if the stencil point numbers are increase (Mohanty & Sigh, 2006).

Considering matrix A, then for 5 or 9 point discretization then if $m \neq n$, where 'm' is the number of horizontal element and 'n' the number of vertical elements. This leads to the adoption of Single Value Decomposition (SVD) as one step to finding the least square minimisation (Golub & Van Loan, 1998) and hence the solution. The SVD is computational more efficient than solution by TDMA algorithm (Gu, et al., 1994). The SVD is not subject to

problems of division by zero as are most Gauss Siegel schemes (Golub & Van Loan, 1998) and also enables the parallelisation of the problem (Berry, et al., 2005).

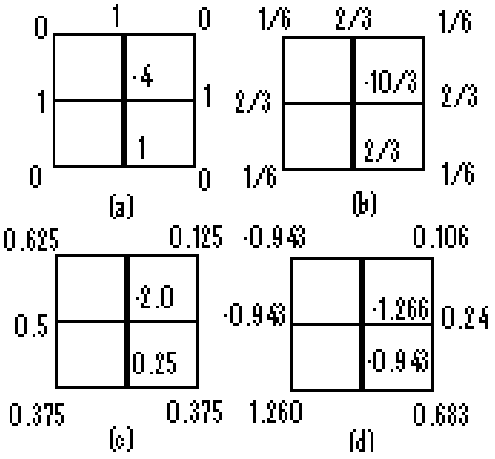

Figure 2-10. Comparison between finite difference (a, c) and mesh-free (Li & Liu, 2004) finite difference (b, d) for the same solution.

The gas-solid interaction of 'char' in a gas flow stream is typically modelled by either an Eulerian–Eulerian or else Eulerian–Lagrange models. There are several commercial codes that use one or both methods such as PDE Solutions Inc or Fluent (Frank, 2001; Valentine & Smith, 2002). The Eulerian–Eulerian method is a continuum method based on the average the particle/gas phase or particle/gas/time in terms of volume fraction of the solid particle to gas phase (Patankar, 1980).

The Eulerian–Lagrange applies the conservation law of matter and uses the Newton Laws of motion to track the movement of the particles in the fluid. While Eulerian–Lagrange models are more realistic than the more elementary Eulerian–Eulerian models they take no account that the forces propelling the particles don't generally combine additive. It is also true that Eulerian–Lagrange or Eulerian–Eulerian cannot manage the dispersals of char because of continuous chemical breakdown of the char constitute. The Eulerian–Lagrange is computational expensive since a large number of particles must be location and tracked in achieving realistic results (Mueller, et al., 2005). The Eulerian–Lagrange cannot account for particle–particle and particle–wall interaction via the fluid aerosol interaction (Andrews & O'Rourke, 1996). The equivalent mesh-free methods to the multiphase component of the problem, has either the Material Point Method (sometimes called Particle in Cell Method) or

alternatively the Lattice Boltzmann Method. The Material Point Method considers the total mass or volume of the continuum and divides by the N particle flowing, (Li & Liu, 2004) and is a dual description (Lagrangian and Eulerian) method. With a Multiphase particle in cell method offer a more detailed look at the motion of both the gas phase and solid particle suspension with a easier solution of the mass and momentum than with Eulerian based methods without the Lagrangian mesh.

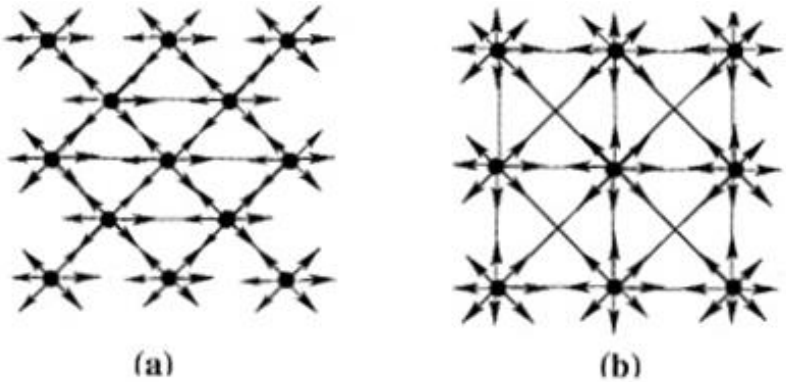

Figure 2-11. Lattice and velocity directions; (a) triangular lattice; (b) Square Lattice

The Lattice Boltzmann considers the average position of a particle in a gas stream within a cell node (Figure 2-11). All theses discrete particles are summed at nodal position to obtain the macro-scale particle density. In a similar way the particle momentum is obtain by averaging the momentum of all the particles at a node point (Liu, et al., 2000). Successful implementation has been made for a gas/solid passing over a cyclical bar and reaction-diffusion problems (Li & Liu, 2002). In common, most mesh-free methods the Lattice Boltzmann Method offers higher resolution with lower computational overheads and can be solved locally, explicitly, and efficiently on parallel computers.

The foundation of most if not all modelling of particle and deposition on superheated tubes in PF Boilers is based on commercial CFD packages such as Fluent by analysis (Tomeczek & Wacławiak, 2009). The modelling is usually in 2-dimensions as 1–dimensional provides a low compliance with the observed results. This limits the modelling of the trajectory of the particle and the relation of the conversion of particles to gas combustion while the particle is in flight in the boiler. It is also not clear how commercial CFD packages can replicate the condensation of gaseous alkaline products because of a change in pressure in the gas. Such

gaseous products can exist in liquid/vapour phase at one instance, then because of a pressure or local temperature change; return to the gas/vapour phase.

This is essentially a multi-scale problem for which conventional meshed CFD programs offer inadequate solutions to the partial differential equation (PDE). It's important here to consider scale length in physics, since at different scale length then different types of physics are used. If the scale of the particles is macroscopic scale (the scale at which our eyes can see) then a continuum model will provide a reasonable approximation. If the particles are mesoscopic (approximately 100 nm (the size of a typical virus) to 1,000 nm) then quantum mechanics is appropriate.

There are solution to the PDE's that encompass the problems geometric scale (multi-scale), molecular interaction both between gas and tube chemistry, particle and tube impact and continuum based fluid motion are available. The least squared finite difference method (LSFD) is a general method of solving PDE's and there will all solve the same encompassed the problems (Li & Liu 2004).

Using the finite difference mesh-free method (Liszka 1984; Liszka & Orkisz 1980) it is possible to devise a numerical switch that conserves the time step between laminar Bernoulli flows into Green – Taylor vortex flow around tubes. This 'switch' commonly known as predictor-corrector one example used from finite element method is the Petrov-Galerkin (Abimael & Fernandes, 2009; Atluri, et al., 2006; Babuška & Melenk, 1997; Frey, et al., 2008).

The plot of the complex analysis function of the flow of a gas around a tube in laminar flow is shown in Figure 2-12 and is called the potential flow (Kreyszig, 2006). The potential flow equation that plot Figure 2-12 is a complex analysis function defined in eq. (2-13). The potential flow does not completely model the flow around a tube because it does not include phenomena such as drag or shedding vortex. In Appendix B there is further information on potential flow theorem.

$$F(z) = \phi(x,y) + i\psi(x,y) = z + \frac{1}{z} \tag{2-13}$$

For a mesh-free solution of the potential flow inverse function then points are set around the tube where there is solution of the streamline function ψ or also called Bernoulli flow (i.e. along the lines drawn in Figure 2 12 that pass around the tube).

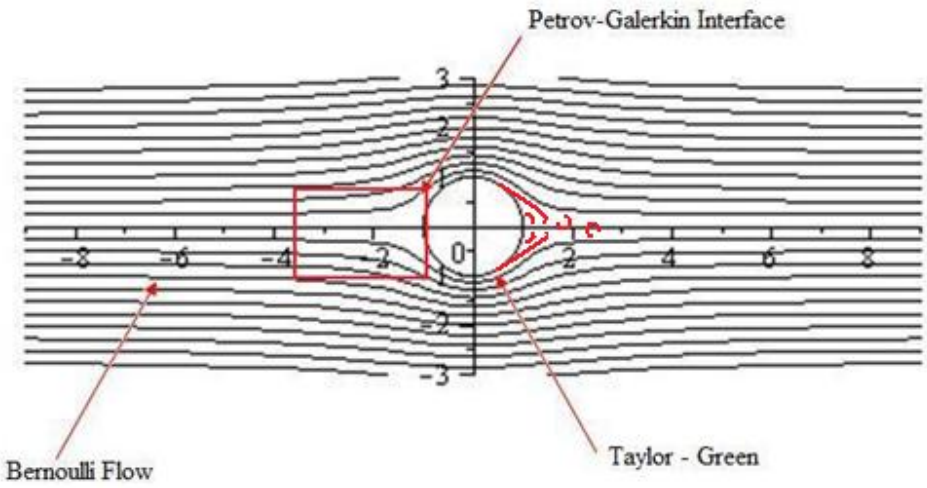

Figure 2-12. Transition between Bernoulli and Taylor – Green vortex flow equations using the Petrov – Galerkin predictor-corrector method.

The predictor-corrector extrapolating a polynomial fit to the derivative from the previous points so test the condition where Bernoulli flow translate to Taylor-Green vortex flow. These methods provide a numerically stable method and have been use to resolve gas – solid reaction (Liu, et al., 1998).The disadvantages of this method are that it uses past information to make prediction of future event. The landing of larger particles on tubes surfaces offer three possible choices either, bounce off the tube, agglomerate with the surface chemistry or flow in the boundary layer and vortex flow around the tube.

At the molecular level scale, the positional/time integral of where gas molecules interact with a tube surface is statistical representation that maps the path of the molecular track. The positional/time integral of the path of the molecule track is a function of Boltzmann constant because of the relationship between the energy of the gas molecule with the temperature. There are examples in the literature of molecular tracking that have use either a Finite Element Method using with Petrov – Galerkin interface (Abimael & Fernandes, 2009; Frey, et al., 2008) or with the lattice Boltzmann method (Chen & Doolen, 1998) Compared to other methods discussed previously, the finite difference method only brings simplicity in solving problems involving molecular impacts because of the use an artificial structure such as a stencil.

2.5 Current vapour deposition models

It is clearly easier to focus on the capture of particles of any size, through the use of laser Doppler velocimeter (Backman, et al., 1999), or through insertion probes into test rigs or boilers or visualising the flow with CCTV cameras (Zhou, et al., 2007) to see where the deposits form on the probe. With vapour deposition, it is substantially more difficult since the vapour will invariably form droplets of liquid which migrate in the gas flow to the tube surface.

The two mechanisms for the deposition of vapours onto the surface of the tubes are heterogeneous deposition and homogeneous deposition of vapour. The heterogeneous deposition and homogeneous deposition of vapour make two of the various modes of vapour deposition. The heterogeneous deposition and homogeneous deposition of vapour must be undertaken from thermodynamic analysis and most papers focus on the formation of depositions onto the tubes via the condensation onto ash deposition (i.e. heterogeneous vapour deposition) (Andersen, et al., 2000). The gas modelling is usually undertaken using thermodynamic steady state assumption based on the physics of aerosol formation (Jöller, et al., 2007). The role of homogeneous deposition is normally considered to be of less importance than heterogeneous deposition in the formation of alkali coating on tubes (Jöller, et al., 2007). However, in terms of boundary deposition and the deposition of NaCl it can be very important (Pyykőnen & Jokiniemi, 2003).

The deposition of NaCl is considered one of the pathways in which alkali and chlorines are released. The release of alkali and chlorines is considered an important source of corrosion. The strong chemical reaction between chlorine with chromium has important financial consideration in power plants. Power plant heat exchangers are manufactured from high chromium alloy steels and are therefore subject to corrosion through chlorine attack (Nielsen, et al., 2003).

Whether heterogeneous or homogeneous deposition is the more important issue for corrosion on fireside superheated tubes is in some ways immaterial, since in every way the net result is damage to the tubes surfaces and the failure of the plant. The movement of gas from vapour to liquid is a problem of scale and the assembly of molecules in a thermodynamic state. The path the molecules take and the thermodynamic state can be resolved mathematically with the equation of state and an understanding the statistical mechanics of the gas/vapour/droplets

ensemble. This will also enable the assessment of the type and chemical composition of matter on the superheater tubes. When considering coal only combustion then (Srivastava, et al., 1997) has review the chemical composition and mechanism for deposits on a range of pure carbon steels to high temperature Cr, Ni, Mo, steels. When burning biomass (Oakey, et al., 2003), shows that accelerate erosion-corrosion wastage on the tube and metal will occur below the ash deposits on tubes surfaces and combustor wall surfaces. Predicting the rate of deposits formation has been widely studied (Becidan, et al., 2009; Becidan, et al., 2009). There has been considerable research into why layers of alkali salts will occur below the ash deposits on tubes. The sub-layering of alkali salts below the ash is associated with models that use a steady-state thickness increase and the known binary phase systems.

The sub-layering of alkali salts below the ash that model any non-steady state behaviour in deposition rates adopts some empirical relationship that includes particle stickiness constant. The use of a stickiness constant to model the sub-layering of alkali salts below the ash is used widely in the literature (Backman, et al., 1999; Tomeczek, et al., 2004; Tomeczek & Wacławiak, 2009).

Since the behaviours of combustion processes are chaotic, it pulls in some comment on the validity of the quasi-static approach. Taking a closer examination of this statement, since it is clear the tubes area in the turbulence mode and quasi-static models have to taken with care. It would be better to examine the energy level and consider the vapour fluid boundary interims equations of state.

The partition function or configuration integral describes the statistical properties of a system in thermodynamic equilibrium. The partition function or configuration can be used in its mathematical abstraction form to describe a dynamic system (i.e. particle motion). The mathematics of partition function is involved but selecting this approach will develop a model that will apply for condensing matter physics and also for the dynamics of combustion products particles.

The partition function of the statistical properties of a system in thermodynamic equilibrium will model the phase change of gaseous furnace products. The basic assumption is that particles at the point of a phase change from gas to vapour form more permanent bonds. In statistical mechanics, the properties of a system of interacting particles are described using the

partition function. For N non-interacting particles, the system is described by the Hamiltonian (Hill, 1987).

$$H_0 = \sum_{i}^{N} \frac{p_i^2}{2m} \tag{2-14}$$

Where H_0 is the Hamiltonian operator that corresponding to the total energy of the system, p_i is the particle momentum and m is the mass.

If the quantum-mechanical energy levels of matter are assumed to obey classical mechanics then Mayer functions $f_{ij}(\gamma_{ij})$ can be used (Bieneke, 1979). The assumption is that either particle or molecule existed as rigid spheres and prevented from approaching each other, more closely than one particle or molecule diameter. Defining the interaction behaviour ϕ as characterized by a pair of molecules i and j at distance r_{ij}. The function *f* has the property of being zero whenever the radius r between interacting molecules i and j with interaction behaviour ϕ then $\phi(r_{ij}) = 0$, that is when r_{ij} is greater than one molecule diameter. Clearly two molecules cannot be less than one molecule diameter in separation since it would cause an overlap.

$$1 + f_{ij} = \exp\left(-\frac{\phi(r_{ij})}{k_B T}\right) \tag{2-15}$$

When two molecules i and j are very close together then the exponential term is small, and f_{ij} is approximately -1. For real molecules, f_{ij} is approximately -1 when r_{ij} is small and passes through 0 as $\phi(r_{ij}) \rightarrow$ large.

$$f_{ij} = \begin{cases} -1, \text{if } r_{ij} < d \\ 0, \text{otherwise} \end{cases} \tag{2-16}$$

The use of the same Mayer functions to model the reactions of particle to the boundary, impact and vortex behaviour is explored latter as a mathematical development of this principle (Mayer & Mayer, 1940).

The reaction of molecules at the surface of the tube is the combination of the Gibbs free energy and the kinetic energy (Matsumoto, 2000). The state of the matter at the surface of the tube is that of condensing gaseous products resulting in change in velocities of all the molecules in the assembly (otherwise the change in kinetic energy) which reduces to a

configuration integral Q(V, T). If the relative molecular distances in Cartesian coordinates are considered a sub system dx, dy, dz and the distance between molecules is of radius r; it forms a partition function *Q*.

$$Q = \prod\nolimits_{k+1 \geq i \geq j \geq 1} f_{ij} dr_1 \cdots dr_{k+1} \tag{2-17}$$

Hence the partition function *Q* in eq. (2-17) can be integrated into the classical configuration integral as

$$(V, T) = \frac{1}{(3N)} \int \text{All possible molecular configuration} \int \exp\left(-\frac{\phi}{kT}\right) Q \tag{2-18}$$

where the integration is taken over all possible configurations of N molecules within the volume V, each configuration being weighted according to its interaction energy represented as ϕ, k_B is Boltzmann constant and T the temperature above absolute zero.

The solution of eq. (2-18) can be derived directly from the decomposition of *f* in eq. (2-15), to rewrite the integral to express all the possible molecular assemblies at the surface of a tube of the condensing gaseous products as

$$Q(V, T) = 1 + (f_{12} + f_{13} + \cdots) + (f_{12} f_{13} + \cdots + f_{12} f_{32} + \cdots) + (f_{12} f_{13} f_{23} + \cdots) \tag{2-19}$$

In this form it is possible to express these integrals in graphical-theoretical terms in such a way that there is a one-to-one correspondence between vertices associates with a graph. Hence, the possible combinational molecules reactions on the tube surface are reduced to vertices, such that if a reaction on the surface is promoted, then vertices that are connected and have the minimum free energy; else an unconnected point have free energy approaching infinity and no reaction is possible.

For terms 1 to N in terms of f_{ij}, the vertices are joined by edges, where the f_{ij} term is absent this edge is omitted. These can be formed into ‘Husimi’ Trees’ or also known as ‘Cacti’ (Husimi, 1950).

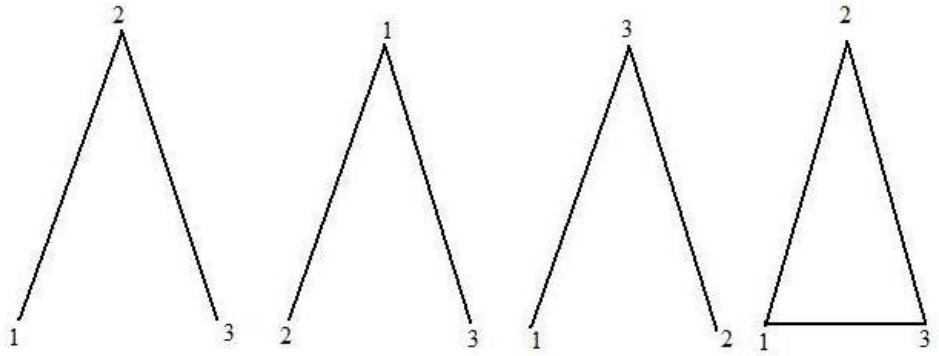

Figure 2-13. A series of connected graphs that illustrating the possible combination for f_{ij}.

Turning to the condensation of gaseous vapour onto tubes, then for changes in the state of the gas to condensate key state variables are pressure, volume and number of moles. From the classical ideal gas law is not adequate to account for the agglomeration of particles, where p is pressure, V is volume, n is the amount of substance, R is the gas constant and T is the Temperature.

$$pV = nRT \tag{2-20}$$

Therefore, the Van der Waals equation of state; with its model of attraction and repulsion of particles offers a better model.

$$\left(p + \frac{a'}{V}\right)(V - b') = RT \tag{2-21}$$

With eq. (2-21) the terms *a'* are the attraction parameter and *b'* the repulsion parameter, V is volume; P is pressure; R is the ideal gas constant and T is temperature A note on the strong evidence that Van der Waals forces inferred by *a'* and *b'* parameters are key to the agglomeration ash particles in fluidised beds is worth mentioning (Latva-Somppi, et al., 1997).

The likelihood of deposits will form on the surface of tubes is the measure of chemical potential called fugacity in the form of adjusted pressure. The energy exchange in the form of work during a deposition is defined by a form of Boltzmann entropy equation.

$$S = k_B \log W \tag{2-22}$$

where S is entropy, k_B is the Boltzmann constant and W is the number of microstate. In any thermodynamic system it's not possible to have such a complete information of the all the microstates of the system as eq. (2-22) suggests. Therefore, the information of the system concerning number of microstates W in eq. (2-22) is therefore approximated using a probability density function Q. The grand canonical ensemble is a study of a system that changes both energy and particles with a reservoir. Therefore this fixes the average values E of the energy H, as E = {H} and the number of particles **N** with the average number of particles $\overline{N}$, as $\overline{N} = \mathbf{N}$ that make up all the possible microstates W. For any set of states *i* possessing energy E_i, then the fractional number of particles N_i/N occupying any single state is

$$\frac{N_i}{N} = \frac{g_i e^{-E/(k_B T)}}{Z(T)} \tag{2-23}$$

where k_B is the Boltzmann constant, T is temperature, g_i is the degeneracy (meaning the number of states having the energy E_i and Z(T) the partition function. The partition function is defined as

$$Z = \sum_{N=0}^{\infty} \sum_{i} \mathcal{Z}^N \exp(-E/k_B T) \tag{2-24}$$

where $\mathcal{Z}$ is the canonical ensemble, E is the energy at state i of particle N, k_B is the Boltzmann constant, and T is temperature. The Boltzmann distribution for the fractional number of particles in a canonical ensemble is defined as eq. (2-23). The Boltzmann distribution is often expressed in as the normalized form of two Lagrange multipliers (Gross, et al., 1994; McComb, 1994) α and β, by

$$D = \frac{1}{Q}\exp(-\beta H + \alpha \mathbf{N}) \qquad Q = \mathrm{Tr}\exp(-\beta H + \alpha \mathbf{N}) \tag{2-25}$$

where D is the density operator, Q is the grand partition operator function, H is the Hamiltonian for of average energy (see Appendix E), and **N** is the eigenvalue average number of the integer number of particles $\overline{N}$. Both H and **N** serve to fix the value for energy and the

number of particles in a reservoir. The 'Tr' is the trace operator of the matrix that contains all the microstates constituents, in which H and **N** will be two constituents

$$\mathcal{H} = \bigoplus_{\mathrm{N}} \mathcal{H}^{\mathrm{N}} \tag{2-26}$$

The density operator D acts in a Hilbert space $\mathcal{H}$ that is the direct sum of $\mathcal{H}^N$each of which describes a fixed number of particles *N*.

In non-relativistic quantum mechanics the number of particles is conserved, which not the case for relativistic quantum mechanics. In relativistic quantum mechanics, the particles are electron, positrons and sub atomic particles. The number of relativistic quantum particles is not conserved. For a gas with many particles the appropriate form of eq. (2-23) for a Boltzmann distribution, is where the Lagangian multipliers λ_i is concerned with the conservation law of matter. Where the chemical potential of a system is the subject of a study, then the Lagrangian multipliers λ_i is directly related to chemical potential μ. As the chemical potential μ is bound by the conservation law of matter, then non-relativistic quantum mechanics is the appropriate form. Therefore in a gas with many particles the chemical potential of a system when at equilibrium, share the same Lagrangian normalised multipliers α and β as the mean energy and mean particle number; thus α, β can be expressed in terms of temperature and chemical potential (Le Bellac, et al., 2004).

$$\beta = \frac{1}{\mathrm{k_B T}} \qquad \alpha = \frac{\mu}{\mathrm{k_B T}} \approx \mathrm{F} \tag{2-27}$$

The Lagrangian λ_i multipliers is normalised with Boltzmann constant k_B to form Lagrangian normalised multipliers α and β. This abbreviation of α and β makes it easier to bridge between microscopic and macroscopic descriptions of an assembly. This resolves into the well known bridging equation of Helmholtz free energy *F* as

$$F = -k_B \mathrm{T} \ln Z \tag{2-28}$$

$$F \approx Z = f = e^{\frac{-F}{k_B}} = e^{-F\beta} = e^{-\alpha}$$

The fugacity f (or sometimes Z) is defined as the potential for a change in state and is also adopted to define the chemical potential of a chemical reaction. Therefore, from eq. (2-27), fugacity for an ideal gas is

$$f = e^{-\beta\mu} = e^{-\alpha} \tag{2-29}$$

The numerical modelling of this potential can be undertaken on a spreadsheet (Lwin, 2000). The equation of state used to determine the fugacity is the Peng-Robinson, a form of Van der Waals equation (Peng & Robinson 1976) as eq. (2-29). However, care is required because the fugacity is substance specific (Atkins & De Paula, 2003) therefore in computational modelling using fugacity adds an unwanted complexity.

$$p = \frac{RT}{V_m - b} - \frac{a\alpha}{{V_m}^2 + 2bV_m - b^2} \tag{2-30}$$

Where p is the pressure, R is the gas constant, V_m is molar volume, T is the temperature with α, a and b are constants determines as

$$\alpha = \left(1 + (0.37464 + 1.54226\omega - 0.2992\omega^2)(1 - T_r^{0.5})\right)^2 \tag{2-31}$$

$$T_r = \frac{T}{T_c} \tag{2-32}$$

$$\omega = -\log_{10}(P_r^{sat}) - 1 \tag{2-33}$$

where T is absolute temperature (Kelvin temperature scale), T_c is the critical temperature and, ω is accretion factor.

$$a = \frac{0.45724R^2T_c^2}{p_c} \tag{2-34}$$

$$b = \frac{0.7724RT_c}{p_c}$$

The factors 'a' and 'b' are determined from the critical pressure (P_c) and critical temperature (T_c) at which condensation occurs.

To factor in the rate of deposition ($\dot{m}_{d,t}$) on tubes per unit surface area is determined from the partial pressure as

$$\dot{m}_{d,t} = \dot{\beta}\frac{\dot{p}_i - p_{si}}{p}p_g \tag{2-35}$$

Where p_i is the partial pressure (Pa) is, p_{si} is the saturation pressure (Pa), p is the absolute pressure (Pa), $\dot{\beta}$ is the mass transfer coefficient (m/s) and p_g the gas density (kg/m^3) (Tomeczek, et al., 2004). The partial pressure is directly related to the fugacity *f* by the fugacity coefficient ϕ for a real gas.

$$f = \phi p_{si} \tag{2-36}$$

The fugacity coefficient ϕ overcomes the reservation concerning the usefulness of fugacity in equations of state calculations.

Calculating the mass transfer coefficient $\dot{\beta}$, the *i*th component in the reaction 'set'

$$\dot{\beta} = \frac{ShD_i}{d} \tag{2-37}$$

where Sh is the Sherwood number or also called the mass transfer Nusselt number a and D_i is the diffusion coefficient of *i*th component through the flue gases, (m^2/s). A list of dimensionless groups is presented in Table 2-2 at the end of this chapter.

2.6 Discussion and conclusions

The literature search has presented current ideas in the field of deposition modelling and a review of areas of research. While reviewing the field of deposition modelling, alternatives that open the discussion on how to replicate the entire physical phenomena link to this problem have been explored.

Deposition is a complex occurrence with many facets as outlined in Figure 2-14, ash in various sizes moves in number of directions. Larger particles fall as bottom ash, lighter particles that sit contain combustible material enter a burnout phase and a phase change. Some of the volatiles will form a vapour and at changes in the local temperature will condense either onto fly ash or to reach a critical temperature and change state in to liquid drops. It is know that the fly ash will have a diameter such that d_m < 100µm (Frandsen et al. 1997) and will undergo several transformation, nucleation and coagulation before leaving the boiler. When bulk of ash is very small (d_m <1 µm), most will not impact the tube but will continue in the flow streamlines around the tubes. The brake away of the streamlines in the turbulence

wake downwind of tube can deposit particles on the downwind side of the tube (Tomeczek & Wacławiak, 2009), the most likely mechanism being turbophoresis and Brownian motion.

The vapour-liquid formation forms an aerosol (together with particles of fly ash) and in the slightly higher pressure in front of the tube condense homogeneous on fly ash particles or heterogeneously from vapour. In the slightly higher pressure in front of the tube particles move at low velocity and may impact the tubes. This low velocity motion of particle impaction can be characterised as a drift motion with the predominate mechanism assessed as being by thermophoresis (Jöller, et al., 2007).

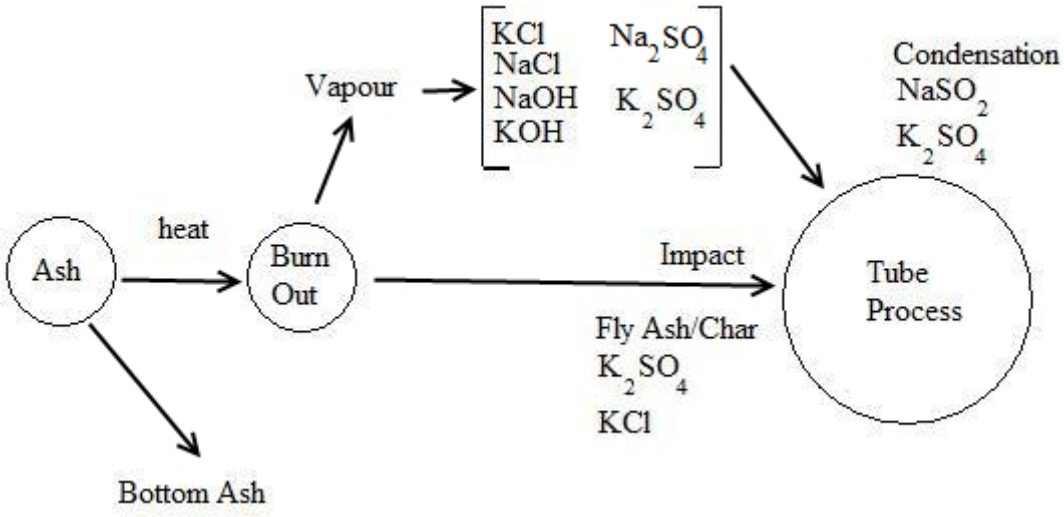

Figure 2-14. A Schematic diagram of PF Boilers ash conversion

The use of CFD to model deposition has draw some interesting result and is often used to support these assumptions. This has some merits, but care must be used; so that the CFD algorithm in operation is not outside its design limits. The user must be aware of some flow regimes display steady state behaviour while other follows a deterministic non-periodic flow (Lorenz, 1962), the same can be applied to the chemical reaction of alkali and chloride deposition on the tubes. Overall the models are mechanistic so therefore offer little insight microscopic behaviour of the system and can see only at a large scale. In any study of the motion of particles, only a rough approximation of position is possible. Ash corrosion of tubes are modelled based on careful studies of the deposit microstructure (Skrifvars, et al., 2010), the study of these structures is outside the underlining technology of CFD that of finite difference based meshed solvers. Ash deposit microstructure influences the mechanical and

transport properties of the bulk gas, by impacting the degree of connection between particles and the porosity of heat transport through the deposit (Baxter, 1998).

A CFD model cannot determine the chemical constitutes of the fly ash, the resulting particle size or the final location any group of particles will land without reference to verification by experimental test (Wang, 2008). This is not true where the prediction is of the deposits structure in complex arrangements of superheater tubes. Given a large scale model of tube deposits, the CFD commercial package Ansys Fluent allows not only the rate of deposition but also the shape and size of the deposits of the final deposit film (Mueller, et al., 2003; Tomeczek & Wacławiak, 2009) if users define subroutine (UDS) is coded. These properties are also available by burning the fuel in a controlled rig or by studying the full scale power plant after a period of time (Lind, et al., 1997). In any model using this pattern of experimental test supported by CFD modelling, the CFD model must undergo comprehensive sensitivity analyses to check for their physical relevance (Liu, et al., 1998). This is especially true if the CFD mode represent a physical phenomenon by applying the same numerical code outside the confines its initial validation data.

This review of CFD combustion and deposition modelling has looked at the limitation and has considered other methods of modelling combustion and deposition. What limits the wholly CFD approach in this instance is the reliance on meshing that effects accuracy of the solution. This can lead to the inability to model a multi-scale problem and the possibility of the modelling systems exhibiting non-determinate periodic instability behaviour either from the numerical solver or from an ill-defined meshing system Setting the modelling construct based extensively on exact solution reduces these factors and improves the reliability and accuracy of the modelling.

Table 2-2. Dimensionless Groups

Dimensionless group	***Equation***	***Constants***	***Description***	***Ref.***
Knudsen, Kn	$\mathrm{Kn} = \frac{\lambda}{\mathrm{L}}$	λ=mean free path L=length scale	Mean free molecular path	(Johnson, 1998)

Mach, Ma	$Ma = \frac{U_\infty}{c_s}$	U_∞= Velocity c_s= speed of sound	Free speed as a function of the speed of sound	(Johnson, 1998)
Nusselt, Nu	$Nu = \frac{hL}{k_f}$	h = convective heat transfer coefficient k_f=thermal conductivity L = characteristic length	Heat transfer with forced convection	(Johnson, 1998)
Péclet, Pe	$Pe = \frac{LV}{\alpha} = Re \cdot Pr$	L = characteristic length V = velocity α = thermal diffusivity	Advection–diffusion problems	(Johnson, 1998)
Prandtl, Pr	$Pr = \frac{\nu}{\alpha}$	ν = kinematic viscosity α = thermal diffusivity	Advection–diffusion problems	(Johnson, 1998)
Reynolds, Re	$Re = \frac{Lv\rho}{\mu}$	ν = kinematic viscosity L = characteristic length ρ= density μ = dynamic viscosity	Ratio of fluid inertial and viscous forces	(Johnson, 1998)
Schmidt, Sc	$Sc = \frac{\nu}{D}$	ν = Kinematic Viscosity D = mass diffusivity	ratio of momentum diffusivity (viscosity) and mass diffusivity	(Frank, 2001)
Sherwood, Sh	$Sh = \frac{\beta D_i}{d}$	β= mass transfer coefficient L = characteristic length d = mass diffusivity	Mass transfer with forced convection	(Frank, 2001)
Stokes Number, Stk	$Stk = \frac{\tau U_o}{d_o}$	τ = relaxation time U_o = fluid velocity d_o = characteristic length of obstacle	Particle dynamics	(Fuchs, 1963)

Strouhal Number, St	$St = \frac{fL}{V}$	f = frequency of vortex shedding L = characteristic length V = velocity	Oscillating/ Vortex flow mechanisms problems	(White, 2008)

3 Particle Impaction Deposition

3.1 Combustion models

Taking an overall view of coal and biomass combustion, large progress has been made to understand the deposition mechanism on heat exchanger surfaces. It is commonly asserted that computational modelling of these processes has not been successful for the following reasons:

- The application of 3D codes from commercial codes to deposit is possible, but codes have not the modules to deal with mineral matter transformations and inorganic vapours. Instead reference state that specially written code is used to perform these functions (Jöller, et al., 2007; Peng & Robinson, 1976).
- Condensation of vapours from hot gases on heat transfer surfaces has not been fully developed for coal combustion. The use of thermodynamics and dimensionless groups is seldom used in references in this area of research preferring to use an aerosol method in the actual CFD modelling.
- Only the concept of stick particles have been modelled, particles adhere to metal surface in PF boiler because particle or the surfaces they land on are 'sticky' (Tomeczek, et al., 2004).
- The approach to the growth of deposits on metal surfaces has been largely 'mechanistic' (Witt, et al., 1997).

When opting for a study of vapour deposition it's noted that many journal papers have been from point of deposition growth from both solid particles and/or condensing vapour. To simulate the composition the overall aim has been to identify the method of formation and composition of the deposits. These studies, whether it is based on the combustion of the feed stock of coal or co-fired with biomass, have often separated the analysis of composition and chemistry from the development of deposits and corrosion models. It is expected that the major contributor to corrosion come from the condensation of NaCl, KCl, Na_2SO_4 and K_2SO_4 onto the walls and tubes. A review of mathematical models that are currently used within the

research material is a good way of moving the discussion forward (Tomeczek & Wacławiak, 2009).

Typically the use of empirical equation based on the following form (Tomeczek, et al., 2004; Tomeczek & Wacławiak, 2009) as,

$$P = S\dot{m}_c \qquad (3\text{-}1)$$

Where $\dot{m}$ = mass rate of deposition per unit surface area, kg/ (m^2s)

S = constant (6.2×10^{-5})

P = probabilities that the particles will impact the target surfaces

This approach is characteristic of many writers in this field. They all offer the following method of obtaining P_1, P_2 impact probabilities as eq. (2-4). Other researches use a general form of stick/impact modelling relationship that determines the probability of impacting a tube P_2 such as eq. (2-6). The probability may be expressed, for example as area or as aspect ratio of the tube face to the empty space around the tube.

The literature review in chapter two has established that reactions in the combustion of biomass fuel, that is fuel containing plant material, is more sophisticated than the models concerning coal combustion with product such as Si, K, Na, S, Cl, P, Ca, Mg, Fe giving rise to ash fouling and 'slagging'. It was also noted that coal combustion will have the same elements but the chemical products may be different, it will depend on the coal used. The principle corrosion constitutes Potassium and Chlorine is contained in the 'Char' formed during combustion. It was stated in the literature review that mechanism for transportation from the combustor components to the heat transfer surfaces is by diffusion (for small particle) or direct impact (large particles). It was shown that effects of deposits can be radically reduced by Co-firing with coal (Buhre, et al., 2007; Robinson, et al., 1984) Gas flow can be in the transition or turbulent flow regime range after initial combustion.

This requires the flow regime and turbulence/laminar flow behaviour to be known before running the combustion and dispersion models simulation. Since when constructing a model of ash/particle/vapour interactions reaction its necessary to be aware that such interactions often fall below the resolution of the mesh and often accuracy can only be maintained by depending on non-continuum empirically derived models (Miltner, et al., 2008).

3.2 Arrhenius rate models

The deposition of products onto cooled metal surfaces requires measure knowledge of the rate at which the fuel, oxygen and by-products pass through in the combustion process. Essentially the combustion conditions in a PF Boiler are non-premixed, where air and powdered coal-biomass mixtures are brought together to form an air-fuel mixture. The air-fuel mixture is then blown through a nozzle and ignited, once ignited the process is continuous until all the air-fuel or oxy-fuel is consumed. Taking into account that most early models are based on chemical kinetics that assumes a chemical equilibrium state, the rate of combustion can be determined by the Arrhenius Law type of calculation. For the purpose of this thesis these models are adequate to model how much of the oxy-fuel is converted to ash and pyrolysis that's available to deposit on the tube surfaces. Since only overall nature of the combustion process is required and the detailed kinetics is of secondary importance. The combustion reaction is assumed occur as fast chemical reactions that run to completion. These reactions are assumed as infinitely fast with the fuel, and oxygen combined in stoichiometric proportions, with s number of reactions to form m number of product reactions; with the general (mathematical) reaction rate $\dot{\omega}$ as.

$$\dot{\omega} = (\text{rate of destruction of molar concentrations of fuel}) + (\text{rate of destruction of molar concentrations of Oxygen})_s \leftrightarrow \sum_{m=s} (\text{rate of production of molar concentrations of products}) \quad (3\text{-}2)$$

The turbulence modelling associated with complex flows caused by the air rush into the combustion chamber and eddies generated by convection updrafts is modelled as turbulence using the two equation k-ε model applied at the wall and tube surfaces. This is the eddy break model of Spalding (Spalding 1976) and is widely used in most CFD packages (ANSYS, 2001; Versteeg & Malalasekera, 1995). The turbulent dissipation rate of fuel, oxygen and products is expressed as -

$$\dot{\omega}_{fu} = -C_r \rho \tilde{m}_{fu} \frac{\varepsilon}{k_{turbulence}} \quad (3\text{-}3)$$

$$\dot{\omega}_{ox} = -\acute{C}_r \rho \frac{\tilde{m}_{ox}}{s} \frac{\varepsilon}{k_{turbulence}}$$

$$\dot{\omega}_{\text{products}} = -\acute{\acute{C}}_r \rho \frac{\tilde{m}_{pr}}{(1+s)} \frac{\varepsilon}{k_{\text{turbulence}}}$$

where C_r, $\acute{C}_r$ and $\acute{\acute{C}}_r$ are model constants, ρ is the density of fuel, oxygen or products, then $\tilde{m}_{fu}$, $\tilde{m}_{ox}$ and $\tilde{m}_{pr}$ are the mass fraction of the fuel, oxygen and products of the total constituents of the gases entering the combustor; k is the turbulence energy, ε is the turbulence dissipation and s is a series integer value (i.e. s=1,2,3...).

The Arrhenius rate equation is a simple but accurate equation for calculating a temperature dependant rate constant eq. (3-4). The Arrhenius rate equation is an empirical relationship for the rate constant k_{rate} is expressed in terms of the Activation Energy E with the Temperature T in Kelvin.

$$k_{rate} = Ae^{-E/RT} \quad (3\text{-}4)$$

Where A is the pre-exponent factor, R is the gas constant, and the reaction rate k is expressed in s^{-1}.

The modelling of non-premixed combustion in turbulent flows in never straight forward and requires averaging of the mass fractions. There is localised heat generation and changes in the density of the combustion reactor and products. For a single step reaction the averaging of the conversion to products is in conflict with the rapid reduction in size as the coal-biomass is consumed in the reaction.

The turbulence energy $k_{turbulence}$ and the dispersion rate ε in eq. (3-2) are based on the wall form of the k-ε turbulence equation. It's logical to focus on the wall form of the k-ε turbulence equation, since clearly the study of gas flow behaviour near to surfaces is of particular interest to deposition. The near a wall the value of $k_{turbulence}$ and ε can be estimated by evaluating the dimensionless near wall factor y^+ (Versteeg & Malalasekera, 1995; Patankar, 1980).

$$y^+ = \frac{\Delta y_p}{v}\sqrt{\frac{\tau_w}{\rho}} \tag{3-5}$$

where Δy_p is the mean velocity profile, υ is the velocity; τ_w is the wall fluid shear stress and ρ is the density of the bulk gas. The velocity profile is considered located at the point tangentially midway from the wall and full velocity as Figure 3-1. The near-wall flow is considered laminar if:

$$y^+ \leq 11.6 \tag{3-6}$$

and turbulent if

$$y^+ > 11.63 \tag{3-7}$$

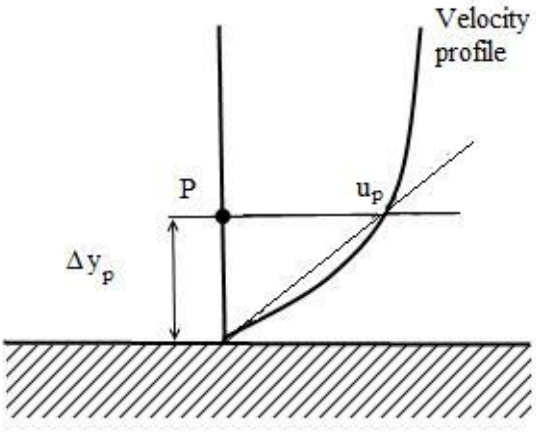

Figure 3-1. Velocity distribution at a wall of Versteeg et al. (Versteeg & Malalasekera, 1995).

Then for turbulent flow the turbulent energy equation at the near wall for the standard k-ε model is

$$k_{turbulence} = \left(\tau_w u_p - \rho C_\mu^{3/4} k_p^{1/2} u^+\right) 1/\Delta y_p \tag{3-8}$$

and the dissipation rate equation is

$$\varepsilon = C_\mu^{3/4} k_p^{3/2} / (\kappa \Delta y_p) \tag{3-9}$$

where C_μ is a constant set as 0.09 (when Reynolds number, Re≈ 4000 i.e. fully turbulent), k_p is the turbulent energy at point p in Figure 3-1, u is the velocity in free flow away from the wall, u_p is the velocity at point p and κ is the Karman's constant where κ = 0.4187 (ANSYS, 2001; Versteeg & Malalasekera, 1995).

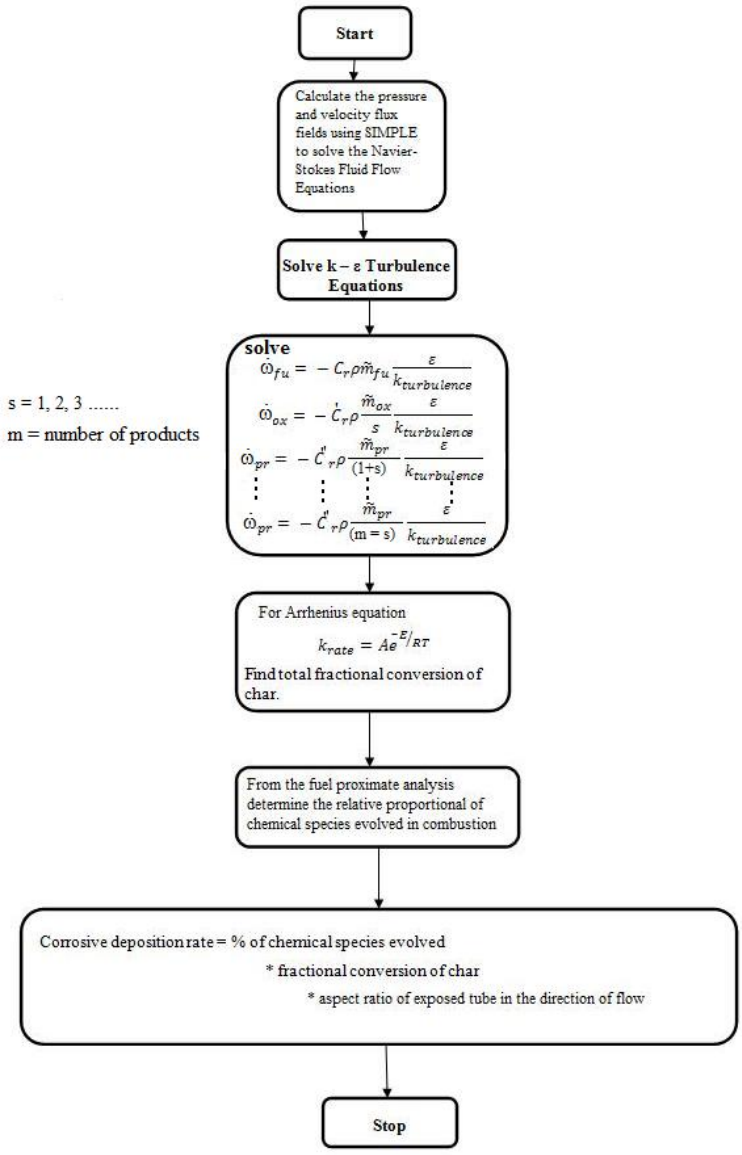

Figure 3-2. The eddy break-up model algorithm flow diagram of combustion products and formation

If the Reynolds number is over 4000 then the flow has fully develop turbulence. If fully develop turbulence flow is present at the wall then the following relationship is used to calculate k_p and to provide the closure of the k-ε equation.

$$k_p = \frac{u^2}{\sqrt{C_\mu}} \tag{3-10}$$

Local gas shear stress will determine the break-up of the laminar flow as described by Durbin et al. (Durbin & Pettersson, 2001). If Re is less than 4000 then k_p is set to unity. It is assumed that ash particles move in straight line up or down or side to side in a PF Boiler. The particles also follow the path of the bulk gas flow. Particles will then have a high probability to coat the tube surfaces if their motion lies in the direct path of the tubes. This is not to say such particles will impact the tubes, this is actually determined by the fluid dynamics of the system and will be considered latter in the thesis.

It is to say that the aspect ratio of the tube offers a measure of the maximum possible collection of particles flowing in the stream. In Figure 3-2 the full algorithm used to calculate the collection of corrosive material in a flow stream which is based on the eddy break-up model of combustion. The start of the process the pressure and velocity fields are determine from the solution of the Navier-Stokes equations. The turbulence factors k –ε are solve in as illustrated in eq. (3-8) and eq. (3-9).

The reactions rate equations for fuel and oxygen conversion are solved for $k_{products}$ using the Arrhenius equation (eq. (3-4)) fitted to first order reaction time λ. From the fuel proximate analysis and the geometry of the tube the relative deposition rate of the solid particles attaching to the tube is available.

3.3 Case study: Gasification of low rank South Australian coal

For this case study the geometry of the model is represented in Figure 3-3. It is a square 'pipe furnace' of approximately 300mm x 300mm in section with a simple square mesh applied in advance of the probe. The configuration of the probe insertion into the pipe furnace represents a heat exchanger tube crossing at right angles to the direction of flow. The aim of this case study is demonstrate the capability of this approach to the capture the ash conversion in the flow regime based on mechanistic modelling approach. In this model the basic regular square "2D" mesh consists of nodes numbers range from {1, 1} to {5, 1}. These centre points are located at the crossing lines on the drawing Figure 3-3. The mesh lines sit on the y, z plane

and cuts the centre line on the x, y plane on the drawing. A general arrangement drawing based on real gasification pilot plant based on the Cranfield University is illustrated in Figure 3-4.

The solution to the pressure and velocity equations associate with the fluid flow, are solved using the Navier-Stokes equation using a meshed finite volume method programme. The Navier Stokes equations are resolve using the SIMPLE algorithm (Semi – Implicit Pressure Linked Equation). An intermediate step required to solve the SIMPLE algorithm is to solve the convection-diffusion problem (c-d problem) so that heat transfers equation will calculate the temperature field in the combustion test rig. A common approach is to solve the c-d problem by applying the Tri-diagonal matrix algorithm (TDMA). The TDMA will be numerical tested using this simple square mesh structure of Figure 3-3.

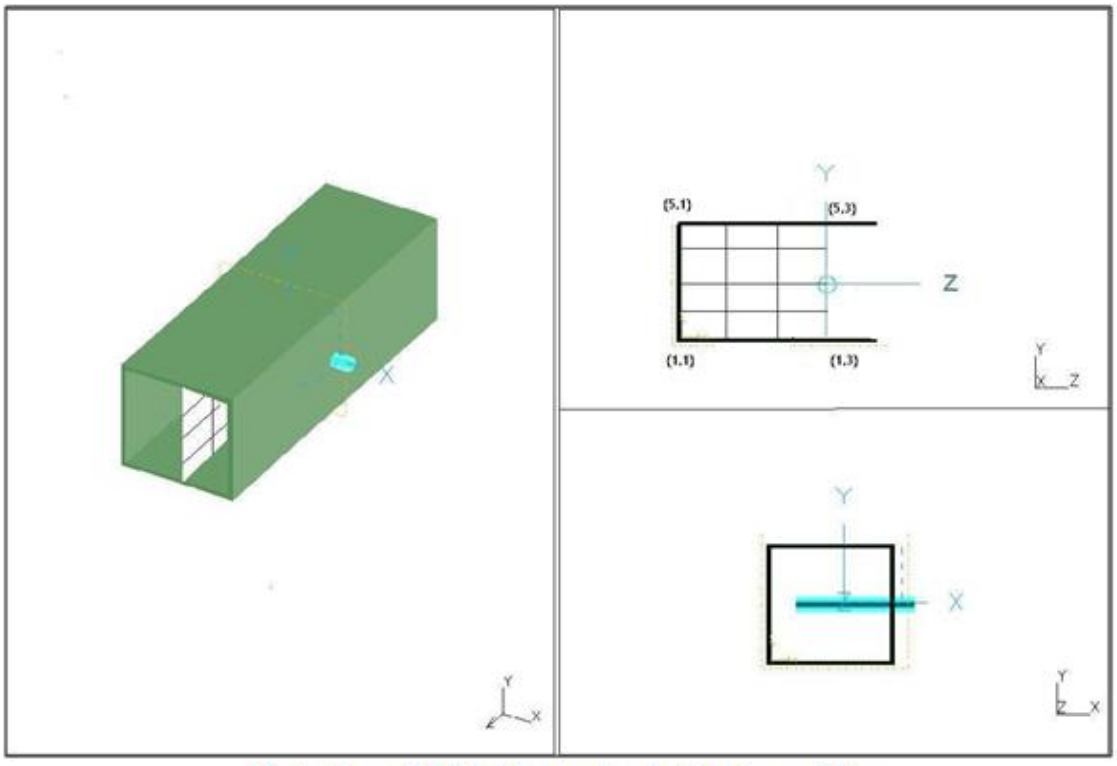

Figure 3-3. Model of 'pipe' combustion test rig with the mesh numbering system exhibited in the top right image.

The boundary conditions are defined as near wall, inlet and outlet states, with each boundary state (wall, inlet and outlet) and independently implemented either as laminar/transitional or

turbulent flows. Near the wall, the Reynolds number will be larger since the irregular wall surface will cause eddies to form in the flow patterns. Wall boundary flow regime conditions are largely ignoring at the laminar and transition phase and assumed to be constant. Also, near to the wall the temperature gradient is assumed to remain constant despite the turbulent flow. In most cases then k_p is set to unity excepting where Re < 4000 (i.e. turbulent flow inside the 'pipe' combustion test rig), in which case k_p is determined by eq. (3-10). The walls are considered adiabatic; therefore there is no heat transfer through the wall material. While the outlet flows are model as opening to free space and the flow considered fully developed as laminar regime with no change in state.

Most common chemical reactions models use the Arrhenius Law, the model assumption considers that fast combustion reactions occurs instantaneously and are completed without intermediate by-products. However, one example of combustion that produces an intermediate phase reaction is the gasification of coal produces. Gasification and use a different chemistry to PF boiler combustion and produces an intermediate phase reaction of char instead ash together with hot gasses particles. As the cost of running a PF boiler to produce ash is justifiable in these trial a publish gasification trial is applied to this case study. The trails are concern at the rate of char/ash and particle production not the process of how the char/ash and gas particles are converted.

Using as a reference the published study of 'Gasification of a South Australian low rank coal with carbon dioxide and steam' (Ye, et al., 1998), the key chemical and physical properties of Bowman's coal are established (Table 3-1). The measure of the available particular material to deposit onto the probe is determine as the amount of char converted to particular products after a period of reaction time λ constant or *frequency factor* (with units s^{-1}) from a fix given mass of 1 molar mass. The first order reaction time in this thesis is referred by the symbol λ instead of T as stated in the general Arrhenius equation in eq. (3-4).

A coal gasification fraction conversion of char has been chosen against a model of coal/biomass combustion because the reaction of coal gasification is simpler. With this simplicity of coal gasification it's easier to design a model to standardise the results for further comparison. The fraction conversion of char follows a straight forward Arrhenius reaction rates for coal gasification vary with the porosity of the coal char (Kajitani, et al.,

2006). Therefore all reactions are considered first order and are assumed to follow the following reaction rate law;

$$mA + nB \rightarrow C \qquad (3\text{-}11)$$

where reactors m quantity A and n quantity of reactor B produce C product.

The analytical study of the fractional conversion of char for kinetic (Laminar flow) combustion will use the Arrhenius law provide data to compare with the computational model. The fractional conversion of char is how much char [A] is converted from the fuel in time t.

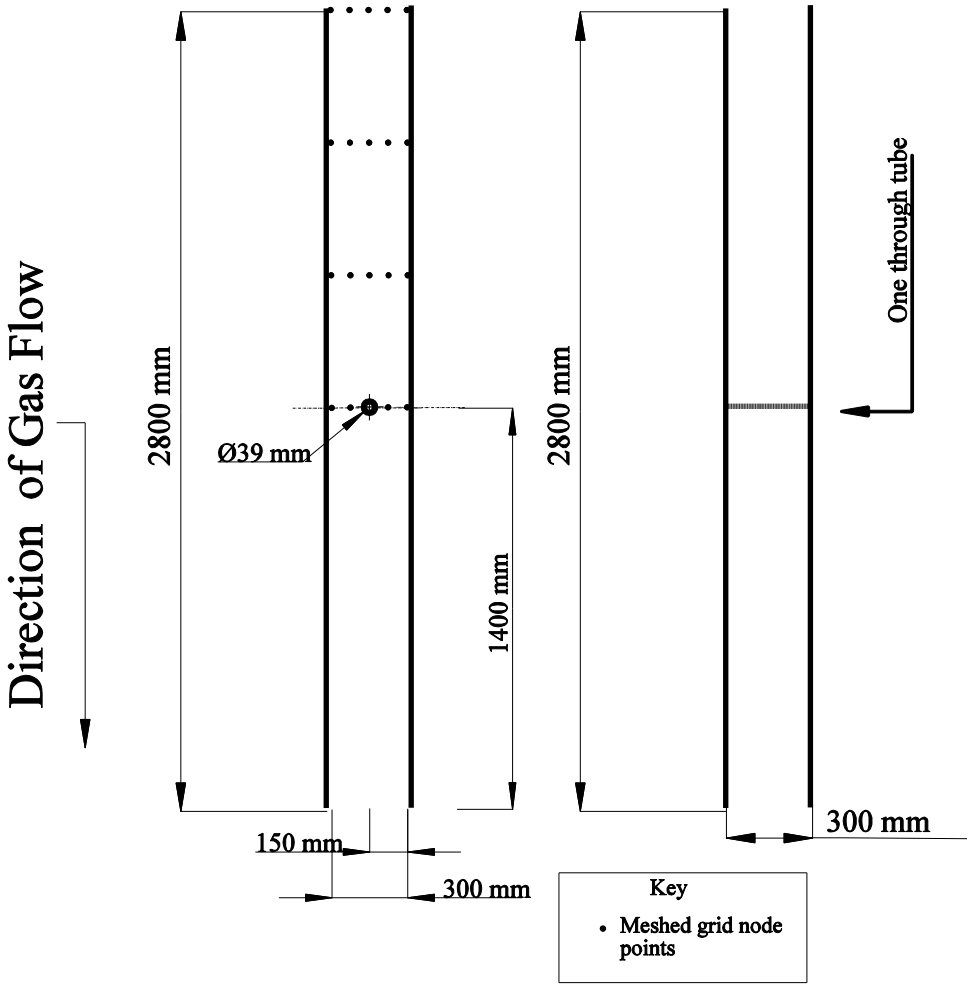

Figure 3-4. The Cranfield University coal gasification pilot plant general arrangement drawing

Then the frequency factor λ is.

$$r = \frac{d[A]}{dt} = d\lambda \tag{3-12}$$

The reaction model assumes a homogeneous model in which the carbon gas reactions occur at active sites on the char particle. The active gasification sites are assumes to be uniformly distributed throughout the particle.

Table 3-1. Reaction Coefficients, Coal Composition and Flow Conditions

Proximate analysis		Kinetic Reaction		Fluid Properties	
Moisture (% d.b.)	56	E (C) (KJ $mol^{-1)}$	30.0	Laminar flow	
Fixed Carbon (% d.b.)	39.5	A (C) (min^{-1})	30.0	Pressure (kPa)	101.132
Volatile Matter (% d.b.)	48.5	A (O_2) (min^{-1})	30.0	u velocity (m^3/s)	2
Ash (% d.b)	12	A (Products) (min^{-1})	1327.0	v velocity (m^3/s)	2.24
		C_r	1.0	Turbulent flow	
		C'_r	1.0	Pressure (kPa)	101.132
				u velocity (m^3/s)	3000
				v velocity (m^3/s)	3000

As the reaction to convert the particle to gas progresses, the particle size is assumed to remain constant. Hence the overall rate of gasification is assumed to be independent of particles size. A mass balance for the first order reaction in a particle in this condition reduces to,

$$\frac{dX}{dt} = \lambda(1 - X) \tag{3-13}$$

or

$$t = -\ln(1 - X)\lambda^{-1} \tag{3-14}$$

where X is the fractional conversion of solid reactants and λ is the first order rate constant, with respect to time t (Ye, et al., 1998). Therefore, if the reaction does not fully complete then there will be particles free to travel in the gas flow. The reaction is therefore arrested before full completion by reducing the temperature below a Stoichiometric ideal reaction.

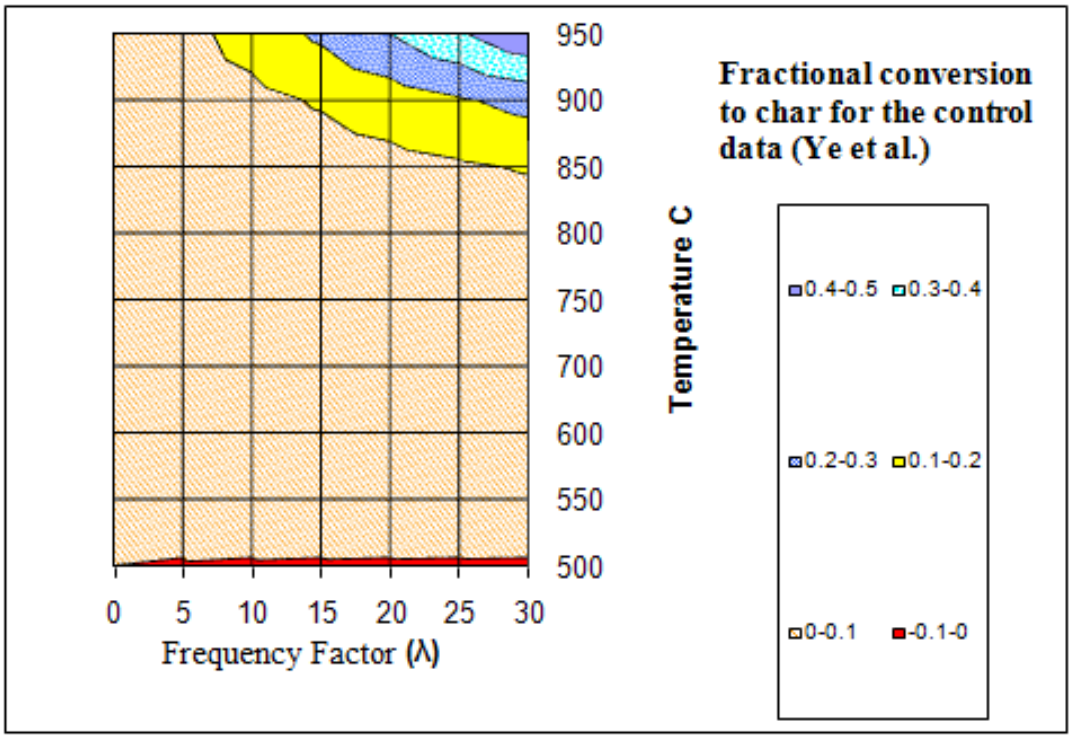

Figure 3-5. The fraction of solid matter remaining as a result of at sub-stochastic gasification reaction of Australian low rank coal

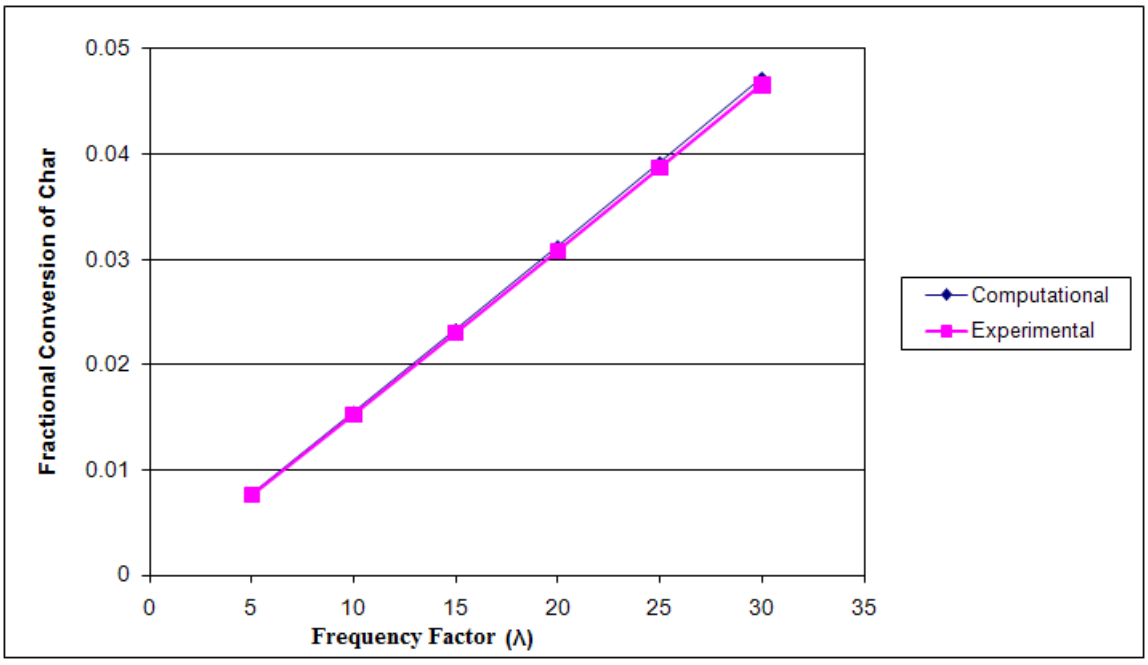

Figure 3-6. Fractional conversion of char for Australian low rank coal at 800° C in laminar/transition flow

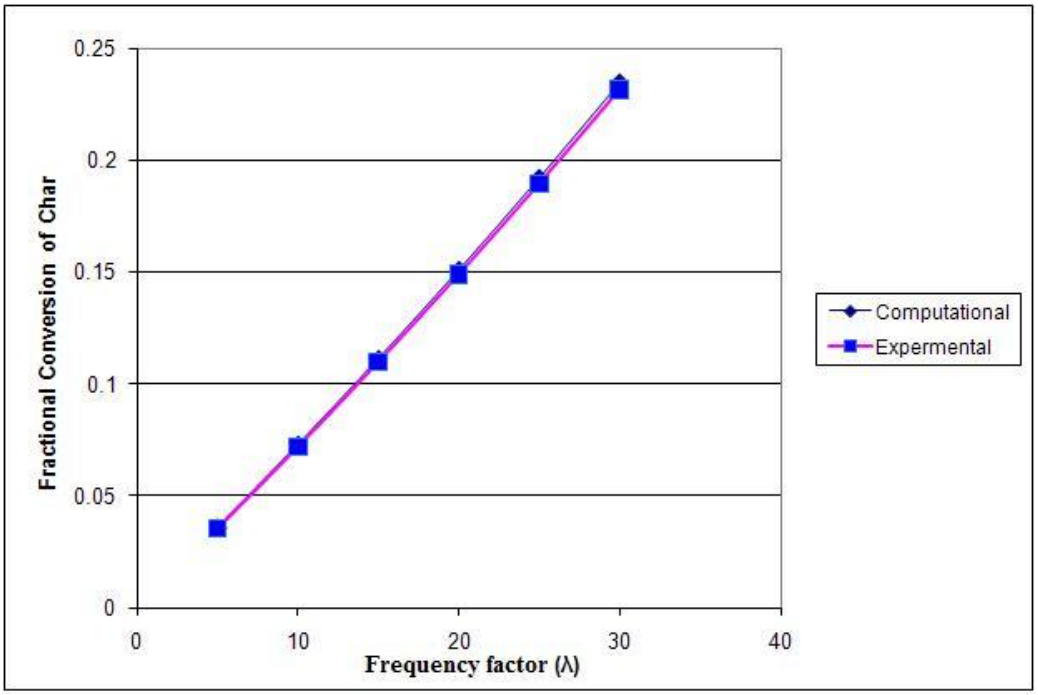

Figure 3-7. Fractional conversion of char for Australian low rank coal at 900˚ C in laminar/transition flow

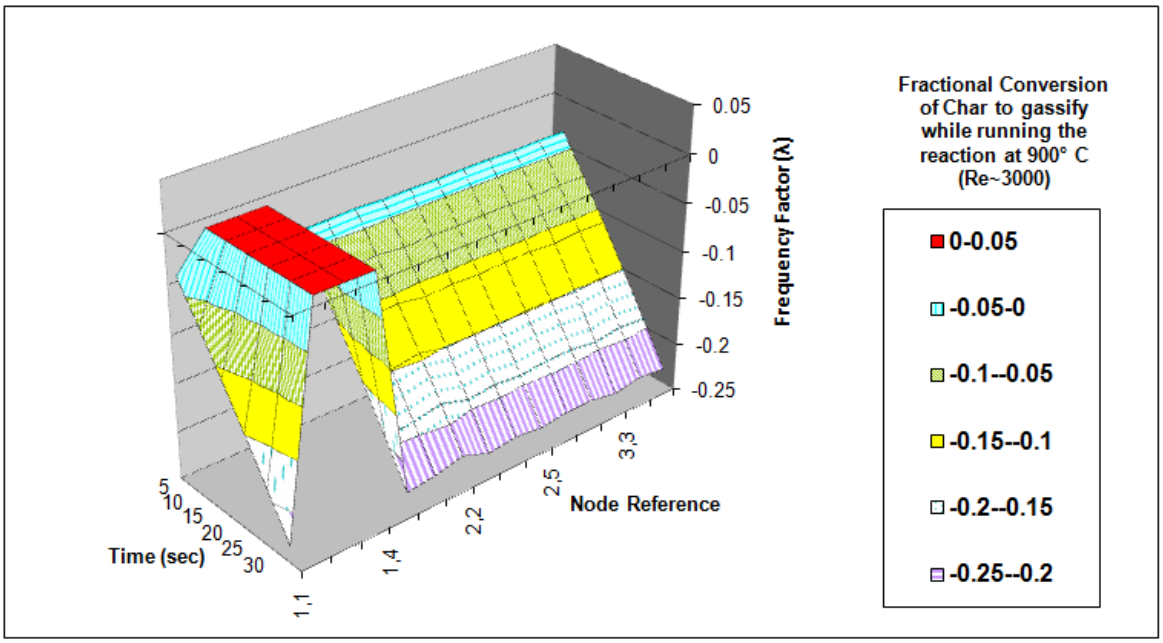

Figure 3-8. Fractional conversion of char in transitional/turbulent inlet flow at 900° C

The proportional of the particles left un-reacted is assumed available to directly impact the test heat exchanger tube.

The results are plotted for temperature between 500° C and 950° C over a frequency factor constant $\lambda = 5\ s^{-1}$ to $\lambda = 30\ s^{-1}$ are shown in Figure 3-5. This gas temperature is quite low for gasification but the explanation has been given previously in the chapter.

Of note is that Figure 3-5 is a sub-stochastic model which means that the Markov analysis of the production and delivery of particles on to the tube is not truly random. The factor that changes the randomness in Figure 3-5 is the temperature which will evolve different quantities of particles left over from the conversion of particles from char to gas.

This study compares the results for the computational model for a kinetic reaction for temperature at 800° C and 900° C and the Arrhenius Law model with the same temperature. For laminar and transitional flow regimes these comparisons are illustrated in Figure 3-5 for 800° C and 900° C illustrated in Figure 3-6. The fractional conversation of char for the model is taken as the mean values over the 15 nodes that the model uses.

The output of the case study is presented in Figure 3-6 and Figure 3-7 and the two show close agreement for this kinetic reaction against the Arrhenius law based experimental values. The output of the standard model is replicated in Figure 3Figure 3-68 and shows reaction rate remains constant in the turbulent region at the inlet with little or no char conversion near to the inlet; define as nodes between {1,2} to {1,4}. Outside the turbulent inlet region there is a kinetic reaction with an increasing char to combustion products conversion the longer the char is in the combustor. The combustion products will contain coal products which have not undergone gasification and are available to impacts the tube. Since the reaction is running below the operating temperature to achieve full gasification, it is clear that the temperature further away from the inlet will be lower. The reduction in temperature drop the further away from the inlet is reproduced in the model. These models produce a convincing qualitative approximation of the behaviour of the char to vapour values and the model values shown in Figure 3-7 are used in the next numerical test.

The fractional solid particles deposited on the tubes as a percentage of the total volume products emitted over the frequency factor $\lambda = 5\ s^{-1}$ to $\lambda = 25\ s^{-1}$, for the tube in a single tube geometry, is reported in Table 3-2 Enclosed in the box in Table 3-2 is a significant region in which ‘gasified’ products cross the path of the probe, therefore the most likely part of the gas stream to deposit solid particles on the probe.

Table 3-2. Fractional conversion of solid particles at 900 on a scaled geometry

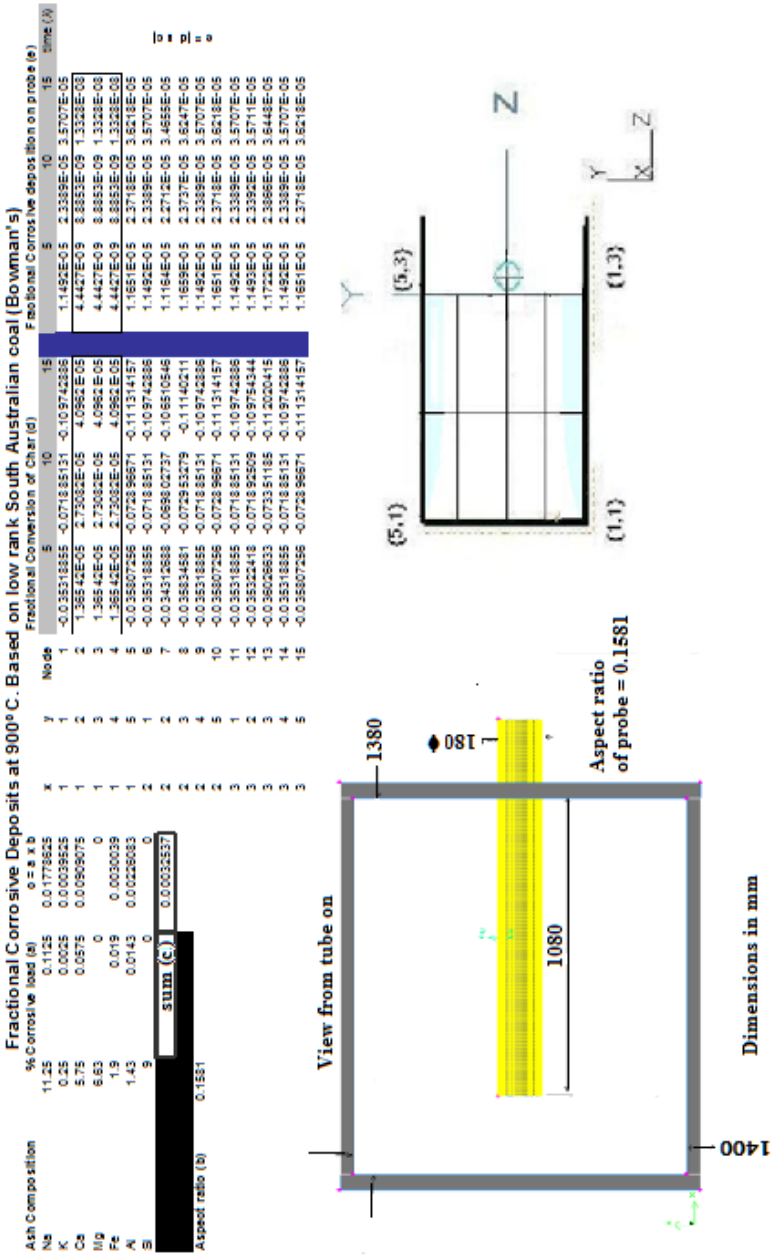

The aspect ratio of the probe is calculated using eq. (3-15)

$$\text{Aspect ratio} = A_f / \left((d \times \pi)/2 \times l_p \right) \tag{3-15}$$

Where A_f is the cross-sectional area of the pipe PF furnace, d is the diameter of the probe and l_p is the distance the probe is inserted inside the furnace. Only half the circumference is of the tube is in the path of the flow of particles therefore (πd)/2 is in calculating the face area of the

tube. The aspect ratio of the probe to the pipe furnace in Figure 3-4 is 0.1576, if the probe is inserted 231.4mm. The aspect of a similar pipe furnace which is scaled by 4.666 is shown in Table 3-2 as 0.1581. The pipe furnace in Table 3-2 is scaled by 4.666 so that there aspect ratios are closely the same.

At the entry to the real combustor with the dimensions based on general arrangement drawing of Figure 3-4 there is almost a constant conversion rate of coal to gas. In the model, there is a proportional reduction in the coal to gas conversion the further away from the inlet coal-gas conversion process occurs. This is still true in the model despite the up scaling of the probe - 'pipe' combustion test model from that of the general arrangement drawing of Figure 3-4.

For coal-biomass co-firing a simplified model has been developed. There are differences in the gasification of coal and combustion of coal-biomass. In both cases of gasification and combustion of coal-biomass it's assumed that the combustion matter will fully convert to heat and products. The key differences in the way particles of coal and biomass fuel burn between gasification and combustion is the speed at which the char burns out. For gasification the char burnout rate is slow and for combustion the char burnout rate is fast (Smoot & Smith, 1985).

In coal-biomass co-firing the fuel contains particles that will not evolve into heat and gas products but remain as solids, such as silica.

The assumption made is that elements of the fuel such as silica absorb heat and reduce the fuel/oxygen conversion. The assumption is that the silica particle is contained within the char and as the char is burned-off more of the silica particles is revelled. Carried in the bulk gas flow, the silica particle will impact the tube and stick to the tube and in doing so bind will vapour deposits to the superheater tubes.

The completion of oxidation of char is considered the key measure of revelling of the silica and this achieved by considering a homogenous reaction of char both inside and outside of the particles. The char particles structure changes during the burnout reducing size and changing geometry. A widely cited model that considers physical structural changes during the char burn-off rate is the Random Pore Model such as (Lin, et al., 2010; Molintas & Gupta, 2011).

$$\frac{dX}{dt} = k_o e^{-E/RT}(1 - X)[1 - \psi \ln(1 - X)]^{1/2} \quad (3\text{-}16)$$

where dX/dt is the reaction rate, k_o reaction constant, E is the activation energy, R is the gas constant, T is the Temperature and ψ is the parameter related to the porous structure of the un-reacted char. The parameter ψ is defined as

$$\psi = \frac{4\pi L_o}{\rho S_0^2} \tag{3-17}$$

where L_0 is the initial mean particles size, ρ is the particle density S_0 is the particle surface area. In this study L_0 and S_0 are not known since the char particle contents also include a particle of silica. However, from papers by Lin *et al* (Lin, et al., 2010) or by Molintas and Gupta (Molintas & Gupta, 2011) the plots of char conversion and time can be modelled by curve fitting the approximating the rate of char burn-off with a first order standard chemical reaction rate equation as

$$\dot{X} = a\left(1 - \exp^{-bx}\right) \tag{3-18}$$

to normalise this eq. (3-15) then a = 1. To complete the kinetic rate model assume that b= k and x = τ, then the model approximation becomes,

$$\dot{X} = 1 - \exp^{-k_{rate}\tau} \tag{3-19}$$

where time constant τ has units of seconds and k is the first-order reaction rate constant.

3.4 Discussion and results

Both the Arrhenius activation energy and the rate constant k_{rate} are experimentally determined and represent macroscopic reaction-specific combustion parameters, which are not simply related to threshold energies and the success of individual collisions at the molecular level. At a macro-scale the Navier-Stokes equations are non linear partial differential equation that describes the velocity of the fluid. The non-linearity in the differential equation makes finding a solution to the numerical system very difficult and the Navier-Stokes equations have no solution outside the special case of laminar flow. The solution of the Navier Stokes equation is described as a velocity field. Turbulence is a chaotic behaviour caused by the inertia of the fluid when the fluid is in motion, while Navier Stokes equation is believed to solve turbulence. There is no known solution for modelling turbulence using the Navier

Stokes equation therefore estimates of the velocity field are based on empirical data. The most common and widely applied turbulence estimate scheme is k-ε model.

The system of solving a tri-diagonal series of equations is solved using Tri-dimensional Matrix Array (TDMA) (Press, et al., 1989). A tri-diagonal system for n unknowns may be written as eq. (3-19)

$$a_i x_{i-1} + b_i x_j + c_i x_i = d_i \tag{3-20}$$

Where $a_1 = 0$ and $c_n = 0$. This algorithm is only applicable to matrices that are diagonally dominant, which is to say in matrix form, this system is written as eq. (3-20).

$$\begin{bmatrix} b_1 & c_1 & & & 0 \\ a_2 & b_2 & c_2 & & \\ & a_3 & b_3 & \ddots & \\ & & \ddots & \ddots & c_{n-1} \\ 0 & & & a_n & b_n \end{bmatrix} \begin{bmatrix} x_1 \\ x_2 \\ x_3 \\ \vdots \\ x_n \end{bmatrix} = \begin{bmatrix} d_1 \\ d_2 \\ d_3 \\ \vdots \\ d_n \end{bmatrix}. \tag{3-21}$$

The first step consists of modifying the coefficients as follows, denoting the new modified coefficients with primes:

$$c'_i = \begin{cases} \dfrac{c_i}{b_i} & ; \quad i = 1 \\ \dfrac{c_i}{b_i - c'_{i-1} a_i} & ; \quad i = 2, 3, \ldots, n-1 \end{cases} \tag{3-22}$$

and

$$d'_i = \begin{cases} \dfrac{d_i}{b_i} & ; \quad i = 1 \\ \dfrac{d_i - d'_{i-1} a_i}{b_i - c'_{i-1} a_i} & ; \quad i = 2, 3, \ldots, n. \end{cases} \tag{3-23}$$

This is the forward sweep. The solution is then obtained by back substitution:

$$\begin{aligned} x_n &= d'_n \\ x_i &= d'_i - c'_i x_{i+1} \qquad ; \; i = n-1, n-2, \ldots, 1. \end{aligned} \tag{3-24}$$

The model in the case study examined in this Chapter 3 performs well for fix values of 500º C, 600 º C, 700 º C, 800 º C and 900 º C but will not work for intermediate values, in most instances it will converge in 85 iterations. At values other than fix values aforementioned, the TDMA solver module encounters a division by zero. This problem division by zero occurs because either a matrix in eq. (3-22) is sparse or else a_i, b_i or c'_n in eq. (3-23) or eq. (3-24) have the value zero. At values of 950 º C and above then the solver exceeds the capacity of the computer to process the large numbers necessary to provide a numerical result to the accuracy required; at which point a numerical oversize error is recorded.

The combustion of coal in a gasification process and extrapolating this to a coal–biomass co-firing brings the following aspects;

- Introduces a problem at a fundamental level in the mathematics of numerical solution that applies especially to modelling combustion problems.
- Fundamental limit that is place on computational calculation is because calculations are always undertaken within finite limits. As computer will always operate within a fix limit of the size of numbers it can operated at, the computer must operated within these limits. In some commercial software the value of zero is reassign as the smallest positive or negative number the computer can handle where a division by zero is encounter. In other instances of encountering an underflow or overflow the maximum or minimum number the computer can process is substituted. This thesis will investigate if an improvements in these methods can be undertaken using a statistical approach and mesh-free methods.
- Instability in the computational mathematics also occurs when calculating pressure within the algorithm SIMPLE. It has been found that for some initial starting values, instead of a positive pressure that expected negative values result. So it is only possible to make prediction by interpolation between the known values where the computational model performs predictably (e.g. provides positive real numbers). This is called explicit form of the solution to a partial differential equation and SIMPLE algorithm is a semi-implicit solution to the Navier-Stokes equation. This semi-implicit form has of the PDE been considered the cause of the periodicity in the solution of the pressure solution. This theorem has been tested by developing an

identical program to the commercial code. It has been found that the same periodicity in the pressure sources can be duplicated.

- This test program to demonstrate periodic behaviour in char conversion and combustion modelling is compiled in FORTRAN 2003 using Intel Fortran under Visual Studio with Microsoft Excel spreadsheet package to post-process the data. A similar pattern of behaviour is exhibited on a commercial CFD package (in this case Ansys Fluent) and later a further study will investigate. However, in developing the coded FORTRAN 2003 model proves independently that this approach using a SIMPLE algorithm, k-ε turbulent model and Arrhenius equation can model the char creation and conversion to ash or combustion products but only from a limited given a starting point.
- Problem of the limited starting point values that will run to a stabilized solution is a by-product of the quasi-static approach in which the SIMPLE algorithm functions when solving turbulence problems. However turbulence models used to close the SIMPLE algorithm equations are valid only as long as the time over which these changes in the mean occur is large compared to the time scales of the turbulent motion containing most of the energy.

4 Vapour Deposition

4.1 Analysis of commercial CFD code for aerosol deposition modelling

The numerical modelling of vapour deposition on superheated tubes in PF Boilers is mostly performed on commercial CFD packages such as Fluent. The most common models applied to vapour deposition are by the analysis of aerosols (Tomeczek, et al., 2004; Tomeczek & Wacławiak, 2009; Wang, 2008). Since aerosols' modelling of heat exchangers vapour deposition is widespread, a common assumption is that it effectiveness for heat exchangers vapour deposition is universal. A test session was prepared using the commercial Finite Volume Code Fluent with the model meshed using the solid modeller, Gambit. Since a real PF boiler used in a power station plant was not available, then the geometry of the PF boiler was based on the Cranfield test facility. The tube layout for the simulated test using Ansys Fluent is illustrated in Figure 4-1.

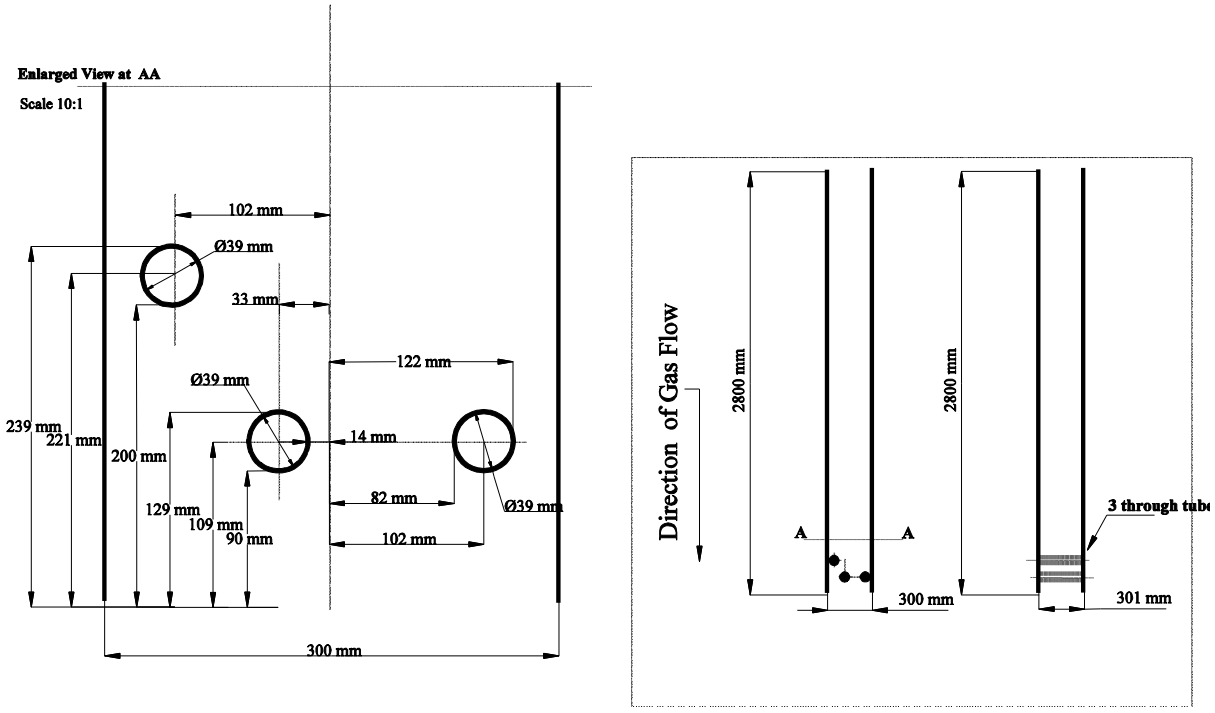

Figure 4-1. The tube configuration of a PF test furnace used in the 'Fluent' test simulation

The initial model was produced in 2-dimensions with grid formation as Figure 4-2. The type of model applied to the problem is one widely use for aerosol packages.

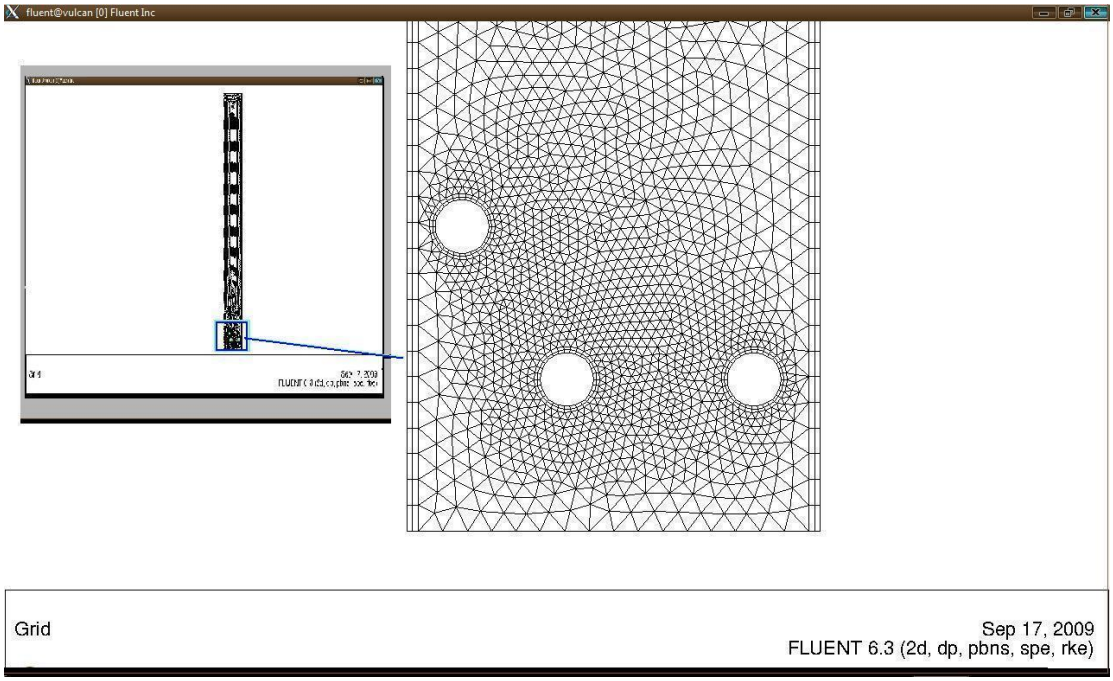

Figure 4-2. A triangular meshes scheme around probes based on the Cranfield University combustor

The combustion model assumes that the combustion process involves a mixture of coal and biomass. The ash is assumes to have a particle size of between 75-150 μm as associated with the literature (Loo & Koppejan, 2008). The ash has a potassium and sodium alkali content of composition level comparable values that is found within the literature (Geiser & Röhle, 2008).

Table 4-1. The coal-wood chip, operation conditions properties inserted into Fluent to operate the pipe furnace model (Figure 4-3).

	Coal Combustion properties	Wood Chip properties	Operating Conditions	
Thermal conductivity $W \cdot m^{-1} \cdot K^{-1}$.	0.054	0.0454	Pressure Pa	101325
Viscosity kg/(s·m)	1.72×10^{-5}	1.72×10^{-5}	Velocity (m/s)	10
Mass Diffusivity m^2/s	2.88×10^{-5}	2.88×10^{-5}	Temperature K	900

The Discrete Phase Model was use to provide tracking of the particles with a Rosin-Rammler statistical distribution providing the distribution of particle sizes injected into the model combustor. The Drag Law parameters were based on the spherical particles with a discrete random walk to formalize the particle trajectory. The output particles sizes never went below 2μm and are therefore not at a molecular scale; for this reason the particles are not true vapour

particles. Other operating conditions are included into Fluent and these are summarised in Table 4-1. In the last chapter centigrade scale has was used as the temperature scale. To standardise the temperature scales and also to move to a molecular mechanics description of the physics the Kelvin scale will be adopted.

After running the Fluent CFD model an accretion layer found to be as Figure 4-3 the deposition rates reach a maximum of 0.004 $kgm^{-2}sec^{-1}$. In other literature sources such as Kerr *et al* (Kaer, et al., 2006) as shows vapour value up to $6gm^{-2}h^{-1}$ (or changing the units to be consistent with Figure 4-3, then $100kgm^{-2}s^{-1}$). The images of Baxter (Baxter, 2004) and Kaer (Kaer, et al., 2006) CFD model deposition rates on a combined heat and power plant are illustrated in Figure 4-4. Kaer and Baxter do not make prediction on the shape of the resulting depositions. A simple explanation why prediction as to the build up of vapours deposits on heat exchanger tubes is so different between Baxter's results in Figure 4-4 and Figure 4-3. Making prediction of the shape and deposition rates is an extremely difficult task to undertake using CFD models.

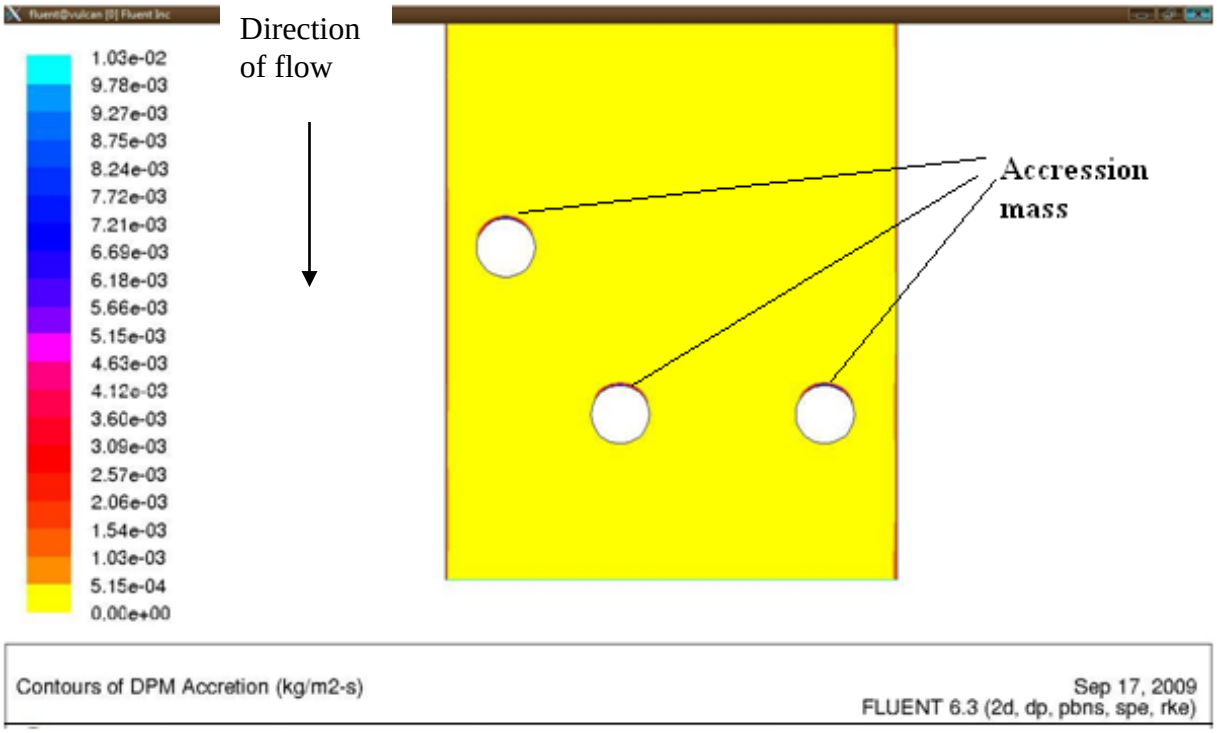

Figure 4-3. A CFD Fluent model of the Cranfield Test Combustor showing the accretion layers marked on the upwind side of the tubes.

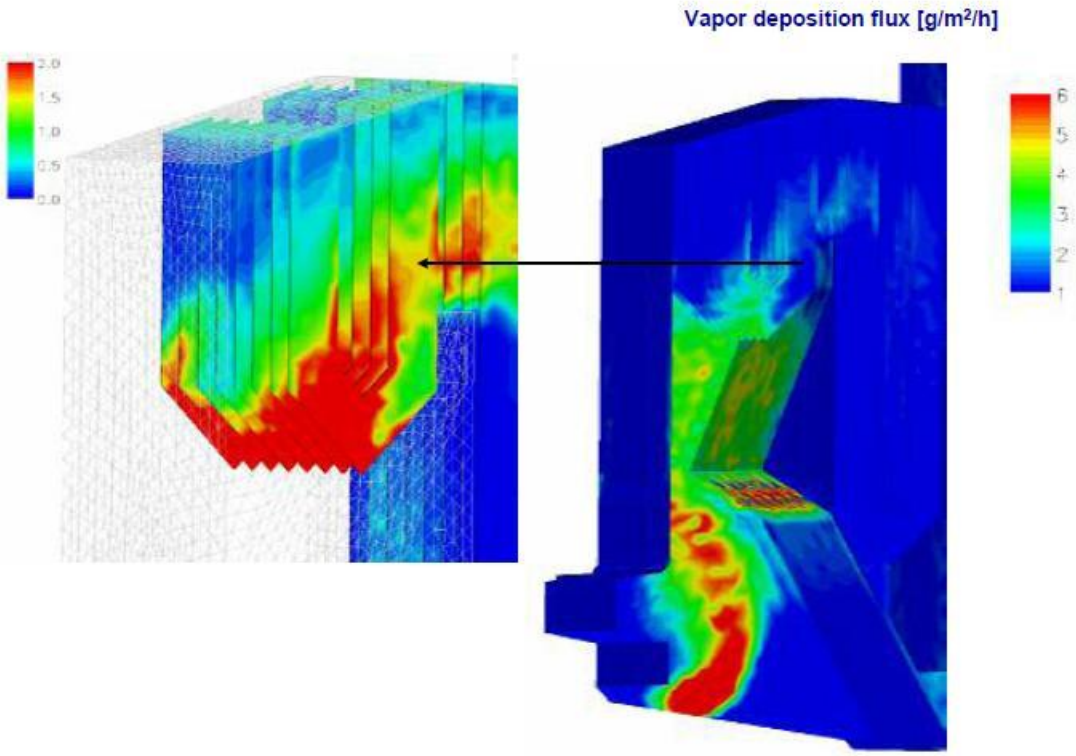

Figure 4-4. A CFD Image of a PF Boiler from literature showing vapour deposition (Baxter, 2004; Kær & Rosendah, 2003)

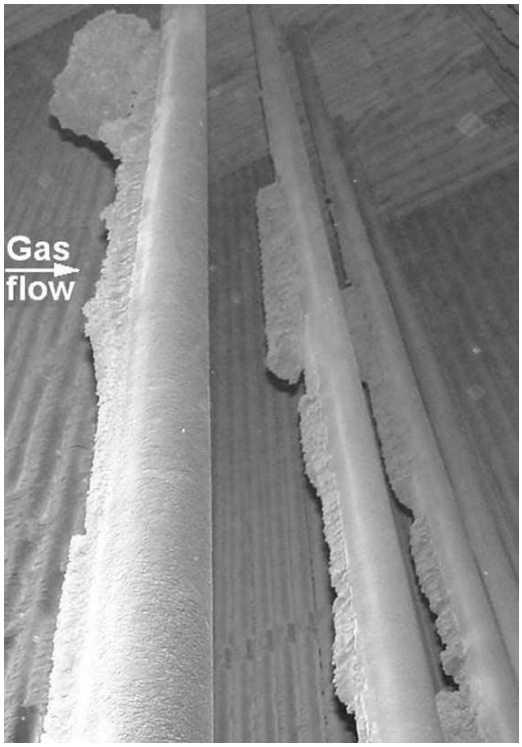

Figure 4-5. Deposit 'fins' and 'bridging' on real superheater tubes (Tomeczek, et al., 2004).

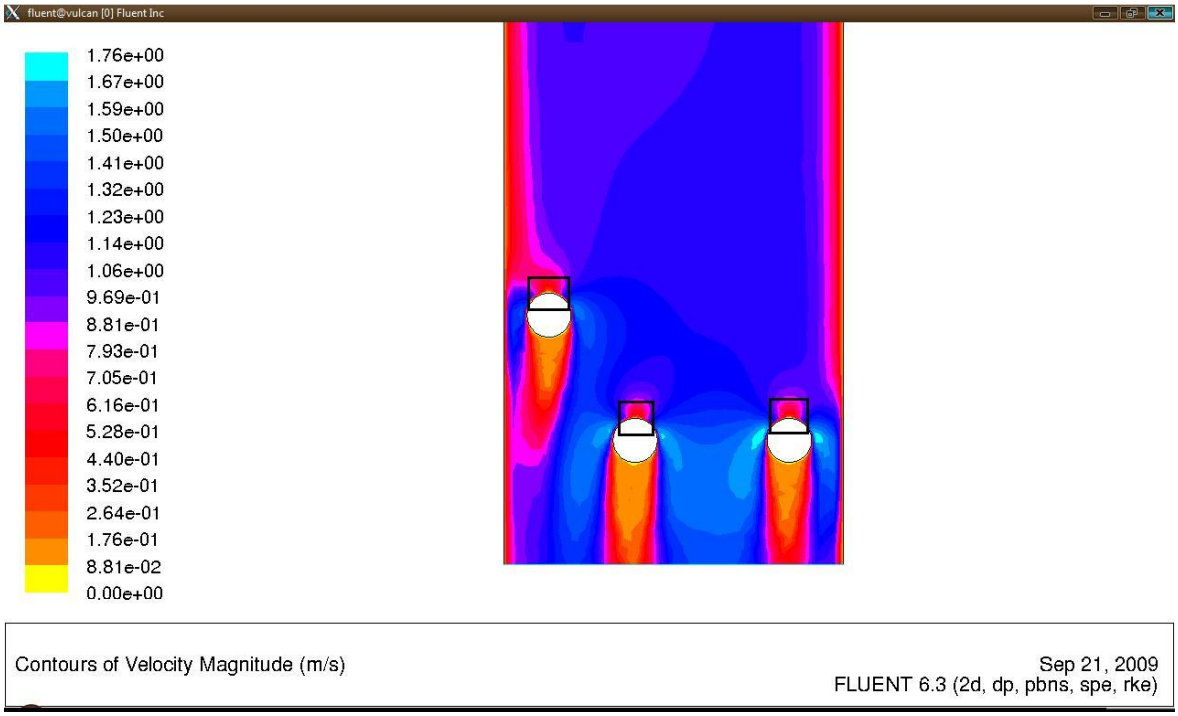

Figure 4-6. Velocity magnitude highlighted around the tubes using Fluent

Consider the shape of the depositions developed by the CFD model of the Cranfield Test Rig in Figure 4-3. The accretions layer is face on the upwind side of the tubes. The CFD model depositions are small and only form on the upwind side as marked.

However, looking at photographs of the accretion found in real PF boilers Figure 4-7. The CFD pattern of deposition does not match the shape or form the real accretions deposits. Real tubes are covered in ash and form fins that rise from the tubes. The model geometry is derived from the geometry of the Cranfield Test Rig. Therefore, the geometry that the accretion model employs can not affect the outcome of the model deposition.

Observing the velocity magnitude near the tube then the size and spread of the velocity is similar to the deposits spread on the tube in Figure 4-8, as shown in the encased boxes within Figure 4-9. This allows for some conclusions as the mode of accretion of deposits on the front of the tubes.

It is an important assertion that particle deposition is not the only route to the build up of solid matter on boiler components such as tubing as shown if Figure 4-4. Vapour deposition is a very important source of material in the build-up of deposits. There are essentially three paths for vapour deposition;

- Direct condensation of hot vapours onto colder tubes.

- Heterogeneous nucleation originated deposition onto ash particles and then impaction onto the boiler tube surface.
- Homogeneous nucleation originated deposition of vapour into droplets because the temperature of the vapour is below its nucleation temperature.

The prevalent means of nucleation is direct condensation; then heterogeneous nucleation, while the least prevalent and the most unlikely to occur is homogeneous nucleation. In direct condensation the driving change in free energy within the vapour is responsible for the change in state (from vapour to liquid or to solid) is the difference in temperature between the surrounding gas and the tube surface. Considering now the heterogeneous form of nucleation, occurs when vapour meets free flowing particle held in suspension within the gas stream. For nucleation will be promoted on the surfaces of the particle because of the wetting – contact angles is greater than zero so encourage the vapour surrounding the particle to condense. The size of the wetting – contact angles is the driving force that is responsible for minimising free energy; with the subsequent change in state.

The study of particles of visible size above 100μm and the molecules of gas that constitute the surrounding transport medium in a gas flow are a multi-phase flow and at multi-scale physics. The diagrams within the preceding text have show some of the shortcomings of CFD in deposition modelling when applied to multiphase and multi-scale flows. The principle risk to a successful implementation is the distortion of meshed elements and high elemental aspect ratio that can make for difficulties in resolving the size gain between particles and molecules.

4.2 An aerosol model of agglomeration, deposition

An aerosol model of agglomeration, deposition is concerned with the evolution of size distributions of aerosol particle and their chemical compositions in various systems. An aerosol is considered to be particles held in suspension in a gas.

In a combustion model concerned with PF Boilers, this thesis is concerned about the combination of particles ‘in flight’ and their tube impacts. In a wider view of this subject, aerosol transport mechanisms could include convection, Brownian diffusion, thermophoresis, gravitational settling and turbulent diffusion and turbophoresis. In the wider context of this subject many references deal with these aspects with widely used and satisfactory

mathematical models (Baxter, 1998; Fuchs, 1963; Jöller, et al., 2007; Tomeczek & Wacławiak, 2009).

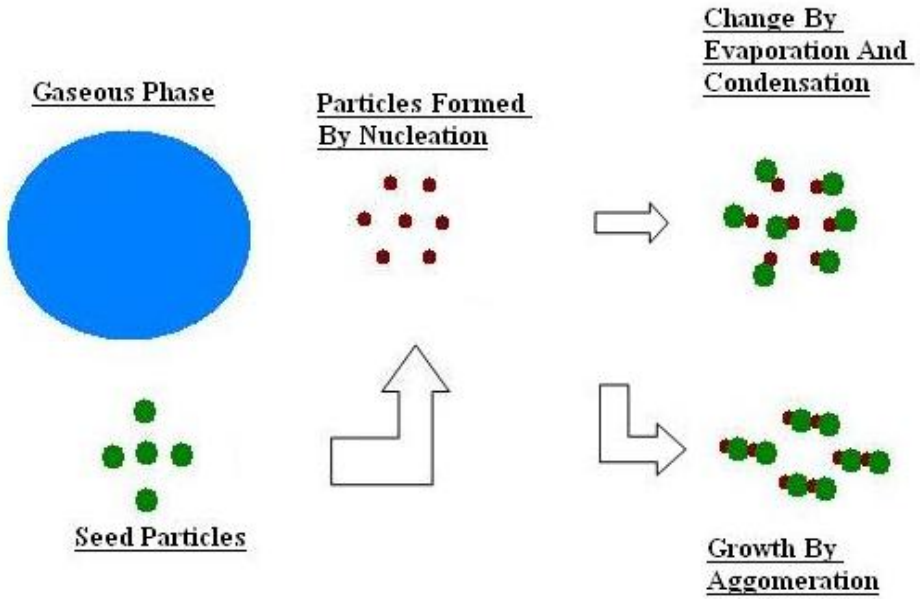

Figure 4-7. A schematic diagram of vapour phase development

The routes that aerosols form are demonstrated in Figure 4-6, in essence gaseous products from a combustion process and seed particles present in the combustor combine with particles that have been formed by nucleation leading to either evaporation (less likely in this circumstance) or condensation.

The paths to deposition illustrated in Figure 4-6 can have the following paths

- Molecules begin nucleation because of change in the properties of the gaseous vapour;
- Molecules can also form vapour by collecting on seed particles such as dust or other larger molecules begin nucleation;
- Subsequently, the nucleated liquid molecules are change by cycles of evaporation and condensation or growth by agglomeration.

Another path is that particle agglomerate through direct impact. Commercial CFD modelling of aerosols are widely used founded on the finite volume method and are based on a macro scale simulation (Kaer, et al., 2006). If the aim is to consider where particles form and how they adhere in flight and on the tube, this Thesis view is that the microscopic scaling should be considered.

For a macro-scale model of the rate of particle deposition one reference source uses the probability of the solid particles to remain on the surface as an indication of the adherence of a particle in a field (Tomeczek & Wacławiak, 2009).

In Chapter 3, a modelling method was adopted to predict the likelihood of particle being trapped onto the surface of the tube. The Chapter 3 particle depositions model assumes that particles are blocked from moving through the combustor by the presence of the heat exchanger tubes. The aspect ratio of the surfaces becomes extremely important to determine the exposure to the flow of particles captured by the tubes. If the particle that adverse effect the steel heat exchanger component is molecular chlorine is this approach relevant.

A mechanistic model is a description of a system in terms of its constituent parts and mechanisms as a series of inputs and outputs for example rate of corrosion or path of particle in a fluid flow. Should an attempt to build a 'staircase' mechanistic models one upon another can lead the user to missing the fundamental science behind the process. There is a thermodynamic process where molecular chlorine within this gas stream needs to reduce its energy; it will migrate to a cooler surface. This migration of chlorine to the surface is called thermophoresis or the Ligwin–Sort effect. The thermophoresis can be seen as thermodynamic process of reducing energy within the system and in reducing the energy in the process the molecular particles adhere to the surface. The adherence to the surfaces is a minimum energy state. In such state there is no 'stick probability' as for eq. (2-4).

To take another example the role mechanistic modelling over thermodynamics analysis, then use a thought experiment. Why is nitrogen not entrapped within the surface of the heat exchanger tubes? If nitrogen is one of the gases present in the intake of gases what happens to compounds of nitrogen present in the furnace atmospheric? What happens to the iron from coal component of co-combustion with biomass? While, at the temperatures found in the PF Boiler the nitrogen combines with oxygen and remains stable, iron oxide is frequency found in deposits. Is it that NO_x products act as a catalysis that promotes the formation of Fe_2O_3? The answer to these questions lies in the availability of free enthalpy to form or break-up compounds.

Compounds of silicon, potassium, chloride and sodium may form a part of the composition of the supporting combustion process and how is it possible to determine which will form vapour deposited onto the fins as shown in Figure 4-4. For example, nitrogen compounds are

present in the furnace but seldom is seen trapped into the build-up on tubes but Iron is often present in the coal and can contribute to dendrite finger growth with the formation of slagging on test probes (Andersen, et al., 2000).

The explanation of the questions posed in the last paragraph about the behaviour of nitrogen and other elements present in the gasses; is these elements either participate or do not participate in the formation of deposit because of the free energy occupies the physical state. That these elements are a gas, liquid or solid based on the excess energy which elements have in any particular point in space and time. While a meshed solution is a common modelling strategy it's a phenomenological theory (a theory that expresses mathematically the results of observed phenomena without paying detailed attention to their fundamental significance). Underlying the movement of both molecules (gas or vapours) and visible particles are particles that move or change state according to the temperature and the air currents present in the furnace.

A general-purpose CFD package will restricted user of these packages to physics model and its scope as supplied by the commercial business. CFD models are capable of simulate and analyze the performance of thermo-chemical conversion equipment such as fluidised beds, fixed beds, combustion furnaces, firing boilers, rotating cone reactor and rotary kilns. CFD programs predict not only fluid flow behaviour, but also heat and mass transfer, chemical reactions (e.g. devolatilization, combustion), phase changes (e.g. vapour in drying, melting in slagging), and mechanical movement (e.g. rotating cone reactor). Compared to the experimental data, CFD model results are capable of predicting qualitative information and in many cases accurate quantitative information. CFD modelling has established itself as a powerful tool for the development of new ideas and technologies. The complexity of CFD modelling for biomass thermo-chemical conversion still face significant challenges due to the complexity of the biomass feedstock and the thermo-chemical process (Wang, 2008). Despite the diverse capabilities of CFD this case study shows that CFD analysis is no guarantee to a solution to a problem. A software routine to answer why free nitrogen is not entrapped in the layers of deposits on the tube or why iron contributes to form dendrite fingers is not available. For a cases where there is lack of an appropriate CFD software routine to model the physics of a particular problem. Then the solution to such problems will require a new approach.

4.3 Numerical modelling of condensation through fugacity

The key parameter that relates the vapour equilibrium to liquid state is its vapour pressure; this equilibrium vapour pressure is an indication of a liquid's evaporation rate or the gas condensation rate. Since all liquids have a tendency to evaporate and all vapours have a tendency to return to liquid or to solid in the right conditions. It relates to the tendency of molecules to escape from the liquid.

In Chapter 2 a brief explanation of fugacity was summarised. Fugacity was explained as a replacement of chemical potential and a derivation from the grand canonical ensemble as eq. (2-22). Fugacity was expressed as in the form of an ideal gas using a pair of Lagrangian multipliers α and β. Considering a non-ideal gas then the fugacity f_i of a gas *i* is simply related to the activity by reference pressure p_o as (Le Bellac, et al., 2004)

$$f_i = p_o e^{\alpha} \tag{4-1}$$

If the reference pressure p_o is defined as the partial pressure. The fugacity coefficient Φ will include the exponential of one of the Lagrangian multipliers e^{α}. The fugacity coefficient Φ will then present degree the idea gas form of the fugacity *f* departs from the ideal gas is,

$$\Phi = \frac{f_i}{p_o} \tag{4-2}$$

As described in Chapter 2 fugacity in this form is the replacement for chemical potential under non-ideal gas conditions as eq. (2-24) states.

If the state of the gas is reduced (non ideal) the reduced temperature T_r (the ratio between the ideal gas temperature T, and the real gas temperature T_c) is defined as:

$$T_r = \frac{T}{T_c} \tag{4-3}$$

For a non-idea gas, the reduce pressure is defined as (the ratio between the ideal gas pressure p, and the real gas pressure p_c) is defined as

$$p_r = \frac{p}{p_c} \tag{4-4}$$

The condensation event does not just involve for a single gas molecule, but for a series of gases with different partial pressure. Here, the Dalton Law of partial pressure is capable of determining the total pressure.

$$\text{Pressure}_{\text{Total}} = \text{Pressure}_{1} + \text{Pressure}_{2} + \ldots \text{Pressure}_{n} \quad (4\text{-}5)$$

It should be noted that Dalton's law of partial pressures is not exactly followed by real gases. Those deviations are considerably large at high pressures. In such conditions, the volume occupied by the molecules can become significant compared to the free space between them. Moreover, the short average distances between molecules raise the intensity of intermolecular forces between gas molecules, substantially changing the pressure exerted by them. Neither of those effects is considered by the ideal gas model.

The saturation pressure at which a change of state occurs can be determined by Raoult's Law where the total saturation pressure p_s is

$$p_s = p_1x_1 + p_2x_2 + p_3x_3 \ldots p_nx_n \quad (4\text{-}6)$$

Where x is the molar fraction, therefore by summing the all the partial pressure the saturation pressure is determined. This law is strictly valid only under the assumption that the chemical interactions between the two liquids are equal to the bonding within the liquids: the conditions of an ideal solution. Therefore, comparing actual measured vapour pressures to predicted values from Raoult's law allows information about the relative strength of bonding between liquids to be obtained. If the measured value of vapour pressure is less than the predicted value, fewer molecules have left the solution than expected.

An indication where vapour condenses using the CFD package Fluent is made by inspection of the static pressure map shown in Figure 4-8. Where the vapour pressure of species held in solution in the bulk gas coincides or is below the static pressure the mixture then these species may condense. If the areas of static pressure indicated blue areas in Figure 4-8 contain high levels of dust the condensation will be the more common heterogeneous condensation. In the case of direct condensation, due to the difference in metal temperature and gas temperature, this form of condensation is directly related to the temperature of the tube. Earlier in this text the assumption was used that condensation initiation is independent mechanism of each species and that, vapour pressure is the key lever of condensation of the gas. This connection

of vapour pressure to species is carried though all the separate mechanism for condensation, whether it is direct condensation, heterogeneous or homogeneous nucleation.

The CFD package does not provide a complete knowledge of the how much nucleation material is present either as dust or larger groups of vapour. The CFD package does not give the rate at which vapour is transfer to the surfaces and cannot provide information on the more unusual homogonous nucleation of vapours and the rate at which this transfers onto the tube. Researchers have model heterogeneous and homogeneous vapour as a lumped value for the rate of vapour deposition (Kaer, et al., 2006; Wang, 2008). This lumped value for vapour deposition is adopted because mechanisms controlling potassium release rates are not sufficiently well understood to model the conversion and release processes in detail (Kær & Rosendah, 2003).

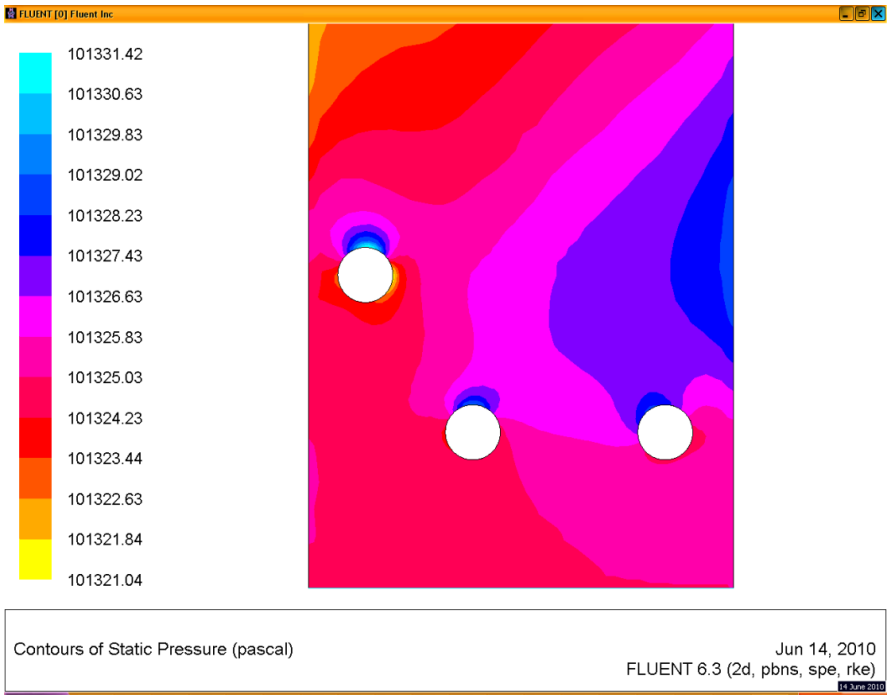

Figure 4-8. Static pressure near or around banks of tubes

The rate of transfer of vapour to the surfaces of the tubes is a function of the mass transfer coefficient, the concentration and the mass transfer area.

$$\dot{n} = \dot{\beta} A \Delta c_A \qquad (4\text{-}7)$$

Where $\dot{n}$ the mass transfer rate, $\dot{\beta}$ (mol/(s·m^2), (mol/m^3) or m/s), $\dot{n}$ is the mass transfer coefficient mol/s, A is the effective mass transfer area (m^2) and Δc_a is the driving concentration difference (mol/m^3).

The mass transfer coefficient $\dot{\beta}$ can be evaluated from Sherwood number derive from the Reynolds and Schmidt Number (see Table 2-2 for Re and Sc), the Froessling equation

$$\mathrm{Sh} = 2 + 0.6\mathrm{Re}^{\frac{1}{2}}\mathrm{Sc}^{\frac{1}{3}} \tag{4-8}$$

The mass transfer coefficient $\dot{\beta}$ can now be derived from this form of the Sherwood Number as for eq. (2-26). The mass transfer coefficient has units of kg s^{-1}; here if the period is known, the mass of material for a particulate species can be determined.

4.4 Case Study: Vapour deposition of potasium sulphate K_2SO_4

The physical model derived from eq. (4-1) to eq. (4-8) can be programmed onto an Excel spreadsheet. With the Excel spreadsheet model, it has been possible to determine the rate of vapour condensation, heterogeneous condensation and homogeneous condensation. The spreadsheet calculates the minimize Gibbs free energy using the Peng-Robinson equation of state. Some basic assumptions are that the deposit system is based on a single-phase model. This allows the use of Raoult's law and hence the saturation pressure for each chemical compound. The partial pressure is determined from the fugacity from eq. (4-1). The flow properties are formulated from the appropriate correlation of Reynolds, Nusselt, Sherwood and Schmidt numbers (See Table 2-2 in chapter 2 for definition).

The heat transfer equation, the Churchill–Bernstein equation (See Appendix A7), is applied to find the surface averaged Nusselt number for a cylinder in cross flow. The Churchill–Bernstein equation is valid for a wide range of Reynolds numbers and Prandtl numbers, as long as the product of the two is greater than or equal to 0.2, as defined above. The Churchill–Bernstein equation is important because its validity is independent of the flow regime, whether laminar or turbulent flow. Hence, the Churchill–Bernstein equation is also valid when the flow is turbulent and when temperature and concentration profiles are independent of one another. In a turbulent flow regime the Churchill–Bernstein equation becomes a combination of the Reynolds and the Schmidt number as,

$$\mathrm{Sh} = 0.3 + \frac{0.62\mathrm{Re}_D^{1/2}\mathrm{Sc}^{1/3}}{[1+(0.4/\mathrm{Sc})^{2/3}]^{1/4}}\left[1+\left(\frac{\mathrm{Re}_D}{28200}\right)^{5/8}\right]^{4/5}, \mathrm{ScRe}_D \geq 0.2 \quad (4\text{-}9)$$

where Sh is the Sherwood number, Re is the Reynolds number and Sc is the Schmidt number. In terms of fugacity and Gibbs free energy equation, the Peng–Robinson equation can be solved using the following parametric form as eq. (4-10)

$$\boldsymbol{Z^3 - (1-B)Z^2 + (A - 2B - 3B^2)Z - (-AB - B^2 - B^3) = 0} \quad (4\text{-}10)$$

where

$$\mathrm{A} = \frac{\mathrm{a}\alpha\mathrm{p}}{\mathrm{R}^2\mathrm{T}^2} \quad (4\text{-}11)$$

and

$$\mathrm{B} = \frac{\mathrm{bf}}{\mathrm{RT}} \quad (4\text{-}12)$$

The terms ‘a’ and ‘b’ come from eq. (2-35), while α is from eq. (2-32). The variable R is the Universal Gas constant, *f* is the fugacity in terms of pressure and T is the temperature. Excel solves Peng-Robinson equation (eq. (2-31)) by solving the cubic equation for the coefficients A, B (eq. (4-11) and (4-12)) and Z so that cubic eq. (4-10) equates to zero.

The study has focus on the thermodynamic stability of condensate and as all condensates are a process of minimisation of energy minimization of Gibbs free energy there is no requirement to consider other forms of condensates. Hence, direct condensation, heterogeneous or homogeneous deposition is simply classified as one thermodynamic process defined by an equation of state. The results of this cases study are illustrated by taking a particular compound that is Potassium Sulphate (K_2SO_4). To separate the fraction of vapour depositions that comes either from condensation, heterogeneous or homogeneous deposition require further analysis. The rate of homogeneous deposition rate from gas to liquid at a particular temperature is show in Figure 4-9 and in SI units.

The analysis of what fraction of the total vapour deposition is derived from condensation, heterogeneous or homogeneous route is undertaken with the aid of graph theory. How graph and perturbation series is used to separating the fraction of vapour deposition is attributed to one or more on the deposition routes is discussed further in Chapter 7.

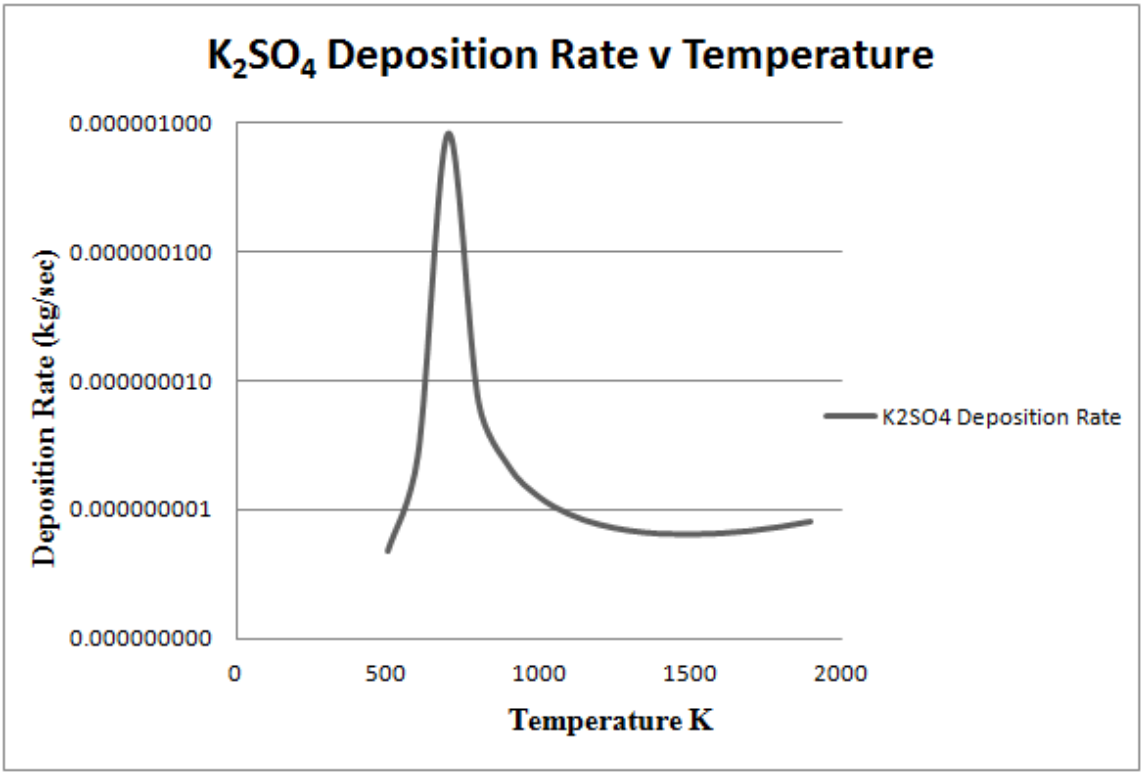

Figure 4-9. Homogeneous gas to liquid deposition rate for K_2SO_4 using the Peng – Robinson equation

4.5 Discussion and results

Some sources in the literature (Baxter, 2004) present a homigenised vapour depostion and can demostrate that CFD will provide a generalised data usefull for reports in area such as industry business case studies on biomass for energy and climate protection studies. However, in areas of study on the effects of corrosive deposition it's important to determine the contribution is from direct condensation, heterogeneous or homogeneous deposition.

While, this confirmation source from a CFD program is not ideal, similar work with electroplate and over methods of deposition use a similar method determine the deposition rate. Further references on the chemical vapour deposition (Bouteville 2005) the same use of Sherwood number and partial pressure method. If Potassium Sulphate deposits onto the surfaces of the furnace and superheater heat exchanger tubes the subsequent chemical deposition reaction is undesirable. In light of these references to CFD modelled data and sources from other fields is possible make some statements on the solution of the physics of

vapour deposition. This statement is that Gibbs free energy and Peng-Robinson equation of state are able to model heterogeneous or homogeneous deposition at a fundamental level.

The key points from this chapter are;

- This physics is not recent; in fact, it has been available since the mid 20th century and is widely used in chemical vapour deposition (Geiser & Röhle 2008).
- In this chapter the physics of statistical thermodynamics has been pushed to the front because of periodic deterministic factors can interfere with the resolution of problems using mechanistic models.
- In the term ‘mechanistic model’ is one that uses force or implied force in a continuum to drive the path of the particle motion. For example the determination of heterogeneous or homogeneous deposition by using Euler method or Runge-Kutta solvers in the CFD package Fluent (ANSYS 2001) to solve heterogeneous or homogeneous vapour PDE.
- In general, mechanistic models are designed to simplify the complex but can have unwanted side effects if they are push to far and over simplify the problem to be solved. These side effects are the result of the scale of the particles, at micron aerosols size the physics is different to the physics at molecular sizes particles. The limits to the mechanistic models used in CFD can lead to poor results and argued here is for the statement that as the power of computer advance the need for simplification is reduced.
- It is clear from the use of Gibbs free energy (free entropy), it is possible to answer the entire question posted earlier, and in than Nitrogen compounds will not occur in the slag depositions because its vapour pressure is much higher than the static pressure around the tube. In the same way iron slagging and dendrite formations is a function of particle impaction deposition from condensate and not vapour deposition. Nitrogen compounds remain as a gaseous state since there vapour phase is much lower than the temperature inside the PF boiler.
- To expand the difference between condensate and vapour deposition, then vapour deposited onto a cooler surface from the surrounding gas and condensate grows from the build up of compounds on the surface of the tube.

- This approach adopted in this thesis uses statistical thermodynamics that will be developed further as the subject will explore, through continuum statistical mechanics, using a mesh-free method. With the Ansys Fluent CFD Models, convergence was a major problem. In the case of static pressure acceptance of convergence of the solver was assumed when the stable result was confirmed. This stable result took 300 iterations and demonstrates the limitation of a meshed finite volume based CFD solutions.

5 Combined Case Study: Combustion, deposition and vapour model

5.1 Solutions of partial differ equation using meshed systems

When solving partial differential equation (PDE) there are instances when an unreliable, and inaccurate solutions occurs or have no solution at all (Lewy, 1957). The solution turns out be unstable or strongly diffusive in such a way that the solution obtained is inaccurate even in very simple equations. Applying a mesh to a geometric surface and solving PDE at the intersection of the grid, has been seen to be a way of stabilising the result. The concept behind the use of a mesh is to reinforcing the iterative process used in the numerical solution of PDE. There are however, many cases where the opposite effect will occur and considerable time will be spent on re-meshing over the form's geometry in order to obtain a result that will converge.

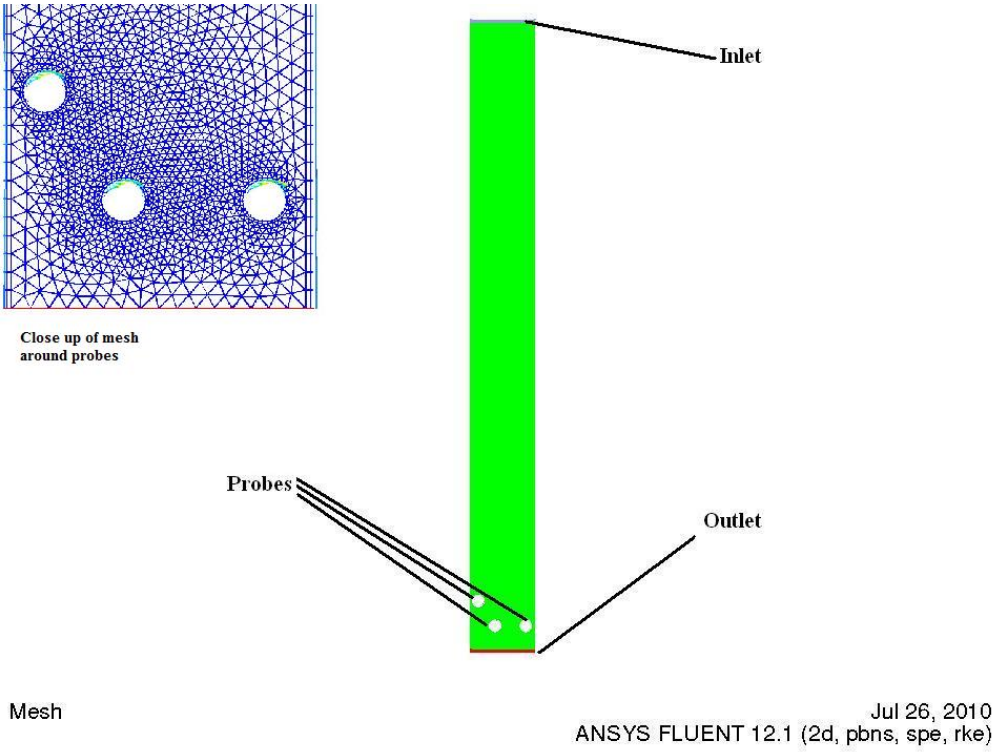

Figure 5-1. Full pipe furnace model showing key boundary features

Consider two geometries, one form represents a pipe test furnace and the other represents a series of connected and simplified geometries that models PF boiler close to the primary superheater location that was previously shown in Figure 2-1.

For the pipe test furnace, the geometry has already been shown in close-up of the three inserted circular probe in Figure 4-2 and for completeness the full pipe furnaces is redrawn to full height in Figure 5-1. The second geometry considers the primary superheater and a single tube are modelled to derive the accretion on these tubes. The model in Figure 5-2 uses geometry that is symbolic of the geometry of a power station boiler. The dimensions of the PF boiler are scaled proportionally and the geometry is design to show that periodic deterministic patterns in CFD solvers are geometrically independent of geometrical form.

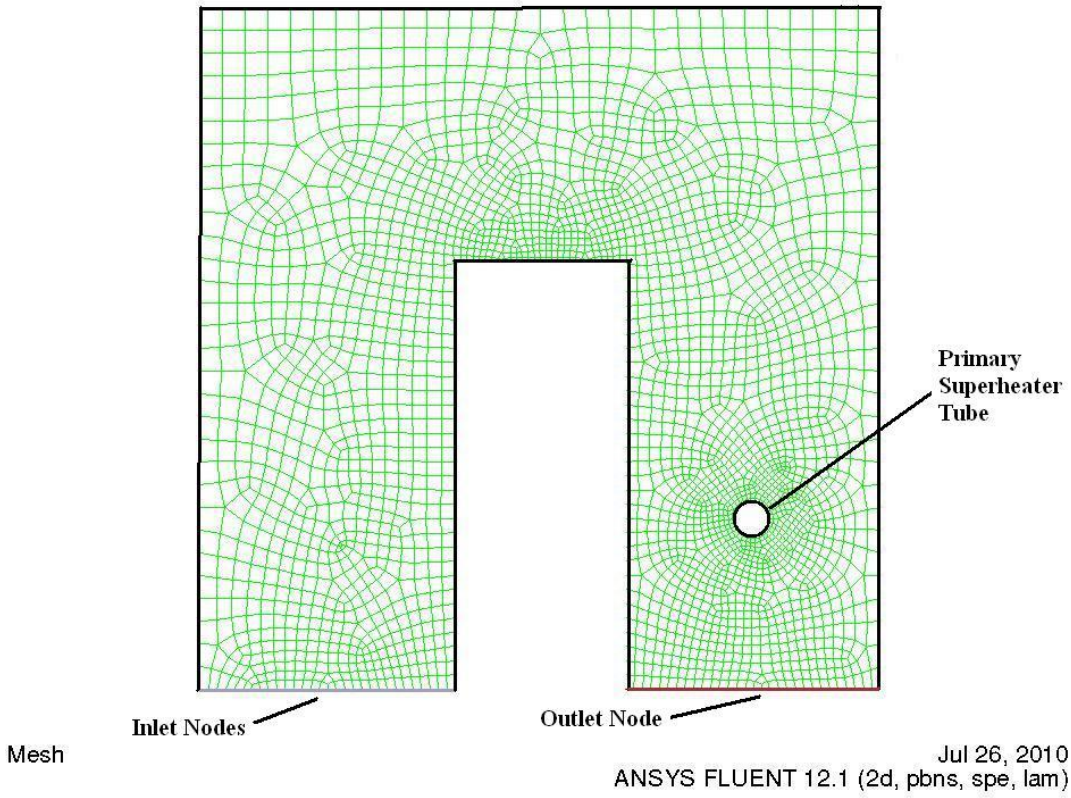

Figure 5-2. A CFD mesh simplified PF Boiler with a single primary superheater tube.

Both these models are prepared using Fluent Version 12 with the initial properties of velocity, pressure, kinetic energy of turbulence, turbulence dispersion and volatile content of fuel to the values shown in Table 5-1 at the start of the run. While running both models the residual

errors are monitored to assess the stability of each model. The residual error plots of both the pipe furnace and the PF boiler will be analyse to measure its deterministic behaviour.

Table 5-1. Initial start values for solution deposition models using Fluent

	Temperature	Velocity	Pressure	k	ε	Hv (b vol)l
Pipe Furnace	1075 K	10 ms^{-1}	10325 pa	0.015 m^2s^2	0.004312417%	0.12%
PF Boilers	1075 K	10 ms^{-1}	10325 pa	N/A	N/A	0.12%

The CFD package (Fluent) applies the particle injector option to model the discharge of ash into the pipe furnace. The CFD package then applies an ash discharge model based on Rosin-Rammler distribution to model the dispersion of the ash into both vessels. These models are co-fired with a simulation of coal-biomass mixture where the hydrogen (Hv) is evolved from the biomass is measure as a percentage of the total mass of the biomass fuel. In a stepped increase starting a 0.1% the Hv value was increased by increments of 0.05% until instability in the solution of the solver used to resolve the PDE cause the program to stop. At the limit of stability in the program the Hv values where 0.12% as shown in Table 5-1, where on a residual error plots was plotted.

In the case of PF boiler model, the k-ε turbulence model is not utilised in the calculation of the path of the ash particle since the model considers only the flow of gas in the furnace and not the motion of ash particles. The PF boiler test case in Figure 5-2 considers only the vapour deposition on the tube. The pipe furnace in Figure 4-1 is concerned with the path and final impact of the ash. When both are run, both the pipe furnace and PF boiler completes to a partial convergent solution.

The residual error plots, illustrated in Figure 5-3, for the pipe furnace shows that x-y velocity, hydrogen and continuity reach a stable convergent solution. While other residual error plots shows kinetic energy of turbulence (k) are not stable and oscillate in an error range between 1 x 10^{-2} and 1 x10^{-3}.

The residual error plots, illustrated in Figure 5-4, for the PF boiler test case models show only partially converges. The data shows that x-y velocity and continuity will convergence but this time the hydrogen volatiles do not converge and they oscillate widely.

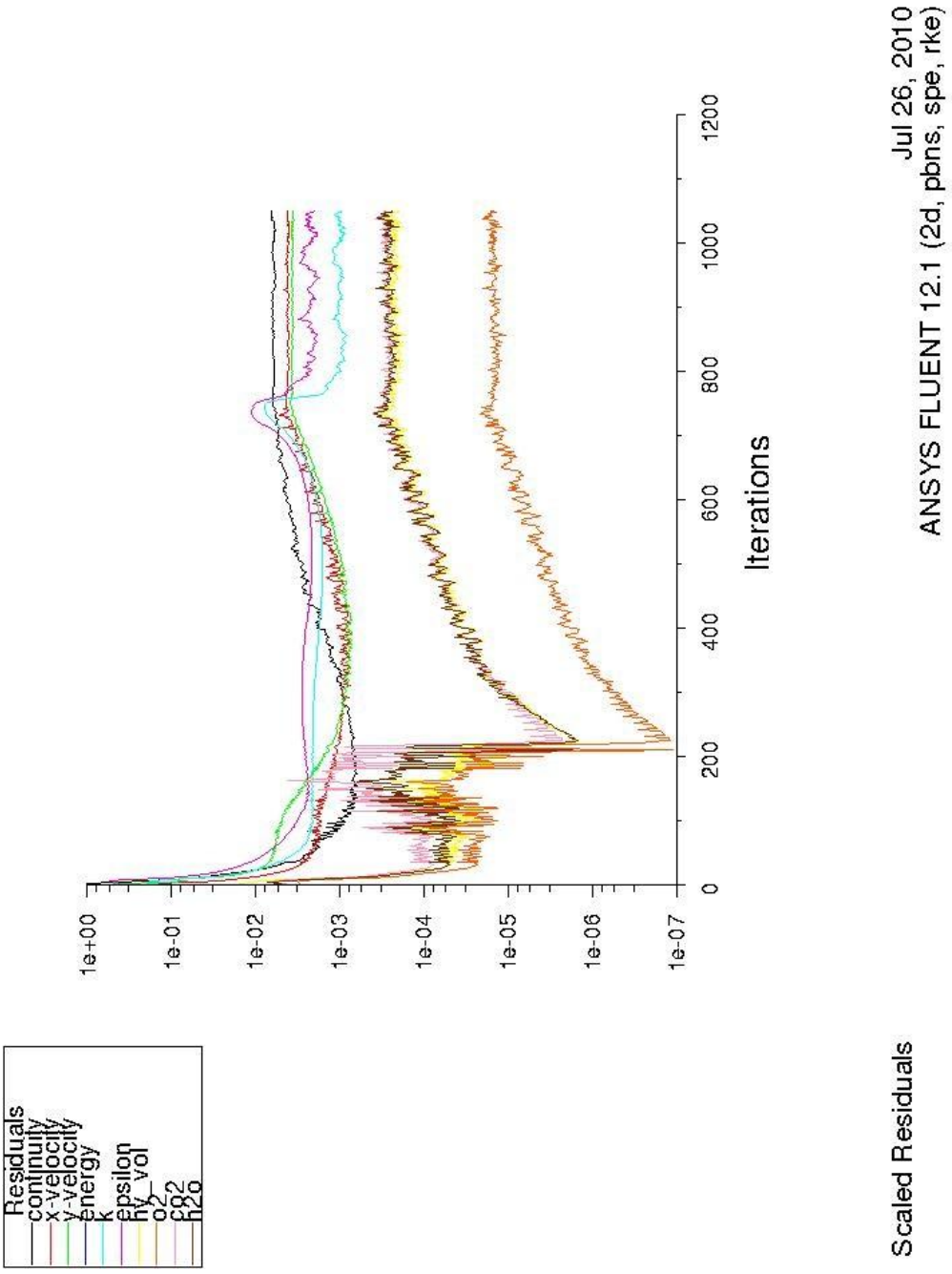

Figure 5-3 A Residual error plot of pipe furnace from Figure 5-1

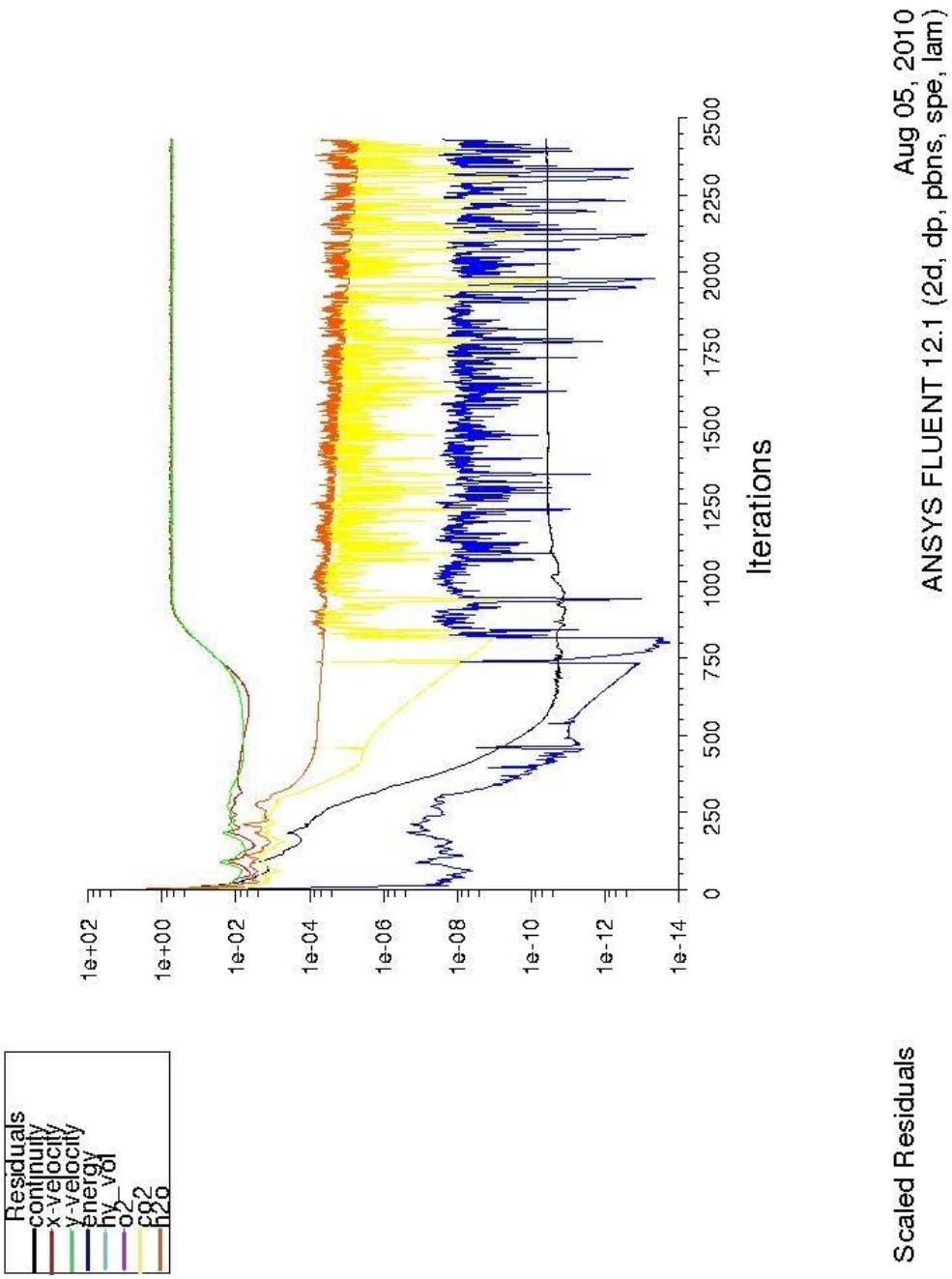

Figure 5-4. Residual error plot for PF Boiler from Figure 5-2

This variability in the solution is a key aspect to search for the other schemes for solving PDE other than the meshed finite difference method.

A universally accepted mathematical definition of either a random process or a chaotic process has not been agreed. This is because identifying the difference between a random process and a chaotic process can only obtained by measuring the determinism of the system. The determinism for a system that contains a pure signal, can be obtained using the following

1. Pick a test state
2. Search the time series for a similar or 'nearby' state; and
3. Compare their respective time evolutions.
4. Observe the behaviour of the growth, decrease (damping) or constant error between the test state and the 'nearby' state.

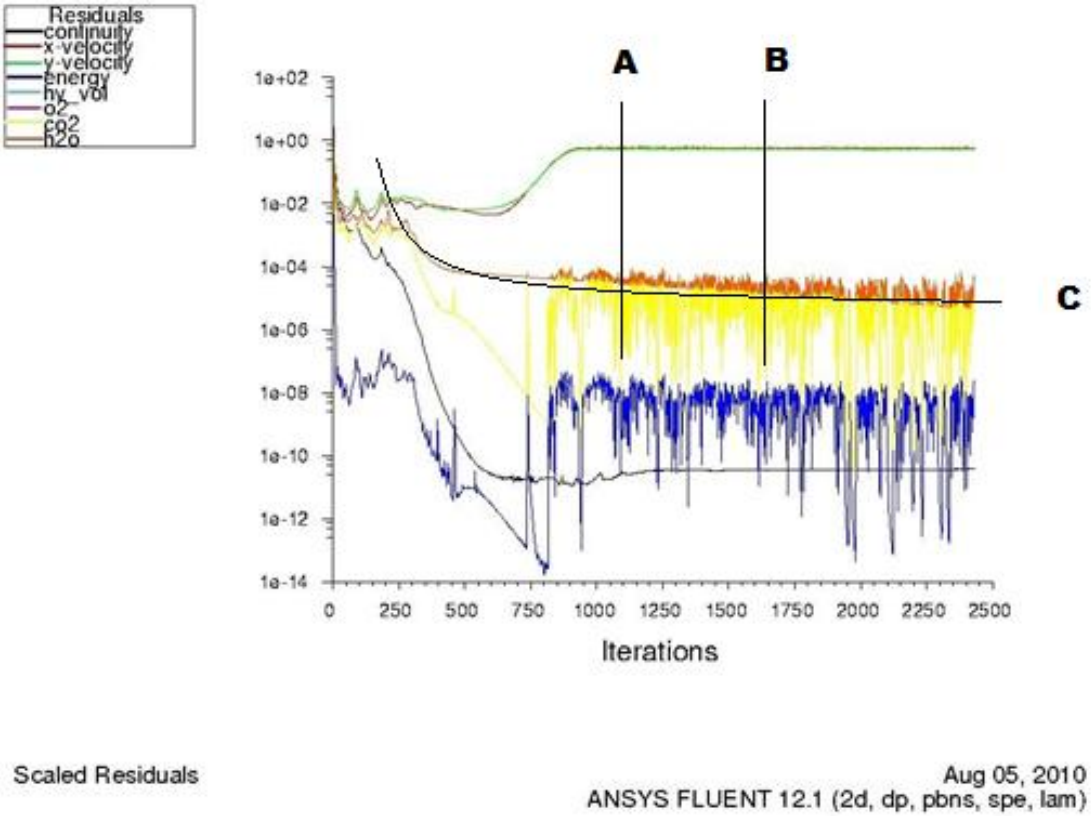

Figure 5-5. Analyse of the degree of deterministic behaviour in the pipe furnace solver

A deterministic system will have an error that either remains small (stable, regular solution) or increases exponentially with time (chaos). A stochastic system will have a randomly distributed error.

Pipe furnace boiler residuals error plots shown in Figure 5-3 are tested for its degree of deterministic behaviour. By marking the residual error plot Figure 5-3, by suitable lines A, B

and C a test of the deterministic behaviour can be undertaken. In Figure 5-5 the residuals for energy (blue), CO_2 (yellow) and X direction velocity (red) between A and B are the subjects of test of deterministic behaviour. Closer examination of Figure 5-5 show that there are a number of periodic repeat patterns in the signal and so the solution set for the PDE for energy, CO_2 levels and X velocity is randomly scattered. The periodic patterns are not increasing exponentially with time so therefore the systems can be stated as having largely stochastic components.

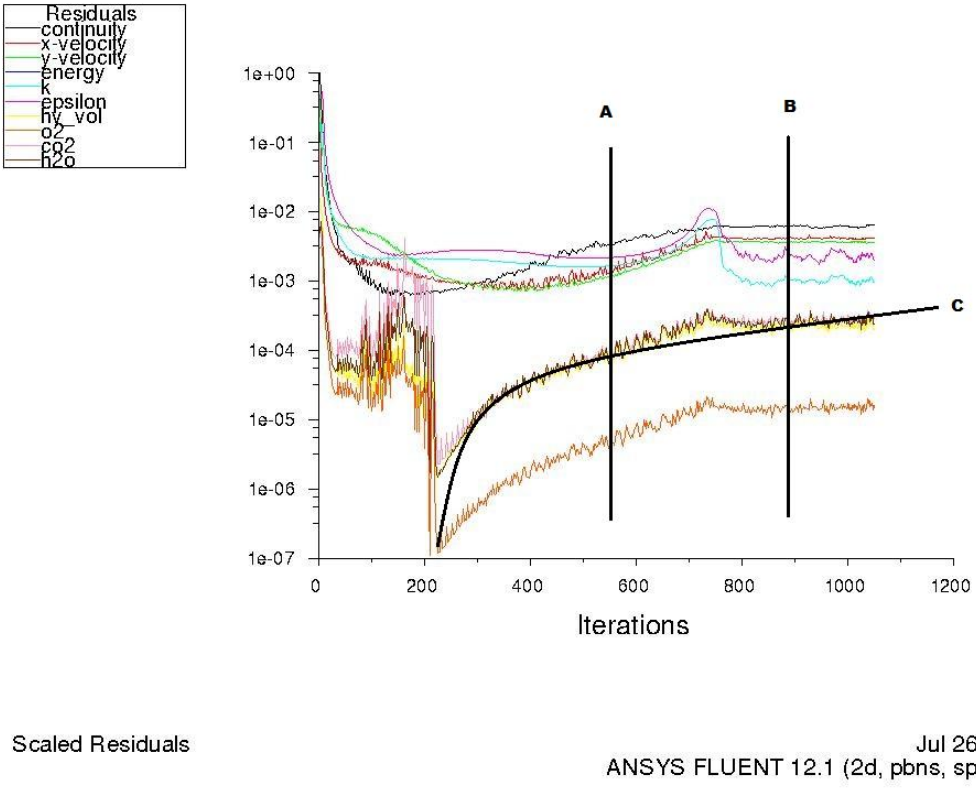

Figure 5-6. Analyse of the degree of deterministic behaviour in Primary Superheater solver.

To analyse PF boiler residuals error plots in Figure 5-4 one uses the same deterministic test in the pipe furnace in Figure 5-6. The residual test for the PF boiler consider residuals for energy (blue), CO_2 (yellow) and X direction velocity (red) between A and B illustrated in Figure 5-4. If a trend line C is drawn as illustrated in Figure 5-6, the residual error revels that there are a number of periodic repeat patterns in the signal and so the solution set for the PDE for energy, CO_2 levels and X velocity are randomly scattered. While the general trend line C shows that

the data is not growing exponentially, has a sinusoidal shape and without periodic breaks in the sinusoidal wave form, the systems can be stated as having largely stochastic components. The pipe furnace boiler deterministic test and the PF boiler deterministic test have demonstrated that both the pipe furnace and the PF boiler both have stochastic pattern behaviour. The stochastic behaviour of these solution sets provides a strong case for the solution methods that use a stochastic approach. The fluid flow and combustion gas constitutes are modelled using PDE. The stochastic behaviour of the PDE can make the numerical solution of the underpinning PDE more uncertain to converge. Methods of solving PDE that will cope with this stochastic behaviour will be discussed next.

5.2 Solutions of Navier - Stokes equations using SIMPLE algorithm

To examine the solution of fluid dynamics equation around a cylindrical tube mathematically, an example of tube in laminar flow is considered. A cylindrical tube in cross-section and stationary in a laminar fluid (or gas) flow is characterized by an elliptical form of the Poisson equation. Potential flow or fluid flow characterised by lines with similar properties as illustrated in Figure 5-7. These lines of constant properties are called streamlines. In Appendix B the difference between the potential flow and the real flow are discussed in more detail.

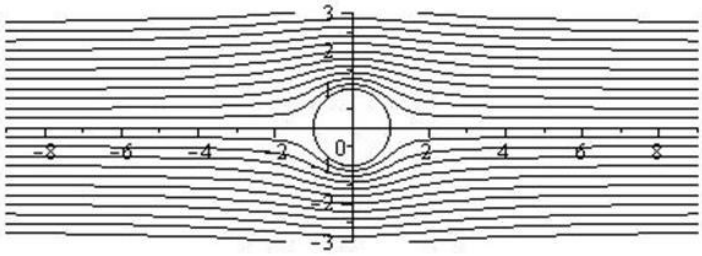

Figure 5-7. Potential flow around a tube

The solution of this equation involves the solution of subsidiary equations that are connected to the resolution of the Navier-Stokes equations in laminar flow.

$$\frac{\partial(\rho\phi)}{\delta t} + \mathrm{div}(\rho\phi\mathbf{u}) = \mathrm{div}(\Gamma\ \mathrm{grad}\ \phi) + S_\phi \qquad (5\text{-}1)$$

where ρ is the fluid density, ϕ is a general variable for conservative form of quantities like temperature and pressure etc, Γ is the diffusion conductance and S is the momentum sources for the fluid. Solving this equation enables the pressure field around the tube to be resolved. In other words it can be stated as

Rate of increase of ϕ of fluid element	+	Net rate of flow of ϕ out of fluid element	=	Rate of increase of ϕ due to diffusion	+	Rate of increase of ϕ due to sources

The transport equations for each velocity component – momentum equation that satisfies continuity are derived by replacing ϕ with u, v, and w respectively, μ the viscosity of the fluid, t the transitory time function and S_u the momentum term without diffusive properties.

x momentum;

$$\rho\left(\frac{\partial u}{\partial t}+u\frac{\partial u}{\partial x}+v\frac{\partial u}{\partial y}+w\frac{\partial u}{\partial z}\right)=-\frac{\partial p}{\partial x}+\mu\left(\frac{\partial^2 u}{\partial x^2}+\frac{\partial^2 u}{\partial y^2}+\frac{\partial^2 u}{\partial z^2}\right)+S_{u_x} \tag{5-2}$$

y momentum;

$$\rho\left(\frac{\partial v}{\partial t}+u\frac{\partial v}{\partial x}+v\frac{\partial v}{\partial y}+w\frac{\partial v}{\partial z}\right)=-\frac{\partial p}{\partial y}+\mu\left(\frac{\partial^2 v}{\partial x^2}+\frac{\partial^2 v}{\partial y^2}+\frac{\partial^2 v}{\partial z^2}\right)+S_{u_y} \tag{5-3}$$

z momentum;

$$\left(\frac{\partial w}{\partial t}+u\frac{\partial w}{\partial x}+v\frac{\partial w}{\partial y}+w\frac{\partial w}{\partial z}\right)=-\frac{\partial p}{\partial z}+\mu\left(\frac{\partial^2 w}{\partial x^2}+\frac{\partial^2 w}{\partial y^2}+\frac{\partial^2 w}{\partial z^2}\right)+S_{u_z} \tag{5-4}$$

Continuity equation

$$\frac{\partial \rho}{\partial t}+\frac{\partial}{\partial x}(\rho u)+\frac{\partial}{\partial y}(\rho v)+\frac{\partial}{\partial z}(\rho w)=0 \tag{5-5}$$

where μ is the viscosity of the fluid, t the transitory time function and S_u the momentum term without diffusive properties.

With just 2-dimensions the $w = 0$ and $z = 0$ and at low Mach numbers the flow is incompressible therefore ρ = constant.

Using the notation for stencil boundaries, ‘w’ and ‘e’ are the limits of the control volume ‘p’ for the meshed finite difference 1-D example illustrated in Figure 5-8. A set of discretization coefficient a_w, a_e and a_p the represent the rate increase in momentum defined as

$$a_p u_p^* = a_w u_w^* + a_e u_e^* + S_u \qquad (5\text{-}6)$$

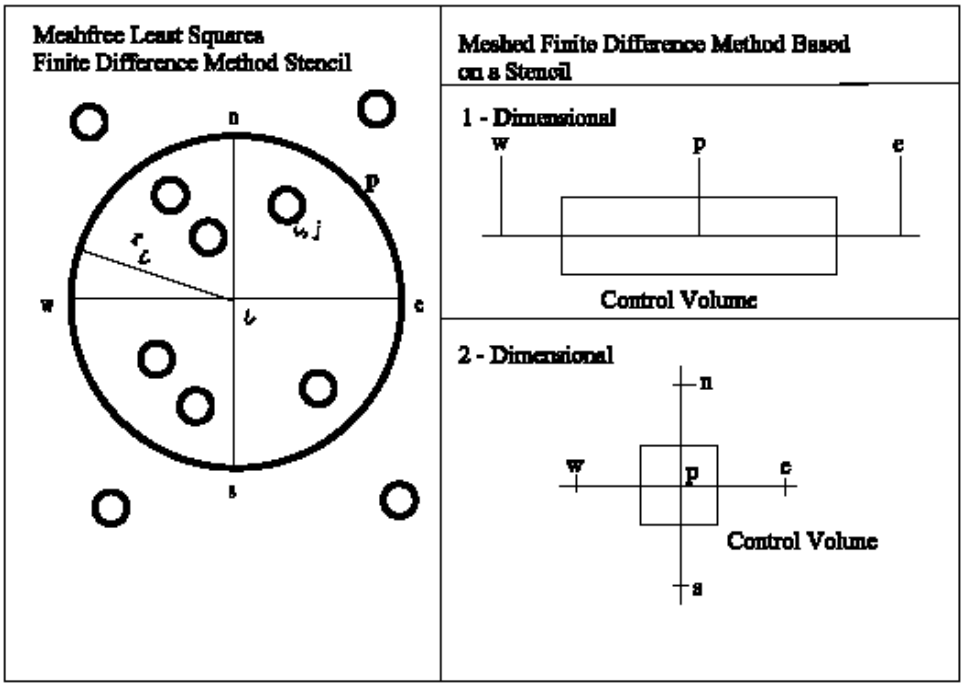

Figure 5-8. The comparisons between finite difference and mesh-free least squares finite difference stencils.

The terms u is velocity and S_u is the source term due to the increase in momentum of the system. In 2D, the stencil boundaries ‘w’ and ‘e’ are supplemented with addition stencil boundaries ‘n’ and ‘s’ represented the dimension 90˚ to the line between ‘w’ and ‘e’ and completing the 2D control volume ‘p’

5.3 Meshed solutions of partial difference equations

The steady state ‘convection – diffusion’ equation can be derived from the general transport equation shown in eq. (5-7).

$$\mathrm{div}(\rho\phi\mathbf{u}) = \mathrm{div}(\Gamma \mathrm{grad}\phi) + S_\phi \qquad (5\text{-}7)$$

Setting the integration of eq**.** (5-7) over a control volume gives

$$\int_A .(\rho\phi\mathbf{u})dA = \int_A n.(\Gamma grad\phi)dA + \int_{CV}\mathbf{dV} \quad (5\text{-}8)$$

To sense the direction of flow and hence the direction of convection-diffusion, an upwind difference finite difference stencil is used. The combined upwind stencil and the general form of convection - diffusion discretization scheme in 1-dimension in Figure 5-9 has the notation for the discrete equation of eq. (5-8) as eq. (5-9)

$$a_p\phi_p = a_w\phi_w + a_e\phi_e \quad (5\text{-}9)$$

with central coefficients, and

$$a_p = a_w + a_e + (F_e + F_w)$$

with neighbour coefficients

A form of notation for the neighbour coefficients of upwind difference method that represents the notation of both flow directions is given below (Versteeg & Malalasekera, 1995):

	a_W	a_E
$F_w > 0, F_e > 0$	$D_w + F_w$	D_e
$F_w < 0, F_e < 0$	D_w	$D_e - F_e$

Here a_w, a_e and a_p are the discretization coefficient representing the rate increase in diffusion flux D and with F the mass flux per unit area.

a_W	a_E
$D_w + max(F_w, 0)$	$D_w + max(0, -F_e)$

On a 2 – D Cartesian coordinate frame the coefficients a_w and a_e representing the x axis, with a_n and a_s are introduced to represent the momentum terms in the y axis.

5.4 Assembly of the system of PDE into a mesh-free form

In the last section the various elements are assembled and the PDE are solved on a meshed system, an example of 1-D and 2-D geometric problems are illustrated in Figure 5-8. In this section a strategy for solving PDE without a mesh will be developed based on mesh-free LSFD of Li *et. al,* (Li & Liu, 2002). Following Li *et. al,* any strategy for solving PDE using

'mesh-free' method in a geometric space is called a framework. The basic solution for mesh-free LSFD is given in eq. (2-7) and in Figure 5-8 show how LSFD differs from a meshed system of solving PDE. This framework is selected because it enables discrete points in space to be mapped so to apply a multi-scale approach for both a large particles size and also the formation and motion of vapours at molecular level.

The aim in the remainder of this chapter is to construct a model that is multi-scale and can model the motion of small semi-solid particles, the products of combustion, and also the combination of molecules in the combustion products while they are free bodies or after impacting superheater tubes. To achieve the latter aim the LSFD method needs to be extend to 3-Dimensions and in this scheme, the centre points *i*, has been replaced with 'billiard balls' with points *i, j* representing atoms within the molecule.

This is represented by a cluster construction scheme that is borrowed from classical statistical mechanics. This also opens a method of solving problems on 2D and 3D geometry by adapting a stencil that maps to the molecular lattice structure of the solid or liquid understudy as well as the movement and consolidation of larger particles over 2 μm in a turbulent vortex stream.

5.5 Mayer functions

The use of combined cluster expansion and graph theory was pioneered by Mayer and Mayer (Mayer & Mayer 1940). The feature of this application of cluster theory is to map the relationship between particles as star nodes to a centre node. The aim is to configure the star nodes in a state where all the particles are in equilibrium and share the equal contribution in respect to the centre node. If stars nodes are considered to represent molecules in a gas, the aim is find the equilibrium position that occupies the lowest energy state for a given set of properties.

In an ideal gas, interactions between molecules do not occur, but in a real gas they do. Mayer and Mayer (Mayer & Mayer 1940) developed a theoretical treatment of the virial coefficients in terms of their cluster integrals. A virial coefficient is defined as how far the real gas departs from the ideal gas, which is at its simplest model, are two hard spheres molecules that occupy a space but are not bonded together.

To illustrate the Mayer's functions we take three molecules that are bonded together, there are four possible ways that they can be bonded.

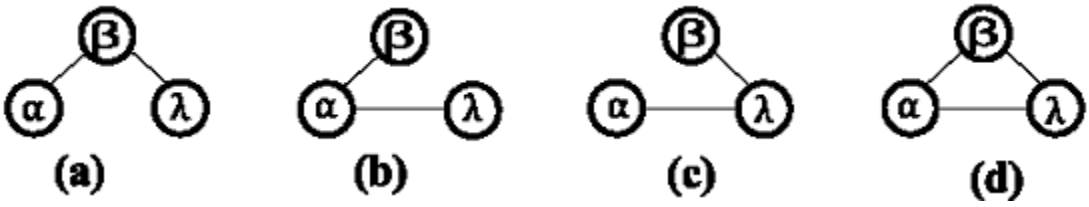

Figure 5-9. A cluster graph showing the unions of 3 molecules pairs (Bieneke, 1979)

In the molecular unions of a, b, c and d in Figure 5-9 for each set of molecular groups the minimum radius between any pair $r_{\alpha\beta}$, $r_{\beta\gamma}$ and $r_{\alpha\gamma}$ is given by the interaction energy ϕ between the N molecular pairs as in eq. (5-10).

$$\phi = \sum N_{\alpha,\beta,\gamma}\phi_{\alpha,\beta,\gamma} \tag{5-10}$$

The example in Figure 5-9 can be extended further to demonstrate that cluster graphs can be generalised for all possible configurations of N molecules. The 6 molecular pairings problem of Figure 5-9 consist of 3 molecules (α, β and γ) with only 2 distinct ways to construct groups ((b) and (c)) making 4 pairings, plus one paring each of (a) and (d) equating a total of 6. The cluster graph that operates on the volume and temperature of the molecules assembly is defines as Q(V,T) (sometimes abbreviated to Z in the literature). The 6 molecular parings problem reduces to the high order infinite sum configuration integral of eq. (2-18) to that of eq. (5-11).

$$Q(V,T) = \frac{1}{6N}\int \text{All possible interactions energy } \phi \int \exp\left(-\frac{\phi}{k}\right) \tag{5-11}$$

where k_B is the Boltzmann constant, N is molecular pairs at each configuration at an equilibrium state (for 6N pairs in Figure 5-9 these are a, b, c or d and r is the radius between each pairing). The equilibrium state is considered be active when the free energy of the system is at minima. Care must be taken to recognise the differences in a system based on chemical potential energy from one based on thermodynamic potential energy. When considering a system based on chemical potential, Gibbs free energy is used and for a system based on thermodynamic potential, Helmholtz free energy is employed. It's also important to

note that thermodynamic information is conserved in a physical system. The property of a system to conserve information and the deployment of Mayer's functions will assist in calculation of the grand canonical ensemble by a mesh-free method in a geometrical space.

From eq. (2-15) a general form of the relative position of each molecule within the system can be expressed algebraically as using Mayer f-cluster notation, for a pair of molecules f_α and f_β, then

$$1 + \mathrm{f}_{\alpha\beta} = \exp\left(-\frac{\phi(\mathrm{r}_{\alpha\beta})}{\mathrm{kT}}\right) \tag{5-12}$$

It is now possible to decompose eq. (5-12) to all possible connections by renumbering the molecular pairs index (α, β, γ) illustrated in Figure 5-9 as indices of pairs of vertices l = 1, 2, 3, 4 … Then $f_{\alpha,\beta,\gamma}$ becomes;

$$\begin{aligned} 1 + \mathrm{f}_{\alpha\beta\gamma} = 1 + (\mathrm{f}_{12} + \mathrm{f}_{13} + \cdots) + (\mathrm{f}_{12}\mathrm{f}_{34} + \mathrm{f}_{12}\mathrm{f}_{13} + \cdots) \\ + (\mathrm{f}_{12}\mathrm{f}_{34}\mathrm{f}_{23} + \mathrm{f}_{12}\mathrm{f}_{13}\mathrm{f}_{23} + \cdots) \end{aligned} \tag{5-13}$$

Simplifying eq. (5-13) in terms of cluster integrals, with V being the volume occupy by the molecular group the first cluster group in Cartesian form is

$$\Omega_1 = \frac{1}{1!\,\mathrm{V}} \int \mathrm{dx}_1 \mathrm{dy}_1 \mathrm{dz}_1 = 1 \tag{5-14}$$

The second cluster group is

$$\Omega_2 = \frac{1}{2!\,V} \int_{(3)} \cdots \int f_{12} \cdots dx_1 dy_1\, dz_1 dx_2 dy_2 dz_2 \tag{5-15}$$

The third cluster group is

$$\Omega_3 = \frac{1}{3!\,V} \int_{(6)} \cdots \int f_{12} f_{23} f_{13} \cdots dx_1 dy_1\, dz_1 dx_2 dy_2 dz_2 dx_3 dy_2 dz_3 \tag{5-16}$$

If the virial coefficient is expressed in the form of a Cartesian cluster integral such as

$$\Omega_\mathrm{i} = \frac{1}{V} \int_{(6)} \cdots \int f_{12} dx_1 dy_1\, dz_1 dx_2 dy_2 dz_2 \tag{5-17}$$

then the general form of Ω for i cluster group is

$$\Omega_i = \frac{1}{k!\,V}\int \underset{(3k+1)}{\ldots} \int \begin{pmatrix} \text{all irreducible} \\ \text{graph of order } l+1 \end{pmatrix} dx_1 dy_1 dz_1 \cdots dx_{k+1} dy_{k+1} dz_{k+1} \qquad (5\text{-}18)$$

where *l* is the number of molecules in the molecular group and k is the order number.

For more than 3 chain clusters it becomes extremely complex to express molecular pairs in this form, so it is advisable to use a cluster diagram. The key definition for forming a cluster diagram is the irreducible cluster, for any cut vertex Ω_i, has a factorised integral similar to that of eq. (5-18) but denoted as Ω_1 that corresponding to the first cluster group.

More generally, a graph like  with a cut vertex, each 'irreducible sub-graph' contributed to a factor to the integral. Hence, a graph Ω_3 has an irreducible cluster integral defined as eq. (5-14) to eq. (5-16) as Ω_1=1, $\Omega_2 = \frac{1}{2!V}\int$ and $\Omega_3 = \frac{1}{3!V}\int$  and has an irreducible cluster integral Ω_1 =1. The 'irreducible sub-graph' for the general case of eq. (5-18) will be $\Omega_i = \frac{1}{k!V}\int$  and the lowest irreducible cluster integral will be Ω_1 =1, the second cluster group will be $\frac{1}{2!V}\int$  and so on up to $\Omega_i = \frac{1}{k!V}\int$  .

It is simpler to define these networks in terms of 'Husimi trees' (Husimi 1950) which are formed by joining together polygons and edges in this manner, using in this particular case, the cluster graphs from Figure 5-10. A combination of simple cluster diagrams will form graphs like Figure 5-10, these 'Husimi trees' are representation of molecular groups. Therefore from a simple root polygon, a very complex structure can be constructed (Hill 1987). An alternative name of 'Husimi Trees' is 'Cacti'.

The term cut vertex refers to the breaking up of the molecular grouping pairs a, b, c and d in Figure 5-9 from the more complex forms in Figure 5-10. So breaking the complex forms in the Husimi tree of Figure 5-10 back to the simplest structure of the type of Figure 5-9. The molecular pairs group α, β and γ are never broken as they assumed to the smallest stable structure. Since the term molecules have mention up to now it would be more correct to use the convention in mesh-free methods term these molecules as particles.

In Figure 5-9 the basic form shown is of a basic amorphous structure at a molecular level. However, more complex structure can be built at micro particle size; developing the concept

as a fully multi-scale modelling process. This is illustrated with the development of a model of combining particles in a combustion gas flow system which will be developed next.

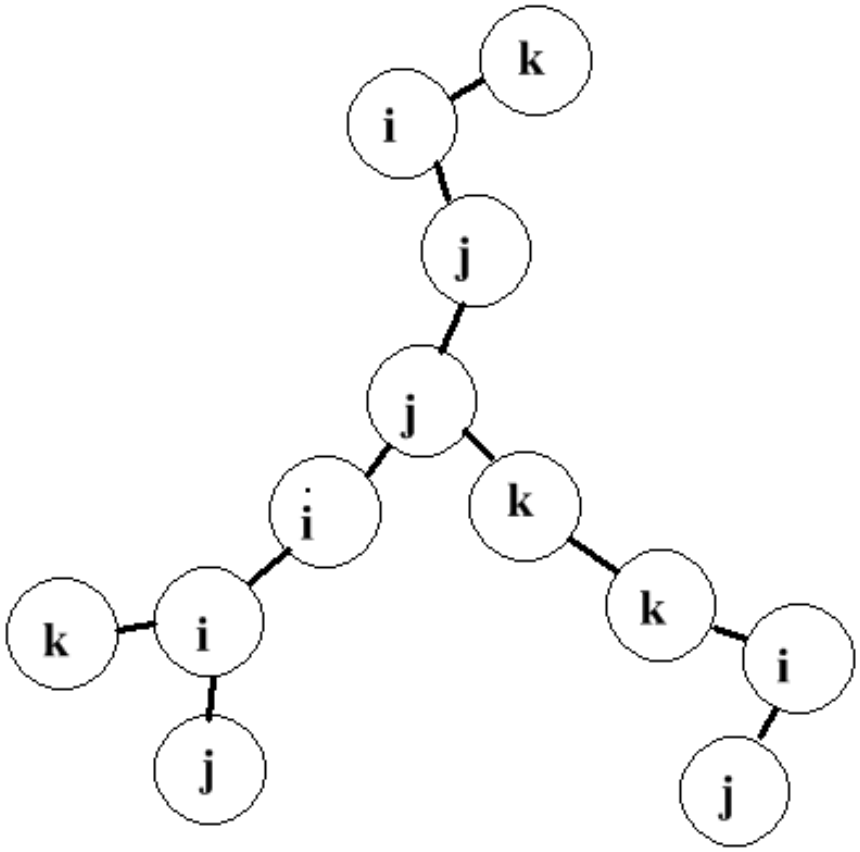

Figure 5-10. Custer graph 'Cacit' product from the irreducible cluster in Figure 5-9 (Bieneke, 1979)

The development of the cacti of Figure 5-10 is the expansion of the function g(r), where r is the minimum space which two particles can occupy while still being as independent entities. The expansion is continued over 5 particles, which is normally shown as a pentagon.

However, to visualise the line by line solution of the modified SIMPLE algorithm; the form of Figure 5-11 is used and then ninth and nineteenth terms of series $\frac{1}{v^2}$ are grouped into the cacti of Figure 5-12. This choice of grouping is arbitrary but it permits the SIMPLE algorithm mesh finite difference method to convert from a meshed scheme to a particle mesh-free method. The SIMPLE algorithm is used to find the approximate solution to the Navier-Stokes equation for fluid flow, so determine the pressure and velocity.

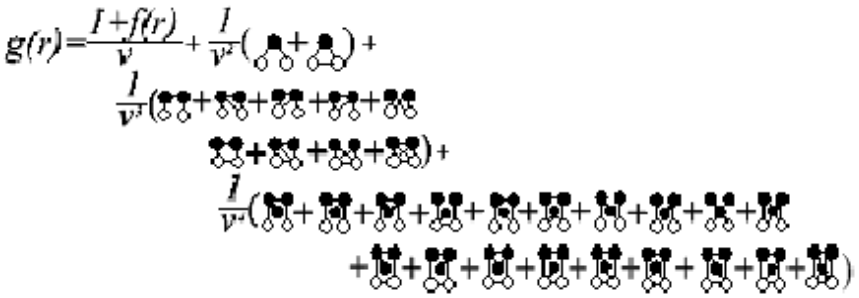

Figure 5-11. Fourth order expansion of virial distribution function.

A closed node such as indicates where the partition function Q restricts the molecule from approaching to occupy a space less then unity where

$$Q = \prod_{kk+1 \geq i > j \geq 1} f_{ij} dr_1 \ldots dr_{k+1} \tag{5-19}$$

Connecting the end nodes to form faces areas; the use of subscripted letters for the momentum coefficients on each faces is explained in Table 5-1 and referring to the star node numbers in Figure 5-12. Illustrated in Figure 5-12 is the graph of the minimum connection between the centre node 10 and boundaries defined by the star nodes 1 to 9 and 11 to 19. The mesh-free 'stencil' has a volume of unity and is constructed from two fourth order terms of the expansion of virial distribution function$\left(\frac{1}{v^4}\right)$ where *v* is all position that groups of molecule could occupy from a pair of molecules up to a groups of 5. To explain the terms $\frac{1+f(r)}{v}$, this is the probability of finding two molecule r distances apart. Therefore, 19 point discretization stencil shown Figure 5-12 is formed of fourth order terms $\left(\frac{1}{v^4}\right)$ connected into cacti, that is the graph terms (i.e.).

The area terms constructed from the end nodes are evaluated as being unity for all terms with the distance between each node summing to a length of unity. Each u, v and w momentum term are evaluated line by line and formed in to a 19 x 3 element array of coefficients of 19 simulations equation in form of Ax=B The solution of these simulations equations is achieved by using the Jacobi method (Versteeg & Malalasekera, 1995). Earlier the centre node and point used the notation *i* as the centre node and *i, j* as the 2-dimension Cartesian distance between the points. The adaption of this stencil scheme to 3-dimension then a numbering

system is used, in this case the particle/atoms point are numbered 1 to 9 and 11 to 19 with the centre node numbered 10.

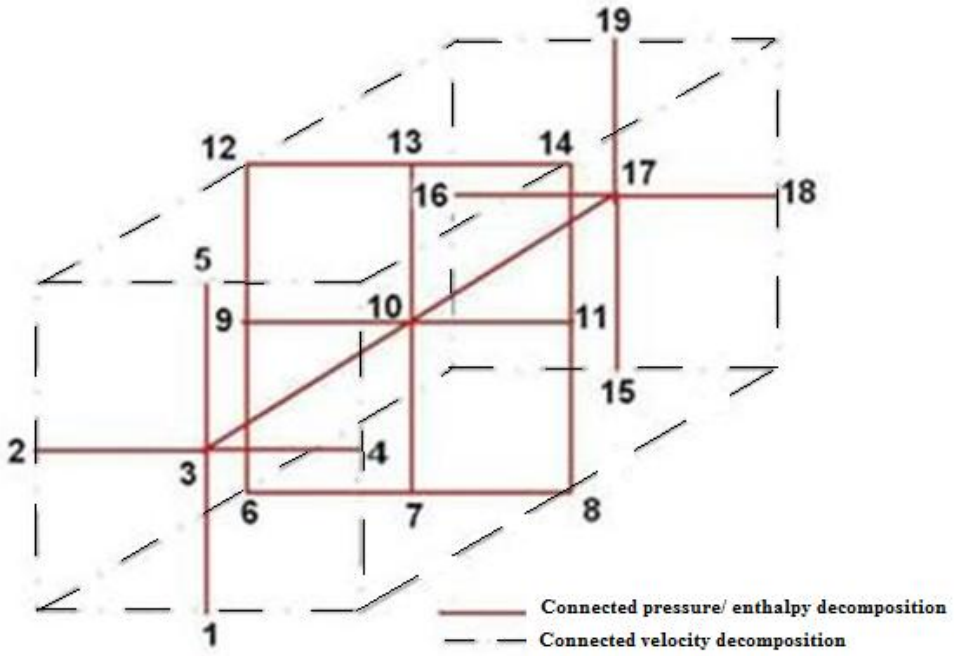

Figure 5-12. Graph of the minimum connection between the mesh-free 'stencil' and the properties model

This enables the faces on the control volume p to be mapped as a series of numbered atoms/points outlined in Table 5-2

Table 5-2. Discretization of the momentum coefficients

momentum coefficients u,v,w	Node numbers that form face areas $A_{(nb)}$	Velocity $u_{(nb)}$	Diffusion $D_{(nb)}$	Force $F_{(nb)}$
a_w	2,6,9,12,16	u_w	$\Gamma_w/Area_{(w)}$	$\rho_w u_w Area_{(w)}$
a_e	4,8, 14,18,11	u_e	$\Gamma_e/Area_{(e)}$	$\rho_e u_e Area_{(e)}$
a_n	1,2,3,4,5	u_n	$\Gamma_n/Area_{(n)}$	$\rho_n u_n Area_{(n)}$
a_s	15,16,17,18,19	u_s	$\Gamma_s/Area_{(s)}$	$\rho_s u_s Area_{(s)}$
a_t	5,12,13,14,19	u_t	$\Gamma_t/Area_{(t)}$	$\rho_t u_b Area_{(t)}$
a_b	1,6,7,8,15	u_b	$\Gamma_b/Area_{(b)}$	$\rho_b u_b Area_{(b)}$

With this approach the field sources terms can be applied to the faces of the control volume based on a compass point configuration.

5.6 Particle deposition and k-ε turbulence modelling

In the standard version of SIMPLE, as used in meshed format, the transport properties are commonly located on a staggered grid. This approach is chosen to avoid unrealistic flow pattern arising as occurs when using collocated format (Versteeg & Malalasekera, 1995). The solution of each velocity, source and pressure field is evaluated line by line, with pressures and source terms determined at the star nodes and the velocities between the star nodes. The extreme star nodes take the pressure, source and velocity from the neighbouring centre particle nodes Figure 2-13 or from the appropriate boundary conditions for constant pressure, internal flow, external flow, wall, inlet flow and outlet flow schemes (Atluri, et al., 2006).

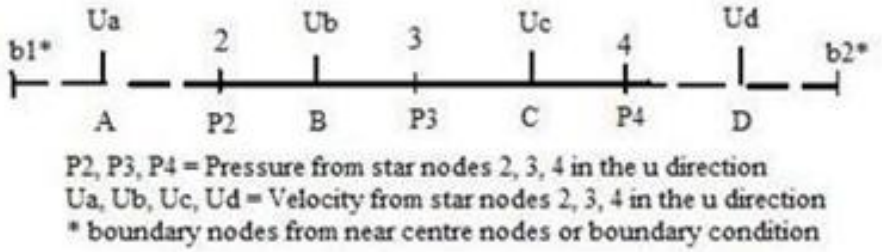

Figure 5-13. Finite difference discretization for star nodes 2, 3 and 4 in the u- direction

In line with the common solution algorithm for SIMPLE the following procedure is observed;

i. Collect all data to form an initial guess for pressure, source and velocity p^*, ϕ^*, u^*, v^*, w^*.
ii. Solve discretized momentum equations in u, v, w directions.
iii. Solve the pressure - correction equation to obtain the adjustment p' at the star node (nb).

a. $p_{nb} = p^*_{nb} + p'_{nb}$
b. $u_{nb} = u^*_{nb} + \frac{Area_{(nb)}}{u_{nb}}(p'_{nb-1} - p'_{nb})$
c. $v_{nb} = v^*_{nb} + \frac{Area_{(nb)}}{v_{nb}v -}(p'_{nb-1} - p'_{nb})$
d. $w_{nb} = w^*_{nb} + \frac{Area_{(nb)}}{w_{nb}}(p'_{nb-1} - p'_{nb})$

iv. Correct the pressure and velocities.
v. Solve all other discretized transport equations ϕ^*.
vi. Test for convergence $p' \approx 0$.
vii. If convergence fails set $p^* = p_{nb}$, $\phi^* = \phi_{nb}$, $u^* = u_{nb}$, $v^* = v_{nb}$, $w^* = w_{nb}$ an return to (ii) above

To implement the SIMPLE algorithm into a mesh-free frame work based on LSFD, node 10 in Figure 5-14 is set as the centre node with the other stars nodes providing the part of the solution through this centre node. Since the particles occupy a 3d framework it requires that the eq. (2-7) is extended from 2d to 3d. Then assuming that a solution exist as scalar function is the resultant of the transport terms evaluate with SIMPLE. Then the change dimension space from (2D to 3D) mesh-free least finite difference of eq. (2-7) will be valid, then the key criteria that points (x1-9, x11-19, y1-9, y11-19, z1-9, z11-19) is sufficiently differentiable at the centre node (x10, y10, z10) will be meet. Using Taylor series expansion for each star node i, located within the stencil illustrated in Figure 5-12 and the centre node be denoted by (x0, y0, z0), then $1 \leq i \leq m$ its demonstrable that, where:

$$f_i = f_0 + h_i \frac{\partial f_0}{\partial x} + k_i \frac{\partial f_0}{\partial y} + l_i \frac{\partial f_0}{\partial z} + \frac{h_i^2}{2}\frac{\partial^2 f_0}{\partial x^2} + \frac{k_i^2}{2}\frac{\partial^2 f_0}{\partial y^2} + \frac{l_i^2}{2}\frac{\partial^2 f_0}{\partial z^2} + h_i k_i l_i \frac{\partial^2 f_0}{\partial x\,\partial y\,\partial z} + \cdots \mathcal{O}(\Delta^3) \tag{5-20}$$

where

$$h_i = x_i - x_{0\,,}\; k_i = y_i - y_{0\,,}\; l_i = z_i - z_{0\,,}\; \Delta = \max_{1 \leq i \leq m} \left\{ \sqrt{{h_i}^2 + {k_i}^2 + {l_i}^2} \right\}$$

Let

$$\{\partial f\}^T = \{f_1 - f_{0,} f_2 - f_{0,\ldots} f_m - f_0\} \tag{5-21}$$

The set of linear algebraic equations, such that $m \geq 5$

$$[A]\{Df\} = \{\delta f\} \tag{5-22}$$

with

$$[A] = \begin{bmatrix} h_1 & k_1 & l_1 & h_1^2/2 & k_1^2/2 & l_1^2/2 & h_1\,k_1\,l_1 \\ h_2 & k_2 & l_2 & h_2^2/2 & k_2^2/2 & l_2^2/2 & h_2\,k_2\,l_2 \\ \vdots & \ddots & \cdots & \cdots & \cdots & \cdots & \cdots \\ \vdots & \cdots & \ddots & \cdots & \cdots & \cdots & \cdots \\ \vdots & \cdots & \cdots & \ddots & \cdots & \cdots & \cdots \\ \vdots & \cdots & \cdots & \cdots & \ddots & \cdots & \cdots \\ \vdots & \cdots & \cdots & \cdots & \cdots & \ddots & \cdots \\ h_m & \cdots & \cdots & \cdots & \cdots & \cdots & h_m\,k_m\,l_m \end{bmatrix} \tag{5-23}$$

where seven unknown derivative at the point ($x_{0,}\, y_0,\, z_0$) are

$$[\mathrm{Df}]^{\mathrm{T}} = \left\{ \frac{\partial \mathrm{f}_0}{\partial \mathrm{x}}, \quad \frac{\partial \mathrm{f}_0}{\partial \mathrm{y}}, \quad \frac{\partial \mathrm{f}_0}{\partial \mathrm{z}}, \quad \frac{\partial^2 \mathrm{f}_0}{\partial \mathrm{x}^2}, \quad \frac{\partial^2 \mathrm{f}_0}{\partial \mathrm{y}^2}, \quad \frac{\partial^2 \mathrm{f}_0}{\partial \mathrm{z}^2}, \quad \frac{\partial^3 \mathrm{f}_0}{\partial \mathrm{x}\, \partial \mathrm{y}\, \partial \mathrm{z}} \right\} \tag{5-24}$$

Since the particle distribution is regular and $m > 5$ the system in eq. (5-24) is an over determined set of algebraic equations. Its solution can be obtained from the singular value decomposition (Golub & Van Loan 1998) using based on the solution linear least squares problem which has the form $M = A^T x$, i.e.

$$[\mathrm{Df}]^{\mathrm{T}} = (\mathrm{U}\Sigma\mathrm{V}^{\mathrm{T}})^{-1}\{\delta \mathrm{f}\} \tag{5-25}$$

where $[Df]^T$ is derivatives at the point (x_0, y_0, z_0) from eq. (5-26), $(U\Sigma V^T)^{-1}$ is the pseudo-inverse of $\{\delta f\}$.

The partition of the solution space defined for f in eq. (5-25) is necessary since the underpinning this method is the concept of partition of unity (Li & Liu, 2004) where unity contains all possible solutions of Df and the partition offers the single unique solution to Df. This partition is determined as the minimum positive real value for the residual f at the centre node i, it is defined as meeting the following delta condition eq. (5-26).

$$\mathrm{f_i} = \begin{cases} \mathrm{D(f)} \approx 0, 1 \leq \mathrm{i} \leq \mathrm{m} \\ \\ \delta \mathrm{f_{min}} > 0, f \in \mathbb{R} \end{cases} \tag{5-26}$$

The final resolution of the vector at node 10 is determine adding the residual as shown in eq.(5-27) is in terms of pressure, velocity and temperature mapped the as the L_2 norm.

$$\mathrm{r} = \mathrm{b} - \mathrm{Af} \tag{5-27}$$
$$[\mathrm{Pressure}]_{(\mathrm{node\ 10})-} = [|\mathrm{Pressure_{nb}}|] + \mathrm{r}[|\mathrm{Pressure}|]_{\mathrm{L_2}}$$
$$[\mathrm{Velocity}]_{(\mathrm{node\ 10})-} = [|\mathrm{Velocity_{nb}}|] + \mathrm{r}[|\mathrm{Velocity}|]_{\mathrm{L_2}}$$
$$[\mathrm{Temperature}]_{(\mathrm{node\ 10})-} = [|\mathrm{Temperature_{nb}}|] + \mathrm{r}[|\mathrm{Temperature}|]_{\mathrm{L_2}}$$

The resolution of single partition value using eq. (5-28) can be applied to any source terms defined generally as ϕ, whether the source might be an frequency factor, molecular separation between molecular species or some other flux potential. The geometric scaling of the source term is not important, so the method is true multi-scale.

To solve the flow problem using a mesh-free method a system of initial and boundary condition are required and Table 5-3 summarises these. It's important to select the correct boundary condition that relates to appropriate the geometrical conditions.

Table 5-3. Initial and boundary conditions available to solve flow problems using the mesh-free method

Initial Conditions	**Velocity**	**Pressure**	**k**	**ε**	**Momentum**	**Notes**
External flow	As calculated in the SIMPLE solution	As calculated in the SIMPLE solution	See eq. (5-33) for solving k	See eq. (5-34)	As calculated in the SIMPLE solution	Fluid flow in a uncontain -ed space
Inlet	u, v, w set to a constant values	P is set to a reference pressure	Estimate as 1-6% of fully developed flow	Estimate as 1-6% of fully developed flow	M_u, M_v and M_w set to a constant value	Flow into an enclosed space
Outlet	$u, v, w = \frac{m_{in}}{m_{out}}$ m= momentum	P_{xyz}= 0	See eq. (5-33) for solving k	See eq. (5-34)	Computed across the faces of Figure 5-12	Flow out of an enclosed space
Constant pressure	As calculated in the SIMPLE solution	P_{xyz} = constant	See eq. (5-33) for solving k	See eq. (5-34)	As calculated in the SIMPLE solution	Apply a fixed pressure
Wall	u, v, w calculated based on the local geometry	P_x, P_y and P_z calculated based on the local geometry	See eq. (5-33) for solving k	See eq. (5-34)	Solve as a source term Φ based on the flow regime	Fluid flow near a wall

5.6.1 **k-ε Turbulence model at the wall boundaries.**

With the potential terms known a standard k - ε model is utilised for the wall boundaries. This is defined for the turbulent energy function k as eq. (5-28).

$$k = \left(\tau_w u_p - \rho C_\mu^{3/4} k_p^{3/4} u^+\right) \Delta V / \Delta y_p \qquad (5\text{-}28)$$

where t_w is the fluid shear stress, up is the velocity of fluid, ρ is the fluid density, C_μ is the specific heat capacity, k_p is the linearized k from the last iteration within the current mesh-free stencil, u+ is the intersection of the linear flow profile with the log-law reduction in velocity from the wall surface ΔV is the change in volume across flow path near the wall and Δy_p is

the distance that marks the end of the transition from free flow to wall boundary. The net turbulent energy per unit volume is set against the dissipation of the turbulent energy over time.

For the rate of dispersion ε then the following function is defined as eq. (5-29).

$$\varepsilon = C_{\mu}^{3/4} k_p^{3/2} / (\kappa \Delta y_p) \tag{5-29}$$

where C_{μ}, k_p and y_p are defined the same as previously stated for turbulent energy function, with κ being the Karman constant equal to 0.4187.

5.6.2 The relationship between particle oscillation and Strouhal numbers in the wake of tubes.

In real bulk gas around cylinder tubes, the gas molecules peel off the tube surface. It causes the bulk gas flow to oscillate in a wave like pattern after passing the tube. The frequency of oscillation of the bulk gas from the wake of a tube is defined by the aid of the Strouhal number (Table 2-2) as eq. (5-30).

$$f = \frac{StL}{V} \tag{5-30}$$

where *f* is the frequency of vortex shedding, *L* is the characteristic length and *V* is the velocity of the bulk gas flow. For large Strouhal numbers (order of 1), viscosity dominates fluid flow, resulting in a collective oscillating movement of the fluid "plug". For low Strouhal numbers (order of 10^{-4} and below), the high-speed, quasi-steady state portion of the movement dominates the oscillation. Oscillation at intermediate Strouhal numbers is characterized by the build-up and rapidly subsequent shedding of vortices (Sobey, 1982). This thesis maintains that if a fluid plug is made, this will build a deposit that will become the initiator of bridging across tubes.

5.6.3 Solving in a geometrical plane with initial value and boundary conditions

Earlier the SIMPLE algorithm was use to solve the Navier-Stokes equation within the mesh-free form using the stencil that was illustrated in Figure 5-12. If the mesh-free method is applied to a geometrical form for example a surface in a 2D space then the scheme to pass

information between each mesh-free node will exist. Such a scheme that will pass information will consider the initial and boundary conditions that are necessary to solve the probe.

Consider each boundary condition in Table 5-3 the direction of information exchange between mesh-free centre nodes can be illustrated in Figure 5-14 to Figure 5-18 as,

- External

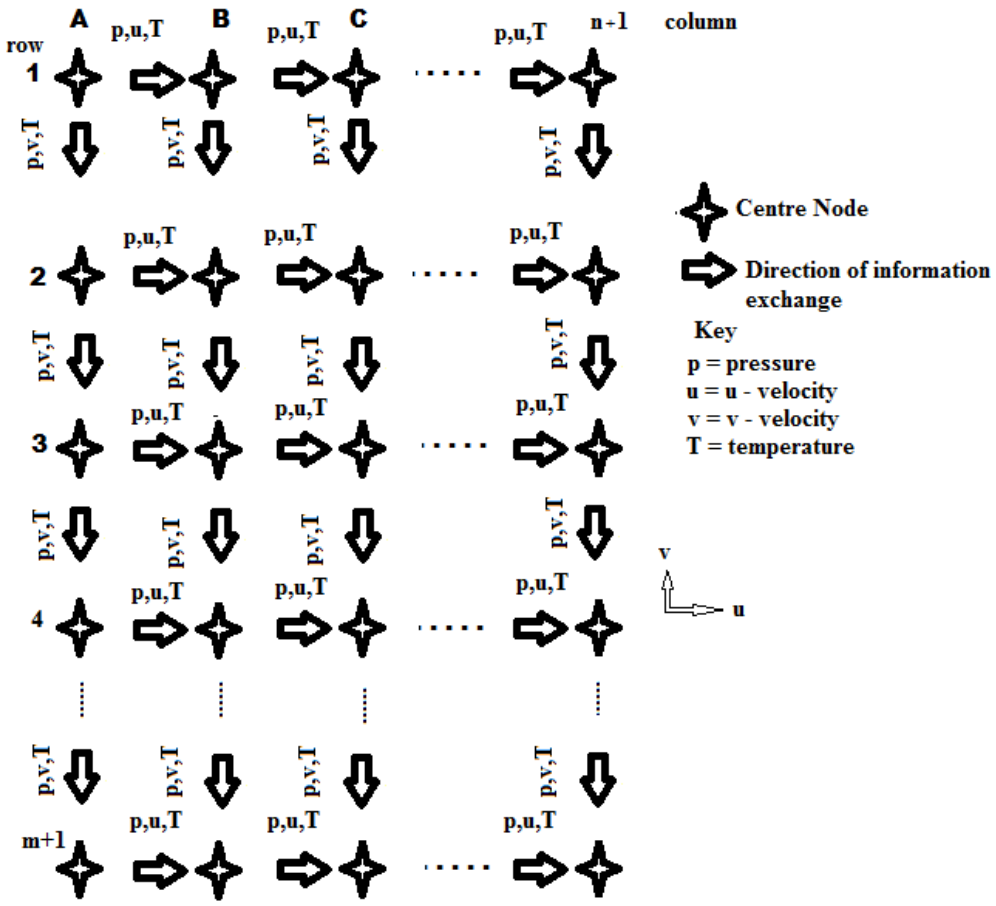

Figure 5-14. External flow boundary condition propagates thermodynamic information onto close neighbours stencils

In Figure 5-14 thermodynamic properties v, u and T are solved at stencil column A row 1 and passed between mesh-free stencil centre nodes that are nearest in the direction of the arrows. Starting with node in column A row 1 thermodynamic information is passed from the centre node on node A1 to all the supporting nodes on A2, B1 etc, This continues row to row column to column until column n + 1, row m + 1 is reached.

- Internal flow boundary condition

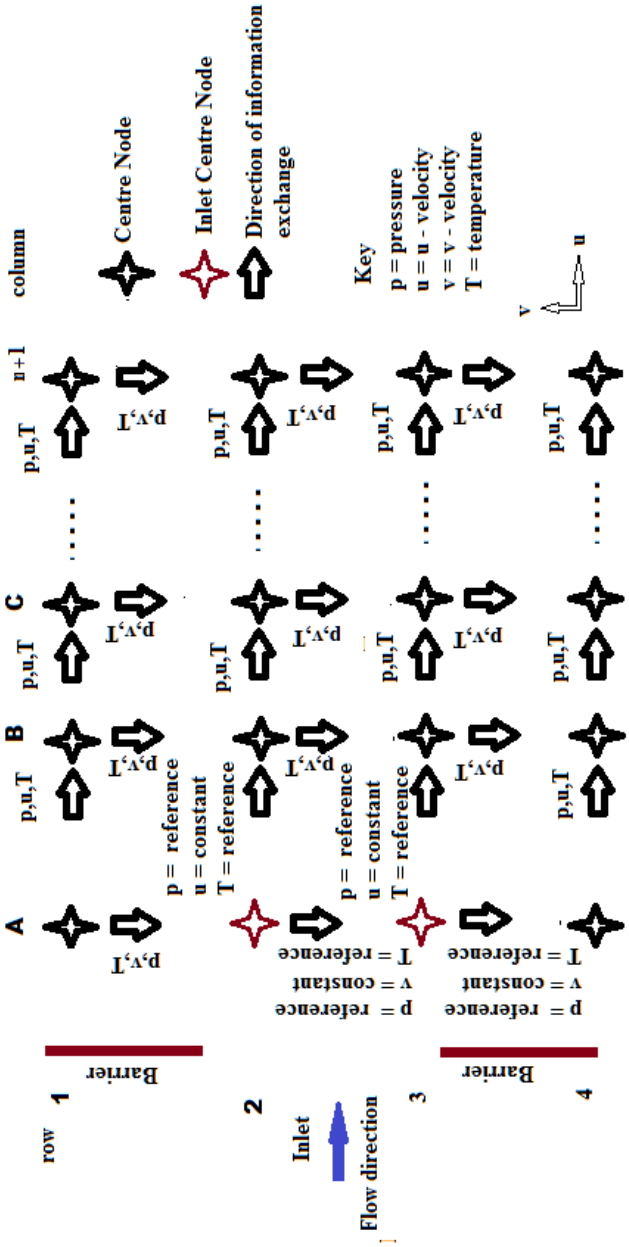

Figure 5-15. Internal flow boundary condition propagates thermodynamic information onto close neighbours stencils.

Illustrated in Figure 5-15 the inlet nodes pass thermodynamic information p = reference pressure, v = constant velocity, u = constant velocity and T = reference temperature between centre nodes that are nearest. Starting with node in column A row 2 the thermodynamic information is passed from the centre node on node A3 to the entire near mesh-free stencil

centre node A4, B2 and B3. All other centre nodes pass information as local initial and boundary conditions are set.

- **Outlet Initial and Boundary conditions**

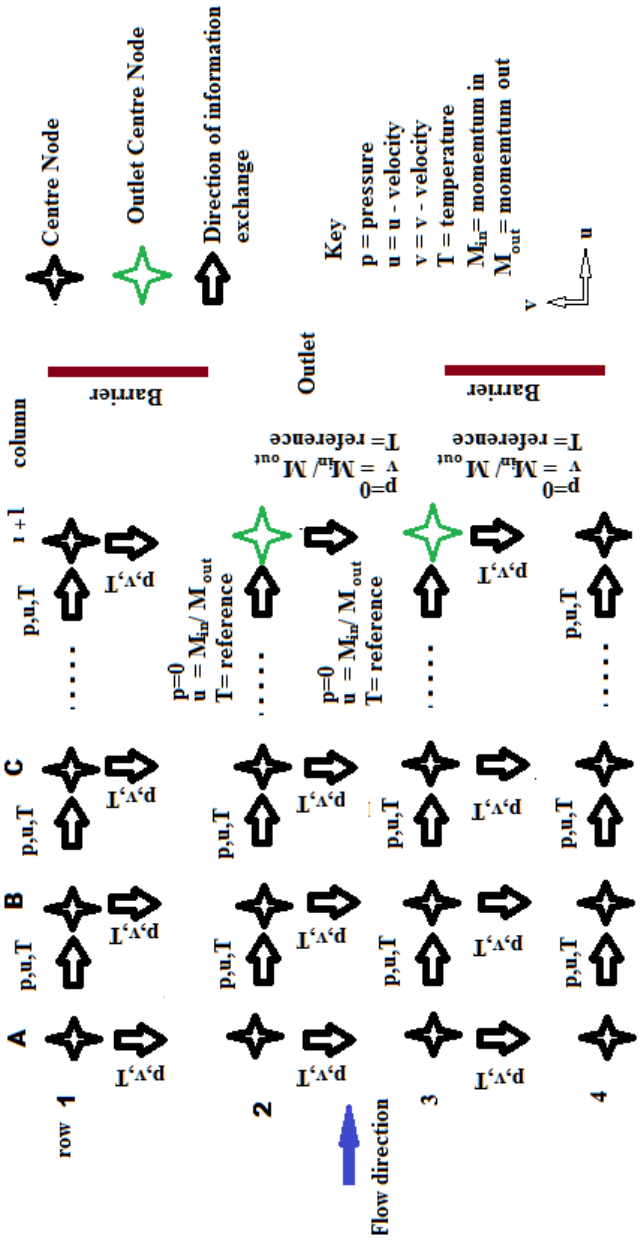

Figure 5-16. Outlet flow boundary condition propagates thermodynamic information onto close neighbours stencils

Illustrated in Figure 5-16 outlet nodes pass thermodynamic information p = 0, v = M_{in}/M_{out}, u = M_{in}/M_{out} and T = reference temperature from the centre nodes at column C row 2 and C3 to

that are nearest outlet mesh-free stencils centre node on column n+1, row 2 and column n+1, row 3.

- **Constant Pressure Initial and Boundary conditions**

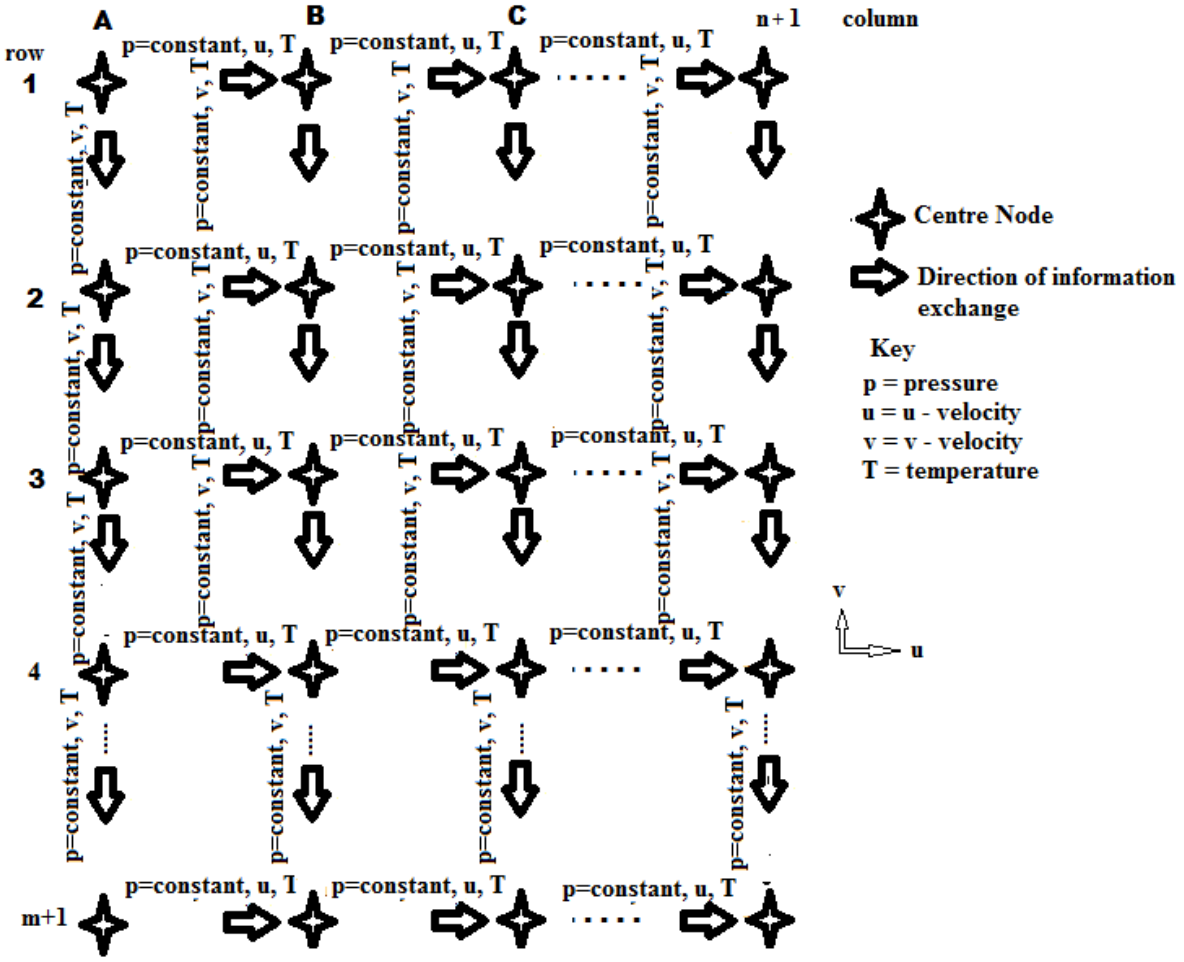

Figure 5-17. Constant pressure flow boundary condition propagates thermodynamic information onto close neighbours stencils.

Illustrated in Figure 5-17 the constant pressure initial and boundary conditions passes information of a fix pressure p = constant, u velocity, v velocity and temperature. The information is passed starting from the centre node at column A row 1 to all mesh-free stencils centre node in the u and v direction.

- Wall Initial and Boundary conditions

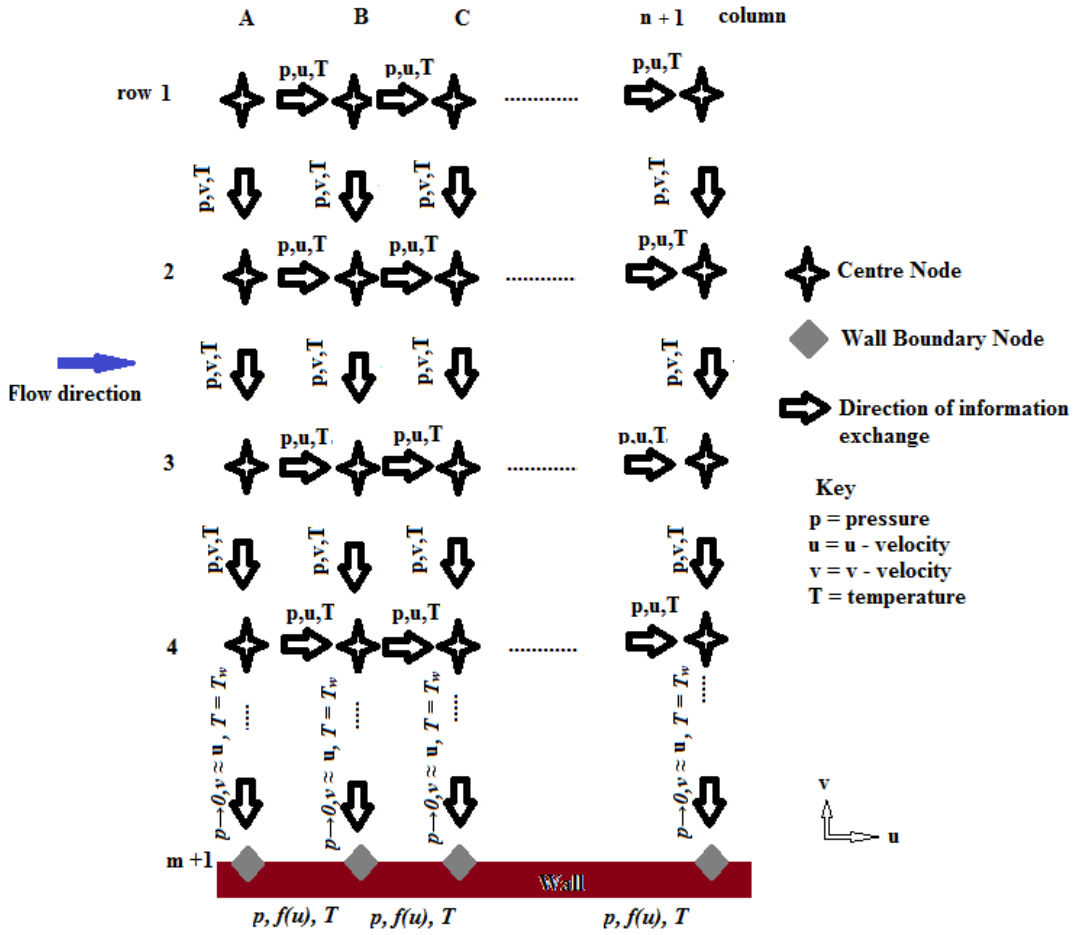

Figure 5-18. Wall flow boundary condition propagates thermodynamic information onto close neighbours stencils.

Illustrated in Figure 5-18 is the wall initial and boundary conditions which is set such that the flow is in the u direction and thermodynamic information for wall mesh-free stencils centre node is located at row m+1. In the u direction p= pressure is calculated with the mesh-free 'XMLSimple' algorithm to approximate the solution of the Navier-Stokes equation. The velocity in the u direction is the function u=*f*(u) where the function *f*(u) depending the flow regime (i.e. laminar or turbulent). The u direction temperature is T= temperature of the bulk fluid flow. In the v direction $p \rightarrow 0$, v=u and $T=T_w$ where T_w is the temperature of the wall.

A further note on the wall boundary condition will consider the direction of flow is on the v direction. In the v direction into the wall the pressure $p \rightarrow \infty$, $v \approx 0$ and $T = T_{(\text{bulk flow direction})}$. In the u direction $p \rightarrow 0$, u = v, $T = T_{wall}$

The initial and boundary condition above are describes for 2D geometry. For 3D geometry the initial and boundary conditions are applied in the z Cartesian axis with the column/row coordinates designated as l. The thermodynamic information will pass between centre nodes and the nearby supporting nodes through l, m and n coordinates. In the condition where the 3D geometry meets a boundary wall in the z Cartesian axis, then same for both x and y Cartesian axis boundaries, a wall boundary condition is applied.

5.6.4 The solution of convection - diffusion problems within the mesh-free 'stencil'

When a fluid undergoes heating there are both convection and diffusion. Locally the result of heating by an exchange from a source is a change in temperature. In the absents of a heat source from eq. (5-31)the steady state convection and diffusion property Φ in one dimensional flow field u governed by the transport equation (Versteeg & Malalasekera, 1995). When ρ is the fluid density and Γ is the diffusion coefficient the rate of change in diffusion property Φ, in the absence of a source term, is;

$$\frac{d}{dx}(\rho u \Phi) = \frac{d}{dx}\left(\Gamma \frac{d\Phi}{dx}\right) \tag{5-31}$$

The flow must also satisfy continuity, so

$$\frac{d(\rho u)}{dx} = 0 \tag{5-32}$$

The faces of the mesh-free stencil face areas equal to unity as illustrated in Figure 5-12. The numbering scheme for these faces, described in Table 5-2, is identical for convection - diffusion problems as for solving the momentum terms problem. If the faces either side of a centre node 10, the unit area that make up the faces of the mesh-free stencil are labelled $Area_{(w)}$, $Area_{(e)}$, $Area_{(n)}$, $Area_{(s)}$, $Area_{(t)}$ and $Area_{(b)}$. Focusing on an arbitrary pair of faces of $Area_{(w)}$ and $Area_{(e)}$, the centre node 10 will form a control volumes *w*, and *e* as illustrated in Figure 5-19. Based on the control volume around the centre node 10 in Figure 5-19 convection - diffusion occurs across the faces areas $Area_{(w)}$ and $Area_{(e)}$ of a mesh-free stencil. The velocity of the bulk gas flow is u_w on the west face 'w', and u_e on the east face 'e' of the control volume as shaded in Figure 5-19.

Integration of the transport eq. (5-31) over the control volume of Figure 5-19 and substituting A for the face area gives.

$$(\rho uA\Phi)_e - (\rho uA\Phi)_w = \left(\Gamma A \frac{\delta\Phi}{\delta x}\right)_e - \left(\Gamma A \frac{\delta\Phi}{\delta x}\right)_w \tag{5-33}$$

and integration of the continuity eq. (5-32) yields

$$(\rho uA)_e - (\rho uA)_w = 0 \tag{5-34}$$

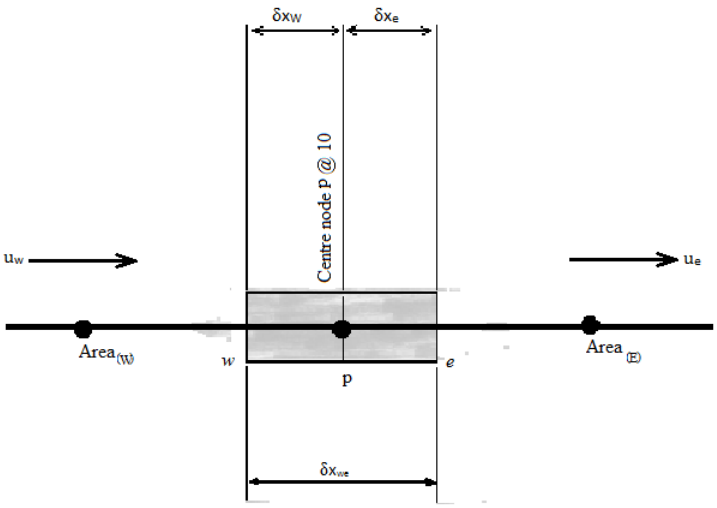

Figure 5-19. The central differencing method for the solution of convection – diffusion problems (Versteeg & Malalasekera, 1995)

To obtain the discretized equations for the convection-diffusion problem we must approximate the terms in eq. (5-34). It is convenient to define two variables *F* and *D* to represent the convection mass flux per unit area and the diffusion conductance at cell faces.

The convection mass flux per unit area and the diffusion conductance are

$$F = \rho u \text{ and } D = \frac{\Gamma}{\delta x} \tag{5-35}$$

The cell face values and the variables F and D can be written as

$$F = (\rho u)_w \text{ and } F = (\rho u)_e \tag{5-36}$$

For the shaded volume in Figure 5-19 and D is also defined by the same shaded volume as

$$D = \frac{\Gamma_w}{\delta x_{wp}} \text{ and } D = \frac{\Gamma_e}{\delta x_{pe}} \tag{5-37}$$

This technique for solving convection- diffusion (c-d) problems assumes that $A_w = A_e = A_n = A_s = A_t = A_b = A$, therefore returning to the arbitrary pair of faces $Area_{(W)}$ and $Area_{(E)}$ in Figure 5-19 as δx_{wp} and δx_{pe} are small; it follows that $Area_{(W)} = Area_{(E)} = A_{(w,\,e)}$.

Applying a central difference method to represent the contribution either side of the central node n, the contribution of the convection terms can be balance by contribution of the diffusion terms. The integrated convection-diffusion eq. (5-37) is now written as

$$F_e\Phi_e - F_w\Phi_w = D_e(\Phi_E - \Phi_p) - D_w(\Phi_p - \Phi_w) \tag{5-38}$$

and the integrated continuity eq. (5-38) as

$$F_e - F_w = 0 \tag{5-39}$$

If the velocity is known then F_e and F_w will be known, but to solve eq. (5-38) the transport property Φ must be known. It's therefore only possible to solve eq. (5-38) at by calculating Φ at the *e* and *w* faces. Two schemes used to solve the Φ at the *e* and *w* faces are central differencing scheme and upwind differencing schemes (Versteeg & Malalasekera, 1995) which are combined to form a hybrid difference scheme (Spalding, 1976). When solving convection diffusion problems both central differencing and upwind differencing schemes are required. Each scheme (central differencing and upwind differencing schemes) has limits to which so they are stable, reliable and that discretization method will meet the fundamental properties applicable in solving any series of algebraic equations.

There are four properties of that any discretization method must be satisfied when solving numerically, convection-diffusion (c-d) problems. These are;

- Conservatives – the ability to represent the flux transfer through the control volume in a consistent manner
- Boundedness – since c-d problems are solved using a series of algebraic equation, then this is the ability of these algebraic equations can
    - can converge to a solution,

  - will converge within the boundary values (i.e. a solution will be found within boundary temperatures of 500K and 800K and not outside them), and
  - that the sign is consistent with the physical system (i.e. not minus 200 Kelvin which is impossible).

- Transportiveness - is the ability of a c-d problem to reflect the direction of flow of the bulk gas.
- Accuracy – is how close and stable is the solution to a c-d problems

The formation of the discretization problem and the solution is through the hybrid differencing scheme (Spalding 1970). The hybrid differencing scheme is based on the combination of the central difference and upwind difference scheme. The central difference scheme is second order accurate, is employed for small Péclet numbers (Pe < 2) and upwind scheme, which is first order accurate but accounts for transportiveness, is employed for large Péclet numbers (Pe≥2). The Péclet number is define in Table 2-2.

The central difference approximation is a mid-point linear interpolation and for the uniform distances of $\delta x_w n$ and $\delta w_e n$ the values of the transport property Φ is

$$\Phi_e = \frac{\Phi_e + \Phi_p}{2} \qquad (5\text{-}40)$$
$$\Phi_w = \frac{\Phi_p + \Phi_w}{2}$$

Substituting eq. (5-40) into convective terms of eq. (5-38) yields

$$F_e\left(\frac{\Phi_e + \Phi_p}{2}\right) - F_w\left(\frac{\Phi_p + \Phi_w}{2}\right) = D_e(\Phi_e - \Phi_p) - D_w(\Phi_p - \Phi_w) \qquad (5\text{-}41)$$

This can be rearrange to give

$$\left[\left(D_w - \frac{F_w}{2}\right) + \left(D_e + \frac{F_e}{2}\right)\right]\Phi_p = \left(D_w + \frac{F_w}{2}\right)\Phi_w + \left(D_e - \frac{F_e}{2}\right)\Phi_e \qquad (5\text{-}42)$$

simplify

$$\left[\left(D_w + \frac{F_w}{2}\right) + \left(D_e - \frac{F_e}{2}\right) + (F_e - F_w)\right]\Phi_p = \left(D_w + \frac{F_w}{2}\right)\Phi_w + \left(D_e - \frac{F_e}{2}\right)\Phi_e \qquad (5\text{-}43)$$

Identify the coefficients of Φ_e and Φ_w as a_e and a_w the central differencing expressions for the discrete convection – diffusion equation are

$$a_p\Phi_p = a_e\Phi_e + a_w\Phi_w \tag{5-44}$$

where

a_e	a_w	a_p
$\left(D_w + \frac{F_w}{2}\right)$	$\left(D_e - \frac{F_e}{2}\right)$	$a_w + a_e + (F_e - F_w)$

As the bulk gas velocity increase the flow direction becomes more significant and is significant factor in the solution of a c-d problem (Versteeg & Malalasekera, 1995). The central differencing is unable to identify the flow direction and hence the adoption of the upwind differencing scheme where the velocity of the bulk gas produces large Péclet numbers (Pe≥2).

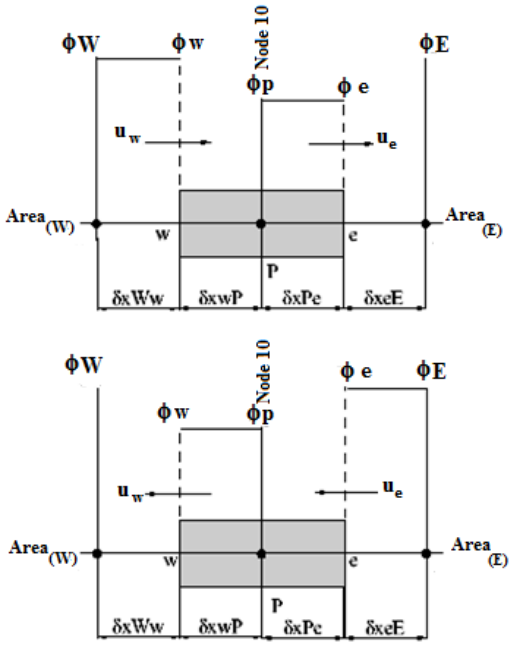

Figure 5-20. Upwind differencing scheme (Versteeg & Malalasekera, 1995)

When the flow is positive direction, $u_w > 0$, $u_e > 0$ ($F_w > 0$, $F_e > 0$), the upwind scheme sets as in Figure 5-20 (upper) with bulk gas flow in the positive direction from E (upper) and bulk gas flow in the negative from face E to W (lower).

$$\Phi_w = \Phi_W \text{ and } \Phi_e = \Phi_P \tag{5-45}$$

and the discretized eq. (5-48) becomes

$$F_e\Phi_P - F_w\Phi_W = D_e(\Phi_E - \Phi_P) - D_w(\Phi_P - \Phi_W) \tag{5-46}$$

which can be rearranged as

$$(D_w + D_e + F_e)\Phi_p = (D_w + F_w)\Phi_w + D_e\Phi_E \tag{5-47}$$

to give

$$[(D_w + F_w) + D_e + (F_e - F_w)]\Phi_p = (D_w + F_w)\Phi_W + D_e\Phi_E \tag{5-48}$$

When the flow is in the negative direction, $u_w < 0$, $u_e < 0$ ($F_w < 0$, $F_e < 0$), the scheme takes

$$\Phi_w = \Phi_P \text{ and } \Phi_e = \Phi_E \tag{5-49}$$

The discretized equation for the negative direction is

$$F_e\Phi_E - F_w\Phi_P = D_e(\Phi_E - \Phi_P) - D_w(\Phi_P - \Phi_W) \tag{5-50}$$

transpose so that terms related to Φ_P are on one side

$$[D_w + (D_e - F_e) + (F_e - F_w)]\Phi_p = D_w\Phi_W(D_e - F_e)\Phi_E \tag{5-51}$$

Identifying the coefficients as Φ_W and Φ_E as a_W and a_E for eq. (5-48) and eq. (5-50) enables the general form to be written as

$$a_p\Phi_p = a_W\Phi_W + a_E\Phi_E \tag{5-52}$$

with the central coefficients

$$a_p = a_w + a_E + (F_e - F_w) \tag{5-53}$$

and the neighbour coefficients

	a_W	a_E
$F_w > 0, F_e > 0$	$\mathrm{D_w} + \mathrm{F_w}$	$\mathrm{D_e}$
$F_w < 0, F_e < 0$	$\mathrm{D_w}$	$\mathrm{D_e} - \mathrm{F_e}$

The general form of neighbour coefficients of the upwind difference method that covers flow in both directions is given below:

a_E	a_W
$\mathrm{D}_w + \max(\mathrm{F_w}, 0)$	$\mathrm{D}_w + \max(0, -\mathrm{F_e})$

By using both the central difference method when the Péclet number is less than two and the upwind difference method when the Péclet number is equal or greater than two, then this hybrid difference method has the benefits of both methods (Versteeg & Malalasekera 1995).

Table 5-4. Hybrid differencing scheme for 3-D bulk gas flow (Versteeg & Malalasekera 1995)

a_{W}	$\max\left[\mathrm{F}_w, \left(\mathrm{D}_w + \frac{\mathrm{F}_w}{2}\right), 0\right]$
a_{E}	$\max\left[-\mathrm{F}_e, \left(\mathrm{D}_e + \frac{\mathrm{F}_e}{2}\right), 0\right]$
a_{S}	$\max\left[\mathrm{F}_s, \left(\mathrm{D}_s + \frac{\mathrm{F}_s}{2}\right), 0\right]$
a_{N}	$\max\left[-\mathrm{F}_n, \left(\mathrm{D}_n + \frac{\mathrm{F}_n}{2}\right), 0\right]$
a_{B}	$\max\left[\mathrm{F}_{\mathrm{s}}, \left(\mathrm{D}_{\mathrm{s}} + \frac{\mathrm{F}_{\mathrm{b}}}{2}\right), 0\right]$
a_{T}	$\max\left[\mathrm{F}_t, \left(\mathrm{D}_t + \frac{\mathrm{F}_t}{2}\right), 0\right]$
a_{P}	$\mathrm{a_W} + a_{\mathrm{E}} + a_{\mathrm{S}} + a_{\mathrm{N}} + a_{\mathrm{B}} + a_{\mathrm{T}} + \Delta\mathrm{F}$
$\Delta\mathrm{F}$	$\mathrm{F}_e - \mathrm{F}_w + \mathrm{F}_n - \mathrm{F}_s + \mathrm{F}_t - \mathrm{F}_b$

The general form of all the coefficients of this equation are listed in Table 5-4
The central difference is second order accurate for small Péclet numbers, while the upwind difference is first order accurate but account for the bulk gas flow direction.
The discretization equation that covers 3-Dimensions for the hybrid differencing scheme are given in eq. (5-54).

$$a_P\Phi_P = a_W\Phi_W + a_E\Phi_E + a_S\Phi_S + a_N\Phi_N + a_B\Phi_B + a_T\Phi_T \quad (5\text{-}54)$$

The values of F and D in Table 5-4 are evaluated using the formula listed in Table 5-5. In Table 5-5 ρ is the bulk gas density and u, v, w is the bulk gas velocity in Cartesian coordinates in x, y, z planes of the mesh-free stencil in Figure 5-12.

Table 5-5. Expression to calculate convection F and diffusion D values

Face	w	e	s	n	b	t
F	$(\rho u)_w A_w$	$(\rho u)_e A_e$	$(\rho v)_s A_s$	$(\rho v)_n A_n$	$(\rho w)_b A_b$	$(\rho w)_t A_t$
D	$\frac{\Gamma_w}{\delta x_{WP}}$	$\frac{\Gamma_e}{\delta x_{PE}}$	$\frac{\Gamma_s}{\delta y_{SP}}$	$\frac{\Gamma_n}{\delta y_{PN}}$	$\frac{\Gamma_b}{\delta z_{BP}}$	$\frac{\Gamma_t}{\delta z_{PT}}$

At the boundaries condition illustrated in Figure 5-14 to Figure 5-18 (i.e. external, internal constant pressure, wall, internal and inlet boundary conditions) , the large diffuse behaviour found in real gas flows is representing by adding additional source terms of S_u and S_p. These additional source terms are included into eq. (5-60) as flows

$$a_P\Phi_P = a_W\Phi_W + a_E\Phi_E + a_S\Phi_S + a_N\Phi_N + a_B\Phi_B + a_T\Phi_T + S_u \quad (5\text{-}55)$$

$$a_P = a_W + a_E + a_S + a_N + a_B + a_T + \Delta F - S_p \quad (5\text{-}56)$$

The construction of the values of S_u and S_p will vary depending on the local circumstance. However the literature offers a wide solution to the source terms S_u and S_p at the boundaries (Versteeg & Malalasekera 1995) for the finite differencing method. Two common expressions used in the central difference scheme and upwind differencing scheme for inlet or outlet conditions are found.

Table 5-6. The Source terms Su and Sp for central differencing scheme and upwind differencing scheme.

Boundary Condition	S_p	S_u
Inlet	$-(2D + F)$	$(2D + F)\Phi_{Fac\ e\ Area}$
Outlet	$-2D$	$2D\Phi_{Fac\ e\ Area}$

In Table 5-6 is set out a method of calculating the values of source terms S_p and S_u for inlet and outlet boundary conditions.

The source terms for both S_p and Su are the smallest non-zero value for constant pressure, internal and external boundary condition. On encountering zero the following conditions applies for both S_p and S_u as shown in eq. (5-57).

$$S_p = min(10^{-30}, \Phi) \qquad S_u = min(10^{-30}, \Phi) \tag{5-57}$$

This is a control to avoid problem with division by zero character 'NaN' is not passed into any calculations then the limits set by eq. (5-62) are adopted. The mesh-free software (XMLSimple) conforms to the IEEE 754-2008 (IEEE 754, 2008) for floating point arithmetic and captures overflow and underflow error conditions.

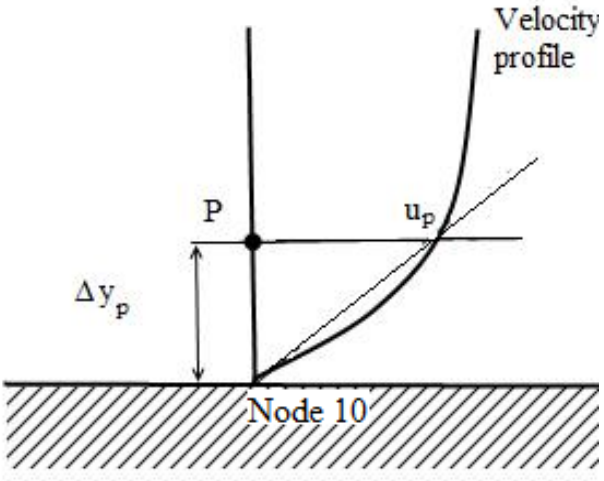

Figure 5-21. The Velocity up distribution near to a wall varies with distance Δy_p for a mesh-free stencil with a centre node at P.

The wall boundary conditions will alter the method of calculating S_p and S_u depending on whether the flow regime is laminar or turbulent and if there is a heat source through the wall.

If the wall is adiabatic (no heat source) then $S_p = S_u = 0$ in both laminar and turbulent flow cases, else the source term will vary depend on the distance from the wall with the velocity distribution. For the mesh-free stencil in Figure 5-12, the centre node 10 is fixed at the wall and one face area is within the wall; while the other face area is in the free bulk gas flow as Figure 5-21. Heat transfer q_s from the wall at fix temperature T in a laminar flow regime is calculated as

$$q_s = -\frac{\mu}{\sigma}\frac{C_p(T_p - T_w)}{\Delta y_p}A_{(\text{Stencil face area ie. w,e,b,t,s,n})} \tag{5-58}$$

where C_p is the specific heat capacity of the fluid, T_p is the temperature corresponding to an outer face area of the mesh-free stencil and σ is the laminar Prandtl number (Table 2-2). The face areas of all stencils are unity therefore the term $A_{Stencil\ face\ area}$ is unity but is included for conformity. The associate source terms for S_p and S_u based on the temperature equations given in eq. (5-58) are

$$S_p = -\frac{\mu}{\sigma}\frac{C_p}{\Delta y_p}A_{(\text{Stencil face area})} \text{ and } S_u = \frac{\mu}{\sigma}\frac{C_p T_w}{\Delta y_p}A_{(\text{Stencil face area})} \tag{5-59}$$

Any fixed heat flux enters the source terms directly by means of the normal source term linearization. In the case of both the laminar flow and turbulent the heat flux entering the source as

$$q_s = S_u + S_p T_p \tag{5-60}$$

When the flow regime is turbulent and parallel to the wall the star node below the centre node are suppressed and the coefficient for that particular face is set to zero. For example if the flow is parallel to coefficient a_b then $a_t = 0$ together with the convection term F_t. The source term S_p for the velocity flow in the u direction becomes (Versteeg & Malalasekera 1995)

$$S_p = -\frac{\rho C_\mu^{1/4} k_P^{1/2}}{u^+}A_{(\text{Stencil face area})} \tag{5-61}$$

where ρ is the bulk gas density at temperature T_p and C_μ, k_p and u^+ are turbulent energy variables. Where the flow direction is not parallel to the wall the source terms Sp and Su are define as

$$S_p = -\frac{\rho C_\mu^{1/4} k_P^{1/2} C_p}{T^+} A_{(\text{Stencil face area})} \quad (5\text{-}62)$$

$$\text{and } S_u = -\frac{\rho C_\mu^{1/4} k_P^{1/2} C_p T_{wall}}{T^+} A_{(\text{Stencil face area})}$$

where ρ is the density at temperature T^+, C_p is the specific heat of the bulk gas, T_{wall} is the wall temperature and C_μ, k_p and u^+ are turbulent energy variables defined in equation. The term T^+ is defines by eq. (5-63)

$$T^+ = \sigma_{T,t}\left(u^+ + P\left[\frac{\sigma_{T,l}}{\sigma_{T,t}}\right]\right) \quad (5\text{-}63)$$

where $\sigma_{T,t}$ is the turbulent Prandtl number, $\sigma_{T,l}$ is the laminar Prandtl number and P is the 'pee' function of Spalding et al as eq. (5-64).

$$P \equiv 9.24\left\{\left(\frac{\sigma_{T,l}}{\sigma_{T,t}}\right)^{3/4} - \left(\frac{\sigma_{T,l}}{\sigma_{T,t}}\right)^{1/4}\right\} \quad (5\text{-}64)$$

Returning the circumstance where the flow boundary is parallel to a wall then eq. (5-59) and eq. (5-61) provide a method for calculating the values of source terms S_p and S_u independent of the fluid flow geometry.

When Sp and Su are determined the c-d coefficient from Table 5-4 all Cartesian axis can be assembled as in eq. (5-65).

$$\begin{aligned} a_{Pw} &= a_E + a_W - S_p \\ a_{Pe} &= a_W + a_E - S_p \\ a_{Pn} &= a_N + a_S - S_p \\ a_{Ps} &= a_S + a_N - S_p \\ a_{pt} &= a_T + a_B - S_p \\ a_{pb} &= a_B + a_T - S_p \end{aligned} \quad (5\text{-}65)$$

To solve the c-d problem the coefficients are assemble for all six faces of the mesh-free stencil and solved by assembling these into a 6 x 6 diagonal matrix in the form of Ax=B with the source terms from each the boundaries S_p and S_u.

$$\begin{bmatrix} a_E & & & & & \\ & a_W & & & & \\ & & \ddots & & & \\ & & & a_T & & \\ & & & & a_B & \end{bmatrix} \begin{bmatrix} \Phi_{\mathrm{E}} \\ \Phi_{\mathrm{W}} \\ \Phi_{\mathrm{N}} \\ \Phi_{\mathrm{S}} \\ \Phi_{\mathrm{T}} \\ \Phi_{\mathrm{B}} \end{bmatrix} = \begin{bmatrix} a_{p\mathrm{e}} \\ a_{p\mathrm{w}} \\ a_{p\mathrm{n}} \\ a_{ps} \\ a_{p\mathrm{t}} \\ a_{p\mathrm{b}} \end{bmatrix}$$

The diagonal matrix is solved using the Jacobi iteration method to yield values for transport properties Φ_E, Φ_W, Φ_N, Φ_S, Φ_T and Φ_B.

It should be stressed that the convection – diffusion solution method described in this section are only applied to the mesh-free stencil of Figure 5-12. Since the objective is to calculate values of the grand canonical ensemble, the solution remains local to mesh-free stencil where the solution is applied. The temperature is passing between mesh-free stencils, across the domain, as the initial value for the next mesh-free stencil. How temperature is passing between mesh-free stencils as illustrated in Figure 5-14 to Figure 5-18. Values are calculated by starting the discretization at one mesh-free stencil on an inlet edge and solving the value of temperature then passing the values to the neighbour mesh-free stencil. The neighbour stencil repeats the process until the domain has been completed.

5.7 Case study: Calibration of mesh-free solution using potential flow at low Reynolds number

Before the mesh-free method is used in a wider context it's important to benchmark the mesh-free method to establish the margins of error that can be expected in solving a problem. The benchmarking is set so that the mesh-free method models the velocity, pressure and temperature around single circular tube in a laminar flow at low Reynolds number. The potential flow around a (geometrically) two-dimensional circular cylinder is a mathematical ideal case in which a stable validation of the accuracy and geometric similarity. At very low Reynolds numbers, the flow is steady and symmetrical. The single circular tube was validated the key validation property is the static pressure; since the SIMPLE algorithm adjusts the pressure correction value to converge to a solution this seems reasonable. Another key validation property is that the flow properties are symmetrical. In Appendix B, the mathematical proof of potential flow demonstrated.

In the case of the mathematical potential flow solution of maximum static pressure upwind of the tube is

$$P + \frac{1}{2}\rho v^2 = P_o \tag{5-66}$$

where P is the static pressure, ½ρv^2 is the dynamic pressure consisting ρ as the density, v is the velocity and P_0 is the total pressure. The mean gas velocity, is set as v = 10 m/s and set at a distance upwind of the tube so that there is no influences in changes in velocity near to the tube. The density of air assumed to be ρ= 0.34 kg/m^3 at 800˚C. Atmospheric pressure is set at 10325.0 Nm^{-1} then

P= 10325.0 - ½ x 0.34 x (10)^2 = 10342.0 Nm^{-1}.

At a minimum the lowest pressure is

$$P - P_o = -\frac{3}{2}\rho v^2 \tag{5-67}$$

The geometry for the mesh-free method is the same for Figure 3-4. The mesh-free model is constructed from 9 x 9 centres nodes place at regular spaces as with Figure 5-22.

Illustrated in Figure 5-22 is the dimension of the Cranfield PF combustor and the basic proportions and tube diameter tube are those as shown in Figure 3-4 with the tube diameter being 39 mm. The PF combustor model is configured, as it might be assemble for the laminar flow benchmarking test. The direction of bulk gas flow is from top to bottom and the mesh-free calculation start at the top right corner marked as start point working to the vertical midline of the PF combustor.

The initial conditions are set so that the nodes closes to the tube will only calculate the pressure and velocity without allowing for wall boundary functions. The wall boundary functions are governed by the eq. (5-28) and eq. (5-29). The flow is assumed incompressible, inviscid (viscous forces are small in comparison to inertial forces), there is no friction and therefore no drag. Therefore factors that are linked to boundary condition for friction flow such as with equation eq. (5-28) and eq. (5-29) are not considered. An inlet boundary condition is included and flow travels from top to bottom.

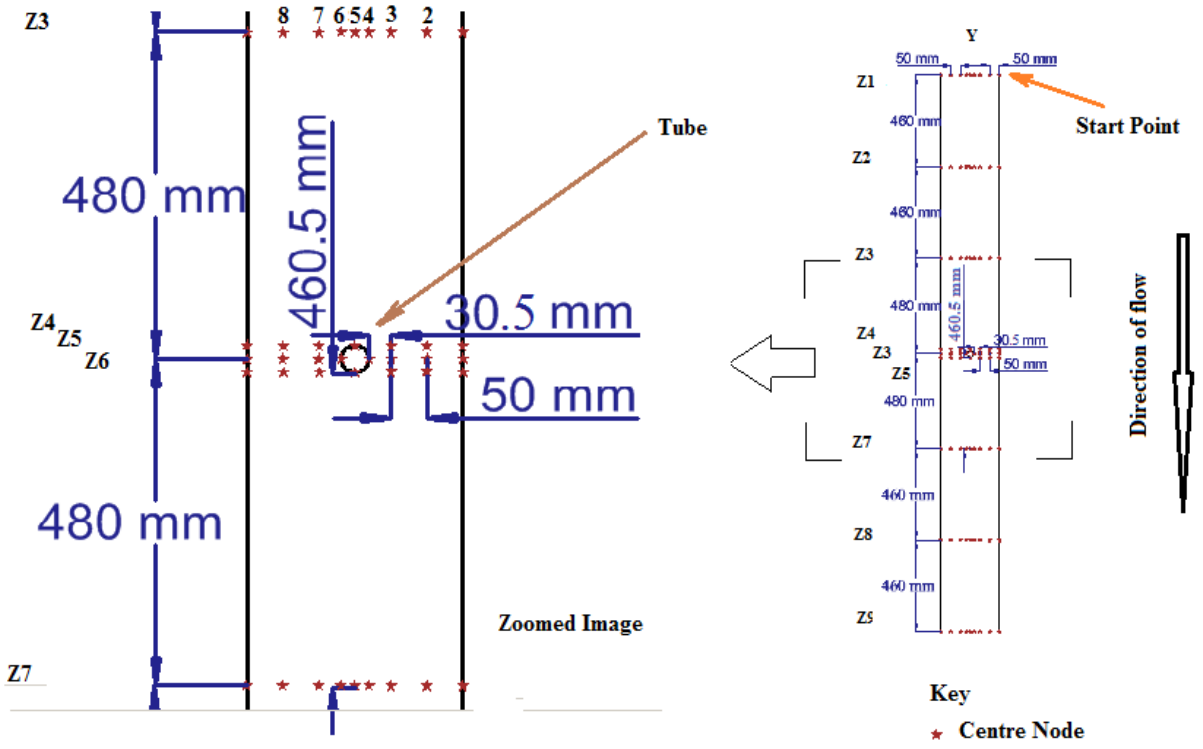

Figure 5-22. The mesh-free nodes configuration for the laminar flow benchmarking test.

The mesh-free method is used to calculate the grand canonical assembly and generate information on the intensive variable (pressure, temperature and chemical potential) of a collection of particles that have a minimum connection. The grand canonical ensemble information is passed by a particle from one centre node at node 10 in Figure 5-12 to the group of mesh-free stencils. In this transfer of thermodynamic information, a particle would expect to contain kinetic energy. The kinetic energy of a multi particle system is not easy to compute. However, velocity can be used as a measure of kinetic energy since for unit mass, kinetic energy ($KE = \frac{1}{2}v^2$). Therefore, to simplify the transfer of grand canonical assembly intensive variables as information passing between mesh-free stencils identical to Figure 5-12. Moving particles in a fluid will have kinetic energy. The velocity of these particles will not be greater than the velocity of the fluid unless by an action of an external energy source. Therefore in a steady state the maximum kinetic energy of the bulk fluid represents the twice the square root of kinetic energy of the particles. The mesh-free method using the minimum connection of Figure 5-12 has unit volume; therefore each mesh-free centre node is transferring pressure, volume and temperature in direction as defined by a velocity vector. In

any dynamic system involving fluid flow, the mass flow through the boundaries of a system is conserved. The conservation of matter problem is resolve using the approximation of the Navier-Stokes equation based on the algorithm SIMPLE.

To evaluate the limits of this mesh-free method two tests run using a mesh-free program called XMLSimple are prepared. The computer program XMLSimple is a mesh-free solver and pre-processor designed to solve thermodynamic and fluid flow properties on a particle at a point in space and time. The program XMLSimple uses the algorithm SIMPLE to approximate a solution of the Navier-Stokes equation. The program XMLSimple finds the solution of thermodynamic properties using the mesh-free stencil of Figure 5-12.

This is a new approach based on the mesh-free mathematics of (Li & Liu, 2004) its behaviour is not proven to reproduce the correct pressure and temperature output information for given input information. Therefore a series of test will determine the accuracy of the mesh-free method when particular nodes are loaded and others are set to zero. In these two numerical test the extremes of loading all the supporting nodes or star nodes and in the opposite test only the centre node is loaded. In one test run the centre node is loaded with the information from the preceding centre node and the star nodes are set to zero. In loading the centre node of the mesh-free stencil with the input information the software XMLSimple distributes the centre node information to the supporting star nodes. The distribution of input information is applied to the star nodes as the velocity vector acting in the direction of bulk gas flow as Figure 5-23. The contribution of each vector norm direction is analysed and mapped to the discretization momentum coefficients in Table 5-2. This test will aim to show that the mesh-free stencil will correctly resolve the pressure and velocity of a mathematically derive laminar potential flow regime.

In a second test, the support nodes are loaded from the information from the proceeding centre node and the centre node is set to zero. This software XMLSimple interpreters the action of setting the centre node as zero and supplying supporting star nodes the input information as applying a constant pressure boundary condition. This second test will prove for a given input pressure that a constant pressure boundary condition will output a constant pressure field. This constant pressure field will act on the velocity input information in such a way the continuity equation is maintained and mass is conserved. The expected output from

this second test is that pressure will be constant and velocity will be altered from the input value by a boundary condition. Therefore the velocity will not be constant the geometric domain but will change by an explicit boundary condition set at commencement of a run. These explicit boundary predefined conditions will have wall, inlet, outlet or external boundary conditions instigated as the local geometry dictates.

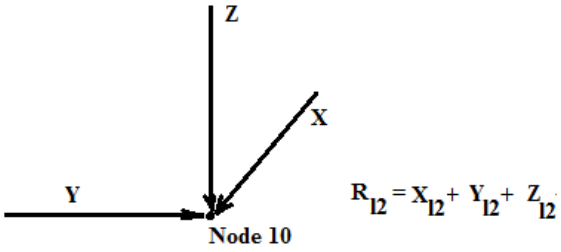

Figure 5-23. Velocity vector norm Rl2 of the velocity applied to the centre node of the particle as represented within the mesh-free stencil in Figure 5-12.

Since velocity is vector that acts at the centre node 10 in mesh-free stencil of Figure 5-12. The vector of the velocity acts at a single point as Figure 5-12 and is defined as the vector sum R_{l2} of the L2 norm of all the velocity. The action of vector sum R_{l2} coincides on the centre node 10 of the mesh-free stencil. Since the mesh-free stencil of Figure 5-12 is 3D and the test will be constructed in 2D one Cartesian dimension will be preload to the initial valve.

To calculate the pressure across the 2D potential flow using the mesh-free method a strategy is used to pass thermodynamic information. At each stencil the thermodynamic information on the properties of the system for the illustrated in Figure 5-24 is passed to the next horizontal row stencil from the start point indicated to the axis of symmetry ZZ. The first row will be inlet stencil. There after the information on the flow is passed one packet at a time from the Z stencil to the Y stencil in the next row of centre nodes.

This transfer of thermodynamic information continues for the internal boundary condition as Figure 5-14 where thermodynamic information is past across row 1 to 4 and A to n-1. In the test case the thermodynamic information is only calculated in the area AB. There after the thermodynamic information is past by a reflection area AB along the axis line ZZ and then reflection the area AB and AC along the axis line YY. This reflection is possible because the potential flow problem is mathematically symmetrical and has been choosing because of its

symmetric properties. The symmetrical property of the potential flow problem means that at any streamline illustrated in Figure 5-7, the exact pressure and velocity is known.

In these test based on the potential flow theory both velocity and pressure will have a streamline with constant value φ at a radius r from the centre of the cylinder of radius, which is equal to 1.

$$\varphi = \frac{(-1 + r^2)\sin(\theta)}{r} \tag{5-68}$$

This enables the prediction of velocity and pressure at some point away from the centre of the tube. The solution to eq. (5-68) is best achieved using by converting the Cartesian points about the centre of the tube in Figure 5-7 to polar coordinates (r, θ). To convert Cartesian to polar coordinates then:-

A polar radius r based on the coordinate system in Figure 5-7.

$$r = \sqrt{Y^2 + Z^2} \tag{5-69}$$

and polar angle in radians

$$\theta = \tan^{-1}(Y/Z) \tag{5-70}$$

For the potential flow velocity V at the coordinates points (r, θ) for a tube of radius 'a' for bulk gas flow of velocity U. Then from eq. (5-68) V is

$$V = U * r\left(\left(\frac{a^2}{r^2} - 1\right)\sin(\theta)\right) \tag{5-71}$$

Converting the values of Y and Z to polar coordinates and setting a = 0.0195 and U =10 ms^{-1}, will produce the lower spreadsheet in Table 5-9 for the polar values (r, θ).

Illustrated in Figure 5-24 shows how the use of symmetry is adopted to both simplify the computational task and ease the application of inlet and wall boundary condition. The mesh-free method calculates pressure, velocity and temperature in the Area AB. There after symmetry is applied to areas BC, DC and AD by reflection of the calculations about the lines of symmetry ZZ and YY.

If the flow is obstructed by the tube the potential flow pressure will be at p and have a velocity u. If the flow is not obstructed and assumed to be free flowing, the pressure will be p' and have a velocity U. The pressure change as the result of the change in velocity is therefore p-p'. The dynamic pressure in a stream is $\frac{1}{2}\rho u^2$. From the simplified form of Bernoulli's equation the total pressure is

$$\mathbf{p = p' + \frac{1}{2}\rho u^2} \tag{5-72}$$

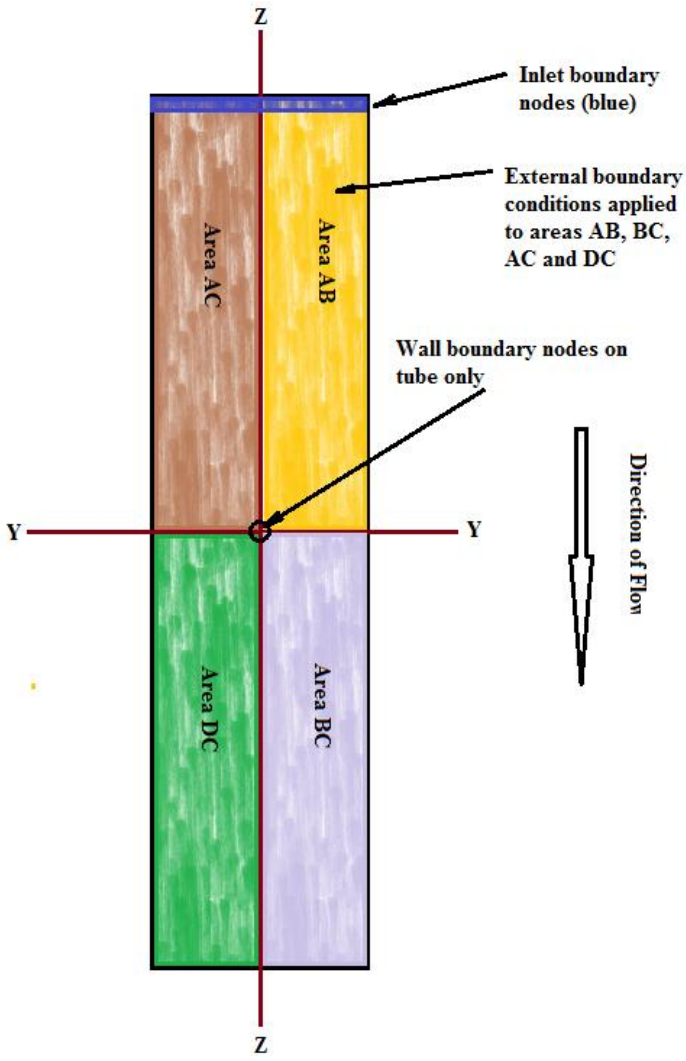

Figure 5-24. Boundary conditions and reflection of node information in the single tube test.

Before running the mesh-free software XMLSimple some initial values are set for both tests as in Table 5-7.

Table 5-7. Gas properties used in the validation test on a single tube with a diameter of 0.039 m

Gas Properties used in mesh-free solver XMLSimple		
Gas Density (Kg/m^3)	0.328972306	
Fluid Dynamic viscosity (N s/m^2)	3.625	
Diffusivity (m²/s)	0.9	
Temperature (K) all nodes 1 to 19	1027	
Initial Pressure at inlet on all nodes 1 to 19 for both test (Pa)	101325	
	Test node 10 only (Figure 5-12)	Test node 1 to 9 and node 19 (Figure 5-12)
Initial Velocity at inlet (m/s)	10	10

For test that supplies thermodynamic information directly to node 10 in Figure 5-12 the results for the mesh-free solution across the domain of the Cranfield PF combustor in Figure 5-22 are in the upper portion of Table 5-8 for pressure, Table 5-9 for velocity and Table 5-10 is velocity of bulk gas at constant pressure.

In the case of the second series of numerical tests which supplies information directly to the star or supporting nodes. The mesh-free stencil the results for the mesh-free solution across the domain of the Cranfield PF combustor in Figure 5-22 are listed in the upper portion of Table 5-10. Since the second test is set at a constant pressure there is no need to display a pressure table, therefore only a velocity table is shown upper most and the potential flow velocity result is lower.

The results for both tests are analysis in the same pattern. The conformance of the mesh-free stencil pressure P_m at node (Y_m, Z_n) to the potential flow pressure P_F at node (Y_m, Z_n) test can be addressed as the residual P_r at node (Y_m, Z_n) as

$$P_r = P_m - P_f \tag{5-73}$$

The pressure residual for each nodes at Cartesian positions (Y_1, Z_1) to (Y_9, Z_9) is found in the upper table in Table 5-9. The pressure residual standard deviation from the mean is defined as $P_r \sigma_B$ for the wider mean including all entries is $P_r \bar{m}_A$ and $P_r \sigma_B$ the standard deviation for the

Table 5-8. Pressure field for mesh-free (upper) and potential flows (lower).

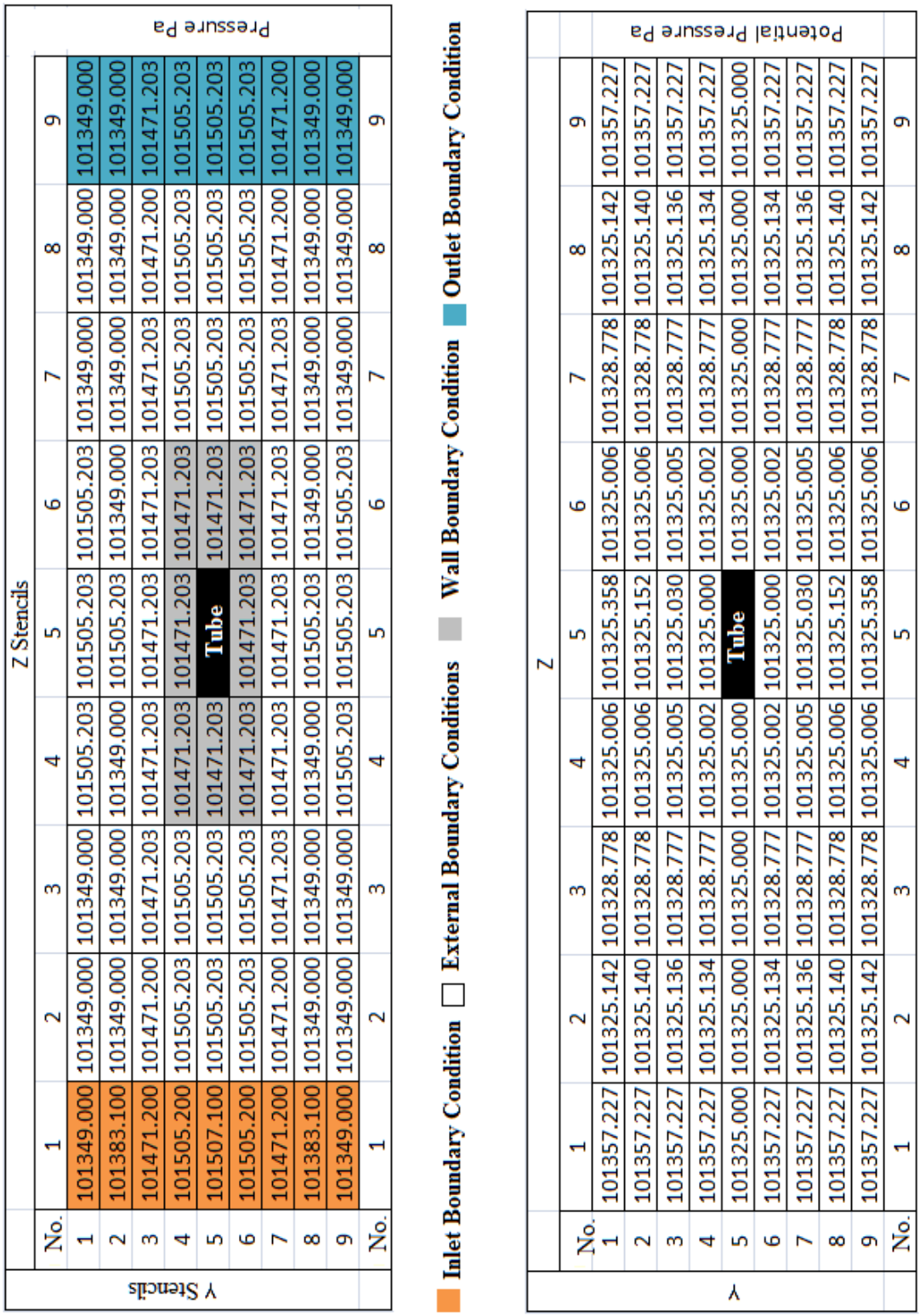

Y Stencils	Z Stencils: Pressure Pa								
No.	1	2	3	4	5	6	7	8	9
1	101349.000	101349.000	101349.000	101505.203	101505.203	101505.203	101349.000	101349.000	101349.000
2	101383.100	101349.000	101349.000	101349.000	101505.203	101349.000	101349.000	101349.000	101349.000
3	101471.200	101471.200	101471.203	101471.203	101471.203	101471.203	101471.203	101471.200	101471.203
4	101505.200	101505.203	101505.203	101471.203	101471.203	101471.203	101505.203	101505.203	101505.203
5	101507.100	101505.203	101505.203	101471.203	Tube	101471.203	101505.203	101505.203	101505.203
6	101505.200	101505.203	101505.203	101471.203	101471.203	101471.203	101505.203	101505.203	101505.203
7	101471.200	101471.200	101471.203	101471.203	101471.203	101471.203	101471.203	101471.200	101471.200
8	101383.100	101349.000	101349.000	101349.000	101505.203	101349.000	101349.000	101349.000	101349.000
9	101349.000	101349.000	101349.000	101505.203	101505.203	101505.203	101349.000	101349.000	101349.000
No.	1	2	3	4	5	6	7	8	9

Inlet Boundary Condition ☐ **External Boundary Conditions** **Wall Boundary Condition** **Outlet Boundary Condition**

Y	Z: Potential Pressure Pa								
No.	1	2	3	4	5	6	7	8	9
1	101357.227	101325.142	101328.778	101325.006	101325.358	101325.006	101328.778	101325.142	101357.227
2	101357.227	101325.140	101328.778	101325.006	101325.152	101325.006	101328.778	101325.140	101357.227
3	101357.227	101325.136	101328.777	101325.005	101325.030	101325.005	101328.777	101325.136	101357.227
4	101357.227	101325.134	101328.777	101325.002	101325.000	101325.002	101328.777	101325.134	101357.227
5	101325.000	101325.000	101325.000	101325.000	Tube	101325.000	101325.000	101325.000	101325.000
6	101357.227	101325.134	101328.777	101325.002	101325.000	101325.002	101328.777	101325.134	101357.227
7	101357.227	101325.136	101328.777	101325.005	101325.030	101325.005	101328.777	101325.136	101357.227
8	101357.227	101325.140	101328.778	101325.006	101325.152	101325.006	101328.778	101325.140	101357.227
9	101357.227	101325.142	101328.778	101325.006	101325.358	101325.006	101328.778	101325.142	101357.227
No.	1	2	3	4	5	6	7	8	9

Table 5-9. Mesh-free velocity supplied to centre node and potential flow velocity passing over an infinite length tube in Figure 5-7.

Y Stencils	Z Stencils									Velocity ms^{-1}
	No.	1	2	3	4	5	6	7	8	9
	1	10.0000	3.6607	2.0583	1.6989	2.4063	1.6989	2.0583	3.6607	1.6575
	2	10.0000	3.6607	1.8116	2.4399	2.4755	2.4399	1.8116	3.6607	1.7220
	3	10.0000	2.0583	1.6607	2.4664	2.4814	2.4664	1.6607	2.0583	1.6664
	4	10.0000	1.6989	1.5984	1.7078	1.6786	1.7078	1.5984	1.6989	1.6581
	5	10.0000	1.5936	1.5851	1.6786	**Tube**	1.6786	1.5851	1.5936	1.9026
	6	10.0000	1.6989	1.5984	1.7078	1.6786	1.7078	1.5984	1.6989	1.6581
	7	10.0000	2.0583	1.6607	2.4664	2.4814	2.4664	1.6607	2.0583	1.6664
	8	10.0000	3.6607	1.8116	2.4399	2.4755	2.4399	1.8116	3.6607	1.7220
	9	10.0000	3.6607	2.0583	1.6989	2.4063	1.6989	2.0583	3.6607	1.6575
	No.	1	2	3	4	5	6	7	8	9

Inlet Boundary Condition **External Boundary Conditions**

Wall Boundary Condition **Outlet Boundary Condition**

Y	Z									Potential Velocity ms^{-1}
	No.	1	2	3	4	5	6	7	8	9
	1	13.9973	0.9286	4.7928	0.1918	1.4747	0.1918	4.7928	0.9286	13.9973
	2	13.9973	0.9210	4.7924	0.1879	0.9620	0.1879	4.7924	0.9210	13.9973
	3	13.9973	0.9085	4.7922	0.1693	0.4240	0.1693	4.7922	0.9085	13.9973
	4	13.9973	0.9012	4.7921	0.0975	0.0000	0.0975	4.7921	0.9012	13.9973
	5	0.0000	0.0000	0.0000	0.0000	**Tube**	0.0000	0.0000	0.0000	0.0000
	6	13.9973	0.9012	4.7921	0.0975	0.0000	0.0975	4.7921	0.9012	13.9973
	7	13.9973	0.9085	4.7922	0.1693	0.4240	0.1693	4.7922	0.9085	13.9973
	8	13.9973	0.9210	4.7924	0.1879	0.9620	0.1879	4.7924	0.9210	13.9973
	9	13.9973	0.9286	4.7928	0.1918	1.4747	0.1918	4.7928	0.9286	13.9973
	No.	1	2	3	4	5	6	7	8	9

Table 5-10. Mesh-free (upper) supplied to support nodes and potential Flow (lower) of Figure 5-7 where pressure is a constant.

Y Stencil	Z Stencil									Velocity ms^{-1}
	No.	1	2	3	4	5	6	7	8	9	
	1	1.494	1.542	2.409	2.453	2.456	2.453	2.409	1.542	1.494	
	2	1.494	2.509	2.590	2.629	2.587	2.629	2.590	2.509	1.494	
	3	1.494	2.509	2.607	2.614	2.611	2.614	2.607	2.509	1.494	
	4	1.494	2.509	2.608	1.494	1.494	1.494	2.608	2.509	1.494	
	5	1.494	2.509	2.608	1.494	Tube	1.494	2.608	2.509	1.494	
	6	1.494	2.509	2.608	1.494	1.494	1.494	2.608	2.509	1.494	
	7	1.494	2.509	2.607	2.614	2.611	2.614	2.607	2.509	1.494	
	8	1.494	2.509	2.590	2.629	2.587	2.629	2.590	2.509	1.494	
	9	1.494	1.542	2.409	2.453	2.456	2.453	2.409	1.542	1.494	
	No.	1	2	3	4	5	6	7	8	9	

Inlet Boundary Condition External Boundary Conditions

Wall Boundary Condition Outlet Boundary Condition

Y	Z									Potential Velocity ms^{-1}
	No.	1	2	3	4	5	6	7	8	9	
	1	13.997	0.929	4.793	0.192	1.244	0.192	4.793	0.929	13.997	
	2	13.997	0.921	4.792	0.188	0.811	0.188	4.792	0.921	13.997	
	3	13.997	0.908	4.792	0.169	0.358	0.169	4.792	0.908	13.997	
	4	13.997	0.901	4.792	0.098	0.000	0.098	4.792	0.901	13.997	
	5	13.338	0.857	4.566	0.000	Tube	0.000	4.566	0.857	13.338	
	6	13.997	0.901	4.792	0.098	0.000	0.098	4.792	0.901	13.997	
	7	13.997	0.908	4.792	0.169	0.358	0.169	4.792	0.908	13.997	
	8	13.997	0.921	4.792	0.188	0.811	0.188	4.792	0.921	13.997	
	9	13.997	0.929	4.793	0.192	1.244	0.192	4.793	0.929	13.997	
	No.	1	2	3	4	5	6	7	8	9	

narrower mean which excludes inlet and outlet boundary conditions and the mean is $P_r\overline{m}_B$. While the pressure ratio across each individual stencil between the mesh-free and potential flow is

$$P_{(m/f)} = \frac{\text{Pressure}_{\text{Mesh-free(n)}}}{\text{Pressure}_{\text{Potential flow(n)}}} \tag{5-74}$$

Table 5-11. Pressure residuals Pm - Pf and pressure ratio Pm/Pf benchmarks of mesh-free stencils pressure Pm against potential flow pressure PF.

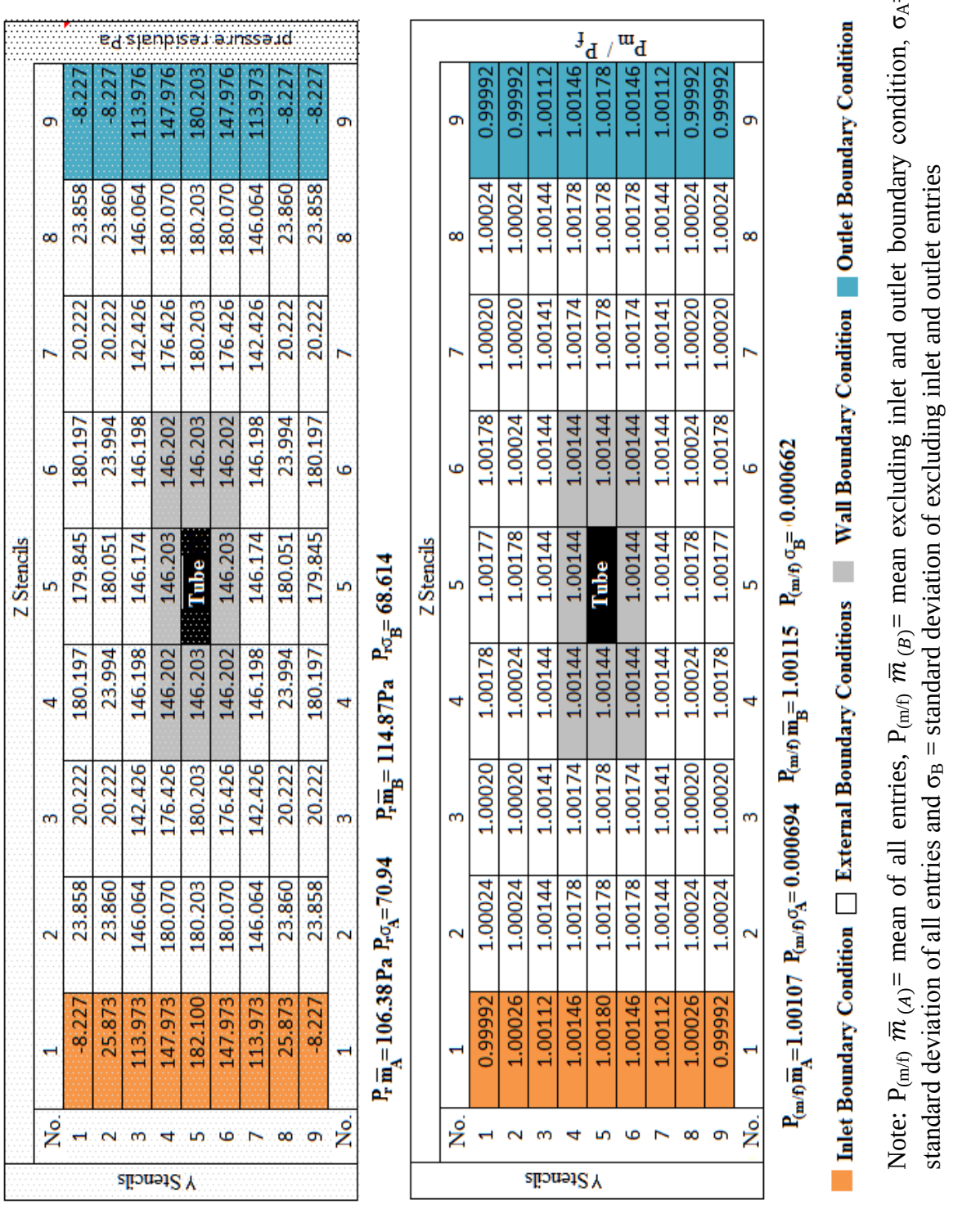

Note: $P_{(m/f)}\ \bar{m}_{(A)}$= mean of all entries, $P_{(m/f)}\ \bar{m}_{(B)}$= mean excluding inlet and outlet boundary condition, σ_A= standard deviation of all entries and σ_B = standard deviation of excluding inlet and outlet entries

Hence $P_{(m/f)}\sigma_A$ for the wider pressure ratio mean including all entries and $P_{(m/f)}\sigma_B$ the standard deviation for the narrower pressure ratio mean which excludes inlet and outlet boundary conditions. Likewise, $P_{(m/f)}\,\bar{m}_A$ is the mean including all entries and $P_{(m/f)}\,\bar{m}_B$ is the mean excluding inlet and outlet. These differences in mean residual are because potential flow does not have disturbances from inlet or outlet boundary conditions, while the mesh-free model will accounts for these using the inbuilt boundary conditions.

As measure of the efficiency of the mesh-free method, the use of pressure residuals has some drawbacks. Picking the difference between mesh-free stencil and potential flow as 'residuals' can see swings widely in mean and standard deviation of the mean pressures residuals. This can down rate the performance of the mesh-free method worse than should be credited. To set a performance measure that considers these swings issues the mesh-free method pressure against the potential flow pressure then the pressure ratio P_m/P_f is adopted. The entries for P_m/P_f are complete the lower spreadsheet of Table 5-11 and are used to benchmark the mesh-free method in so far as pressure The velocity residual $V_m - V_f$ comparing potential flow V_f against mesh-free method V_m are reported in Table 5-12.

The differences between the velocities of the mesh-free stencil and the potential flow method at a fix Cartesian point are defined as the residual $V_m - V_f$. The use of $V_m - V_f$ sets a benchmark for mesh-free method against the how effective the velocity (or kinetic energy) component of the thermodynamic information is calculated locally.

The case where thermodynamic information is supplied to the centre mode 10 in Figure 5-12, the residuals velocity is shown in Table 5-12. In case where thermodynamic information is supplied to the supporting nodes or star nodes (nodes 1-9 and 11-19) the upper spreadsheet of Table 5-13 shows the velocity. In case where thermodynamic information is supplied to supporting nodes residuals analysis is in the lower of Table 5-13. In Table 5-13 $V_m - V_f$, as for pressure the benchmark; uses two arithmetic mean and standard deviation. The wider arithmetic mean $\bar{m}_A$ and standard deviation σ_A which includes all mesh-free centre nodes (Y1, Z1) to (Y9, Z9). The narrower mean $\bar{m}_B$ and standard deviation σ_B excludes the inlet boundary conditions and outlet boundary condition.

Table 5-12. The velocity residual $V_m - V_f$ where thermodynamic information is supplied to the centre node

Y Stencils	Z Stencils									
	No.	1	2	3	4	5	6	7	8	9
	1	-3.997	2.732	-2.734	1.507	0.932	1.507	-2.734	2.732	-12.340
	2	-3.997	2.740	-2.981	2.252	1.514	2.252	-2.981	2.740	-12.275
	3	-3.997	1.150	-3.132	2.297	2.057	2.297	-3.132	1.150	-12.331
	4	-3.997	0.798	-3.194	1.610	1.679	1.610	-3.194	0.798	-12.339
	5	10.000	1.594	1.585	1.679	Tube	1.679	1.585	1.594	1.903
	6	-3.997	0.798	-3.194	1.610	1.679	1.610	-3.194	0.798	-12.339
	7	-3.997	1.150	-3.132	2.297	2.057	2.297	-3.132	1.150	-12.331
	8	-3.997	2.740	-2.981	2.252	1.514	2.252	-2.981	2.740	-12.275
	9	-3.997	2.732	-2.734	1.507	0.932	1.507	-2.734	2.732	-12.340
	No.	1	2	3	4	5	6	7	8	9

Velocity residuals ms^{-1} $V_m - V_f$

$\bar{m}_A = -1.055\ ms^{-1}$ $\sigma_A = 4.5938$ $\bar{m}_B = 0.553\ ms^{-1}$ $\sigma_B = 2.1852$

Note: $\bar{m}_A$ = mean of all entries, $\bar{m}_B$ = mean excluding inlet and outlet boundary condition, σ_A= standard deviation of all entries and σ_B = standard deviation of excluding inlet and outlet entries

The intensive property pressure has been considered together with the non-intensive property velocity, where velocity represents the kinetic energy of particle at the mesh-free centre nodes (Y1, Z1) to (Y9, Z9). Each mesh-free stencil has a volume that is the unity since the length of the mesh-free stencils of Figure 5-12 is also unity.

The benchmark test for diffusion-convective flow involves the mesh-free model in one instance as pure convective flow and then a highly diffusive convective-diffusion flow. The result of temperature is considered in Table 5-14 that represent the grand canonical ensemble intensive property of temperature, in the upper table in table shows pure convective flow (diffusivity is 0) where the inlet temperature is 1073K. The second test in the lower of table in Table 5-14 receive a bulk gas at temperature of 1073 and the centre tube has a fixed temperature of 550K and a diffusion coefficient of 0.9. The initial velocity and pressure set to the values in Table 5-7.

The initial values of Table 5-7 are supplied to the centre node (numbered 10 in Figure 5-12) in the first iteration of the mesh-free finite difference stencil and then passed between centre nodes for all other stencils. This passing of output solution from n-1 mesh-free finite

difference stencil to the next stencil is how thermodynamic information is transferred across the geometric domain.

Table 5-13. Velocity supplied to the star node for each mesh-free stencil (upper) and residual V_m - V_f comparing potential flow V_f against mesh-free stencil V_m (lower).

Y Stencils \ Z Stencils	1	2	3	4	5	6	7	8	9
1	1.494	1.542	2.409	2.453	2.456	2.453	2.409	1.542	1.494
2	1.494	2.509	2.590	2.629	2.587	2.629	2.590	2.509	1.494
3	1.494	2.509	2.607	2.614	2.611	2.614	2.607	2.509	1.494
4	1.494	2.509	2.608	1.494	1.494	1.494	2.608	2.509	1.494
5	1.494	2.509	2.608	1.494	Tube	1.494	2.608	2.509	1.494
6	1.494	2.509	2.608	1.494	1.494	1.494	2.608	2.509	1.494
7	1.494	2.509	2.607	2.614	2.611	2.614	2.607	2.509	1.494
8	1.494	2.509	2.590	2.629	2.587	2.629	2.590	2.509	1.494
9	1.494	1.542	2.409	2.453	2.456	2.453	2.409	1.542	1.494

Velocity ms^{-1}

Inlet Boundary Condition **External Boundary Conditions**

Wall Boundary Condition **Outlet Boundary Condition**

Y Stencils \ Z Stencils	1	2	3	4	5	6	7	8	9
1	-12.504	0.613	-2.384	2.262	1.212	2.262	-2.384	0.613	-12.504
2	-12.503	1.588	-2.202	2.441	1.775	2.441	-2.202	1.588	-12.503
3	-12.503	1.600	-2.186	2.445	2.253	2.445	-2.186	1.600	-12.503
4	-12.503	1.608	-2.184	1.397	1.494	1.397	-2.184	1.608	-12.503
5	-11.844	1.652	-1.958	1.494	Tube	1.494	-1.958	1.652	-11.844
6	-12.503	1.608	-2.184	1.397	1.494	1.397	-2.184	1.608	-12.503
7	-12.503	1.600	-2.186	2.445	2.253	2.445	-2.186	1.600	-12.503
8	-12.503	1.588	-2.202	2.441	1.775	2.441	-2.202	1.588	-12.503
9	-12.504	0.613	-2.384	2.262	1.212	2.262	-2.384	0.613	-12.504

Velocity Residuals ms^{-1} $V_m - V_f$

$\bar{m}_A$=-2.349ms^{-1} σ_A=5.704 $\bar{m}_B$=0.578ms^{-1} σ_B=1.852

Note: $\bar{m}_A$ = mean of all entries, $\bar{m}_B$ = mean excluding inlet and outlet boundary condition, σ_A= standard deviation of all entries and σ_B = standard deviation of excluding inlet and outlet entries.

The mesh-free method calculates the grand canonical ensemble intensive property of temperature with microstates at specific location in the domain as illustrated in Figure 5-22.

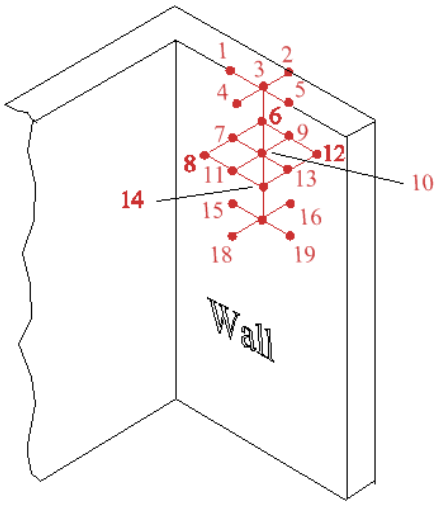

Figure 5-25. The mesh-free stencil part embedded into the wall to form a wall boundary

Illustrated in Figure 5-25 the mesh-free stencil, highlighted in red, is part embedded into the wall at the start point, as well as other parts of the PF combustor wall and tube wall simulation at points illustrated in Figure 5-22. The calculations of all thermodynamic properties are under taken to resolve nodes 1 to 9 and 11 to 19 through node 10. However, at the wall boundaries part of the stencil reports the wall properties (for example temperature).

The initial temperature for the mesh-free stencil located at (Y1, Z1) is supplied a set of initial values and gas properties. Part of the mesh-free stencil (Y1, Z1) is buried in the wall in such a way nodes 2, 6, 9, 12 and 16 reports the wall temperature as shown in Figure 5-25. All wall centred mesh-free stencils are embedded into the wall in the similar way. The wall centred mesh-free stencils make use of both the values of the intensive and non-intensive properties of the bulk gas and the tube wall. The wall of the PF combustor simulation is considered adiabatic but the tube is not and can receive a transfer of heat flux across the tube from the bulk gas.

The mesh-free stencil performance is assessed across the PF combustor simulation by a comparison with convection - diffusion in a potential flow problem. This form of convection - diffusion problem utilising in a potential flow problem and is a pure mathematical construct that is not representative of a real fluid. Like the pressure and velocity properties relating to

the flow of viscous fluid; there are few exact solutions to the convection - diffusion problem in which to make a comparison of the performance of the mesh-free stencils. The potential flow is an exact solution that encapsulates the whole mathematics or physics of the problem without using an approximation. When solving c-d problem using potential flow, since this approach is also an exact solution, the Péclet number is not used.

For a fluid with a specific heat capacity *C* and constant thermal conductance *K*, the heat flux vector is $F\rho C$ (Pillow 1970). The heat flux density vector *F* is the sum of the convective and diffusive components, such that

$$\mathrm{F} = -\mathrm{k}\nabla\mathrm{T} + \mathrm{uT} \tag{5-75}$$

where *T(r, t)* is the temperature field and *u(r, t)* is the velocity field; *k* is thermal diffusivity when $k = K/\rho C$. The conservation of heat energy requires the mass-area density *m(r,t)* of the inflowing fluid be balance with the out-flowing fluid and zero over the system. Since the heat density is ρCT, it follows that

$$\frac{\mathrm{d}}{\mathrm{dt}}\left[\int_{\mathrm{S}} \mathrm{Tds}\right] = -\oint_{\partial \mathrm{S}} \mathrm{ds}\mathbf{n} \cdot \mathrm{F} \tag{5-76}$$

or, locally, for suitably differential fields,

$$\frac{\partial \mathrm{T}}{\partial \mathrm{t}} + \mathrm{div}\ \mathrm{F} = 0 \tag{5-77}$$

The conservation of mass-area density *m(r, t)* means that locally

$$\mathrm{div}\ \mathrm{q} = 0 \tag{5-78}$$

Therefore, eq. (5-77) can be written as

$$\frac{\partial \mathrm{T}}{\partial \mathrm{t}} + \mathrm{q} \cdot \nabla\mathrm{T} = \mathrm{k}\nabla^2\mathrm{T} \tag{5-79}$$

In terms of stream functions ψ of lines of constant temperature as for Figure 5-7 and eq. (B4) in Appendix B in Cartesian coordinates (x, y)

$$\frac{\partial \mathrm{T}}{\partial \mathrm{t}} = \frac{\partial(\Psi, \mathrm{T})}{\partial(\mathrm{x}, \mathrm{y})} + \mathrm{k}\nabla^2\mathrm{T} \tag{5-80}$$

in two dimensions.

In the axisymmetric case with polar coordinates (r, θ) centred at the Cartesian position (x, y) in centre of the tube in Figure 5-7, then

$$\frac{\partial \mathrm{T}}{\partial \mathrm{t}} = \frac{1}{\partial}\frac{\partial(\Psi, \mathrm{T})}{\partial(\mathrm{r}, \theta)} + \mathrm{k}\nabla^2\mathrm{T} \tag{5-81}$$

where

$$\nabla^2 \equiv \frac{\partial^2}{\partial\theta^2} + \frac{1}{\theta}\frac{\partial}{\partial\theta} + \frac{\partial^2}{\partial \mathrm{r}^2} \tag{5-82}$$

by separating the variables as $F = \rho u$ *for* the convection transport mass flux term along and $D = \Gamma/\delta r$ for the diffusive conductance term along the streamline ψ, where Γ is the diffusion coefficient.

If the inlet conductive terms are represented as $\Phi_{F,}$ while from the centre of the cylinder $\Phi_{(r,\theta)}$ radiate equal-potential lines signified as φ

$$\frac{\partial \varphi}{\partial \theta} = \Phi_{\mathrm{F}} - \Phi_{\mathrm{r},\theta} = \exp(\rho \mathrm{u}_{\mathrm{F}}/\theta) - 1 \tag{5-83}$$

and the diffusive terms represented as flow $\Phi_{F,}$ along the constant streamlines as

$$\Psi\frac{\partial \psi}{\partial \mathrm{r}} = \Phi_{\mathrm{D}} - \Phi_{(\mathrm{r},\theta)} = \exp(\Gamma_{\mathrm{D}}/\delta \mathrm{r}) - 1 \tag{5-84}$$

In the case of the cylinder the complex potential function in polar coordinates is applied from

$$z = x + iy \text{ and } \mathrm{w} = \varphi + \mathrm{i}\psi \tag{5-85}$$

$$z = re^{i\theta} + \frac{1}{re^{i\theta}}$$

then, writing z in polar coordinates $z = x + iy = re^{i\theta}$, then

$$\varphi = A_F\frac{(1 + r^2)\cos(\theta)}{r} \tag{5-86}$$

and

$$\psi = A_D\frac{(-1 + r^2)\sin(\theta)}{r}$$

Table 5-14. Temperature fields across the PF combustor with different diffusion coefficient Γ

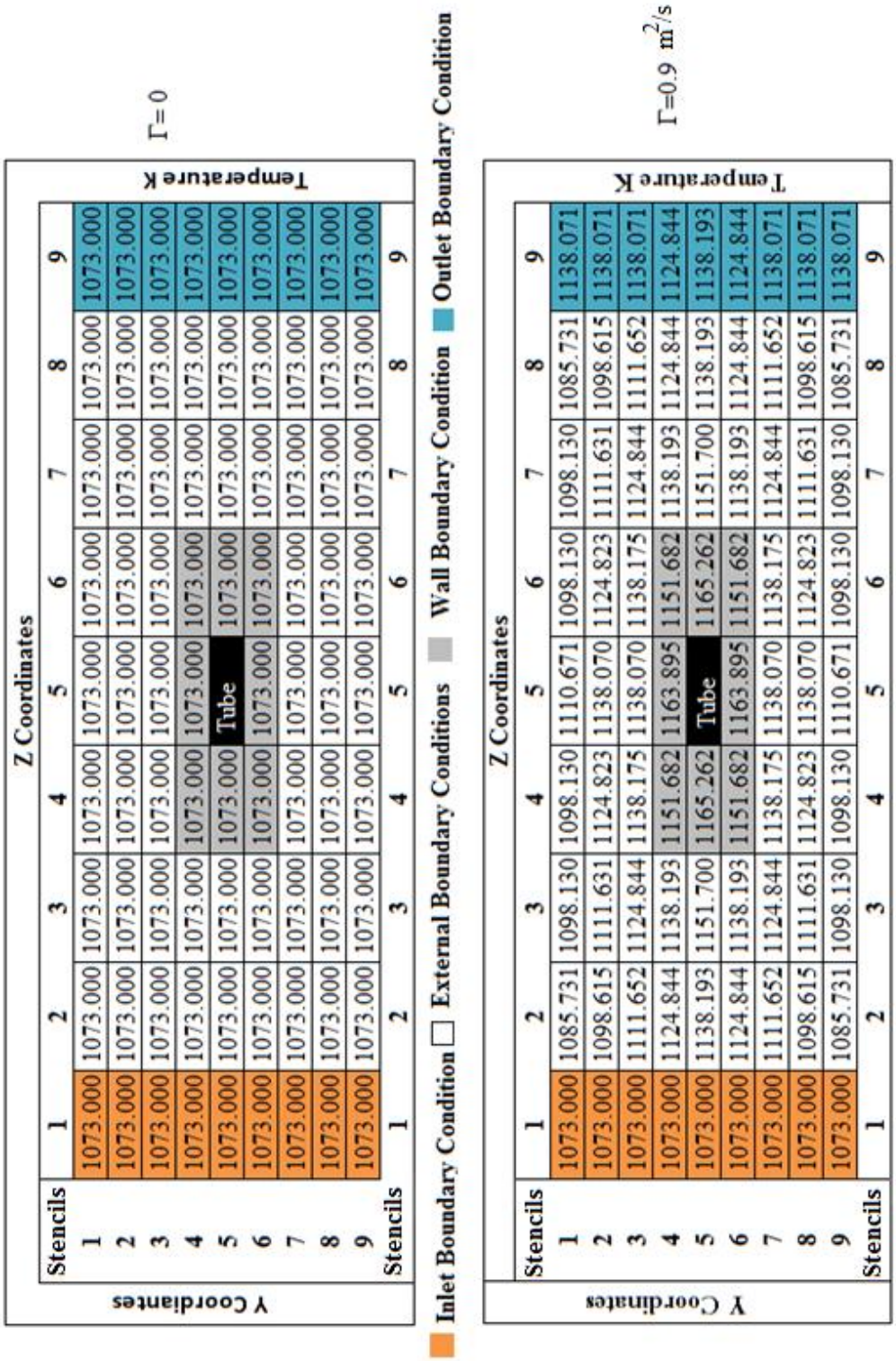

Where A_F is define as eq. (5-87)

$$(\rho u_F/\theta) - 1 \text{ for } A_F \tag{5-87}$$

and A_D is eq. (5-88).

$$(\Gamma_D/\delta r) - 1 \text{ for } A_D \tag{5-88}$$

The values for u_F are derived from the potential velocity used to complete Table 5-14, while δr is calculated from the cylinder centre $r_{(r,\theta)}$ and Γ is a constant.

There are two measurements used to define the measure of fit between the reference values, which is temperature across the Cranfield PF combustor where the convection and diffusion equation has a solution based on potential flow. The mesh-free solution of the convection – diffusion equation and its comparator and has two distinct regions. The complete data set in the lower table of Table 5-15 is measures the average residual error $\bar{m}_A$ and the standard deviation σ_A of the spread of error around the mean that is in one standard deviation. The lower data set in Table 5-15 includes the contribution from mesh-free stencils that are configured as inlet and outlet values. The residual differences values are determined using the following eq. (5-89).

$$\text{Residual Error} = \text{Temperature}_{\text{Mesh-free solution}} - \text{Temperature}_{\text{Potential Flow}} \tag{5-89}$$

The potential flow solution is not configured to have an inlet or outlet and this wider data set that is represented by the average residual error $\bar{\boldsymbol{m}}_A$and the standard deviation $\sigma_A$may skew the data in the lower part of Table 5-15. Temperature in a conductive - diffusive potential flow over a cylinder (upper tables) and the residuals errors of mesh-free stencils against of the temperature in a conductive- diffusive flow (lower table) takes a dataset that excludes the inlet and outlet. In Table 5-15 the coordinates (Z1, Y1) to (Z1, Y9) and (Z9, Y1) to (Z9, Y9) are excluded from determining residual error $\bar{\boldsymbol{m}}_B$ and the standard deviation σ_B.

The mesh-free finite difference method has made the calculation of values of intensive properties of pressure, temperature and the non-intensive properties of velocity that form the grand canonical ensemble as outlined in this chapter. If compared with a potential flow then a measure of the effectiveness of this mesh-free finite difference method to capture the

Table 5-15. Potential temperature field (Upper) and Mesh-free Temperature field (Lower)

Y Coordinates	Z Coordinates									Potential Temperature K
Stencil	1	2	3	4	5	6	7	8	9	
1	1073.002	1138.455	1092.314	1100.047	1179.199	1101.253	1243.880	1196.341	1758.350	
2	1073.001	1121.707	1087.003	1092.898	1141.108	1093.766	1196.868	1164.308	1535.044	
3	1073.001	1105.186	1082.027	1085.086	1099.793	1085.560	1152.841	1132.823	1350.723	
4	1073.000	1088.969	1077.365	1076.650	1073.000	1076.731	1111.610	1102.535	1198.581	
5	1073.000	1073.000	1073.000	1073.000	Tube	1073.000	1073.000	1073.000	1073.000	
6	1073.000	1088.969	1077.365	1076.650	1073.000	1076.731	1111.610	1102.535	1198.581	
7	1073.001	1105.186	1082.027	1085.086	1099.793	1085.560	1152.841	1132.823	1350.723	
8	1073.001	1121.707	1087.003	1092.898	1141.108	1093.766	1196.868	1164.308	1535.044	
9	1073.002	1138.455	1092.314	1100.047	1179.199	1101.253	1243.880	1196.341	1758.350	
Stencil	1	2	3	4	5	6	7	8	9	

Inlet Boundary Condition ☐ External Boundary Conditions Wall Boundary Condition Outlet Boundary Condition

Y Coordinates	Z Coordinates									Temperature residuals K
Stencils	1	2	3	4	5	6	7	8	9	
1	-0.002	-52.724	5.816	-1.917	-68.528	-3.122	-145.750	-110.610	-620.279	
2	-0.001	-23.091	24.629	31.925	-3.038	31.056	-85.236	-65.693	-396.973	
3	-0.001	6.466	42.817	53.089	38.277	52.615	-27.997	-21.171	-212.652	
4	0.000	35.875	60.827	75.033	90.895	74.951	26.582	22.309	-73.737	
5	0.000	65.193	78.700	92.262	Tube	92.262	78.700	65.193	65.193	
6	0.000	35.875	60.827	75.033	90.895	74.951	26.582	22.309	-73.737	
7	-0.001	6.466	42.817	53.089	38.277	52.615	-27.997	-21.171	-212.652	
8	-0.001	-23.091	24.629	31.925	-3.038	31.056	-85.236	-65.693	-396.973	
9	-0.002	-52.724	5.816	-1.917	-68.528	-3.122	-145.750	-110.610	-620.279	
Stencils	1	2	3	4	5	6	7	8	9	

$\bar{m}_A = 24.265$ K $\sigma_A = 55.546$ $\bar{m}_B = 9.692$ K $\sigma_B = 59.401$. Note: $\bar{m}_A$ = mean of all entries, $\bar{m}_B$ = mean excluding inlet and outlet boundary condition, σ_A= standard deviation of all entries and σ_B = standard deviation of excluding inlet and outlet entries.

thermodynamic properties can be determined. The accuracy of the mesh-free finite difference, based on the mean error and the standard deviation, is summarised in Table 5-16.

Table 5-16. A summary of the effectiveness of the mesh-free finite difference method to solve the intensive and non-intensive properties of the grand canonical ensemble

Property	Type	$\bar{\boldsymbol{m}}_A$	σ_A,	$\bar{\boldsymbol{m}}_B$	σ_B
Pressure_{10} (Pa)	Intensive	106.38	70.94	114.877	65.614
Pressure (Pa)	Intensive	1.000107	0.000694	1.00115	0.000662
Velocity_{10} (ms^{-1})	Non-Intensive	-1.055	4.5938	0.553	2.1852
Velocity (ms^{-1})	Non-Intensive	2.349	5.704	0.578	1.852
$^{(1)}$Temperature (K)	Intensive	0	0	0	0
$^{(2)}$Temperature (K)	Intensive	24.4	53.546	9.692	59.401
Notes: Pressure_{10} evaluated at constant pressure, Velocity_{10} evaluated at constant pressure, $^{(1)}$Temperature for pure conductive with $\Gamma = 0$, $^{(2)}$ Temperature with $\Gamma = 0.9$					

The nineteen nodes within the mesh-free stencil will all contribute to the convergence of the solution. In some cases some of the nodes within the stencil will form a face that will not converge. When groups of nodes in the mesh-free stencil do not converging the explanation is that groups of nodes bridge the boundary of the vessel.

At the boundary of the vessel the mesh-free stencil will calculate values of thermodynamic properties as very small and that approach zero. In such cases the XMLSimple (the mesh-free solver software) resets the contribution from such nodes to values at the limited of the floating point that a computer can manage. This value adopted by the mesh-free finite difference solver XMLSimple for overflow is 10^{308} (IEEE 754, 2008).

The wider data set which fixes the average residual error $\bar{\boldsymbol{m}}_A$ and the standard deviation σ_A, is supported with a narrower average residual error $\bar{\boldsymbol{m}}_B$ and the standard deviation σ_B. As a measure of how effective the mesh-free finite difference solver XMLSimple is operating the percentage of how many nodes in one stencil converge are calculate as eq. (5-90)

$$100 - \left(\frac{\text{number of nodes failed to converge}}{19} 100\right) = \%\ \text{convergence} \tag{5-90}$$

Table 5-17. Percentage of node in a stencil that converge at a coordinate point Y, Z

Y coordinates \ Z coordinates (Stencil)	1	2	3	4	5	6	7	8	9	Percentage of nodes that converged
1	50.00	100	100	100	100	100	100	100	72.81	
2	50.00	100	100	100	100	100	100	100	72.81	
3	50.00	100	100	100	100	100	100	100	72.81	
4	50.00	100	100	100	100	100	100	100	72.81	
5	50.00	100	100	100	Tube	100	100	100	72.81	
6	50.00	100	100	100	100	100	100	100	72.81	
7	50.00	100	100	100	100	100	100	100	72.81	
8	50.00	100	100	100	100	100	100	100	72.81	
9	50.00	100	100	100	100	100	100	100	72.81	
Stencil	1	2	3	4	5	6	7	8	9	

Note: Inlet boundary condition Outlet boundary condition
Wall Boundary Conditions External boundary conditions

The percentage of the node at a particular stencil coordinates that have converged is figured in Table 5-17.

By using a 19-node stencil to solve intensive and non-intensive properties using this mesh-free finite difference method it is clearly demonstrated in Table 5-17 that at minimum of 9 to 10 nodes will converge. This capability of this mesh-free finite difference method to tolerate imprecise initial conditions at the boundaries is a key advantage over conventional finite difference methods based on meshed geometry.

The number of iteration in this mesh-free finite difference method is defines as the point where further improvement in the output of the mesh-free solver (XMLSimple) cannot benefit with more nodes reaching convergence. In the case of inlet and outlet boundary conditions, the XMLSimple solver will achieve convergence within 3-5 iteration. The XMLSimple solver will achieve convergence for external and wall boundary conditions in 2 iterations. The run time of XMLSimple to solve the two intensive thermodynamic properties and one non-intensive thermodynamic property with the external boundary conditions within 2 iterations is

approximately 2.43 seconds. These run times are based on running the XMLSimple solver on a computer with an ADM Turion 64 bit processor. The software package is design to operate on a parallel processing system and is written in FORTRAN 2003.

5.8 Case Study: Stokes Numbers around 4 tube superheater.

Since the study of the pressure field confirms the validity methods it is possible to considering the case using the dimensionless inertial number, the Stokes number with 4 tubes

The assumption is that a single-phase flow around a circular cylinder is presented and the velocity field around the pipe will produce a Stokes number map around the four tubes.

The Stokes Number is defined in Table 2-2, but before examining the use of Stokes numbers for multiple tube banks the flow induced vibration should be examined. Flow induced vibration can cause the failure of a superheater by inducing fatigue fracture in the tubes.

The spherical or cylindrical objects with Reynolds number between 800 < Re < 20,000 have two co-existing frequencies. The Strouhal number is related to this range of Reynolds number for flow around a cylinder is approximated as 0.21. With the known value of Strouhal number, the velocity data from Table 5-7 (10m/s), and diametrical data from Figure 5-22, the upper frequency of the vortex shedding off the tube can be calculated using eq. (5-31) as

$$f = \frac{0.21 \times 0.039}{10} = 8.19 \times 10^{-4}\ \text{Hz}$$

Then for this Strouhal number and at this Reynolds number, the quasi steady state portion of the movement dominates the oscillation. This applies for a single tube configuration and flow induced vibration will be negligible.

In Figure 5-26 the PF combustor has been configured to have a bank of four tubes with a pitch greater than 1.25. In this configuration the flow induced vibration is defined using Strouhal number of 0.33 (Kuppan, 2000). Apply the Strouhal value to eq. (5-31) produces a frequency of 1.29 $x10^{-3}$ Hz and at this frequency and tube pitch seperation the flow is characterized by the buildup and rapidly subsequent shedding of vortices from each tube. While the designer of the heat exchanger would not design the tubes with such a pitch that it would cause flow induced vibration. The increase in diameter of the superheater tubes because of deposits

growth will have a significant impact and detrimental effect on the frequency of vortex shedding.

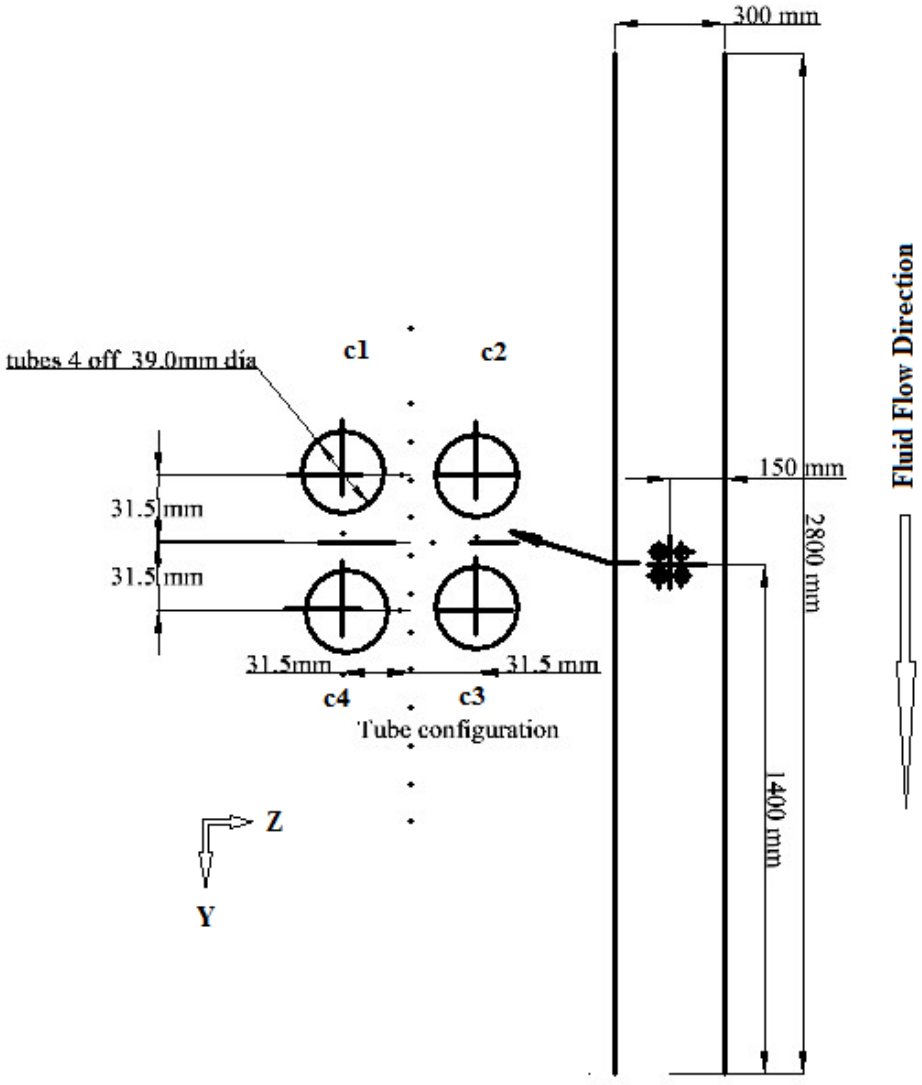

Figure 5-26. PF combustor configured with 4 tubes

The particles of ash or char (partially burnt combustible products) are friable and may reduce in size by combustion depending on the quantity of unburnt carbon present. These particles may also increase or reduce in size by collision at the temperatures within the PF combustor. Depending on the entrapped gas within the particles they can be mottled or hollow (Robertson, et al., 2002). Ash particles tend to be spherical and glassy (Olushola, et al., 2012). To model this property in this case study the particles have sizes chosen at the extremes of

1μm and 400μm, but a common size for coarse fly ash particles would be between 60μm and 100μm (Scharler, et al., 2007).

For a particle to impact a tube then Stokes Number >> 1, therefore for a particle of sizes of 1μm and 400 μm will have a relaxation time τ as define by eq. (5-91)

$$\tau = \frac{\rho_p d_p^2}{18\mu} \tag{5-91}$$

where ρ_p mass density and d_p diameter of the particle, μ is the fluid dynamic viscosity (Scharler, et al., 2007). For a mass density of 2648 kg/m^3 and fluid dynamic velocity 1.386x10^{-5} kg/(m s) , the relaxation time for 1μm is 10.6141 sec and for 400μm is 4246 sec. The Stokes number is therefore:

at 1μm

$$Stk = \frac{10.6141 * 10}{0.039} = 2721.558277$$

at 400μm

$$Stk = \frac{4246 * 10}{0.039} = 1088623.311$$

Hence for both particles sizes an impact should occur, with the particle producing a larger Stokes number than the more likely than otherwise. Studies on banks of tubes show that the particle mass fraction impacted on the tubes not only depend on the Stokes number of the particles but also to a lower extent also on the velocity of the flue gas (Scharler, et al., 2007).

As shown in chapter 4 depositions of particles onto superheater tubes is a complex process consisting of many sub-processes. For a particle to stay attach to the tube the surface of the particles will have a coating of vapour which on contact with the cooler tube change phase and solidify. If this was not the case the particle would probability bounce of the tube. The Vapour deposition mechanisms can be any one or a mixture all of heterogeneous condensation, homogeneous condensation and vapour deposition. When a particle is not in line with the centre line of the tube, the particle can still be forced away from the tubes by actions such as vortices and turbulence.

Other influences on particles that will move particles to impact a tube that would otherwise miss is Brownian motion which effects particles with dimensions are near or below 1μm For

sizes from 1μm up to 100μm turbophoresis and thermophoresis is important factor in steering particles to impact tubes. For particles which exist in a single phase it's is possible to use Stokes numbers. If the particles undergo a phase change its will form groups of molecules and the mass will no longer have a steady-state mass. This is a problem of scale resolution of mass and requires a solution that is not dependant of Stokes numbers or classical physics.

A numerical study was made using 1μm particles and a method of resolving the complexities in the deposition modelling with deposition particles with very small diametrical sizes. The results of this numerical study are presented for a particle size of 1μm in Figure 5-27 to Figure 5-30.

- Illustrated in Figure 5-27 is the partial temperature field across a PF combustor with 4 test tubes and the temperature near to the surface of the 4 tubes labelled c1, c2, c3 and c4 for a particles size of 1μm. The inlet and outlet to the combustor are labelled i1 and o1 respectively, while the walls of the combustor are labelled v1 and v2. The geometric position data is drawn in Figure 5-27 and the temperature is predicted using XMLSimple mesh-free finite difference solver. The particles realised from the inlets i1 are assumes not to under further combustion.
- In Figure 5-28 is the homogeneous deposition rate field for one mole of KCl at the partial temperature for each stencil cell as illustrated in Figure 5-27 for a particles size of 1μm. A unit mole will contain a fix number of particles as defined by Avogadro number (6.0221415×10^{23}). The inlet and outlet stencils cells to the combustor are labelled i1 and o1 respectively, while the wall stencil cells of the combustor are labelled v1 and v2. The four tubes stencil cells are label c1, c2, c3 and c4. The diagram is constructed with the aid of Peng – Robinson equation of state from section 4.4.
- For Figure 5-29 homogeneous deposition rate field for one mole of K_2SO_4 at the partial temperature for each stencil cell as illustrated in Figure 5-26. The inlet, outlet and four tubes stencil cells stencils cells are numbers as for Figure 5-28. This diagram is constructed as for the KCl diagram using Peng – Robinson equation of state model in section 4.4.

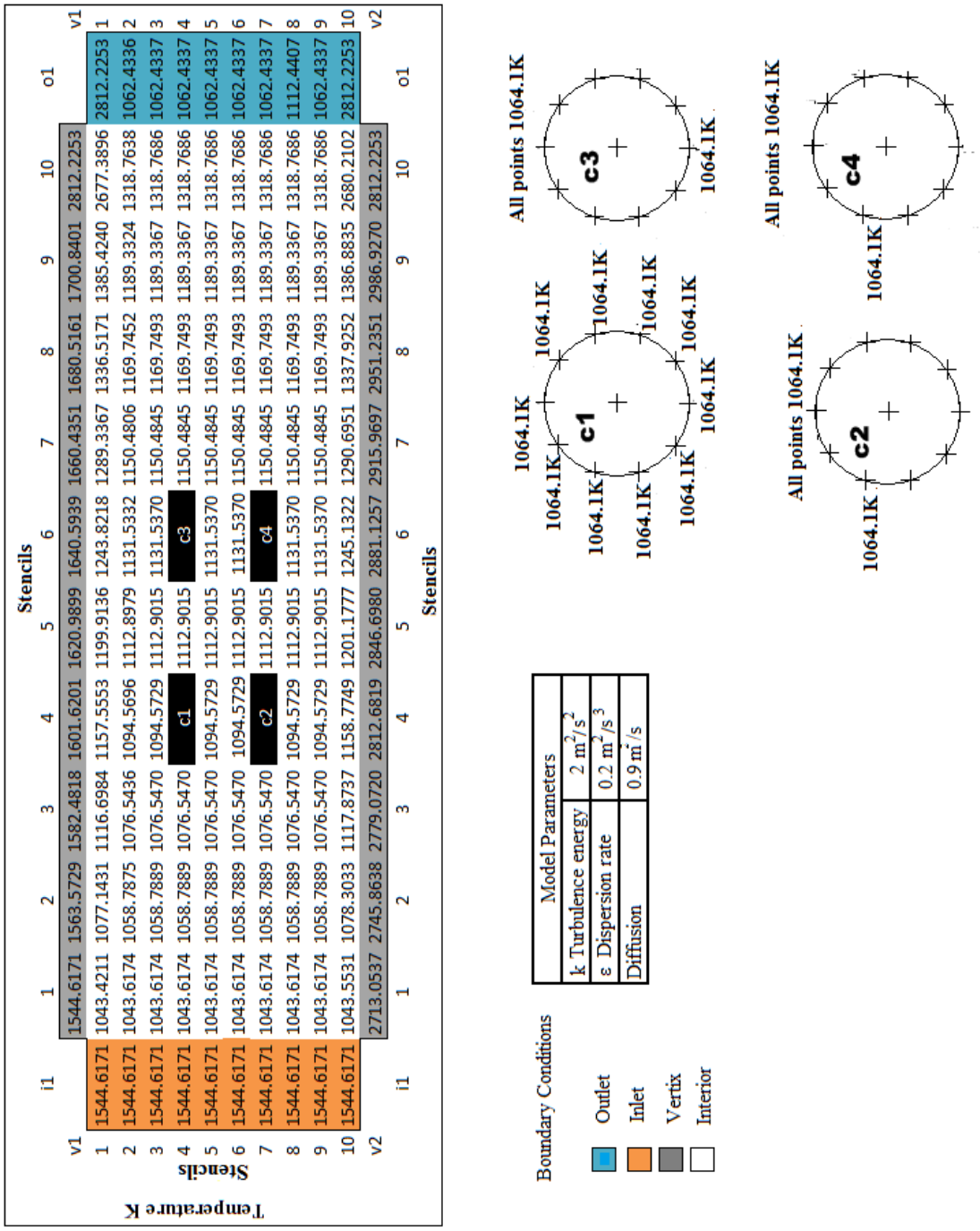

Figure 5-27. The partial temperature field across a PF combustor with 4 test tubes labelled c1, c2, c3 and c4 for a particles size of 1µm

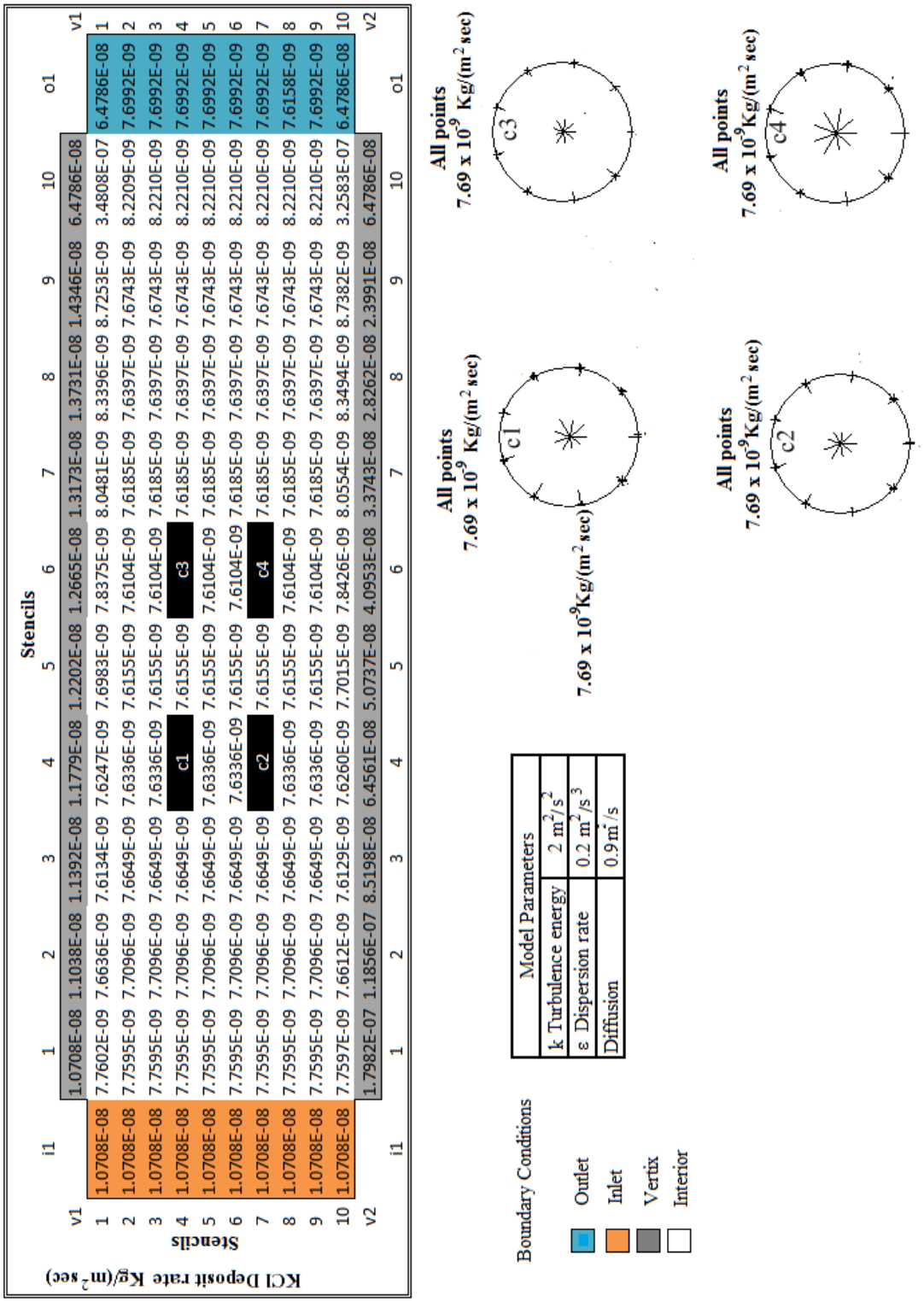

Figure 5-28. The homogeneous deposition rate field for one mole of KCl across the temperature field (Figure 5-27)

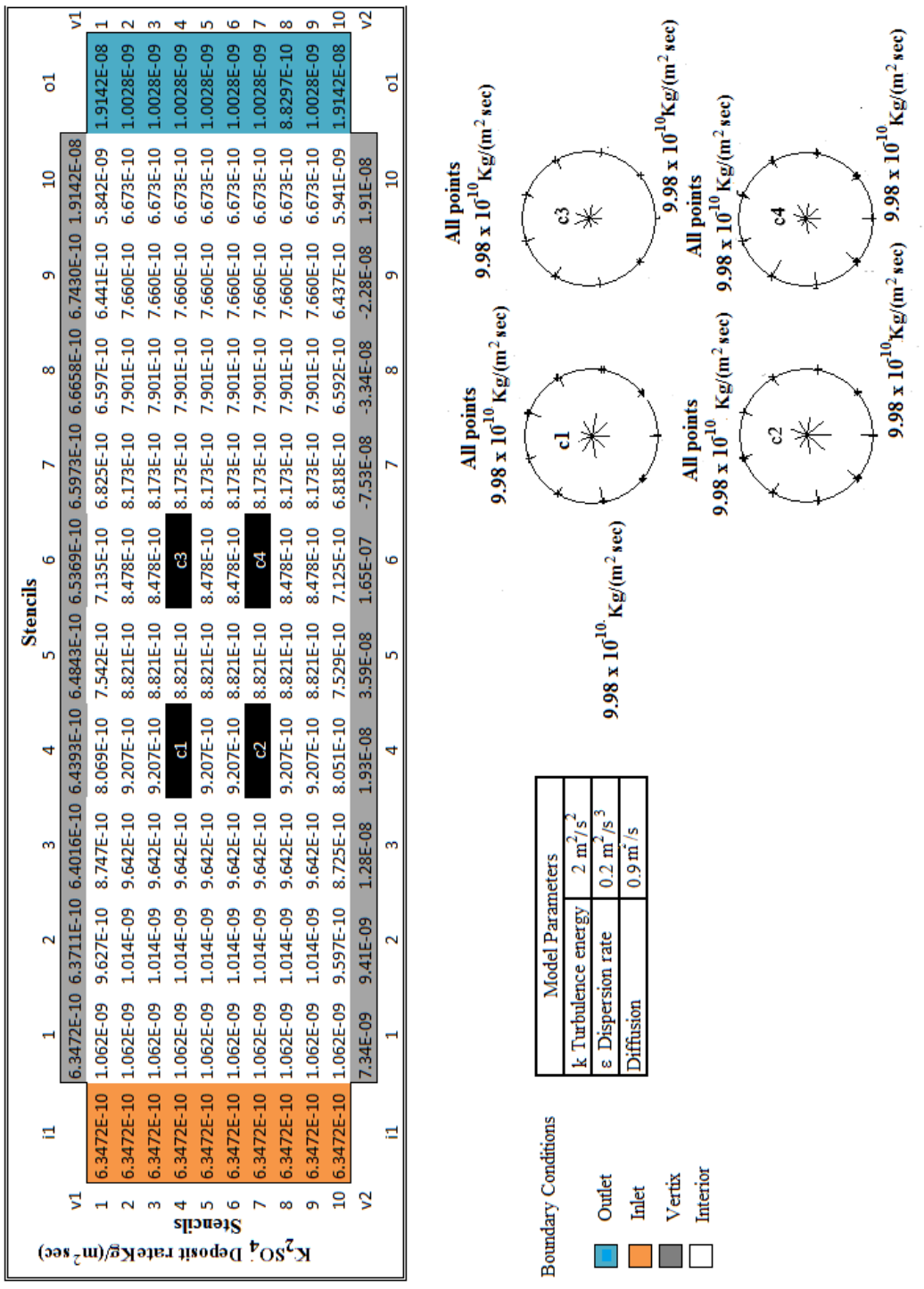

Figure 5-29. The homogeneous deposition rate field for one mole of K_2SO_4 across the temperature field (Figure 5-27)

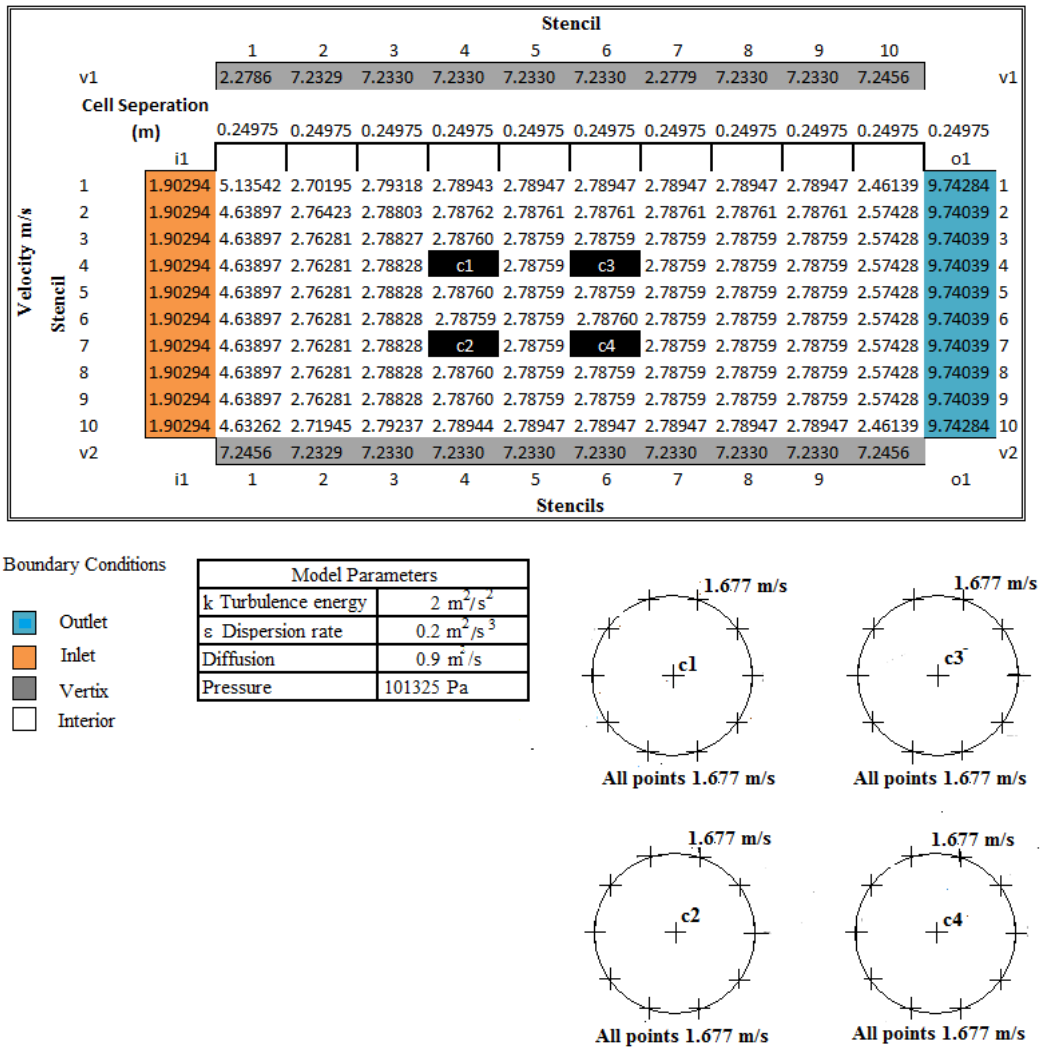

Figure 5-30.The peaks mean velocity between stencil cells for a particles size of 1µm.

- In Figure 5-30 the peak mean velocity between stencil cells which in this instance represents a measure of the kinetic energy per unit mass of a particle for a particles size of 1µm. The separation between each stencil cell in the passage of particles moving in the bulk gas stream is shown. The particle size entering the PF combustor is 1µm. From the separation data the 'time of flight' between each stencil cell is available to calculate the increase mass of from vapour deposition while the particles is in flight after entering the inlet.

To resolve the deposition problem, then a new application of particle theory is used to avoid the problem of scale resolution. The 'many particle theory' is frequently used in sub-atomic particle physics. As many particle theory it is scale independent that is adopted here.

An introduction into graph theory and many particles theory is included in Appendix D and Gross et. al provides a full description (Gross, et al., 1994). The Appendix D shows the foundations of many particles theory, based on the analysis of the energy within the dynamic system and not velocity of the bulk gas. The energy within the dynamic system in which the particles or vapours is solved by applying the Hamilton equation of motion.

Within the dynamic system particle and vapours are perturbed from a motion in a straight line or condense by external influences. These influences are the modelled as the expansion of the motion between two points in space in time t as,

$$\boldsymbol{X}(\mathrm{t}) = \mathbf{G_n}(\mathbf{x}, \acute{\mathbf{x}}) \tag{5-92}$$

in which a function $\mathbf{G_n}$ acts to move a particle between **x** and **x'.** To solve eq. (5-98) the function $\mathbf{G_n}$ expanded by using the polynomial expansion of $\mathbf{G_n}(\mathbf{x}, \acute{\mathbf{x}})$. This is achieved by applying a probability density function P

$$\mathbf{G}(\mathbf{X}, \mathbf{X}' : t, t') = \mathbf{P} \tag{5-93}$$

where under the influence of function **G,** the particle moves from **X** to **X**' between time t to t'. Consider a path of a single particle entering the top of the PF combustion it will move between mesh-free stencils and its tract will be defined as

$$\mathrm{G}(\mathbf{x}, \mathbf{x}') = \mathrm{G}_0(\boldsymbol{x}, \boldsymbol{x}') + \mathrm{G}_1(\boldsymbol{x}, \boldsymbol{x}') + \mathrm{G}_2(\boldsymbol{x}, \boldsymbol{x}') \ldots, \tag{5-94}$$

The particle will follow a number of possible tracts, one being that it will pass through without any interaction within the PF furnace. This path of $\mathrm{G}_0(\boldsymbol{x}, \boldsymbol{x}')$ is the free propagator. In the case of $\mathrm{G}_1(\boldsymbol{x}, \boldsymbol{x}')$ then particle will have one interaction and $\mathrm{G}_2(\boldsymbol{x}, \boldsymbol{x}')$ will have two interactions and so on.

The meaning of interaction is the action of some vapour deposition or particle deposition mechanism having an influence on the particle to move its course away free propagator. This interaction can also be that which change the particle size or shape. To combine all possible scenarios from algebraic form is complex, especially in the first one or two interactions;

therefore the solutions can be simplified by using graph theory. Graph theory is used to represent repeat algebraic forms that constitute the solutions of $\mathbf{G_n}(\mathbf{x}, \dot{\mathbf{x}})$. The graph symbols used to solve the problems of deposition on tubes are illustrated in Appendix D. Having devised the solution graphically the probability of an interaction can be obtained through the 'partial summation' of the motion of $\mathbf{G_n}(\mathbf{x}, \dot{\mathbf{x}})$. In the case of a single particles with three interaction of eq. (5-94) the partial summation is defined by a geometric progression series

$$\begin{aligned} \mathrm{G}(\boldsymbol{x}, \boldsymbol{x}') = \mathrm{G}_0(\boldsymbol{x}, \boldsymbol{x}') + \mathrm{G}_0(\boldsymbol{x}, \boldsymbol{x}')\mathrm{P(A)}\mathrm{G}_0(\boldsymbol{x}, \boldsymbol{x}')\frac{1}{1-\mathrm{P(A)}\mathrm{G}_0(\boldsymbol{x}_\mathrm{A}, \boldsymbol{x}'_\mathrm{A})} + \\ \mathrm{G}_1(\boldsymbol{x}, \boldsymbol{x}')\mathrm{P(A)}\mathrm{G}_1(\boldsymbol{x}, \boldsymbol{x}')\frac{1}{1-\mathrm{P(A)}\mathrm{G}_1(\boldsymbol{x}_\mathrm{A}, \boldsymbol{x}'_\mathrm{A})} + \\ \mathrm{G}_2(\boldsymbol{x}, \boldsymbol{x}')\mathrm{P(A)}\mathrm{G}_2(\boldsymbol{x}, \boldsymbol{x}')\frac{1}{1-\mathrm{P(A)}\mathrm{G}_2(\boldsymbol{x}_\mathrm{A}, \boldsymbol{x}'_\mathrm{A})} \cdots \end{aligned} \tag{5-95}$$

where P(A) is the probability that an interaction will affect the path of the particles or its 'time of flight'.

To complete the analysis of likelihood of a particle impact for one of the four tube, 'we' determined from the graph (see Appendix E for the interpretation of 'we' in graph theory) of a particle released from stencil in Figure 5-27 referenced as cell (Y:4, Z:1); on a path to impact one of the tubes labelled c1, c2, c3 or c4.

In this example illustrated in Figure 5-26 the probability of a particle moving to miss tube c2 is defined by the 68-95-99.7 rule. The values 68, 95 and 99.7 are the percentage standard deviation from the mean path based on the nominal distribution curves. This is the proportion of particles, which is the deviation from a straight path after meeting the mesh-free stencils at each diagram part $\mathbf{G_n}$. For this single particle then $P(A_n) = 0.68$, $P(A_{n+1}) = 0.95$ and $P(A_{n+2}) = 0.997$. Hence for the central route in Figure 5-31 involving only $P(A_n)$ terms, the probability of not impacting P(A) is

$$\mathbf{P(A)} = \left(\mathbf{1} - \mathbf{P}(\mathbf{A_{n+1}})\right)^{\mathbf{2}} \tag{5-96}$$

therefore

$$\mathbf{P}(\boldsymbol{A}) = (1 - 0.997)^2 \tag{5-97}$$

the probability of not impacting P(A) is

$$\mathrm{P}(\mathbf{A}) = 9 \times 10^{-6} \tag{5-98}$$

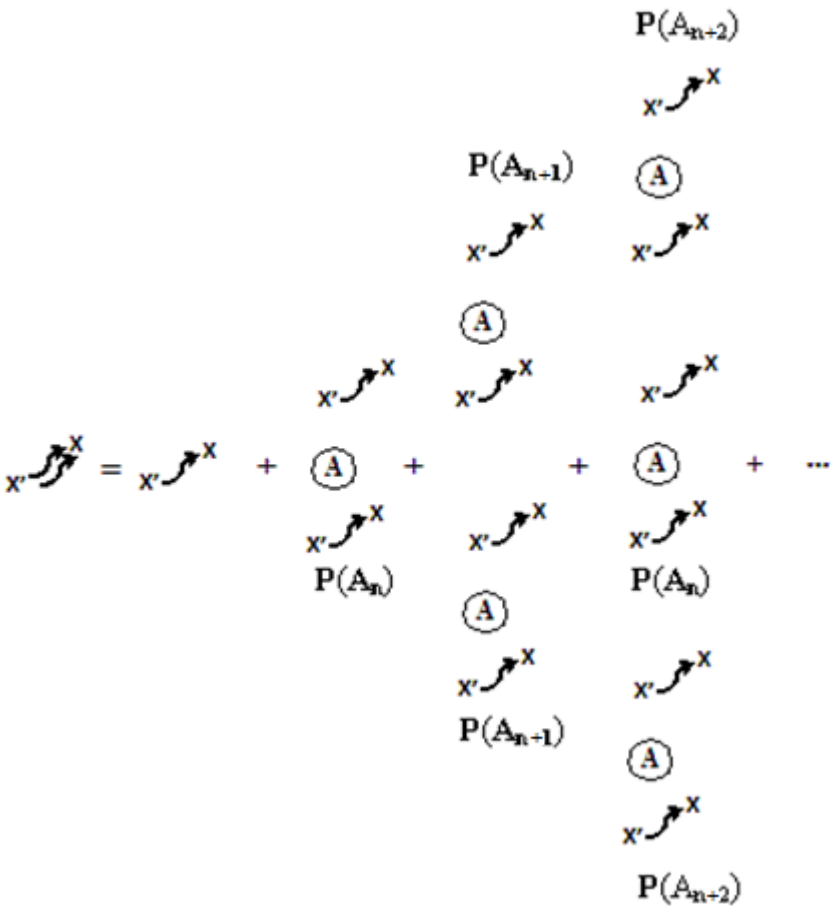

Figure 5-31. The probability density field of the impact of a char particles impacting tube c2 in Figure 5-26

The contribution from $P(A_{n+1})$ and $P(A_{n+2})$ is smaller but for completeness, the contribution that $P(A_{n+1})$ and $P(A_{n+2})$ make a value of

$$\mathbf{P(A)} = (\mathbf{1} - \mathbf{0.68})^{\mathbf{2}} + (\mathbf{1} - \mathbf{0.95})^{\mathbf{2}} \tag{5-99}$$

$$\boldsymbol{P}(\mathbf{A}) = \mathbf{0.00025}6$$

The contribution from $P(A_{n+1})$, $P(A_{n+2})$ and $P(A_{n+3})$ is

$$\mathbf{P(A)} = (\mathbf{1} - \mathbf{0.68})^{\mathbf{2}} + (\mathbf{1} - \mathbf{0.95})^{\mathbf{2}} + (\mathbf{1} - \mathbf{0.997})^{\mathbf{2}} \quad (5\text{-}100)$$

$$\boldsymbol{P}(\mathbf{A}) = \mathbf{0.104}9$$

The eq. (5-100) is called the 'standard case of impact' (SCI) in this thesis and is used to attribute the value for the contribution of other particles over the probability field.

The rules governing the use of graphs in this case allow impacts on any tube where the probability sums from of all contributions of $\mathbf{P}(\mathbf{A_{n!}})$ meets the following criteria

$$\mathbf{P}(\mathbf{A_{n!}}) < 10 \quad (5\text{-}101)$$

As an example if an arbitrary contribution from Brownian motion, turbophoresis and thermophoresis each have the probability density of

$$\boldsymbol{P}(\mathrm{A}_{n!})_{\mathrm{thermophoresis}} = 3 \quad (5\text{-}102)$$

$$\boldsymbol{P}(\boldsymbol{A_{n!!}})_{\mathrm{turbophoresis}} = 2$$

$$\mathbf{P}(\mathbf{A_{n!}})_{\mathrm{Brownian}} = 4$$

The total probability of a particle impacting is

$$\mathbf{P}(\mathbf{A}) = \left(\mathbf{P}(\mathbf{A_{n!}})_{\mathrm{Brownian}} + \mathbf{P}(\mathbf{A_{n!}})_{\mathrm{turbophoresis}} + \mathbf{P}(\mathbf{A_{n!}})_{\mathrm{thermophoresis}}\right) \times 0.1049$$

$$\mathbf{P}(\mathbf{A})\ (2{+}3{+}4)\ \mathrm{x}0.1049{=}0.9441 \quad (5\text{-}103)$$

Since the value of P**(A)** is less than 1 in eq. (5-103), this is a valid graph series.

A random walk is a mathematical formalisation of a trajectory that consists of taking successive random steps defined as $\mathbb{Z}$. For example, the path traced by a molecule as it travels in a liquid or a gas. In this model a random walk is a difficult approach to implement since the particle is not constant in mass. This defines a universal problem in the mathematics of random walk that is how many times will a random walk cross a boundary line (a change in mass or a change in state) if permitted to continue walking forever? For a simple random walk on $\mathbb{Z}$ will cross every point an infinite number of times. This result has many names: the *level-crossing phenomenon*, *recurrence* or the *gambler's ruin*. The reason for the last name is as follows: a gambler with a finite amount of money will always lose when playing *a fair game* against a bank with an infinite amount of money. The gambler's money will perform a random walk, it will reach zero at some point, and the game will be over.

In graph theory there is a theorem that can resolve this crisis in the use of random walk this is defines as:

Theorem: *a graph is transient if and only if the resistance between a point and infinity is finite. It is not important which point is chosen if the graph is connected.*

In other words, in a transient system, one only needs to overcome a finite resistance to get to infinity from any point. In a recurrent system, the resistance from any point to infinity is infinite.

For this reason graph theory is adopted to model the change of mass, the trajectory and bulk gas aerodynamics instability (i.e. turbulence and vorticity) properties

In quantum physics 'many particle theory' will operate successfully because the mass of the particles is small or zero. This is not the case in the modelling of deposition particles on superheater tubes. However, since the impacts do not impose direct damage and effectively land on the tube, insofar as this theory is concerned the mass scaling effect is considered negligible.

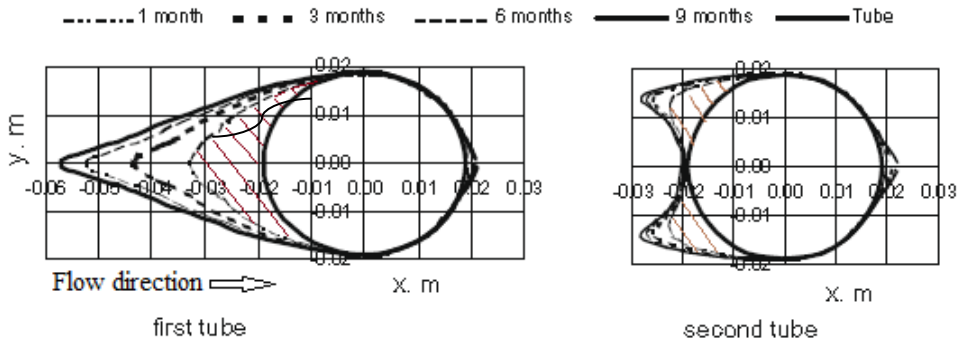

Figure 5-32. Rate of deposition two tubes inline such as c1 and c2 in Figure 5-26 (Tomeczek & Wacławiak, 2009)

The values of $\mathbf{P}(\mathbf{A_{n!}})_{\text{Brownian}}$, $\mathbf{P}(\mathbf{A_{n!}})_{\text{turbophoresis}}$, $\mathbf{P}(\mathbf{A_{n!}})_{\text{thermophoresis}}$ are determined by examine the outline of the deposition of a real test to determine the deposition rate of char. In the first instance, from published work (Tomeczek & Wacławiak, 2009), the areas of deposition are obtained. From the value area of the deposits after 1 month is 0.000456 m^2 (30 days) based on a measurement of the enclose shaded red area of the first tube. The second tube is positioned immediately behind the first and has an area of deposition of 0.000272 m^2 after 1 month. The inscribed area of deposition after 30 days that is hatched red in Figure 5-32

was estimated using Simpson's rule using the centre line as the base line and then subtracting the area of the semi-circle from the inscribed area.

As the flow regime of the bulk gas flow is laminar, the hypothesis of the referencing case is a potential flow, therefore the contribution of $\mathbf{P}(\mathbf{A_{n!}})_{\text{turbophoresis}}$ is very small.

For a particle of size 1μm assumes the particle is spherical and has a radius of 0.5μm and a surface area of $3.14159\text{x}10^{-12}\text{m}^2$. Taking the surface area and not the volume ensures that the coating of semi-solids (e.g. KCl, K2SO4, etc) is that adhesion mechanism more important than the ash particles, which otherwise would bounce off. The number of particles released that will impact the tube J_n onto the first layer of tubes c1 and c2 is

$$\text{Number of particle impacts } J_{\text{n=c1 or c2(}\,first\,\text{tube)}} = \frac{0.000456}{4\text{r}^2\pi} \tag{5-104}$$

$$\text{Number of particle impacts } = \frac{0.000456}{3.14159 \times 10^{-12}}$$

$$Number\ of\ particle \text{ impacts } J_{n=c1\ or\ c2} = 1.451 \times 10^{8}$$

Since the number of particles released and will deposited on tubes will be less those released at the inlet. The total number of particles released from the inlet J_{inlet} for the first tubes c1 or c2, will be

$$\text{Number of particle impacts } J_{n=c3 \text{ or } c4} = \frac{0.000272}{4\text{r}^2\pi} = \frac{0.000272}{3.14159 \times 10^{-12}} \tag{5-105}$$

$$\text{Number of particle impacts } J_{n=c3\ or\ c4} = 8.658 \times 10^{7}$$

and the second tubes c3 or c4 number of particles entering the PF combustor to impact tubes c3 or c4 is

$$J_{inlet} = \frac{J_{n=2nd\ tube}}{SCI} = \frac{8.658 \times 10^{7}}{0.1049} \approx 8.254 \times 10^{8} \tag{5-106}$$

For a particle of size 400μm will have a mean radius of 200μ and the surface area of $2.011\text{x}10^{-6}\text{m}^2$. The number of particles released that will impact the tube J_n onto the first layer of tubes c1 and c2, is

$$Number\ of\ Particles\ impacts\ J_{\text{n=first tube}} = \frac{0.000456}{4r^2\pi} = \frac{0.000456}{5.027 \times 10^{-7}} \qquad (5\text{-}107)$$
$$Number\ of\ particle\ impacts\ J_{n=first\ tube} = 908$$

The number of particles that will impact the tube will be less than the number released at the inlet. The total number of particles released from the inlet J_{inlet} to impact either tubes c1 or c2 will be

$$J_{\text{inlet}} = \frac{J_{n=first\ tube}}{\text{SCI}} = \frac{908}{0.1049} \approx 8648 \qquad (5\text{-}108)$$

The number of particles released that will impact the second tube in Figure 5-32 onto the first layer of tubes c3 and c3, is J_n

$$\text{Number of particle impacts } J_{n=c3\text{ or }c4} = \frac{0.000272}{4r^2\pi} = \frac{0.000272}{5.027 \times 10^{-7}} \qquad (5\text{-}109)$$
$$\text{Number of particle impacts } J_{\text{n=c3 or c4}} = 541$$

the number of particles released from inlet i1 (4,0) for 400μm particle is

$$J_{inlet} = \frac{\boldsymbol{J_{n=2nd\ tube}}}{SCI} = \frac{541}{0.1049} \approx 5159 \qquad (5\text{-}110)$$

This is the minimum number of particles required to fill the area hatched in red illustrated in Figure 5-32 they summing these values over four tubes will give the value of the number particles to enter the furnace. For four tubes then the minimum number of particles to enter the PF combustor will be

- For 1μm particles

$$J_{n=4\text{ tubes}} = (1.384 \times 10^9 + 8.254 \times 10^8) \times 2 = 4.4188 \times 10^9 \qquad (5\text{-}111)$$

- For 400μm particles

$$J_{\text{n=4 tubes}} = (8648 + 5159) \times 2 = 27614 \qquad (5\text{-}112)$$

The shape of the cone and associated bridging across tubes, for real superheater tubes, is illustrated in Figure 4-5 and is formed as the result of flow by the bulk gas over the tube. By changing the values of probability field function **P(A)** will increase number of particle landing

at a particular site on the tube. This changes proportional, the mass of deposits landing circumferentially on the tube, and to a limited extend, can recreate the cone and bridging of the tube.

The change in state of vapour within the PF combustor atmosphere either onto particles in flight (homogeneous) or directly into liquid state (heterogeneous) is resolve using graph theory with Mayer functions. This change of state has already been considered in chapter 4.

The intensive or non-intensive thermodynamic properties that participate in the change of state are supplied by the values calculated at the centre nodes of the mesh-free stencils.

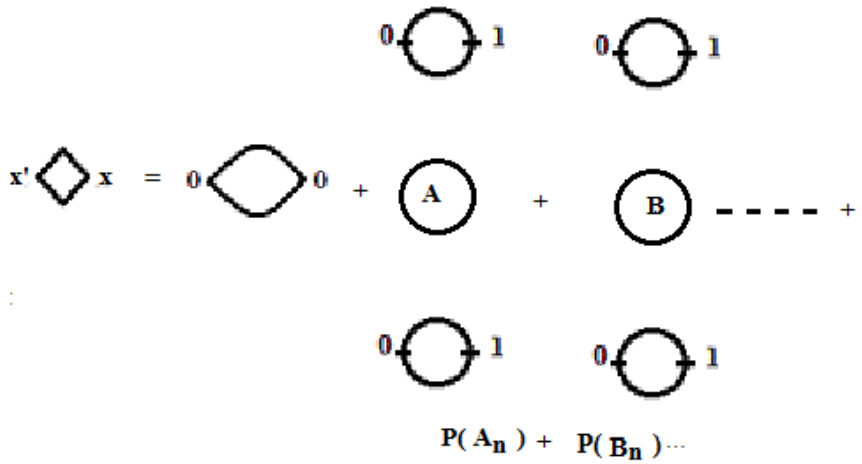

Figure 5-33. The graph of vapour molecule attracting to one or more particles in flight

The probability of vapour particles attracted to one or more free particles and the mass increase can be derived from identical perturbation theory using the graph theory symbols in Appendix D and are irreducibly connected graphs. The form for one or more particles (A, B... etc) with the probability of deposition of $P(A_n)$, $P(B_n)$.... etc can be defined in Figure 5-33

The probability of vapour deposition on particles can therefore be determined in a similar way to the methodology used to find the probability of impact of particles on tubes. The SCI approach is followed to proportion the conversion of vapour to the 'sticky' coating that binds particles together (Tomeczek & Wacławiak 2009). In undertaking this type of analysis the degree of heterogeneous deposition per particle can be quantified.

For the sake of simplicity, one mole of vapour molecules is present near a two particles A and B. Assuming that the pattern for vapour deposition is approximated by the nominal

distribution and using the 68-95-97.5 rule. The particles A and B will have the following pattern.

- The probability of one mole of vapour condensing on either A or B is $P_{A\cup B}$= (1-0.68).
- The probability of one mole of vapour on both A and B is $P_{A\cap B}$= (1-0.95) (homogeneous condensation).
- The probability of vapour not condensing on either particle A or B. as $P_{A\notin B}$= (1-0.997).

Relating these assumptions against a real particle – vapour interaction, then the assumption considers that the boundary between vapour condensation and vapour re-vaporising will operated in both directions. Some vapour might condense on a particle, but then, the change in the thermodynamic properties (including temperature) will vaporise again. But the probability of molecules of vapour condensing on a particle, if vapour is present, is much higher than the probability of vapour not condensing.

To calculate the increase in mass of a particle in flight, consider our particle is released from inlet stencil (4, 0) in the temperature table in Figure 5-27. The period of deposit growth was taken to be one month (30 days) to be consistent with published data.

The inlet i1 temperature is calculated with XMLSimple as 1544.617 K as shown in Figure 5-27. The initial particle mass is based on the density of silica at 2648 kg/m^3, assuming the particle is approximated to a sphere of the radius 0.5μm and disregarding a real particle might be hollow, then

$$mass = 2648 \times {}^{4}/_{3}\,\pi(0.5\times10^{-6})^3 \approx 1.38649\times10^{-15}$$

At this temperature, the vapour depositions are obtained from Figure 5-28 for KCl as 1.0708 x 10^{-8} kg/sec at inlet i1 and from Figure 5-29 for K_2SO_4 as 6.3472 x 10^{-10} kg/ sec. The 'time of flight' between the inlet i1 and the first stencil nodes is calculated from data in Figure 5-30 as the velocity divide by the stencil cell separation. The cell separation is 0.24975m and the velocity is 1.903 m/sec, hence the flight time is 0.1312 sec. The mass increase for KCl deposits is therefore;

$$1.38649\times10^{-15} + [(1.0708\times10^{-8}\times0.1312)\times0.32] = 4.49\times10^{-10}kg \qquad (5\text{-}113)$$

Table 5-18. Cumulative mass increase from heterogeneous deposition onto 1µm particle (i1 to c1 or c2)

Vapour (1 Mole)		Stencil				
		i1 (4, 0)	m4_F_N1 (4, 1)	m4_F_N2 (4, 2)	m4_F_N3 (4, 3)	c1 or c2
		'time of flight' (sec)				
		0.131245	0.053837427	0.090397	0.089571	0.23853
Mass (kg)	KCl	4.497×10^{-10}	6.342×10^{-10}	9.535×10^{-10}	1.28×10^{-09}	1.867×10^{-09}
	K_2S0_4	2.666×10^{-11}	3.759×10^{-11}	5.602×10^{-11}	7.437×10^{-11}	1.506×10^{-10}
Initial particle mass (kg)		1.386×10^{-15}			Mass totals (kg)	2.017×10^{-09}

Table 5-19. Cumulative mass increase from heterogeneous surface deposition onto a 1µm particle (i1 tubes c3 or c4)

Vapour (1 Mole)		Stencil						
		i1 (4, 0)	m4_F_N1 (4, 1)	m4_F_N2 (4, 2)	m4_F_N3 (4, 3)	m4_F_N4 (4, 4)	m4_F_N5 (4, 5)	c3 or c4
		'time of flight' (sec)						
		0.1312	0.0538	0.0904	0.0896	0.04395	8.96×10^{-02}	2.385×10^{-01}
Mass Kg	KCl	4.497×10^{-10}	5.833×10^{-10}	8.064×10^{-10}	1.026×10^{-10}	1.134×10^{-10}	1.352×10^{-10}	1.940×10^{-09}
	K_2S0_4	4.459×10^{-11}	6.288×10^{-11}	9.2196×10^{-11}	1.198×10^{-11}	1.339×10^{-11}	1.592×10^{-11}	2.2978×10^{-10}
Initial particle mass (kg)		1.386×10^{-15}				Mass totals (kg)		2.1698×10^{-09}

The increase in mass from inlet tube c1 because of heterogeneous deposition of KCl onto the released particle can be determined as the sample calculation in eq. (5-113). The mass of the particle will change with the addition of further heterogeneous deposition masses at each change in flight time. Therefore, the last mass of the particle and increase in KCl deposits are cumulatively added together at each subsequent stencil. The same approach can be repeated to determine the heterogeneous deposition of K_2SO_4 on the same released particle. The mass of KCl and K_2SO_4 heterogeneous deposits for particle realised from i1 to c1 or c2 is shown in Table 5-18.

At stencil m4_F_N4 in Table 5-19 the path of the particle meets a tube and so the 'time of flight' is determined by calculating the circumference of the tube as the cell separation and the circumferential velocity around the tube. The build up of deposits for 1μm particle released form i1 (4, 0) is tabulated in Table 5-18; these values can therefore determine the mass increase of the depositions over time.

Previously, an estimated for the number of particles of size 400μm that will fill the shaded area in the first tube in Figure 5-32 was 8648. The cumulative mass gain is based on the partial temperature field shown in Figure 5-34 and the homogeneous deposit rate for KCl and K_2SO_4 shown in Figure 5-35 and Figure 5-36. This cumulative mass gain is tabulated for the release of particles between i1 to c1 or c2 in Table 5-20

Table 5-20. The cumulative mass increase of a 400μm particle because of heterogeneous surface deposition (i1 to c1 or c2)

Vapour (1 Mole)		Stencil				
		i1 (4, 0)	m4_F_N1 (4, 1)	m4_F_N2 (4, 2)	m4_F_N3 (4, 3)	c1 or c2
		'time of flight' (sec)				
		0.10393	0.10928	0.13701	0.13771	0.09312
Mass (kg)	KCl	7.2769×10^{-08}	7.3036×10^{-08}	7.3370×10^{-08}	$7.3707 \times 10^{-08/}$	7.3934×10^{-08}
	K_2S0_4	7.2546×10^{-08}	7.2575×10^{-08}	7.2610×10^{-08}	7.2645×10^{-08}	7.5382×10^{-08}
Initial particle mass (kg)		7.252×10^{-08}			Mass totals (kg)	1.4932×10^{-07}

To consider tubes c3 and c4 then working from temperature field of Figure 5-28 with the deposit area of 0.000272 m^2 and a deposit period of one month. The calculation for the mass using the Peng-Robinson vapour model developed in Chapter 4 for heterogeneous condensates onto particles that impact on tubes c3 and c4. The number of particles released that will deposit onto the second tube from an inlet i1 was 5159. These particles enter the inlet and follow the shortest path from an inlet i1 to tubes c3 and c4.

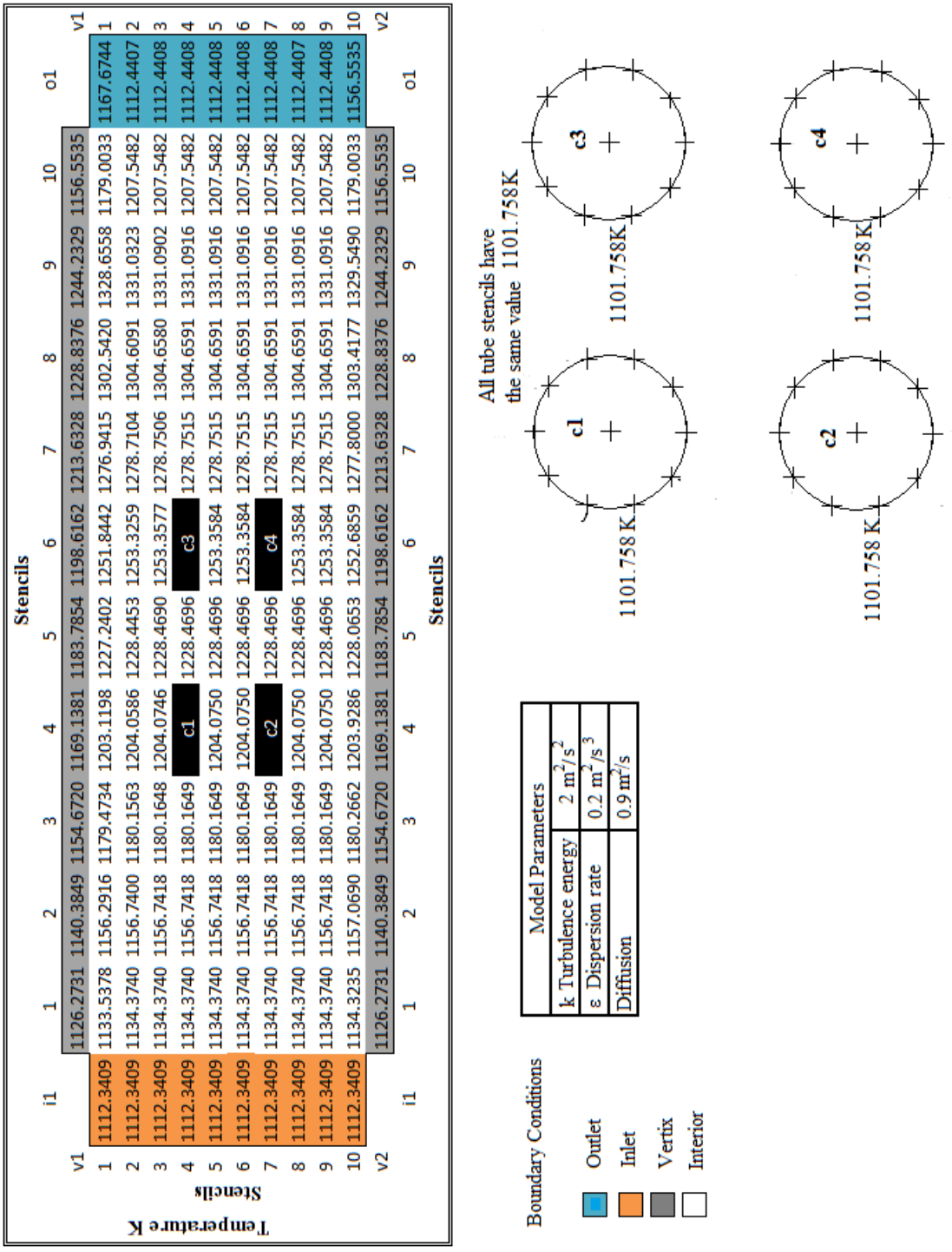
Temperature K
Stencils
Stencils
Stencils
i1
o1
v1
v2
1126.2731 1140.3849 1154.6720 1169.1381 1183.7854 1198.6162 1213.6328 1228.8376 1244.2329 1156.5535
1133.5378 1156.2916 1179.4734 1203.1198 1227.2402 1251.8442 1276.9415 1302.5420 1328.6558 1179.0033
1134.3740 1156.7400 1180.1563 1204.0586 1228.4453 1253.3259 1278.7104 1304.6091 1331.0323 1207.5482
1134.3740 1156.7418 1180.1648 1204.0746 1228.4690 1253.3577 1278.7506 1304.6580 1331.0902 1207.5482
1112.3409 c1 1228.4696 c3 1278.7515 1304.6591 1331.0916 1207.5482
1134.3740 1156.7418 1180.1649 1204.0750 1228.4696 1253.3584 1278.7515 1304.6591 1331.0916 1207.5482
1112.3409 c2 1228.4696 c4 1278.7515 1304.6591 1331.0916 1207.5482
1134.3740 1156.7418 1180.1649 1204.0750 1228.4696 1253.3584 1278.7515 1304.6591 1331.0916 1207.5482
1112.3409

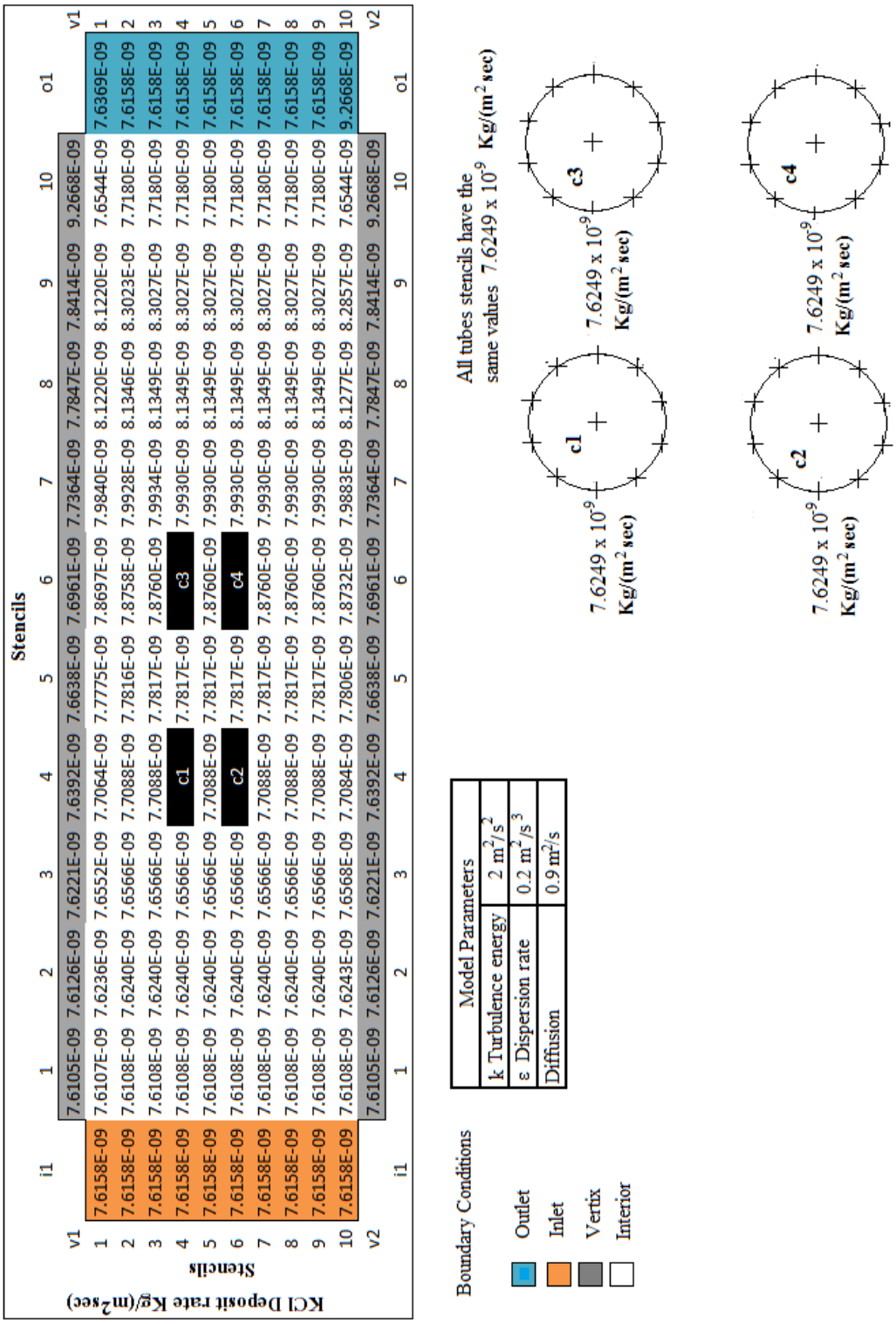

Figure 5-35. Homogeneous deposit rate of KCl with the partial temperature field for 400µm particles (Figure 5-34)

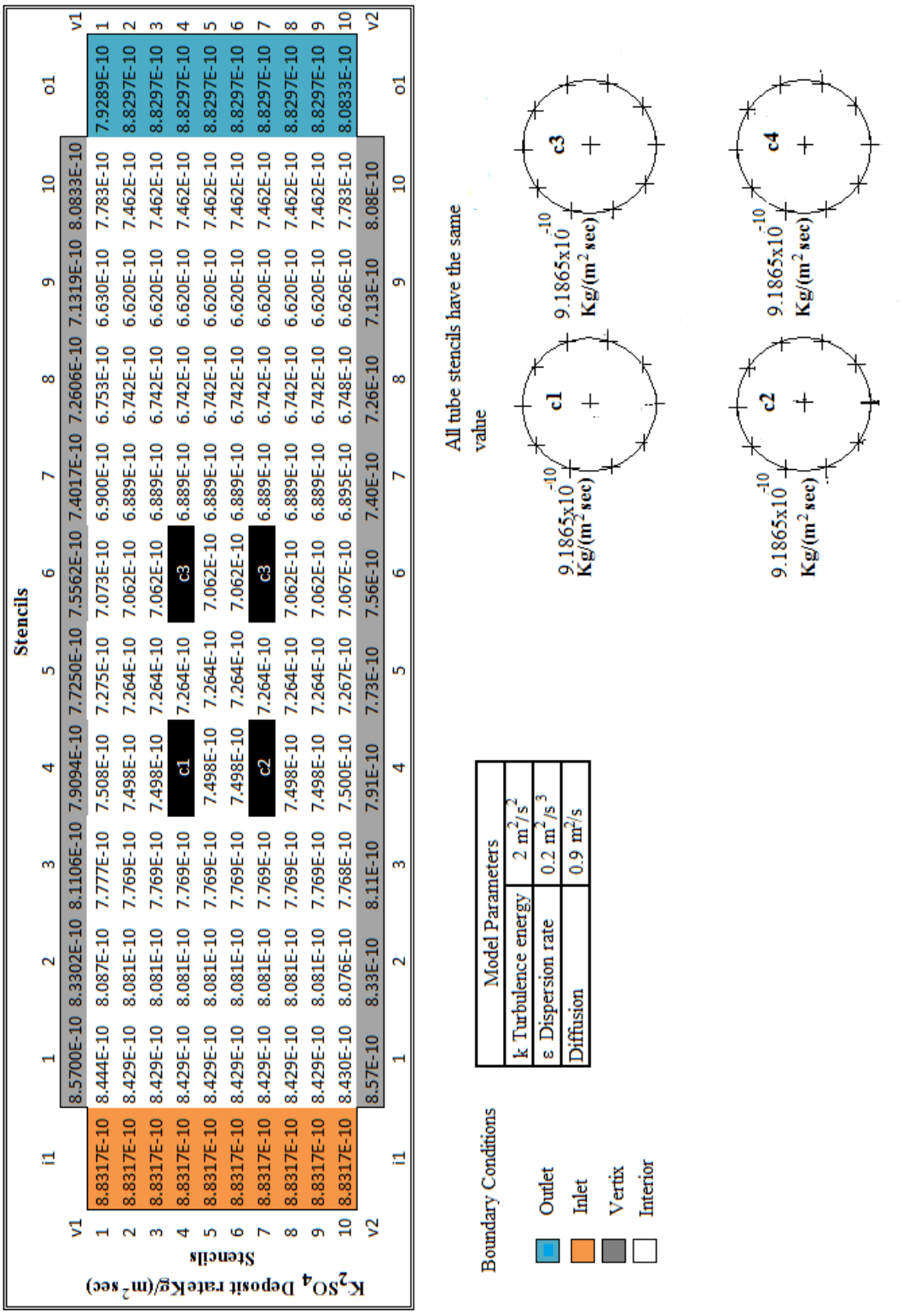

Figure 5-36. Homogeneous deposit rate for K_2SO_4 with the partial temperatures field for 400µm particles (Figure 5-34)

Stencils

		1	2	3	4	5	6	7	8	9	10	
	v1	2.2786	2.2779	2.2779	2.2779	2.2779	2.2779	2.2779	2.2779	2.2779	2.2719	v1
	Cell Seperation (m)	0.0000	0.24975	0.24975	0.24975	0.24975	0.24975	0.24975	0.24975	0.24975	0.24975	
	i1											o1
1	2.40317	1.80428	1.82700	1.82708	1.82708	1.82708	1.82708	1.82708	1.82708	1.82708	1.83325	2.40907	1
2	2.40317	2.28542	1.82292	1.81392	1.81379	1.81379	1.81379	1.81379	1.81379	1.81379	2.27907	2.40127	2
3	2.40317	2.28542	1.82287	1.81363	1.81350	1.81350	1.81350	1.81350	1.81350	1.81350	2.27907	2.40158	3
4	2.40317	2.28542	1.82287	1.81363	c1	1.81349	c3	1.81349	1.81349	1.81349	2.27907	2.40157	4
5	2.40317	2.28542	1.82287	1.81363	1.81349	1.81349	1.81349	1.81349	1.81349	1.81349	2.27907	2.40157	5
6	2.40317	2.28542	1.82287	1.81363	1.81349	1.81349	1.81349	1.81349	1.81349	1.81349	2.27907	2.40157	6
7	2.40317	2.28542	1.82287	1.81363	c2	1.81349	c4	1.81349	1.81349	1.81349	2.27907	2.40157	7
8	2.40317	2.28542	1.82287	1.81363	1.81349	1.81349	1.81349	1.81349	1.81349	1.81349	2.27907	2.40157	8
9	2.40317	2.28542	1.82287	1.81363	1.81349	1.81349	1.81349	1.81349	1.81349	1.81349	2.27907	2.40157	9
10	2.40317	1.82350	1.82709	1.82708	1.82708	1.82708	1.82708	1.82708	1.82708	1.82708	1.83325	2.40725	10
	v2	2.2340	2.2786	2.2779	2.2779	2.2779	2.2779	2.2779	2.2779	2.2779	2.2719		v2
		i1	1	2	3	4	5	6	7	8	9		o1

Velocity m/s

Stencils

Stencils

Boundary Conditions

Outlet
Inlet
Vertix
Interior

Model Parameters	
k Turbulence energy	2 m^2/s^2
ε Dispersion rate	0.2 m^2/s^3
Diffusion	0.9 m^2/s
Pressure	101325 Pa

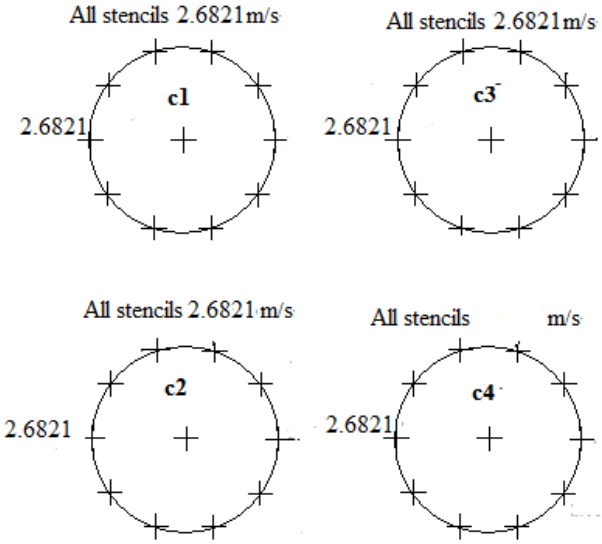

Figure 5-37. The peaks mean velocity between stencil cells for a particles size of 400µm.

The initial mass of a single 400µm particle and as for the 1µm particle disregarding that a real particle would likely be hollow, then

$$mass = 2648 \times {}^{4}/_{3}\,\pi(400 \times 10^{-6})^{3} \approx 7.252 \times 10^{-08}$$

The initial particle mass is therefore 7.252 x10^{-08} and the 'time of flight' between each stencil is calculate from the distance between each stencil and the velocity as shown in Figure 5-37. As for the example given for the 1µm particle where a tube c1 or c2 is encountered the circumferential distance and the velocity around the tube determines the 'time of flight'. The

cumulative mass increase of a 400μm particle from the inlet i1 (4, 0) and the tubes c3 or c4 is tabulated in Table 5-21.

Table 5-21. The cumulative mass increase of a 400μm particle because of heterogeneous surface deposition (i1 to c3 or c4)

Vapour (1 Mole)		Stencil						
		i1 (4, 0)	m4_F_N1 (4, 1)	m4_F_N2 (4, 2)	m4_F_N3 (4, 3)	c1 or c2	m4_F_N5 (4, 5)	c3 or c4
		Time of flight (sec)						
		0.10393	0.10928	0.13701	0.13771	0.02284	0.13772	0.09312
Mass	KCl	2.532 x10^{-10}	5.194 x10^{-10}	8.536 x10^{-10}	1.191 x10^{-09}	1.247 x10^{-09}	1.589 x10^{-09}	1.187 x10^{-09}
Kg	K_2S0_4	2.937 x 10^{-11}	5.885 x10^{-11}	9.428 x10^{-11}	1.285 x10^{-11}	1.352 x10^{-10}	1.672 x10^{-10}	1.946 x10^{-10}
Initial particle mass (kg)		7.252 x10^{-08}					Mass totals (kg)	2.015 x10^{-09}

To consider the homogeneous deposition the condensate into particles is derives from a phase change from a fix number of particles in a period of time. The characteristics of spontaneous formation of vapour is achieved by summing the deposition rate for 1 mole of KCl and 1 mole of K_2SO_4 between the inlet stencil and the tubes stencil c1 and c2 (also the inlet and c3 and c4). The period in which vapour is formed is assumed to be one second in an area of $1m^2$, while the probability of vapour forming and remaining stable using the 68-95-97.5 rule is defined as $P_{A\cap B}$= (1-0.95) or $P_{A\cap B}$= 0.05. The P_A particle destined for tubes c1 and c2 will involve a proportion of the Avogadro number 6.022 x 10^{23}. The exact number is not important but for completeness will be

$$6.022 \times 10^{23} \times 0.05 \approx 3.011^{23} \quad (5\text{-}114)$$

Therefore, 3.011 x 10^{23} KCl particles (P_A) plus the same number of K_2SO_4 particles (P_B) will undergo homogeneous condensation. For P_B particles involved in homogeneous condensation on particles destined for tubes c3 and c4, the number of particles involved is

$$3.011 \times 10^{23} \times 0.05 \approx 1.5055 \times 10^{23} \quad (5\text{-}115)$$

The mass of homogeneous deposition on to each of the tubes is determined by the rate of change from vapour to liquid in period defined as the 'time of flight' between each stencil along the path of the molecule. The path of the molecule is considered from the inlet to one of

the tubes. A sample calculation for the cumulative mass growth of homogenous between i1 (4, 0) and c1 or c2 for homogeneous formation vapour rates provide in Figure 5-28 and Figure 5-29 (1μm particle model) is tabulated in Table 5-22.

Table 5-22. The cumulative mass growth of homogeneous mass deposition from i1 to c1 or c2 (1μm model)

Vapour (1 Mole)	Stencil				
	i5 (4, 0)	m5_F_N1 (4, 1)	m5_F_N2 (4, 2)	m5_F_N3 (4, 3)	c1 or c2
	Time of flight (sec)				
	0.131245	0.053837	0.090397	0.089572	0.148961
KCl Mass (kg)	4.497×10^{-10}	1.334×10^{-10}	2.202×10^{-10}	2.197×10^{-10}	5.865×10^{-10}
K_2S0_4 Mass (kg)	2.666×10^{-11}	1.829×10^{-11}	2.932×10^{-11}	2.764×10^{-10}	7.521×10^{-09}
				Mass totals (kg)	6.617×10^{-09}

The sample calculation for the cumulative mass growth of homogenous between i1 (4, 0) and c3 or c4 is tabulated in Table 5-23 based on Figure 5-28 and Figure 5-29.

Table 5-23. The cumulative mass growth of homogeneous mass deposition from i1 to c3 or c4 (1μm model)

Vapour (1 Mole)		Stencil						
		i4 (4, 0)	m4_F_N1 (4, 1)	m4_F_N2 (4, 2)	m4_F_N3 (4, 3)	c1 or c2	m4_F_N3 (4, 5)	c3 or c4
		Time of flight (sec)						
		0.1312	0.0538	0.0904	0.0896	0.0896	8.9593×10^{-02}	1.4896×10^{-01}
Mass	KCl	4.967×10^{-10}	1.337×10^{-10}	2.230×10^{-10}	2.197×10^{-10}	8.997×10^{-10}	2.183×10^{-10}	5.820×10^{-10}
Kg	K_2S0_4	2.666×10^{-11}	1.829×10^{-11}	2.932×10^{-11}	2.764×10^{-11}	1.167×10^{-11}	2.529×10^{-11}	7.287×10^{-11}
							Mass totals (kg)	6.579×10^{-09}

The sum of homogenous mass deposition for both the numerical trails using 1μm particle and 400μm particles is summarised in Table 5-23.

Table 5-24. Mass of homogeneous formation that migrate into tubes c1, c2, c3 and c4 from stencils m1 to m10

Inlet Stencil	Particle Size	Homogeneous deposition mass (kg) P_A particle		Homogeneous deposition mass (kg) P_B particle	
		c1 , c2	c3, c4	c1 , c2	c3, c4
i1(4,0)	1μm	1.424×10^{-8}	1.843×10^{-8}	1.901×10^{-8}	2.015×10^{-8}
	400μm	1.6429×10^{-8}	2.0786×10^{-8}	2.8673×10^{-8}	3.6522×10^{-8}

In other experimental studies on herbaceous-grass and Miscanthus deposition rates on a single tube experiment are quoted as 9.6×10^{-05} kg/sec (1.9 mg/min) and 1.44×10^{-04} kg/sec (2.4 mg/min) respectively (Kaufmann et al. 2000). These rates are for all deposits that are both direct impact and 'sticky' (homogeneous and heterogeneous) deposits and the seed particles size were generally set between 200nm to 500nm. The collection efficiency of the combustor cited by Kaufmann, et al. is between 0.1 and 0.6, while the the collection efficency for eq. (5-113) and eq. (5-114) is 0.68. The expermantal work by Kaufmann, et al. was run for 2 hours and if scaled up to a real plant the deposit over 1 month (30 days) on a single tube would see the deposits grow to between 0.082 kg and 0.104 kg.

The area of the deposition on the tubes (Figure 5-33) is base on a particle size of 33μm (Tomeczek & Wacławiak, 2009). The assumption of these researcher (Tomeczek and Wacławiak) is that some particles bounce of the tube an they assess the probaility P as

$$P = S\dot{m}_c \qquad (5\text{-}116)$$

where S is 62 kg m^{-2} s^{-1} which is an estimate based on 9 months data on a single tube and $\dot{m}_c$ the mass flux of condensing salts (units are kg m^{-2} s^{-1}). The deposition rate given is 37 $x10^{-06}$ kg/$m^{-2}s^{-1}$ (37 mg/(m^{-2}sec)) for a particle size of 33μm in a test that lasts for 1 day. The area of

the deposit surface is not stated in the paper (Tomeczek & Wacławiak 2009) but from the deposited area in Figure 5-32 for the mass deposited on the first tube over 30 days, calculates as

$$\text{mass of deposits} \quad = 37 \times 10^{-6} \times 0.000456 \times (60 \times 60 \times 24 \times 30)\text{kg}$$

$$\text{mass of deposits}_{\text{(Tomeczek \& Wacławiak 2009)}} = 0.00437 \text{ kg}$$

As a comparison against Tomeczek & Wacławiak et al the data producted in this study is applied to find the toyal particle and deposision mass. For a single seed 1μm particle the deposition mass due to 'sticky' heterogeneous components from Table 5-18 was 2.017 x 10^{-09} kg, hence therefore the number of 1μm particles fills the first tube in Figure 5-32 was 1.451 x 10^{8}. The mass increase is

$$mass\ of\ impacting\ particles$$

$$= mass\ of\ single\ particle\ with\ deposits\ \times number\ of\ particle\ impacts$$

$$Total\ mass\ all\ \ impacting\ 1\mu m\ particles = 2.017 \times 10^{-9} \times 1.451 \times 10^{8}$$

$$Total\ mass\ all\ \ impacting\ 1\mu m\ particles \approx 0.29 \text{ kg}$$

For each particle size and final destination of particles

Table 5-25. A summary of final particle mass deposition tracking from i4 (4, 0)

	Number of particle impacts that stick		Total Mass particle impacts tracking from i4 (4, 0) kg	
	1μm	400μm	1μm	400μm
c1, c2	1.451 x 10^{8}	908	0.2566	0.00019
c3, c4	8.658 x 10^{7}	541	0.1647	0.00012

Up to now the deposition modelling has feature one inlet stream from i1_F_N4 to tubes c1, c2, c3 and c4 through stencils m4. By applying the same computational method it's possible to determine the mass deposits at specific points across all the tubes. Illustrated in Figure 5-38 and Figure 5-39 is a plot of the mass of deposited material from an initial 1μm particle.

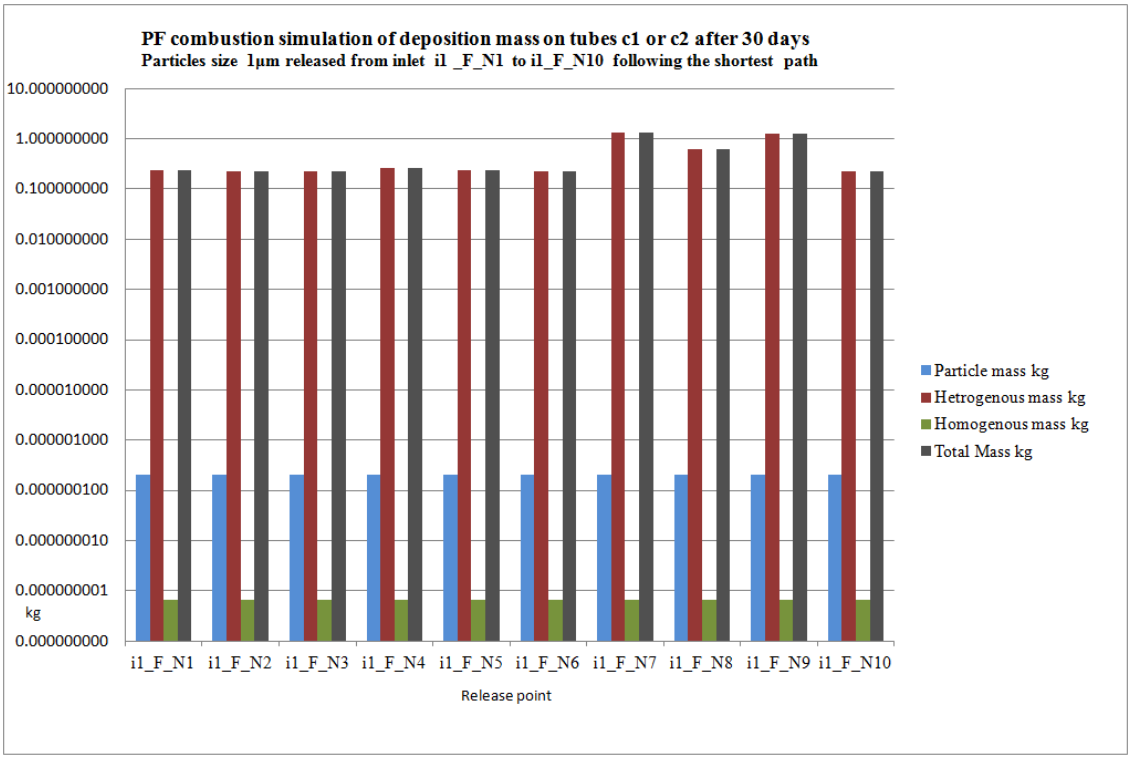

Figure 5-38. Plot of mass deposition on tubes c1 and c2 from a 1µm particle

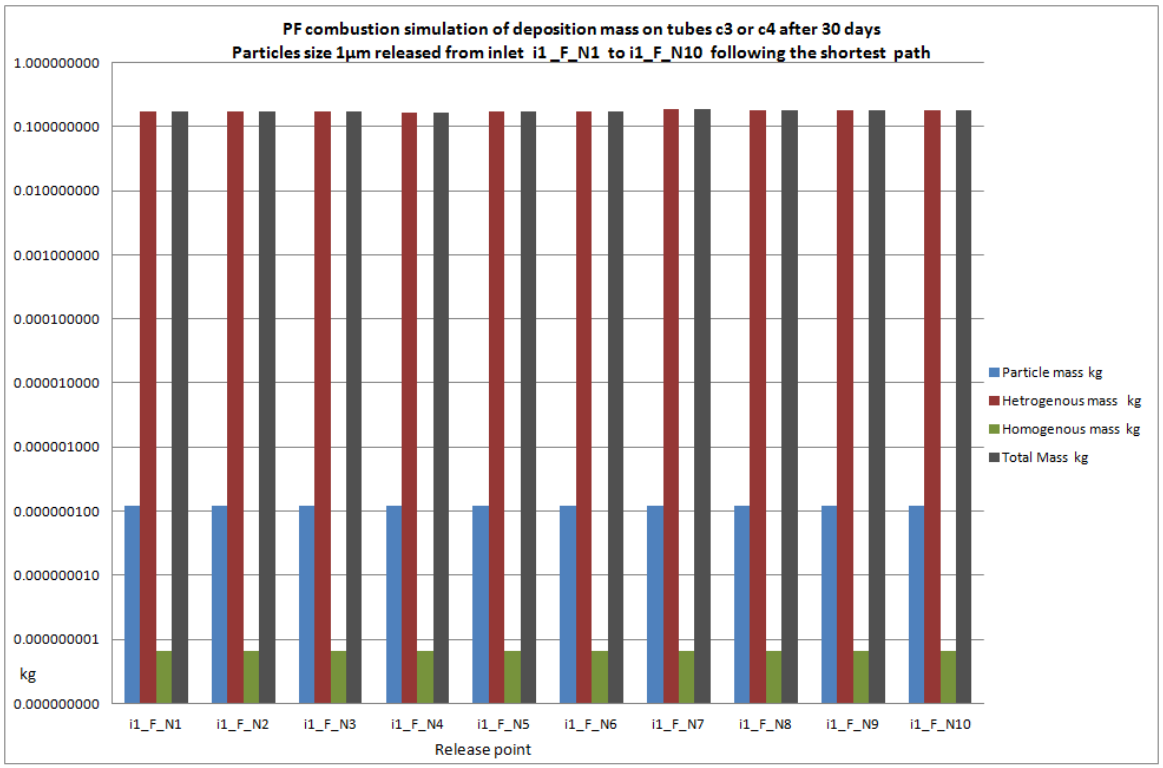

Figure 5-39. Plot of mass deposition on tubes c3 and c4 from a 1µm particle

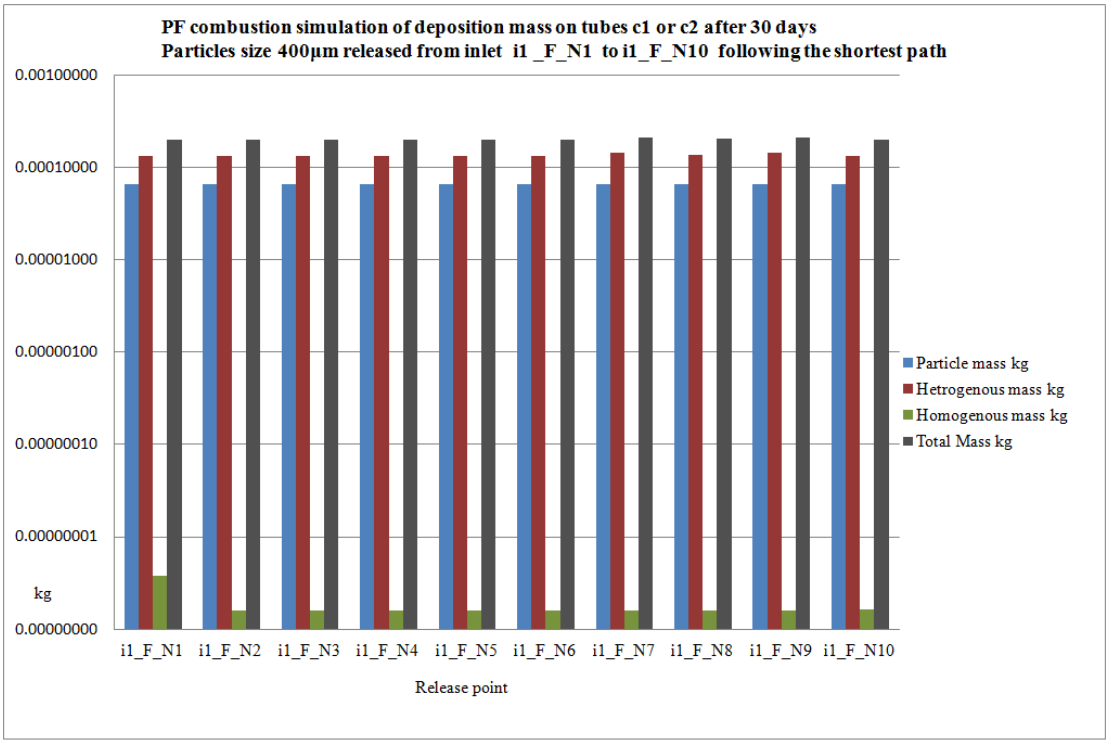

Figure 5-40. Plot of mass deposition on tubes c1 and c2 from a 400µm particle.

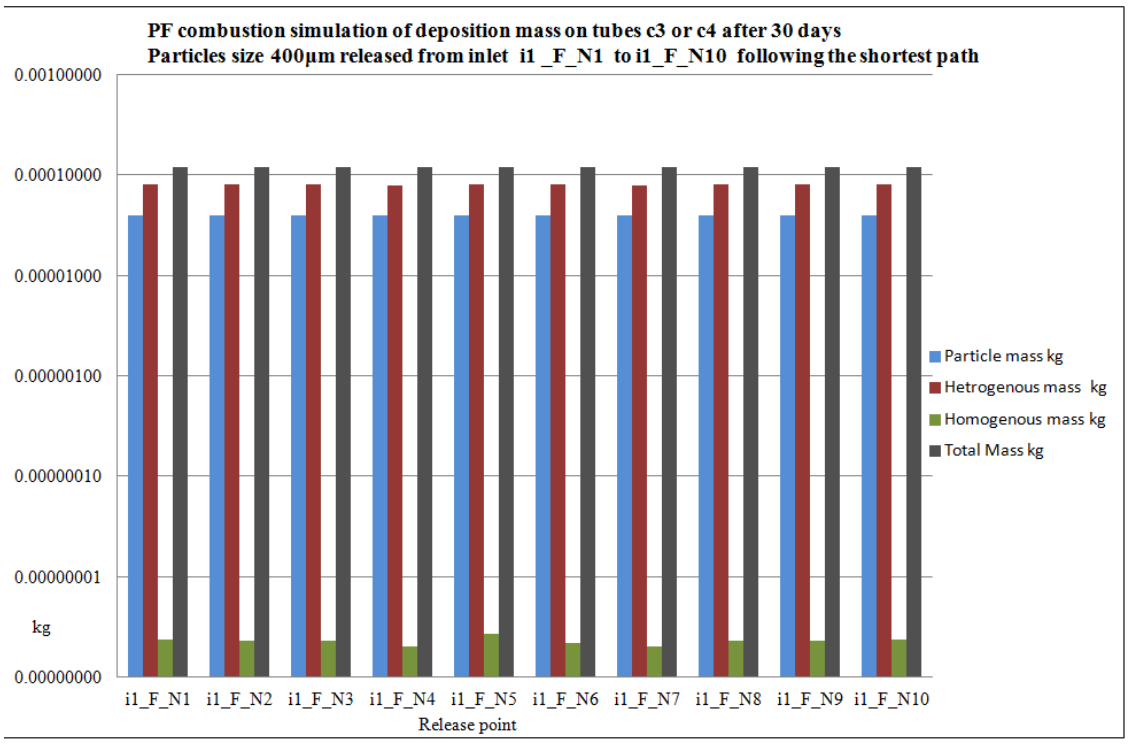

Figure 5-41. Plot of mass deposition on tubes c3 and c4 from a 400µm particle

Illustrated in Figure 5-40 and Figure 5-41 is a plot of the mass of deposited material from an initial 400μm particle.

Based on studies by Kaufmann, et al and also Tomeczek and Wacławiak these values are high for 1μm and low for 400μm particles sizes featured in these trails. For the 1μm size particles would be up to a range of 0.03kg but these trails yields approximately 13.19kg for all four tubes. The 400μm size particle would expect to yield a total mass of between 0.08kg and 0.108kg, but yeilds approximately 0.0063kg for all four tubes.

These estimates Kaufmann, et al and also Tomeczek and Wacławiak highlight the problem of extrapolating such data. Tomeczek and Wacławiak use a coal only combustion and the fuel used in these trial feature in this chapter has not been considered. These studies are based on short time periods, in some cases the combustion test ran for only 40 minutes and then extrapolating this data. Other facts which would contribute to the difference are

- no combustion of the particles is considered in this trail,
- density of the ash particles is not the same because beacue the trial is based on silica ash (Tomeczek and Wacławiak 2700 kg/m^3 and trail 2164 kg/m^3);
- Tomeczek and Wacławiak study had a larger number of flue gas components while the PF combustor trial had only two principle constituents;
- only two tubes feature in Tomeczek and Wacławiak study and Kaufmann, et al a single tube, this trial features four.

As a guide how much ash is produced in power plant, the Tarong Power Station comprises 4 x 350 MW coal-fired electricity generating units and produces 1.9 million tonnes of ash each year (Parsons Brinckerhoff Australia Pty Limited, 2005). Considering the quantities of ash product in a real power plant it's reasonable to assume that the mass predicted in the 1μm particle size model trial in this PF combustor simulation still has merit and is valid. If the 1μm particle size model trial was run for real, a substantial mass of deposits would leave the furnace because it hasn't adhere to the tube or if had adhered; would be dislodged by the air flow around the tube. In a power plant 80% of the ash from coal firing is carried as fly ash in sizes ranging between from 0.5μm to 100μm.

The power plant produces about 20% of total ash as bottom ash (sizes range from 75μm to 2mm) which gets collected in a hopper in the bottom of the plant. The 400μm particle model

produces smaller quantities (by mass) than the 1μm particle (although far from the 20% of the 1μm particle by mass). The PF combustor does replicated a difference in the final quantities of ash produced that is proportional to the initial size introduced into the PF combustor.

This completes the study of XMLSimple mesh-free finite difference solver. This also completes the calibration of PF combustor simulation and the data gain in these trails will allow a confidence in further simulation. These simulations have demonstrated the initial data sensitivity is to certain outputs such as what is correct initial particle numbers supplied to the PF combustor simulation inlet that outputs valid a mass of deposits. This optimization problem can be solved by using the data in Table 5-25 the problem is defined as;

'For a given number of 1μm particles deposition on tubes c1 or c2 will yield a mass of 'A' kg; therefore what is the approximate initial number of 400μm particles will yield 20% of same mass A.'

Solution: List the variables: let x denotes the mass of the 1μm particle; y denotes the mass of 400μm particle and C minimum number of 400 μm particles, h is the number of elements contributing to deposition that are independent of C, x and y. Objective: to minimize proportional quantity difference between 1μm particles to 400μm particles where the proportion of the mass between each particle size is 80/20.

C =: $\left(\frac{Particle\ size_x}{Particle\ size_y} \times \frac{x}{y} h\right)_{\lambda=1}$: Constraint: $x_{c1,c2} = 0.2566kg$. So $\frac{x}{.2} h = 0.05132 * h$:

From this constraint then $y = \frac{x}{.2} = 0.05132kg$:

Substituting this in the objective, we arrive to a function in a single variable $C = (0.2566kg \times 400\mu m \times 0.05132kg)h$ and x +: 1μm × 0.2566kg × $Particle\ size_y$:

Finding a minimum,

Then for h = 2, $C = (x +: \times y)h$. The initial 400μm particle number is estimated at 23181.

If the objective constrains contains more than two independent variables, Lagrange multipliers λ method can be helpful.

This optimization problem can be solved in MS Excel using the 'what if' optimization function.

The trial shows the importance of data that provides accurate particle numbers at the inlet. In the trial using 400μm particle, the numbers entering the can be increased to replicate the 80/20 split in the fly/bottom ash. It has been demonstrated that this model of a PF combustor can be adapted to predict ash deposition rates for any tube configuration. The accuracy of deposition rates could be enhanced by include a model that replicates the continued combustion process of a particle as it move through the combustor. How such calculations are undertaken in a MS Excel spreadsheet that are responsible for the post processing of XMLSimple data have been explained within the text of this chapter. An explanation in the discrepancies between mass of deposits produced in these trails and some peered review papers have been discussed.

5.9 Discussion on results of case studies

The results show that approach has a high degree of accuracy for a small number of stencils with the pressures being the most accuracy having a pressure ratio average of M_a of 1.000107 and standard deviation σ_A is 0.000694. Despite the limited number of mesh-free stencils, the mesh-free method was able to capture the basic flow properties and the temperature. This capability to reproduce intensive and non intensive thermodynamic flow patterns is proved by using a mathematical flow pattern called potential flow, which has calculated from an exact solution, a comparable set of data. On inspection of flow model using the mesh-free finite difference solver XMLSimple compared to the conformity map of Figure 5-7 the exhibits constant lines of both pressure and velocity in Table 5-9.

Turning to the discretization method, the solution of the Jacobi iteration scheme for solving the momentum and pressure correction equations converges within 3-5 iterations. The XMLSimple algorithm is resolved in 2 iterative cycles for the internal node and 3-5 iterative cycles for the constant pressure boundary conditions (Versteeg & Malalasekera 1995) such that p= 0.

However, for inlet, outlet and wall boundary conditions the iteration is stopped when there is no further improvement in the results usually after 10 cycles. Since the SVD algorithm is solved using LAPACK it is not known how many iterations are required to find the least

square minimisation solution. The software package, written in FORTRAN 2003 is very fast and is available to operate on a parallel processing scheme.

It has been shown that after starting in a corner of the geometric domain that is the PF combustor, (Figure 5-14 to Figure 5-17) the solution can rapidly advance. If the mesh-free solver XMLSimple were located on a parallel computer the process would start with one processor at stencil A1. Subsequently, two more processor will operate to solve with the value of stencil A1 to solve stencils B1 and A2. Further, the processing will operated on stencil A3, B2 and C1. This action continues throughout the domain and is very efficient.

To summarise

- 'Many particle theory' has been applied to distribute particles from the input to the tubes and to account for the effect of various patterns that particles and vapour undergo in flight from the inlet to the tube. A test case to find a benchmark in which to ensure that the particle probability distribution has been discussed.
- Review the deposition mass in Figure 5-38 to Figure 5-41 then the particles of size 1μm on c1 and c2 has a lower particle mass deposition to that of heterogeneous and homogeneous mass deposition as Figure 5-38 and Figure 5-39.
- While the particles of size 400μm has the converse, that is a proportionally lower heterogeneous and homogeneous mass deposition to particle as shown in Figure 5-40 and Figure 5-41 than for 1μm particles.
- The change in particle mass to heterogeneous and homogeneous deposition mass from the particle size 1μm to particle size 400μm indicates for smaller particle, 'sticky' heterogeneous and homogeneous deposits are going to be more significant constituents in the final coatings on tubes than particles.
- Larger 400μm particles will have more particles to 'sticky' deposits; these sticky deposits are KCl and K_2SO_4 which form a paste in real PF combustor plant.
- The behaviour of small particles to present fewer silica particle deposits than larger silica particles has been reported in the literature (Kaufmann et al. 2000). This is a significant achievement in this approach to model fireside deposition that has not been possible to model using CFD modelling in earlier chapters in this thesis.

- Particles sizes of 1μm and 400μm show a larger proportion of 'sticky' material (heterogeneous and homogeneous mass deposits combined) in the mass deposition on tubes c3 or c4 as Figure 5-39 and Figure 5-41.
- The bulk of particles are captured by tubes c1 or c2 and therefore tubes c3 and c4 receive most of the 'sticky' deposits.
- The conformation of higher KCl and K_2SO_4 deposit masses to solid particles masses in real deposition test is required by the experiments in this field. The shape of the deposits onto the tube as shown in Figure 5-32 is also the function of fluid flow behaviour and has been extensively reported by (Kaufmann et al. 2000; Tomeczek & Wacławiak 2009)
- Fluid flow behaviour of bridging across tubes and the final geometric shape of deposit growth can be derived by an extension of graph theory approach used in this chapter (McComb, 1994). Although fluid flow behaviour modelling of bridging across tube and deposit geometric form has not used graph theory approach but instead used Strouhal numbers.

The accuracy of mesh-free finite difference method has been examined and some benchmarks as to the performance of the solver that are not XMLSimple. These are:-

- It has been found that this solver is not fully capable to model the random behaviour of the physics in all cases.
- The method of solving the flow, vapour and particle deposition, based on Hamilton equations, has proved very capable to model deposition on tubes.
- However, since it requires that particles are thermodynamic entities the solutions of the Hamilton equations are complex.
- This complexity has been greatly simplified by the use of graph theory to replicate mathematical functions that are required.

Finally, a flow diagram of the stages in operation of XMLSimple is included in Figure 5-42.

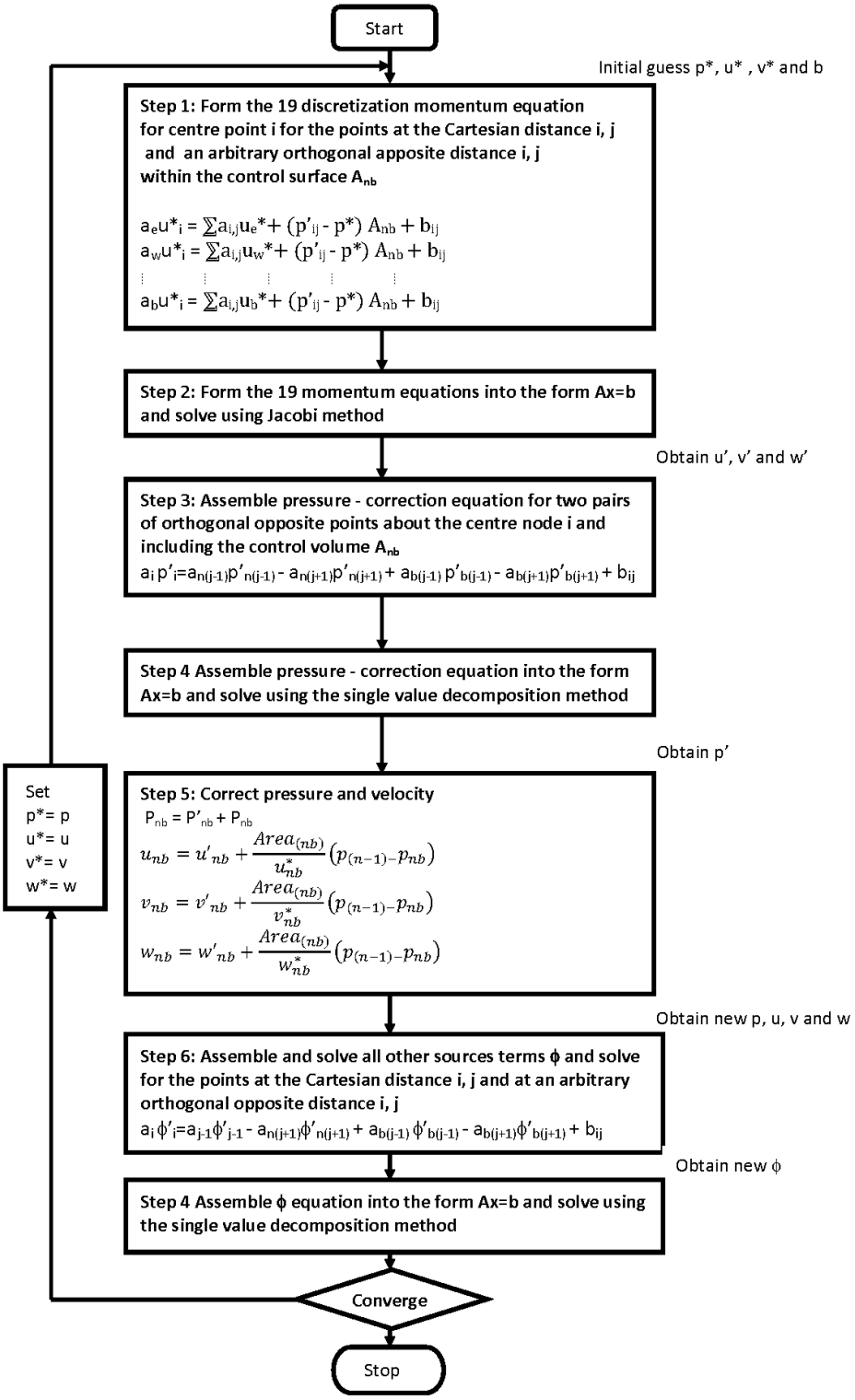

Figure 5-42. The SIMPLE algorithm with LSFD mesh-free method

6 Simulations

6.1 Generalisation of Cases

The case studies in this chapter are based on real geometry and combustion process, which require the following three key steps;

- to design a sampling scheme that defines the different sampling points on the boiler, as well as, the superheater tubes.
- to generate data for the sampling points based on the mesh-free method; and -
- to collect data from the sampling points, and then assemble the data into a structure format for processing.

The geometry (i.e. the boiler and the superheater tube) for the two case studies that will feature here is stored in a graphic form. From the original 'dxf' standard drawing format the drawing is formed into points labelled as p(n) from the top left hand corner of the draw to the bottom right hand corner. All points are denoted as 'p(n)', where n=1, 2, 3, etc. The user picks the points and regards them as vertex (horizontal or vertical boundaries of the furnace).

In these two cases, within this thesis, the following notation applies:

- v(n): n vertex
- i(n): n gas flow inlets
- o(n): n gas flow outlets
- m(n): n moving particles
- c(n): n tubes.

The user declares the number of moving particles appropriate to domain dimensions. These moving particles 'm(n)' will represent the particles at either molecular level or a macroscopic size of combustion products. The tubes are numbered 'c(n)' in the order it is loaded from the drawing.

The geometry is split into component parts but the defined vertices, inlets and outlets items of their point structure hold their interrelationship. For example, a closed structure representing a pipe combustor might be mapped as two vertexes v44 and v45 with the inlet i1 and outlet o1 and having one cylindrical tube c1. More specifically, for example [i1[p88,p90]] means i1 is linked to p88 and p90. The completed decomposition mapping as illustrated in Figure 6-1

show the operations required split the domain into a parametric form. The solution is completed by reassembling the mapping to the original shapes. This enables multiprocessor computation of the problem, so that the appropriate boundary conditions are passed to the instance of the solver active any mesh-free solver operating on a particular processor.

Each element is a reference in the XML plot file with all the properties of pressure, temperature, velocity and position assign to a XMLs node reference code (c1_F_N1). The code is composed of the node referencing the parametric label, for example (c1_F_N1), indicates the particle is fixed or (m1_M_N1) suggesting the particle is moving. The moving particles mesh-free elements represent particles of ash, gas or molecular.

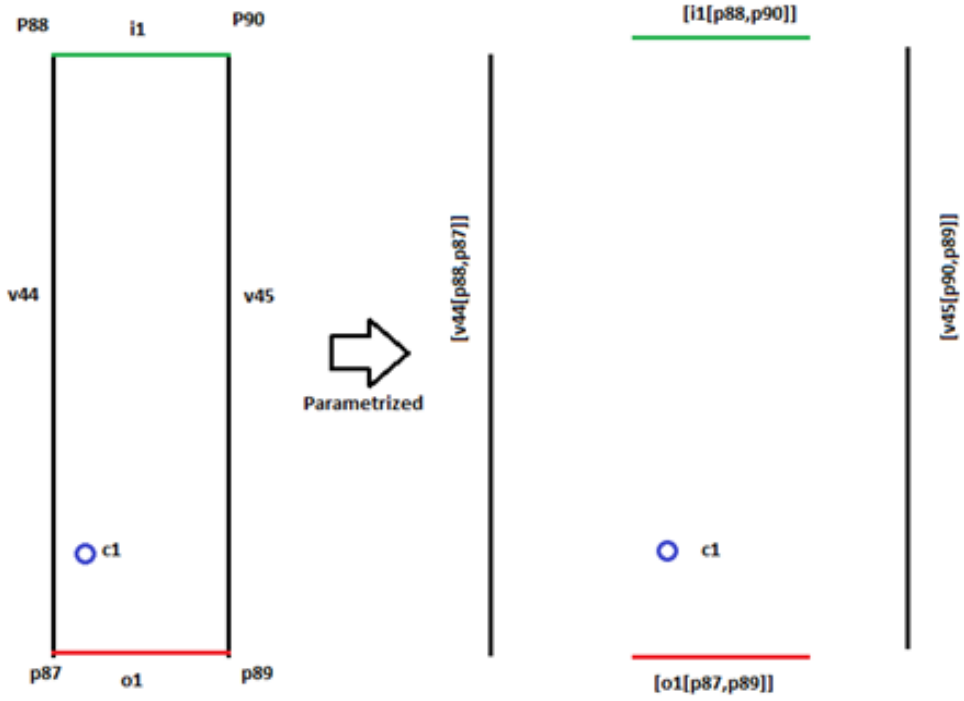

Figure 6-1. Parametric decomposition of pipe furnace (left) into model elements (right)

Mapping of data can be the most important of any model and ease of access and logical structure is vital. To this aim, XML tree format is utilised to enable the data set to be accessible to all the sub-models.

Figure 6-1 includes various probe configurations. These are the types of probe configurations used with discrete particle sizes while burning El Cerrejon coal and biomass in the real pilot plant PF combustor at Cranfield University. The tests in the real PF combustor are used to determine deposit composition.

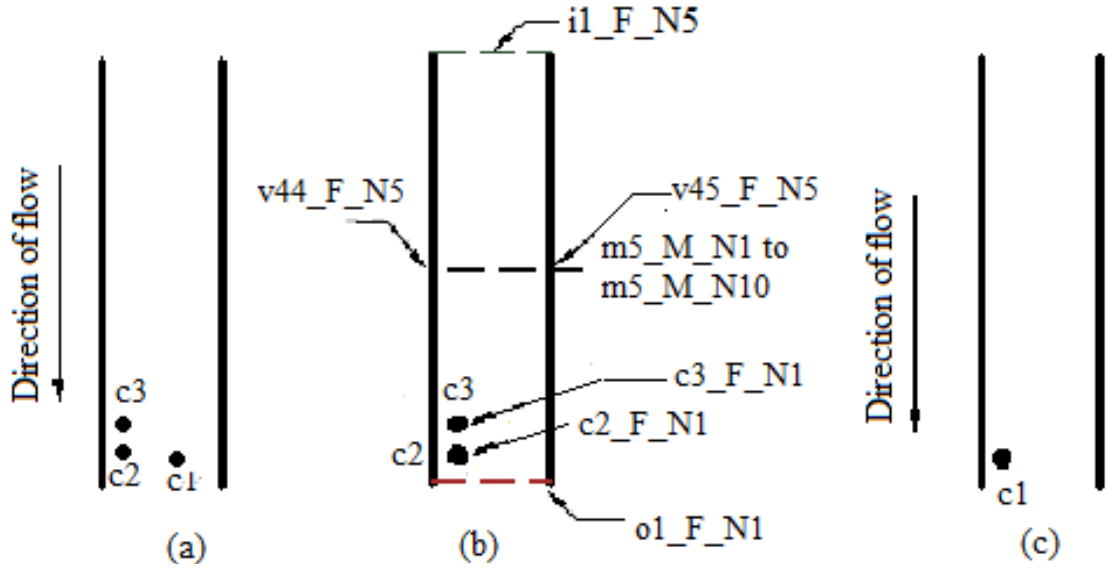

Figure 6-2. Probe configuration within the PF Combustor pilot rig

There are four tree structures that map the representative form of the furnace (as illustrated in Figure 6-3). By using XML data structure data trees and the attendant attributes, holding the model properties, are easily accessed. The solver is written in FORTRAN 2003 using the LAPACK numerical algorithm library, while the GUI and XML processing is coded with Microsoft© Visual Basic 2008

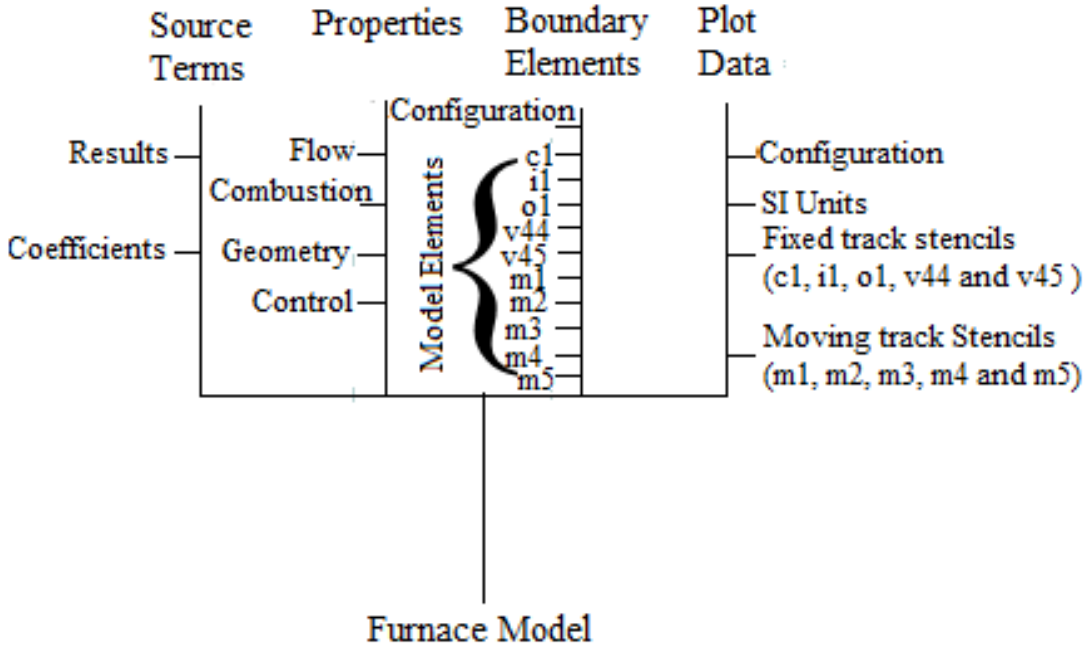

Figure 6-3. Model deconstruction into XML data.

6.2 Case study I: Cranfield University Combustor for El Cerrejon coal

The first test with this model is to determine the track of particles from the combustion of a low rank coal through the pipe furnace used at Cranfield University and illustrated in Figure 5-1. The initial condition for Case I numerical simulation is included in Appendix H. With this model it will be possible to predict the mass of both homogenous and heterogeneous vapours, which deposits on particles. The configurations used for these numerical tests illustrated in Figure 3-3. The test is designed to determine the total mass that will remain on a single tube after 30 days and will show what is predominating mechanism forming deposition on tubes. At the sampling points the mesh-free elements solve the thermodynamic properties, and then the thermodynamic properties are combined with the vapour deposition model described in Chapter 4.

The output data set from the mesh-free solver (e.g. direction particles move, the temperature and pressure around the particle) provides the input data set used to operate the vapour deposition model. Test results from literature show that deposit thickness for coal combustion varies from 0.02μm to 0.31μm after 30 days on new tubes (Wibberley & Wall 1982). In this case study, a deposit thickness of 0.14μm was chosen.

The initial particle sizes for this simulation are set to 50μm. In the literature, it is reported that coal particulate sizes ranges from 40μm to 150μm (Tomeczek 1994).

Since the coal combustion does not release the same quantities of alkali as biomass coal co-firing, the mathematical relationship between the numbers of particles that impact a tube needs to be updated. The number particles of which will statistically impact the tube with a given surface deposit thickness is given by

$$mean\ number\ of\ particles\ impact = \left(\frac{surface\ deposit\ depth}{(Particle\ size * 0.5)^2 \pi}\right) \times \frac{1}{0.1049} \qquad (6\text{-}1)$$

The combustion method is developed without turbulent flow when k and ε are set to zero. With no turbulent flow, the simulation will show the combustion products behaving as a kinetic combustion reaction.

The particles are released from inlet i1_N1 to inlet i1_N10 (coloured sand) and Figure 6-6 to Figure 6-9 illustrate the results.

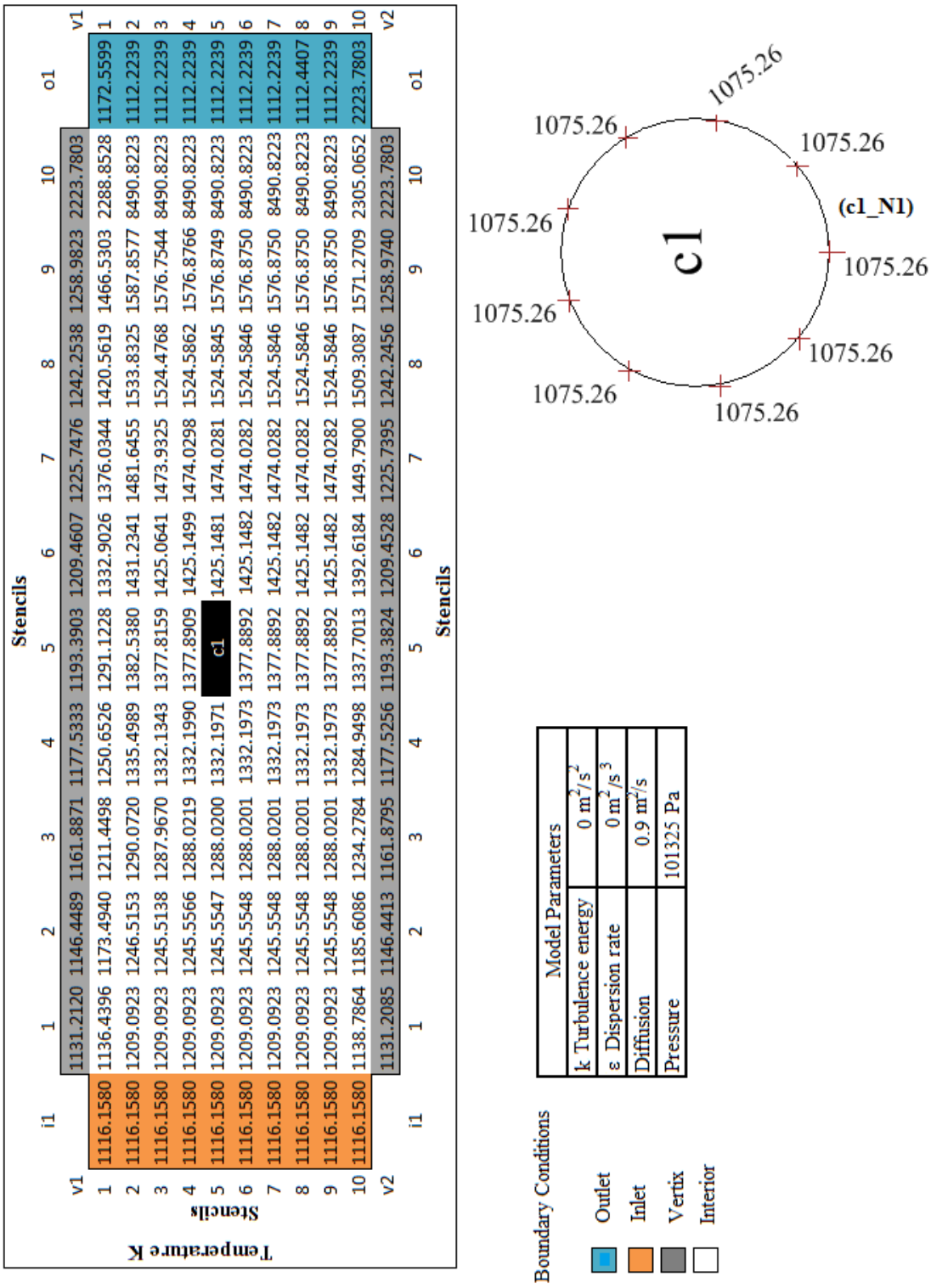

Figure 6-4. Partial temperature field of 50µm coal particle under kinetic combustion conditions (k = 0, ε = 0)

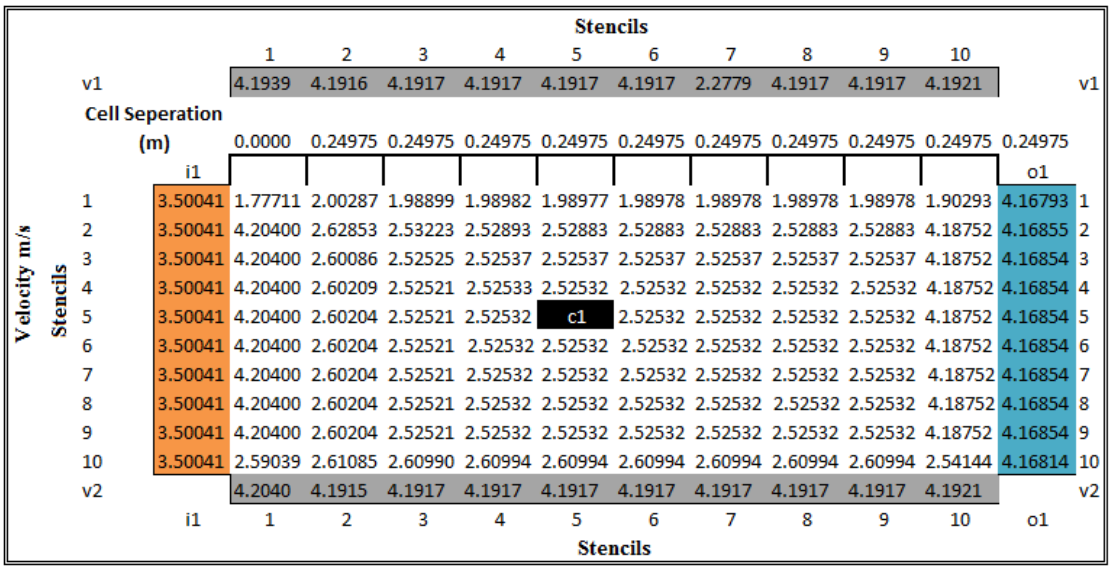

Stencils	1	2	3	4	5	6	7	8	9	10	
v1	4.1939	4.1916	4.1917	4.1917	4.1917	4.1917	2.2779	4.1917	4.1917	4.1921	v1
Cell Seperation (m)	0.0000	0.24975	0.24975	0.24975	0.24975	0.24975	0.24975	0.24975	0.24975	0.24975	0.24975
i1											o1
1	3.50041	1.77711	2.00287	1.98899	1.98982	1.98977	1.98978	1.98978	1.98978	1.98978	1.90293	4.16793	1
2	3.50041	4.20400	2.62853	2.53223	2.52893	2.52883	2.52883	2.52883	2.52883	2.52883	4.18752	4.16855	2
3	3.50041	4.20400	2.60086	2.52525	2.52537	2.52537	2.52537	2.52537	2.52537	2.52537	4.18752	4.16854	3
4	3.50041	4.20400	2.60209	2.52521	2.52533	2.52532	2.52532	2.52532	2.52532	2.52532	4.18752	4.16854	4
5	3.50041	4.20400	2.60204	2.52521	2.52532	c1	2.52532	2.52532	2.52532	2.52532	4.18752	4.16854	5
6	3.50041	4.20400	2.60204	2.52521	2.52532	2.52532	2.52532	2.52532	2.52532	2.52532	4.18752	4.16854	6
7	3.50041	4.20400	2.60204	2.52521	2.52532	2.52532	2.52532	2.52532	2.52532	2.52532	4.18752	4.16854	7
8	3.50041	4.20400	2.60204	2.52521	2.52532	2.52532	2.52532	2.52532	2.52532	2.52532	4.18752	4.16854	8
9	3.50041	4.20400	2.60204	2.52521	2.52532	2.52532	2.52532	2.52532	2.52532	2.52532	4.18752	4.16854	9
10	3.50041	2.59039	2.61085	2.60990	2.60994	2.60994	2.60994	2.60994	2.60994	2.60994	2.54144	4.16814	10
v2		4.2040	4.1915	4.1917	4.1917	4.1917	4.1917	4.1917	4.1917	4.1921			v2
	i1	1	2	3	4	5	6	7	8	9	10	o1	

Velocity m/s

Stencils

Boundary Conditions

- Outlet
- Inlet
- Vertix
- Interior

Model Parameters	
k Turbulence energy	0 m^2/s^2
ε Dispersion rate	0 m^2/s^3
Diffusion	0.9m^2/s
Pressure	101325 Pa

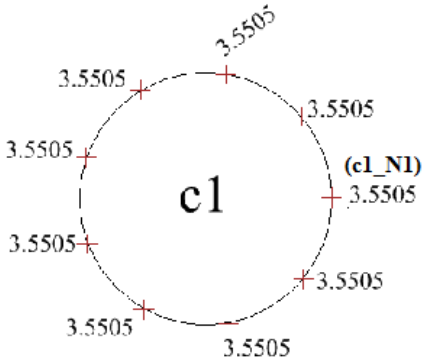

Figure 6-5. Partial velocity field for a 50 µm coal particle under kinetic combustion conditions (k = 0, ε = 0)

The previous examples in Chapter 5 have formed a complete Hilbert Spaces where all the dimensions are specified to a three dimensional Euclidean solution of the vector algebra of the particle position. In applying a combustion model, an infinite dimension is included into the vector algebra at the boundary in this project are virtual temperatures and when applied to the Peng-Robinson homogenous deposition models. These produce KCl and K_2SO_4 rate homogenous phase changes that are higher than the surrounding rate change from gas to vapour phase. These boundary effects manifests itself with a break out from the norm, for example, in Figure 6-4 the temperature at one tube stencil o1_N1 is recorded as 2223.78K while all other o1 stencils are at a temperature of 1172.59K.

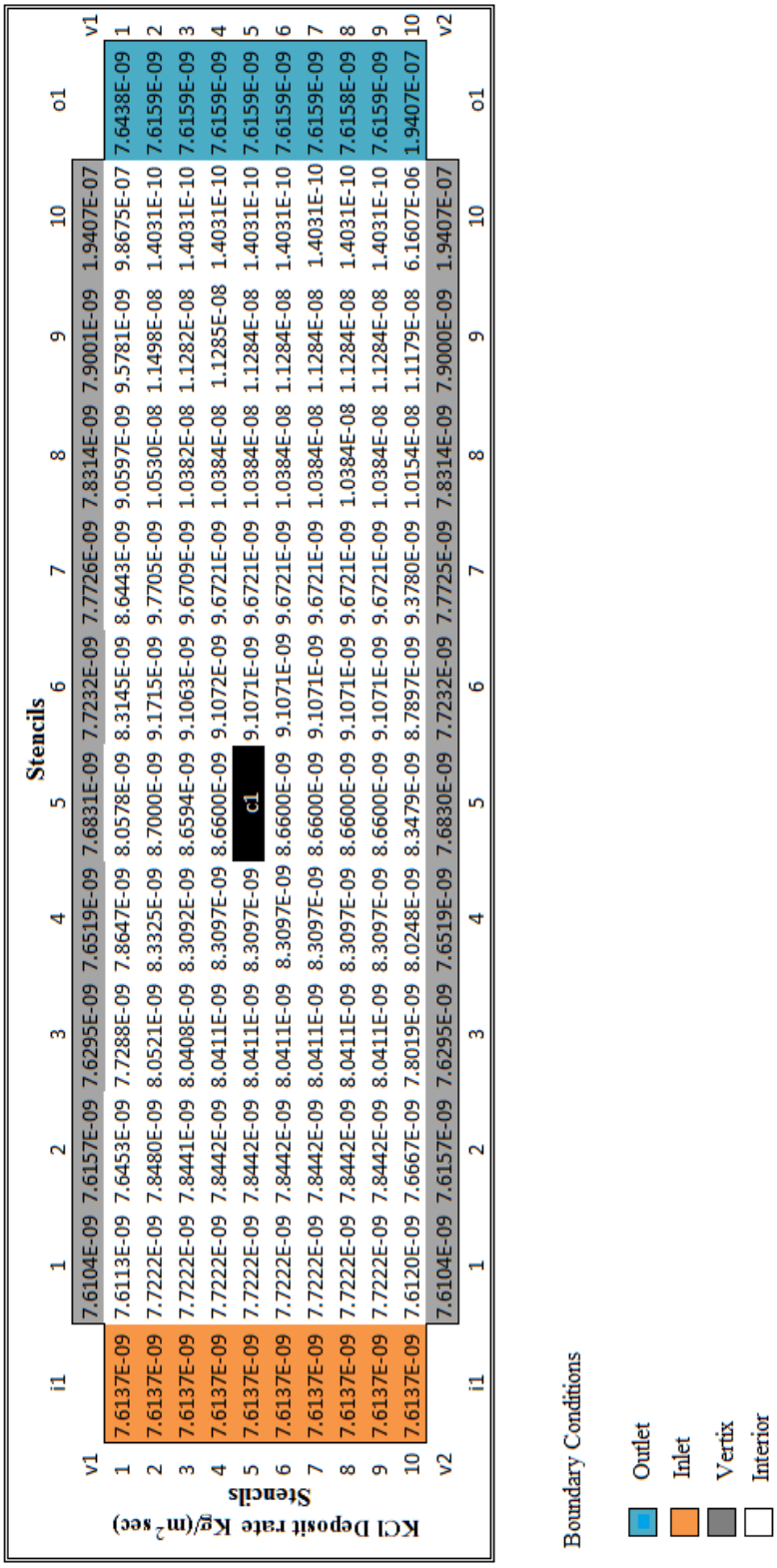

Figure 6-6. The KCl deposition rates for temperature presented in Figure 6-4 for 50µm coal particles

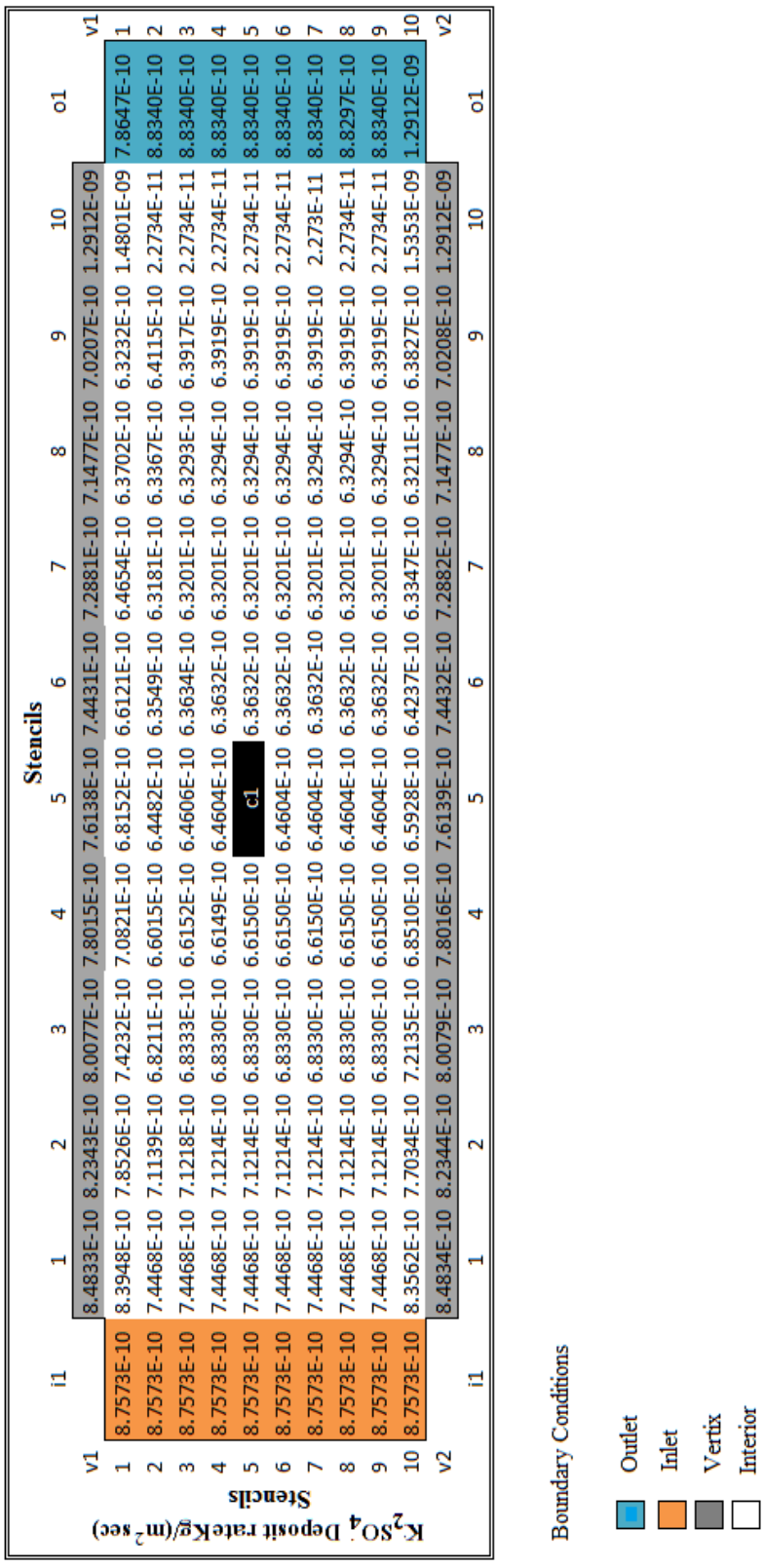

Figure 6-7. The K2SO4 deposition rates for temperature presented in Figure 6-4for 50µm coal particles

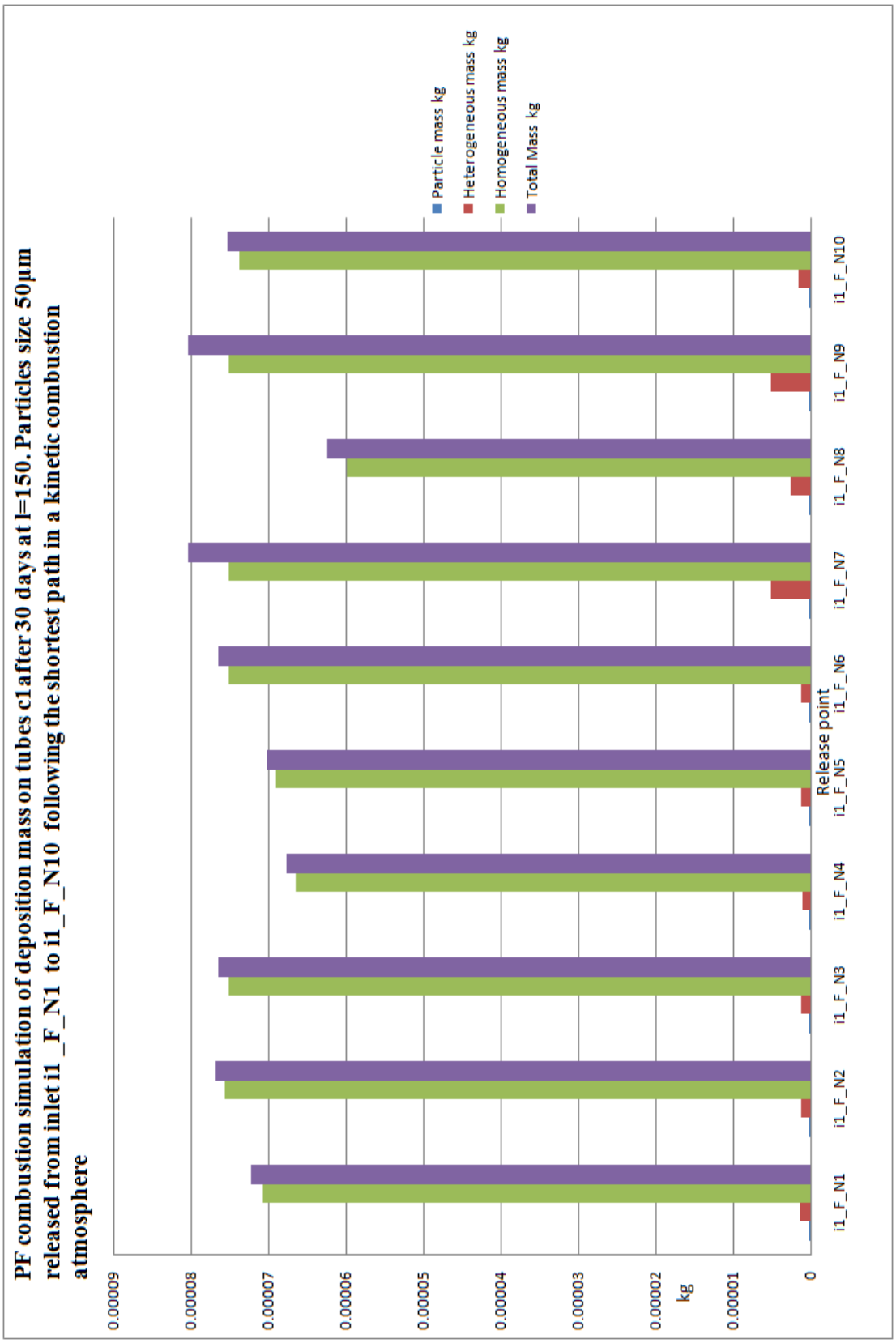

Figure 6-8. Mass deposition of 50µm particles by deposition modes

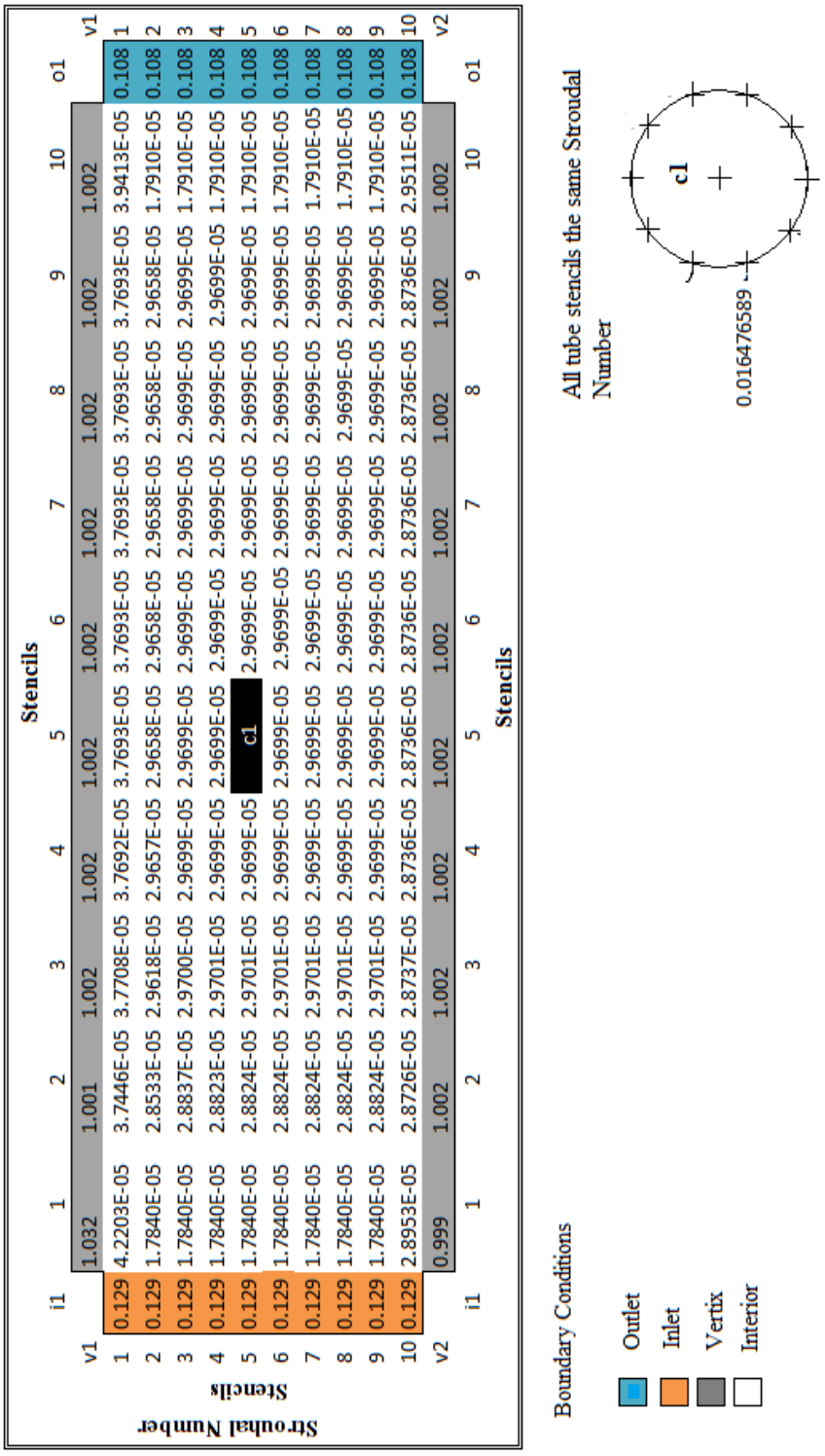

Figure 6-9. The Strouhal Numbers for the surfaces of the PF Combustor (50µm particle)

Further development into increasing the distribution and the number of stencils close to tubes is proposed later in the thesis. There is no requirement to model particle velocities greater than 5m/s and therefore the problems can be solved.

The temperature of 8490.82 K in stencil m2_M10 to m9_M10 in Figure 6-4 is outside the expected temperature range of between 1000 K and 1600 K. These high temperature result in homogeneous deposit rates that are in the order of 10^{10} instead of that of 10^{8}. As the gas flow is recorded as a comparitiely high velocity and temperature high, the desposit rate could be expected to be small. While these are partial temperature and velocities, the real PF combustor at Cranfield University is water cooled, hence the high temperature can reflect a real temperature of the combustion process that is no water. A more likely scenario is the extreme temperature in stencil m2_M10 to m9_M10 comes from the complexities in resolving the numerical solution at the interfaces between moving stencils m2 to m9 with the outlet stencils labelled from i1_N2 to i1_N9. The unexpected high temperature in stencils labelled from m2_M10 to m9_M10 has no effect on the calculation of the mass of KCL and K_2SO_4 deposited on the particles, since the points labelled from i1_N2 to i1_N9 are located down stream of tube c1.

The rate of formation of KCl and K_2SO_4 in the PF furnace is included in Figure 6-6 and Figure 6-7, respectively. As outlined in Chapter 5, particles entering the inlets labelled from i1_N1 to i1_N10 may accumulate to form deposits in the form of homgeneous deposition or in the form of hetrogeneous deposits and exist as vapour droplets. The rate at which formation occurs depends the temperature and the pressure at the time when the particles move to the tube. The initial temperature set for the simulation at 1073 K is too high for a substantial hetrogeneous deposition. Therefore, most of the mass of alkali deposit is from homgeneous deposition as show in Figure 6-8.

The Strouhal number is a dimensionless number describing oscillating flow mechanisms and was introduced to this thesis in Chapter 5. The frequency set for this model was 1.5 Hz and it yields high Strouhal numbers on the walls and around the cylinder as Figure 6-9 of the PF combustor. These areas of high Strouhal numbers on the walls and cylinder (i.e. $> 10^{-4}$) will produce plugs of deposits, which will initiate bridging.

6.3 Case Study II: Cranfield University Combustor for El Cerrajou coal/wheat straw

Case study II will investigate turbulent combustion using biomass. The use of biomass changes the size of particles and the rate that fuel is burned. The particle size has an effect on

the number of particles deposited and the rate at which the fuel burns will affect the temperature.

As for Case Study I, the temperature sets the rate of KCl and K_2SO_4 deposition using the Peng-Robinson 'equation of state' model as discussed in Chapter 4. The analysis of the KCl and K_2SO_4 deposition, by means of the Peng-Robinson equation, results in the deposition rate field as illustrated in Figure 6-12 for KCl and Figure 6-13 for the deposition rate field for K_2SO_4.

Since the deposition field for both KCl and K_2SO_4 is available, the mass of deposition from inlets labelled from i1_N1 to i1_N10 can be determined, together with the source (Particles, heterogeneous or homogeneous). The mass and source of deposition for tube c2 or c3 are illustrated in Figure 6-14. The tube faces the inflow of particles, on which has a large proportion of condensed matter on them. Illustrated in Figure 6-15, for tube c1, are both the mass of deposition and sources of deposition. Since tube c2 obscures tube c1 there are smaller number of particles to impact and less distance for homogeneous deposit to form onto the particles.

Applying the equation for Reynolds numbers from Table 2-2, the Reynolds number at all stencils are shown in Figure 6-16. The Reynolds numbers is derived from the velocity at each stencil and the tube diameter of 0.039m, but for the wall v1 and v2 the characteristic length is taken as 2.8m. The Reynolds number indicates the flow characteristic in the PF combustor, whether the flow is laminar, transitional or turbulent.

Illustrated in Figure 6-17 are the Strouhal numbers that result from velocity field in Figure 6-11. The frequency of vortex shedding from the boundary condition stencils c1, c2, c3, i1, o1, v1 and v2 was set as 1.5 Hz. The vortex shedding occurs at a discrete frequency and is a function of the Reynolds number. The dimensionless frequency of the vortex shedding f of Strouhal number, $St = f D/V$, is approximately equal to 0.21 when the Reynolds number is greater than 1,000.

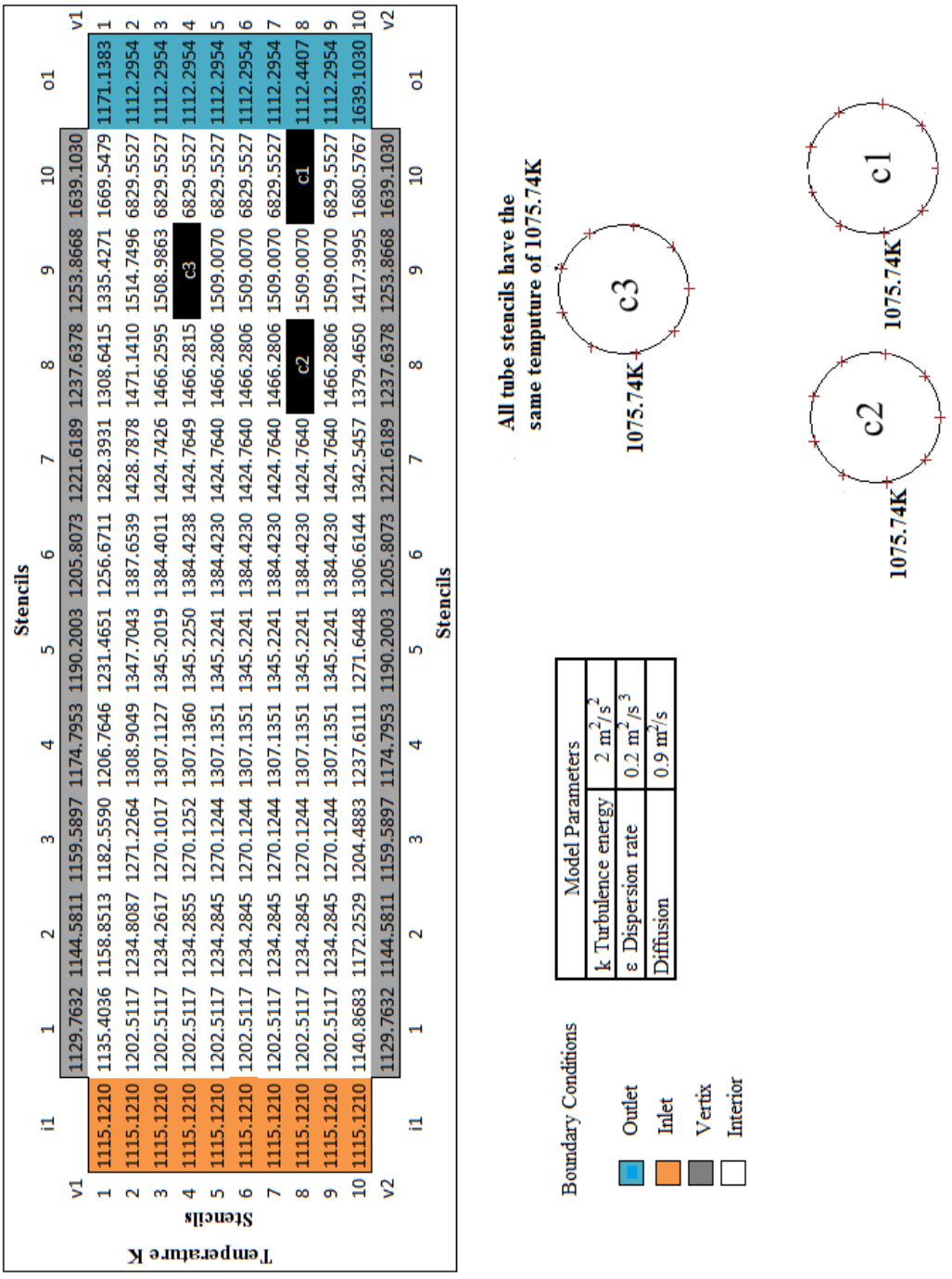

Figure 6-10. Partial temperature field for 10µm co-fired with coal-biomass (turbulent combustion).

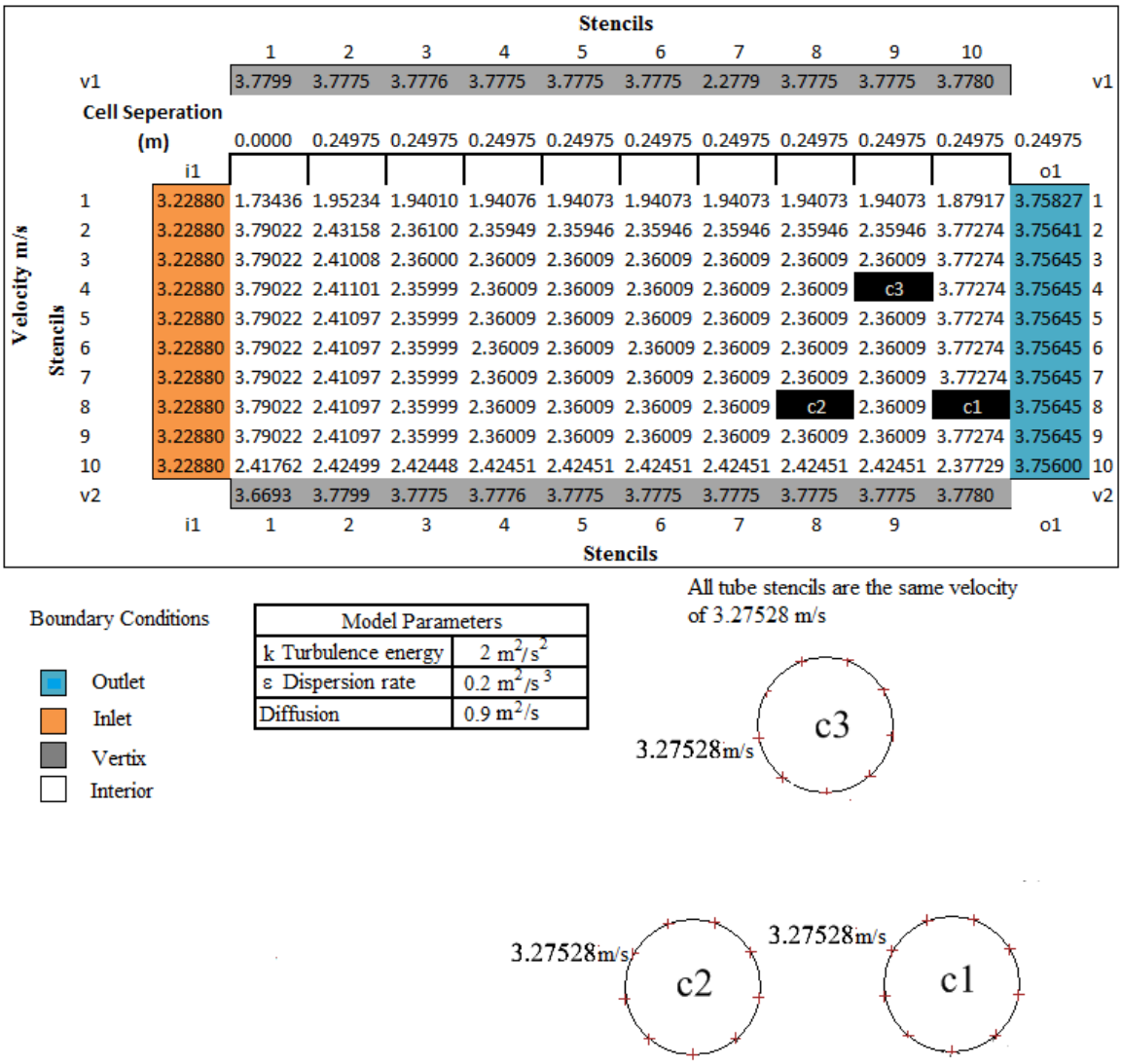

Figure 6-11. Partial Velocity fields for 10µm co-fired with coal-biomass (turbulent combustion).

For a Strouhal number of 0.21 gives a vortex shedding frequency of approximately 2.43 x 10^{-3} Hz when taking the mean velocity at c1, c2, c3, v1 and v2 as 3.2m/s (Figure 6-11). As explain in section 5.6.2 where large Strouhal numbers are present (i.e. Sr <1) viscosity dominates fluid flow, resulting in a collective oscillating movement of the fluid "plug" particles. Together with the case study I, this "plug" particles formation property occurs near the wall of the PF combustor and the tubes. In the narrow space between the tubes these fluid "plug" particles will form a bridge between the tubes. These case studies show that the "plug" particles formation occurs if the frequency is near 1.5 Hz. The formation of 'fins' and 'bridging' across heater exchanger tubes is shown in Figure 4-5 (Tomeczek, et al., 2004).

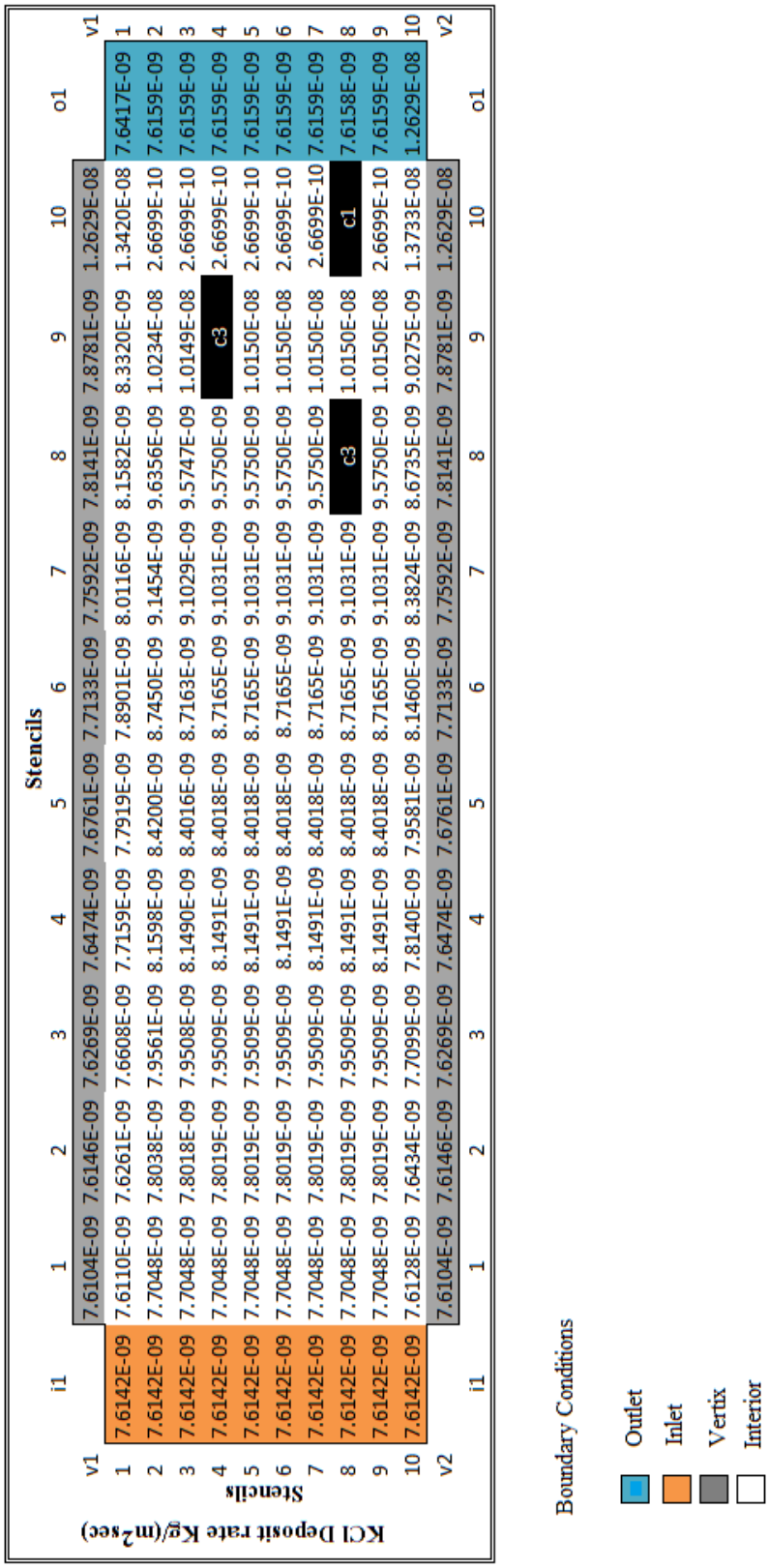

Figure 6-12. KCl homogeneous deposit rates for turbulent combustion (10µm model).

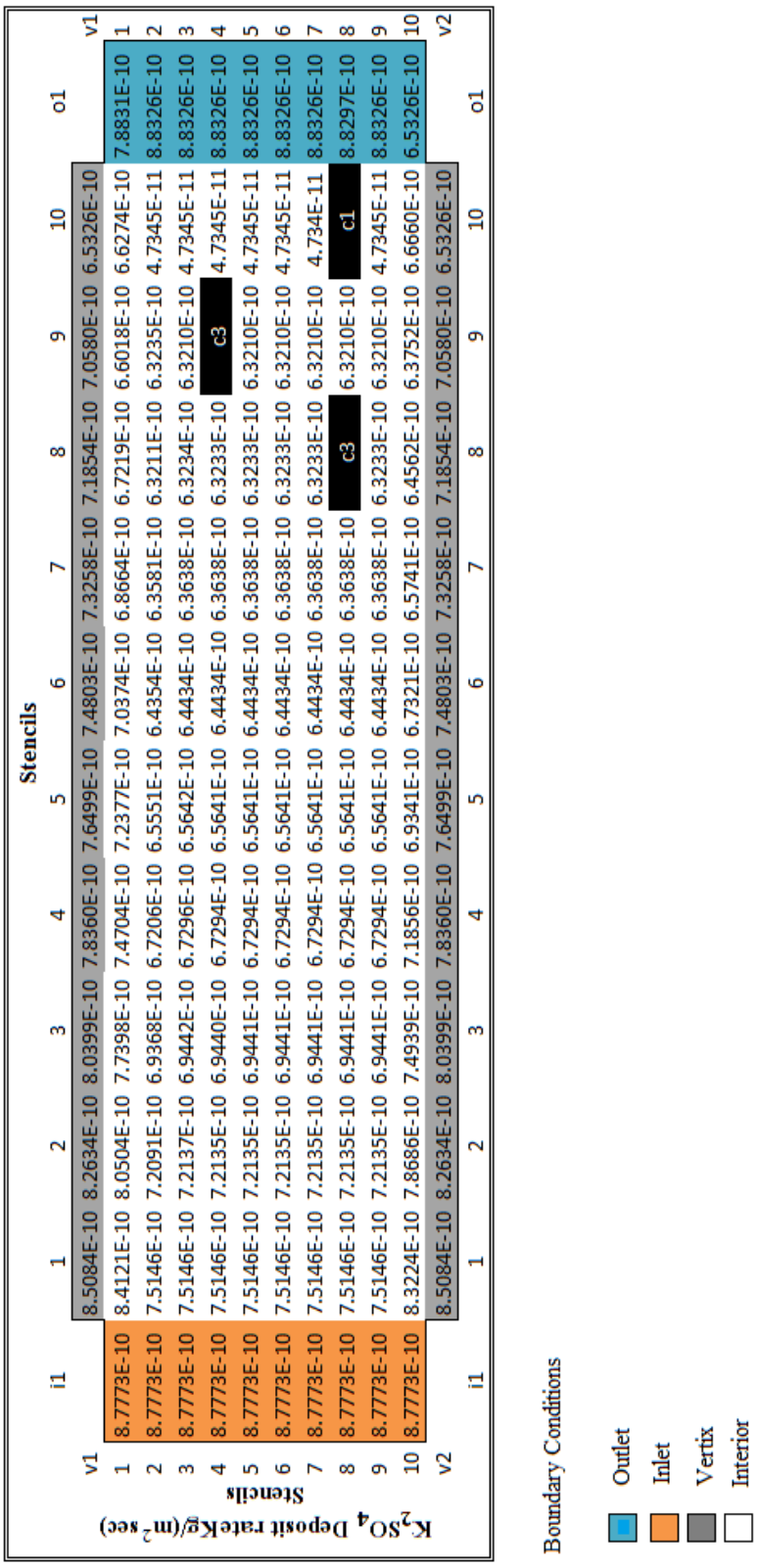

Figure 6-13. K_2SO_4 homogeneous deposit rates for turbulent combustion (10µm model)

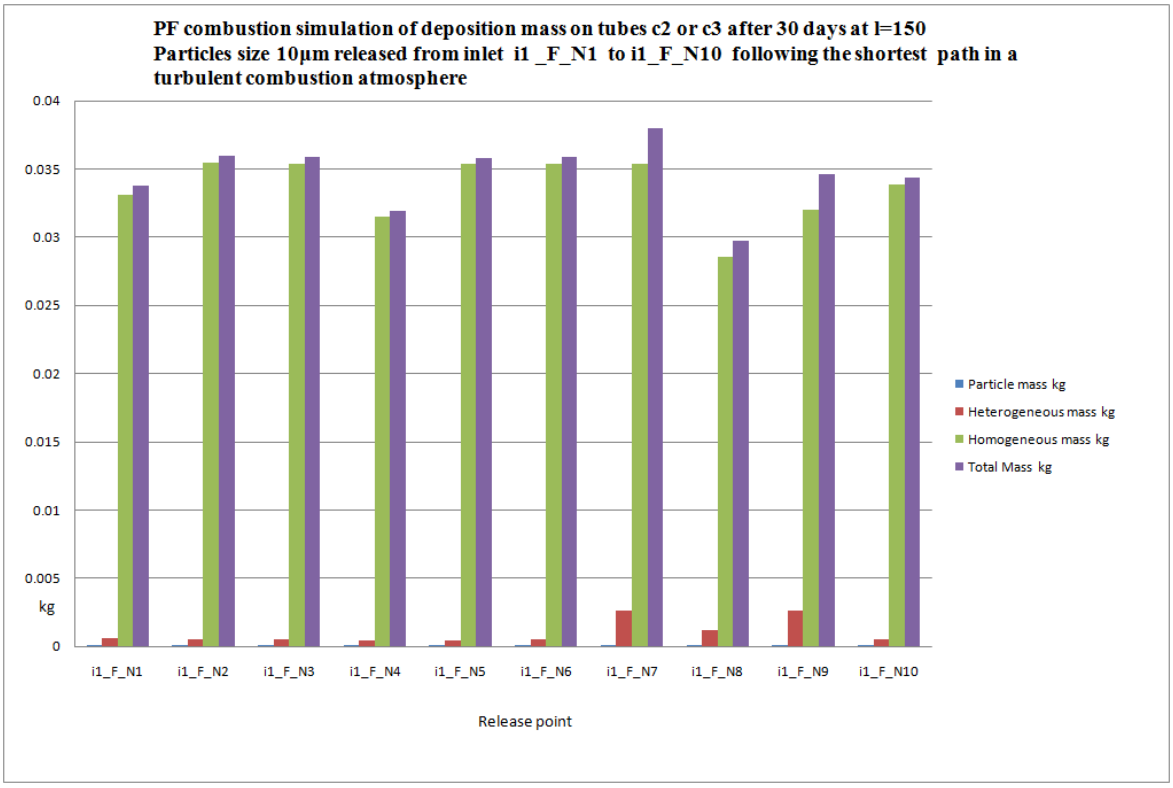

Figure 6-14. Mass of deposits onto tube c2 or c3 from inlets i1_N1 to il_N10

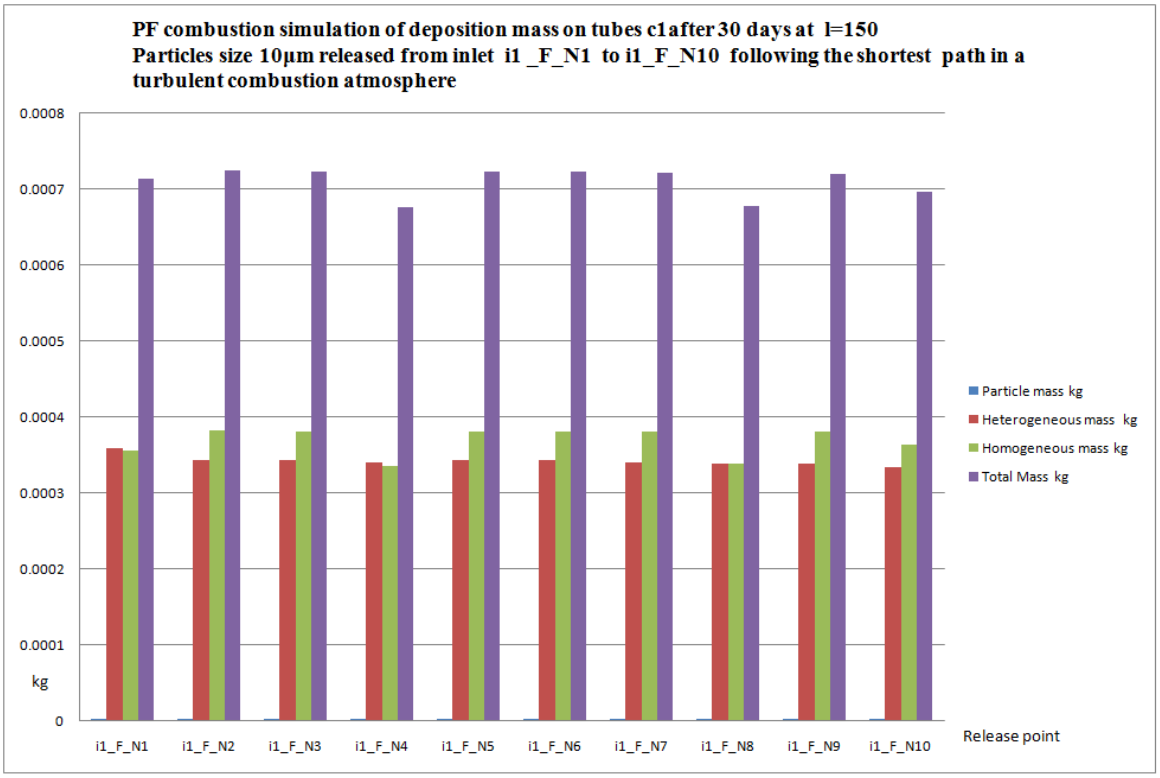

Figure 6-15. Mass of deposits onto tube c1 from inlets i1_N1 to i1_N10

Stencils

Reynolds Stencils	i1	1	2	3	4	5	6	7	8	9	10	o1	
	v1	570919	573317	573788	573778	573778	573778	573778	573778	573778	573686		v1
1	73699	0.2937	0.2783	0.2814	0.2813	0.2813	0.2813	0.2813	0.2813	0.2813	0.3090	42651	1
2	73699	2.0474	0.9536	0.9323	0.9313	0.9312	0.9312	0.9312	0.9312	0.9312	2.0555	42755	2
3	73699	2.0474	0.9724	0.9485	0.9477	0.9477	0.9477	0.9477	0.9477	0.9477	2.0555	42753	3
4	73699	2.0474	0.9716	0.9485	0.9477	0.9477	0.9477	0.9477	0.9477	c3	2.0555	42753	4
5	73699	2.0474	0.9716	0.9485	0.9477	0.9477	0.9477	0.9477	0.9477	0.9477	2.0555	42753	5
6	73699	2.0474	0.9716	0.9485	0.9477	0.9477	0.9477	0.9477	0.9477	0.9477	2.0555	42753	6
7	73699	2.0474	0.9716	0.9485	0.9477	0.9477	0.9477	0.9477	0.9477	0.9477	2.0555	42753	7
8	73699	2.0474	0.9716	0.9485	0.9477	0.9477	0.9477	0.9477	c2	0.9477	c1	42753	8
9	73699	2.0474	0.9716	0.9485	0.9477	0.9477	0.9477	0.9477	0.9477	0.9477	2.0555	42753	9
10	73699	1.0125	1.0044	1.0044	1.0044	1.0044	1.0044	1.0044	1.0044	1.0044	1.0248	42779	10
	v2	570919	573317	573788	573778	573778	573778	573778	573778	573778	573686		v2
	i1	1	2	3	4	5	6	7	8	9	10	o1	

	N1	N2	N3	N4	N5	N6	N7	N8	N9	N10
c1	5561	9581	9581	9581	9581	9581	9581	9581	9581	9581
c2	9581	9581	9581	9581	9581	9581	9581	9581	9581	9581
c3	9581	9581	9581	9581	9581	9581	9581	9581	9581	9581

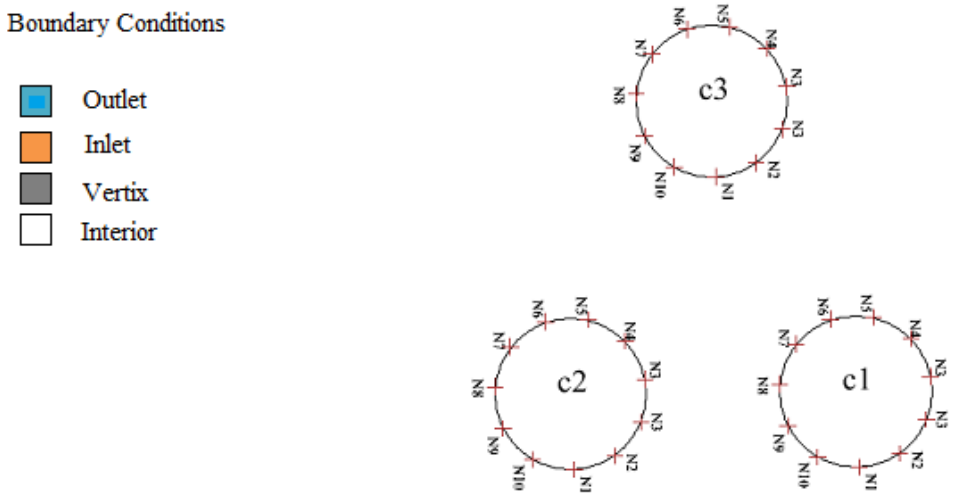

Figure 6-16. Reynolds number within the PF Combustor in a turbulent combustion flow (10µm model)

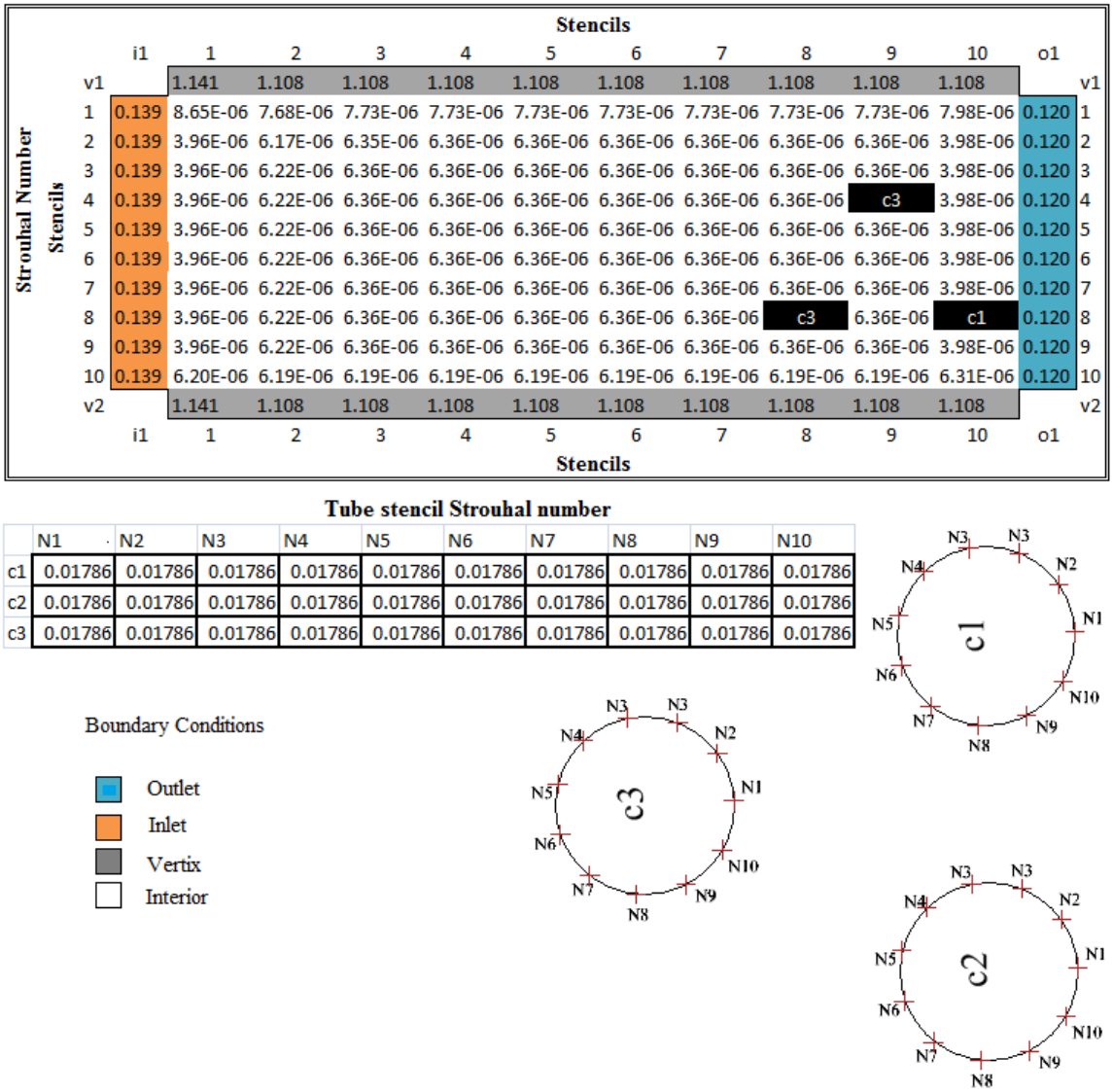

Stencils

Strouhal Number Stencils	i1	1	2	3	4	5	6	7	8	9	10	o1	
	v1	1.141	1.108	1.108	1.108	1.108	1.108	1.108	1.108	1.108	1.108		v1
1	0.139	8.65E-06	7.68E-06	7.73E-06	7.73E-06	7.73E-06	7.73E-06	7.73E-06	7.73E-06	7.73E-06	7.98E-06	0.120	1
2	0.139	3.96E-06	6.17E-06	6.35E-06	6.36E-06	6.36E-06	6.36E-06	6.36E-06	6.36E-06	6.36E-06	3.98E-06	0.120	2
3	0.139	3.96E-06	6.22E-06	6.36E-06	6.36E-06	6.36E-06	6.36E-06	6.36E-06	6.36E-06	6.36E-06	3.98E-06	0.120	3
4	0.139	3.96E-06	6.22E-06	6.36E-06	6.36E-06	6.36E-06	6.36E-06	6.36E-06	6.36E-06	c3	3.98E-06	0.120	4
5	0.139	3.96E-06	6.22E-06	6.36E-06	6.36E-06	6.36E-06	6.36E-06	6.36E-06	6.36E-06	6.36E-06	3.98E-06	0.120	5
6	0.139	3.96E-06	6.22E-06	6.36E-06	6.36E-06	6.36E-06	6.36E-06	6.36E-06	6.36E-06	6.36E-06	3.98E-06	0.120	6
7	0.139	3.96E-06	6.22E-06	6.36E-06	6.36E-06	6.36E-06	6.36E-06	6.36E-06	6.36E-06	6.36E-06	3.98E-06	0.120	7
8	0.139	3.96E-06	6.22E-06	6.36E-06	6.36E-06	6.36E-06	6.36E-06	6.36E-06	c3	6.36E-06	c1	0.120	8
9	0.139	3.96E-06	6.22E-06	6.36E-06	6.36E-06	6.36E-06	6.36E-06	6.36E-06	6.36E-06	6.36E-06	3.98E-06	0.120	9
10	0.139	6.20E-06	6.19E-06	6.19E-06	6.19E-06	6.19E-06	6.19E-06	6.19E-06	6.19E-06	6.19E-06	6.31E-06	0.120	10
	v2	1.141	1.108	1.108	1.108	1.108	1.108	1.108	1.108	1.108	1.108		v2
	i1	1	2	3	4	5	6	7	8	9	10	o1	

Stencils

Tube stencil Strouhal number

	N1	N2	N3	N4	N5	N6	N7	N8	N9	N10
c1	0.01786	0.01786	0.01786	0.01786	0.01786	0.01786	0.01786	0.01786	0.01786	0.01786
c2	0.01786	0.01786	0.01786	0.01786	0.01786	0.01786	0.01786	0.01786	0.01786	0.01786
c3	0.01786	0.01786	0.01786	0.01786	0.01786	0.01786	0.01786	0.01786	0.01786	0.01786

Figure 6-17. The Strouhal Number for 10um particles in turbulent combustion flow

The case study 2 has developed into a 3-D model by taking slices at slices of 25 mm intervals in the Z Cartesian direction. The mass deposit plots on the tubes c1, c2, c3 and the initial start condition used to set up the model for Case 2 numerical simulation are included in Appendix H.

6.4 Discussion and Results

The case studies can be summarised as follow

- Case study I provides a lower yield of Alkalis than Case Study II which reflects the concerns with the research outcome by (Tomeczek, 1994) which is coal based, and

(Lokare, 2006) which is biomass-coal co-firing based. These concerns relate to what is the correct 'standard case of impact' (SCI) and has been covered in Chapter 5. While case study I use only one tubes and case study 2 uses 3 tubes, in this section case study II is concerns with tubes c2 and c3 which are in free flowing bulk gas.

- The mathematical modelling has been undertaken in such a way as to demonstrate the stability performance of the mesh-free solver, Peng-Robinson equation solver and the combustion model.
- Deliberately at the operated at the edge of stability, the model results in a 'break out' (or an unexpected solution) near to the geometric boundaries of the PF combustor; for example between moving stencils and outlet stencils. When modelling complex process, our expectations are that the interaction between processes will create problems of instability.
- It is an important condition of mathematical modelling that the user can be confident of the result is repeatable. In addition the characteristic that indicate a solution that model provides is no longer stable have been identified. These case studies clearly demonstrate the model properties of stability and repeatability.
- Together with case studies in chapter 5 these case studies in this chapter show that initial size of a silica particle determine the mass of deposits they accumulate. For the small particle the mass of the initial particle is small compared to the mass of heterogeneous deposition it acquires in flight. For larger particles the initial mass of the particle will be a more significant than the heterogeneous deposition it acquires in flight from the inlet to the impact site. The particle size has significance to the quantity of KCl and K_2SO_4 present on the particle that will cause the particle to stick to the tube or wall surfaces.
- In the real PF combustor in the area near to where the particles exit, the combustor is water cooled and this can account for some of the higher than expected model temperature. However, these are partial temperature and reflect an earlier step in calculating the mass of KCl and K_2SO_4 material changed from gas to vapour.
- The Strouhal number confirms that the clumping of particles in vortex wake flows is a causing of bridging between tubes is a key investigation finding of this case study.

7 Discussion

7.1 Simulation Results

In this Chapter, the different aspects of modelling fireside deposition on superheater tube are integrated and summarised to highlights the important findings of this thesis.

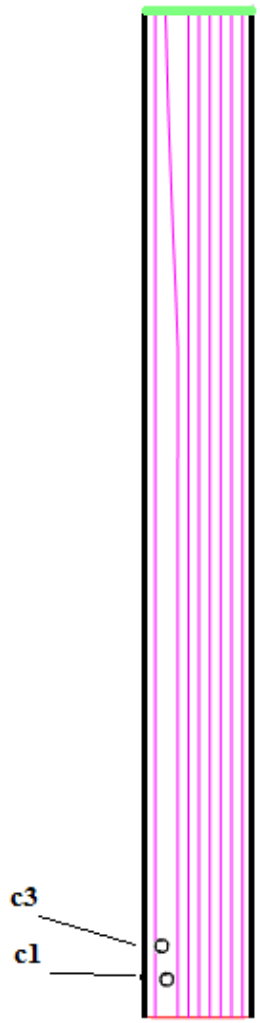

Figure 7-1. Mesh-free particles tracks (coloured pink) do not conform to realistic flow patterns.

The particle tracks illustrated in Figure 7-1 pass two offset tubes and model a numerical simulation using Coal/Biomass fuelled furnace and 18μm diameter particles. The track of the released particle follows an unrealistic motion because the mesh-free method cannot resolve the fidelity of the fluid forces and motion. The choose of 18μm diameter is due to reports by

Tomeczek et al. that 15-18μm particles are expected to produce the largest deposits formations (Tomeczek & Wacławiak, 2009).

The tracks of particles around tubes c1 and c3 are illustrated in Figure 7-1 do not conform to the flow patterns of a potential flow as shown in Figure 5-7. A potential flow is a mathematical description of a flow in a potential field around tubes and a full description is discussed in Appendix B. The mesh-free finite difference method adopted in this thesis is only applicable to the case when calculating thermodynamic properties of real gasses. When it comes to vortex shedding the pattern behind the two tubes does not match the images in Figure 7-2 (Ziada, 2006). The mesh-free finite difference method proposed in this thesis model is not capable of capturing the behaviour of fluid flow in its current form.

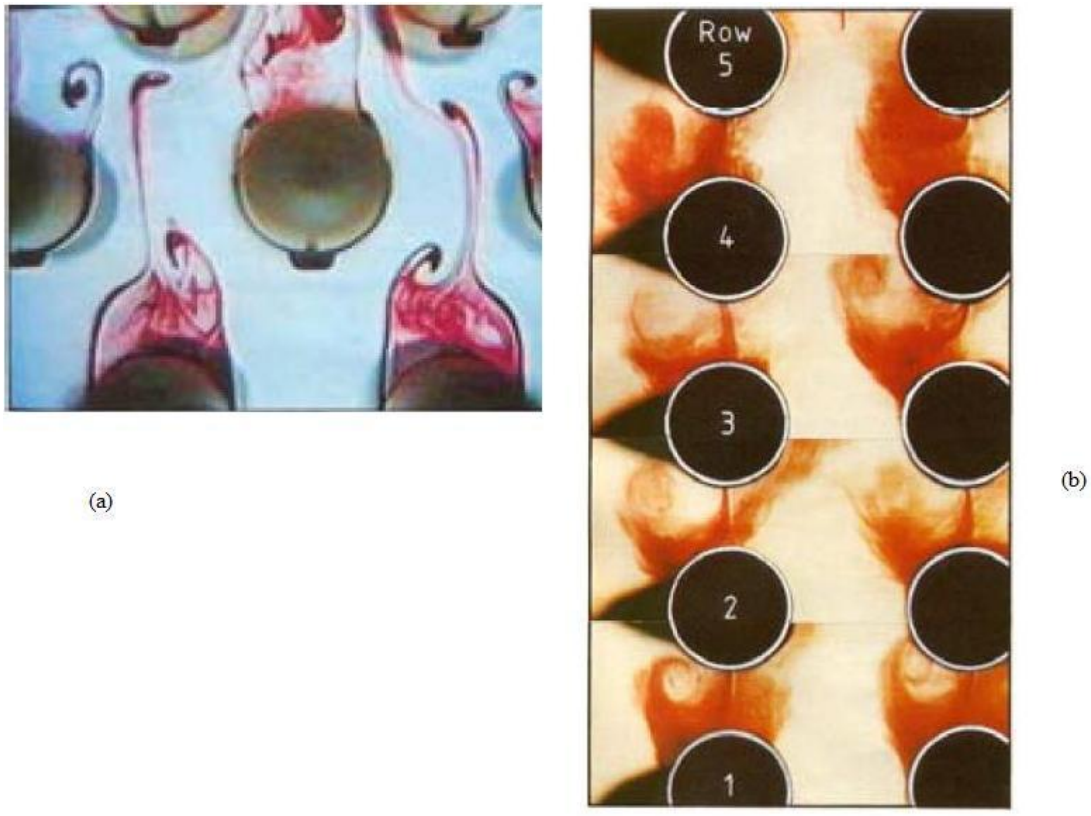

Figure 7-2. Superheater tubes vortex flow (a) staggered tube layout (b) inline tube layout (Ziada, 2006).

To show that the approach of Stokes numbers and the approach aerosol models is of limited benefit, a short test is designed, which aims to measure the influences on the particle with non-standard tubes based on Stokes numbers.

The size of the particle in this biomass numerical experiment is 18μm and the mesh-free solver calculates the particle velocity as 2.813ms^{-1}. The size of the particles that will impact the superheater tube can be calculated using the Stokes number, the tube for the velocity passing tube c3, is 2.813ms^{-1}, the dimensionless time constant in a gas flow $\tau = \rho_p d_p^2/18\mu$ is shown as in Appendix A7 and the diameter of the tube is D = 0.039m. For the dynamic viscosity μ at 1227 K a value of 4.93x 10^{-7} kg/(s·m) was used. The density of silica ρ is set at 2648 kgm^{-3}. For the initial particle diameter of d_p is 18μm where τ is

$$\tau = \frac{\rho_p d_p^2}{18\mu} \tag{7-1}$$

$$\tau = \frac{2648 \times (18 \times 10^{-06})^2}{18 \times (4.93 \times 10^{-07})} = 0.0298$$

and from Table 2-2 Stokes number is

$$Stk = \frac{0.0298 \times 2.813}{18 \times 10^{-6}} = 4.657 \times 10^3 \tag{7-2}$$

Transpose for d_p then adjust τ for the new particle diameter and when St =1

$$d_p = \frac{\tau v}{\mathrm{St}}$$

For a particle to impact a tube, the minimum size of particle d_p must have a Stokes number greater than 1.

$$\mathrm{d_p} = \frac{0.0298 \times 2.813}{1} = 0.0838$$

With these conditions d_p must be at least 0.084 m in diameter for impact. It's clearly impossible for coal/biomass derived particles of size less than 0.084 m to impact the tube. The only available path in this experiment is the one from condensates. Lastly, tube c1 as the identical to tube c3 and has the identical Stokes number value.

Clearly 0.084 m particle size as an example of smallest possible particles that can to impact a tube is wrong. Particle sizes that are smaller than this have been shown to impact the tubes. Studies have predicted impact stokes number have calculate for a range of particles. Therefore, the mass and size of the particles must increase in the travel from the inlet to the impact site. The case studies in this thesis emphasise this issue of heterogeneous growth on

particles increasing their mass and diameters. Other factors that affect particles tracks near tubes are the thermophoresis and turbophoresis.

The Case Study I in Chapter 6 (El Cerrajon coal) with a mean particle size of 50μm has the initial simulation start data properties has been summarised in Appendix H1 and for Case Study II are summarised in Appendix H2. Here, the larger particle size of coal combustion and impact velocity will result in impact of coal derive ash particles. This is confirmed in published work (Lockwood et al. 2000), but is also important to note the different aerodynamic properties between coal derived ash and coal-biomass derived ash.

If coal only option is used then ash particle deposition by impaction will occur on superheater tubes because of the large size range (20-150μm). For coal/biomass combustion, the smaller particles range (20-80 μm), the particles develop aerodynamic lift and become entrapped to the flow around the superheater tube this is turbophoresis.

Particles are found to grade with the large sizes to the upwind side of the tube and the smaller sizes downwind of the tube (Zhou, et al., 2007; Tomeczek, et al., 2004). There is a similar process found in geology, and is called saltation. Saltation is a specific type of particle transport by fluids such as wind or water. It occurs when loose material is removed from a bed and carried by the fluid, before being transported back to the surface. Examples include pebbles transport by rivers, and sand drift over desert surfaces. Particles with sizes less than 100μm experience lift and will midgrade downwind of the tube so falling behind and onto the downwind side of the tube. This action is best solved using the Riemann–Hilbert problem but the Cocks solution is only applied to grading of particle in sand dunes (Cocks 2005). The potential flow as streamline illustrated in Figure 5-7 is bulk gas flow contours around the superheater tube. The track of particles falling out of the bulk gas flow can be represented by contours that are composed of a union of several oriented smooth curves, with no intersections. The + and − sides of the "contour" may then be determined according to the index of a point with respect to Σ. The Riemann–Hilbert problem is to find a pair of functions, M_+ and M_- analytically, respectively, on the + and − side of Σ, subject to the following equation

$$\alpha(z)M_+(z) + \beta(z)M_-(z) = c(z) \qquad (7\text{-}3)$$

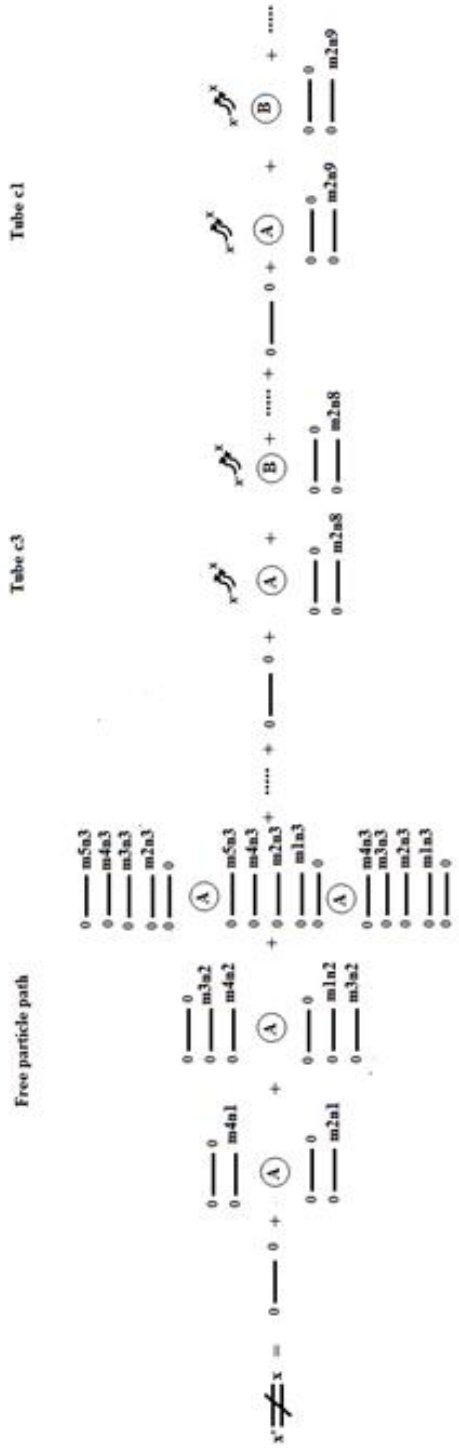

Figure 7-3. The graph series involving particle realised from mesh-free node m3_n1 and just passing by tube c3

where α() β(), and c() are arbitrarily given complex-valued functions, z($\in\Sigma$) is also a member the potential flow function of eq. (5-90) in Chapter 5.

The Riemann–Hilbert problem can be solved using Mayer's functions and combinatorial probability, both of which can be simplified with graph theory (Baik, et al., 1999). The Riemann–Hilbert problem when applied to particle-particle impacts has been left to future work.

The track of the particle can be predicted using a potential flow solution if the modelling assumption is close to the real flows. The track and the forces applied are modelled based on real flows as shown in Appendix C which is combined with perturbation series (as shown in Appendix D). In resolving the particle track the assumption is that the flow has an overwhelming influence on the motion of the particle. The direction of the bulk fluid motion can be defined as a 3-dimensional vector where one vectorial element will be dominate or be the principle direction of motion. The principle direction of a bulk fluid flow always will drive particles to move between two fixed points by the shortest path. Thereafter and closer to the tube, the influences on the motion of the particles will be from Brownian motion, thermophoresis and free surface effects such as drag. In Figure 7-3 the probability of the particles to alter their directions resulting from the because of the forces of fluid flow and free surface effects is delineated as the diagram part Ⓐ. While the influences of Brownian motion, thermophoresis will be defined as a diagram part Ⓑ. Notice that at the site of tube c1 and c3 the interaction can also be a weak form, with the interaction from the neighbouring mesh-free stencils m2_n9 and m2_n8 respectively. The particle can also have a hard impact at any site on either tube c1 or tube c3. The diagram part Ⓐ represents the probability that the particle being influenced weak pertubation interaction from the forces of the fluid flow and drag. The diagram part Ⓑ represents, the weak pertubation interaction forces of Brownian motion and thermophoresis. The strong interaction forces of an impact is represented by diagram part  and the weak interaction forces by diagram part  .

7.2 Deposition yields

The first simulation result feature the rates of deposition of Potassium Sulphate (K_2SO_4) as outlined in Chapter 4, Table 7-1 extracted from a spreadsheet using the Peng-Robinson model for KCL using the 18μm particle model.

Table 7-1 Deposition rates for KCL against temperature rise in Kelvin

Temperature (K)	**523**	**773**	**1023**	**1273**
Fugacity coefficient Φ_n;	$6.73x10^{-06}$	$2.23\ x10^{-07}$	$1.58\ x10^{-07}$	$1.87\ x10^{-07}$
Partial Pressure (Pi) pa	$6.64\ x10^{-11}$	$2.20\ x10^{-12}$	$1.56\ x10^{-12}$	$1.85\ x10^{-12}$
Saturation Pressure (P_{sat}) pa	2.969454731	2.969454731	2.969454731	2.969454731
density (Kg m^{-3})	652.706612	441.61133	333.6906726	2664
Mass Transfer Coefficient $\dot{\beta}$ (kg m^{-2} sec^{-1})	**3310.464553**	**2394.706724**	**1692.446687**	**1415.676992**

From Table 7-1 is a summary of deposition flux for a rise in temperature and these valves are forming the data for the plot in Figure 7-3.

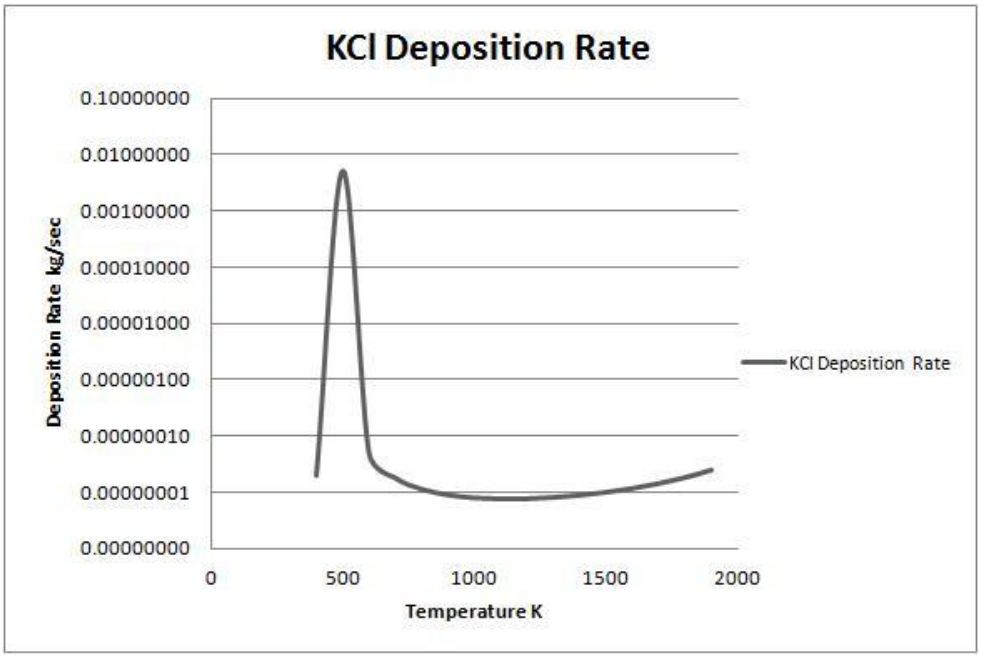

Figure 7-3. A plot of the homogeneous deposition flux KCl against Temperature.

The build up deposits on particles in flight and directly on tubes have been discussed in Chapter 5. It was shown that by using the same 'many particle theory' adopted in the motion of particles the mass of deposition of particle, vapour deposition, heterogeneous and homogeneous can be ascertained. It was shown that the effect of particles size on real PF combustors can be reproduced in model form. This is demonstrated where a particle has a size

of 1μm, the dominant deposit mass will be from the particles impacting on the first line tubes of a bank of tube. This assumes that particles do not pass over the tube because of its small size and that the lift generated by the particle is nullified by the turbulence in the boundary layer around the tube.

For particle with size 400μm, the dominant deposit mass will be the contribution of vapour deposition, heterogeneous and homogeneous masses in built up in flight. The modelling outcomes implies that the particle of 1μm will have less 'sticky' deposits from KCl and K_2SO_4, which are derived from heterogeneous and homogeneous sources and will be inclined to bounce of the tube. Considering the particles with size of 400μm, more 'sticky' deposits are available and therefore the moving particles will bind to the tubes more readily. Another source of sticky deposits is melting ash, for simplicity, and is grouped with particles.

This relationship between the size of the particle and the mass of the 'sticky' deposits deposited is important as it indicates that modelling strategy complies with findings reported by other experimentalist (Kaufmann et al. 2000). The use of mesh-free finite difference method using stencils based on Mayer (Mayer & Mayer 1940) combined with many particle theory is a new effective method of solving particles deposition in real gases. The Mayer combined with many particle theory enables a multi-scale approach that can tackle both bonded particles and condensing matter. This is in contrast to modelling fireside deposition on superheater by the aerosol approach using Stokes, for which odd effects of scale have been outlined earlier in this chapter.

In all the simulated PF Combustor internal temperature fields are illustrated in the Tables and Figures in this thesis. The temperature increases from the inlet to the outlet, whereas in a real PF Combustor the temperature decrease. The change in temperature mirrors the decrease in KCL and K_2SO_4 homogeneous deposition over the length of the combustor and reflects partial or virtual temperature.

To confirm this hypothesis that the position is the inverse of the temperature field requires further data on the temperature field inside the real PF combustor. Obtaining data on the real PF combustor temperature field would confirm that temperature of the simulation would be within the expected bounds in a real PF combustion. This thesis has left for future work the accurate modelling of temperature gradients inside the PF combustor using mesh-free methods.

The modelling of the combusting environment in Chapter 6 together work in Chapter 3 together with subsequent chapters to model the effects of continuous combustion of particles (burn-off) on deposition.

7.3 Boundary Edge Resolution

The form of the geometry is deconstructed in to separate parts as was discussed in Chapter 6. Each part of the deconstructed geometry is labelled with a subscript v for vertex walls, c for tubes, i for inlets, o for outlets and m for moving boundaries or particles. When the form is reassembled it must take into account the contribution of the various parts of the sub-assembly.

The geometry is reassembled from a column vector $\mathbf{x} = |x_j|$, where x_j are members of part of the geometry v, c, i, o and m at the corner or the edge of the form. These paired members are expressed to reassemble the 3-dimensional space (Kreyszig 2006) involves one of the following vector norms

L_2 norm

$$\|\mathbf{x}\| = \sqrt{x_1^2 + \cdots x_j^2} \tag{7-4}$$

and

L_∞ norm

$$\|\mathbf{x}\| = max_j|x_j| \tag{7-5}$$

The edges of the geometry are joined by pairing the edges and vertices as Table 7-2

Table 7-2 Reconstructing the geometry of the PF Combustor

Edge	Paring	With
v1	v1_N10	o1_N1
v2	v2_N10	o1_N10
i1	i1_N1 to i1_N10	m1_M1 to m10_M1
o1	o1_N1 to o1_N10	m1_M1 to m10_M1

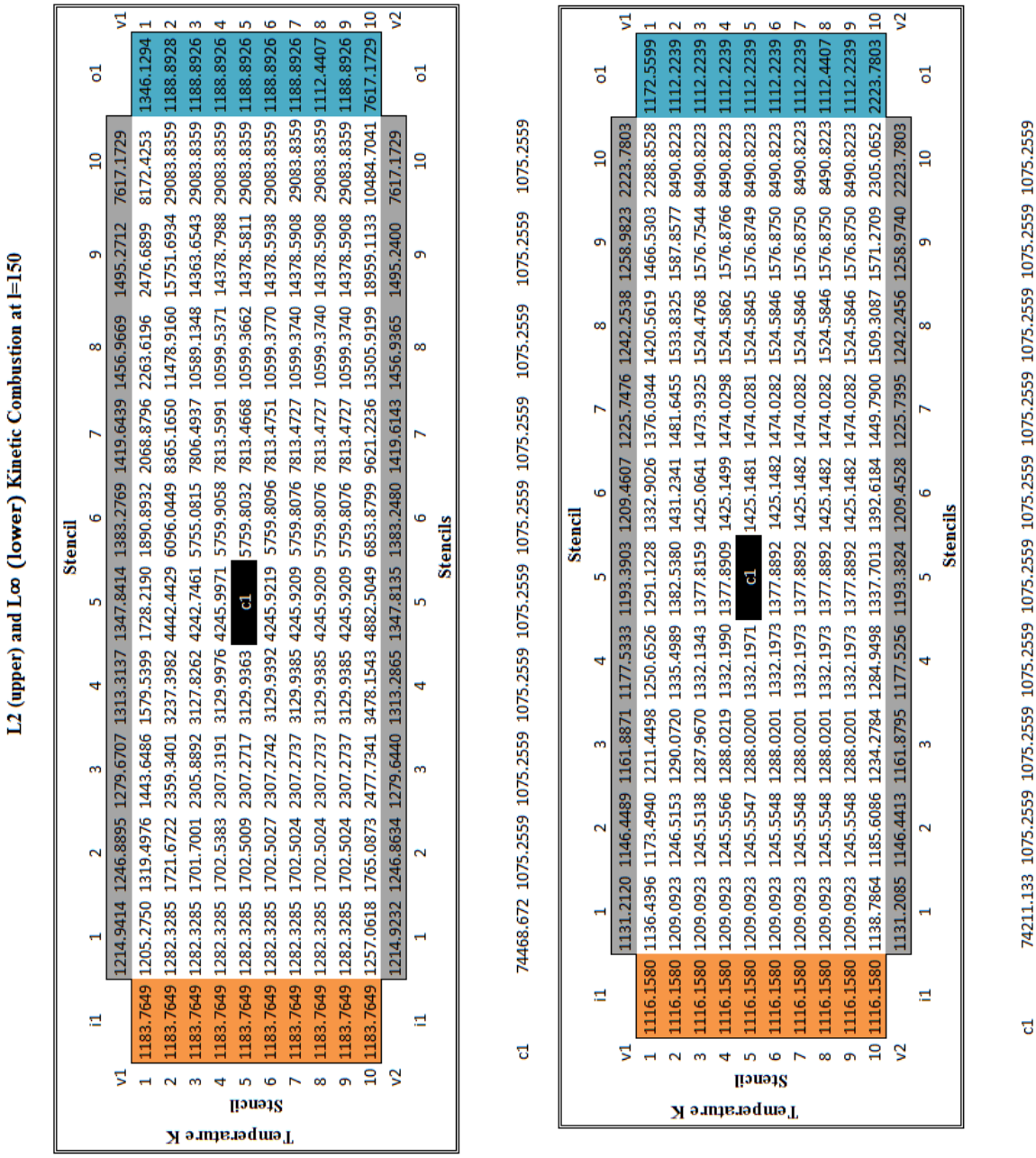

Figure 7-4. Comparison between L2 and L∞ edge reconstruction for case 1 in Chapter 6

The effect of applying $\mathbf{L_{2\ -\ norm}}$ or $\mathbf{L_{\infty\ -\ norm}}$ is illustrated in Figure 7-4 and demonstrates an example where combustion modelled is included as part of the simulated process. It has been found that $\mathbf{L_{2-\ norm}}$ will produce overall larger values at the outlet when an ongoing

combustion is modelled. A $\mathbf{L_{\infty\text{ - norm}}}$ is therefore a better vector norm when particles are modelled with continuous and ongoing combustion while passing through the combustor.

7.4 Further discusion on Case Studies

One of the aims of this thesis is to apply a rigorous examination to vapour deposition onto particle and to offer an explanation of how particles become solidly attached to the superheater tubes. With the majority of current work in the field is based on experimental work conducted experimentally or in the field based studies and is focusing on what sizes of particles can impact the tubes and the composition fowling of superheater tubes. This study has moved the solution of fireside deposition further with reliable simulation and accurate models of vapour deposition in environments around the superheater tubes.

However, despite the complexity of the flow regime, the prevailing ideas in this field concentrate on particle impacts on the tube and form a crust and together with some vapour deposition. Another key finding demonstrates that very small particles do not pick up vapour deposits. As shown in this thesis, the deposition of the combustion products substantially influenced by direct impaction if the size is over 5μm, with the condensation of combustion products, or by the force of lift if the size is under 100μm and then falling back onto the tube. These statements on the source of the deposition on the tube are based on the theoretical examination of the particles using the Peng-Robinson equations of state and the use of Stokes number. Although the approach has been used before, using sophisticated modelling methods of statistical quantum mechanics and mesh-free solution in the numerical solution of partial differential equations has yielded compelling evidence.

The mesh-free method has been used to overcome the limitation of mesh CFD work because the physics in particle deposition is multi-scaled. The use of statistical mechanics has enables a more detailed exploration of the vapour-liquid condensation of particles in flight. This approach holds to multi-scale capabilities claimed because it can capture the 3 ensembles and the respective thermodynamic intensive properties of Temperature (T), Pressure (P), Chemical Potential μ (i.e. Entropy (E)) and other non-intensive properties such as Fugacity (Ƶ), Volume (V) and fixed number of particle (N). The ensembles that are partnered to this project are:

I. The **microcanonical** ensemble pertains to isolated systems (i.e., at fixed E, V, N); the copies in the ensemble are also isolated from each other (i.e., a single isolated system).
II. The **canonical** ensemble pertains to systems in contact with a heat bath (i.e., at fixed T, V, N); the copies in this ensemble are assumed to be in thermal contact, so that they may exchange energy with each other. Thus, all the copies act as a heat bath for any individual copy.
III. The **grand canonical** ensemble pertains to systems in contact with a reservoir with which they can exchange both heat and particles (i.e., at fixed T, V, $\mathcal{Z}$). The copies are assumed to be in both thermal and diffusive contact, so that they may exchange both heat and particles with each other.

Since the mesh-free method described in this thesis has at its theoretical bases based on Mayer's Functions and Boltzmann entropy equation, the mesh-free method is also able to model any one of the above ensembles. Therefore, since the mesh-free method is able model the thermodynamic ensemble, it is also able capture the intensive thermodynamic properties of Chemical Potential (μ), Temperature (T), and Pressure (P). The missing thermodynamic property that is not captured by the mesh-free method is entropy. The entropy of the thermodynamic system is modelled by considering the number of available microstates which the system can attain. The number and availability of microstates is modelled from the graph theory approach as described earlier in this chapter and from the entropy equation which is described in Chapter 5.5.

At the wall boundaries the temperature and the velocity reproduce are higher than expected because the initial modelling assumptions are that the walls are adiabatic and lossless. On inspecting the data the ends of the connected graph, as illustrated earlier in Figure 5-12, shows the same value as the surrounding simulated combustor appear at nodes 1 to 5 and 14 to 19 of the mesh-free element. The pressure values for the wall boundaries are considered valid and the mesh-free method converges to a solution with no more than 3% in error (please refer to Appendix C for details of error calculations within stencils).

Errors of thermodynamic properties of pressure, velocity, temperature in moving particles are subjected validity checks in Table 5-9 to Table 5-16. In Table 5-8 the pressure values demonstrates a realistic higher pressure cone in front of the tube than in the free flowing gas.

Another aspect of the mesh-free method is that for relative few nodes highly accurate results can be obtained in contrast to the large number of mesh elements as shown in Figure 4-2.

Programming for mesh-free method is more complex than for the meshed methods and the underlying theory is complicated. The mesh-free method is faster than meshed calculation, its running time being shorter by 0.5 sec, when based on the meshed single tube model in chapter 3 and mesh-free single tube model chapter 5. Given the complexity, using a symbolic solver such the MathLab package would be easier than using Visual Basic.Net and Intel Fortran, but Microsoft Excel performs expertly in solving the entropy, equation of state and deposition rates for the range of particles featured.

Key problems with this type of physical system modelling include the following,

- It is impossible to gain accurate observations since in measuring the behaviour under study within the furnace will alter the physical characteristics of the phenomenon under examination.
- Modelling of the behaviour of particles can also be conducted in other ways, of which genetic algorithms (GA). For a detailed introduction of the GA, the reader is referred to the book on GA by Goldberg (Goldberg 1989).

8 Conclusions

This thesis advocates the advancement in the study of particle deposition on Pulverised Fuel Boiler surfaces and tubes through mathematical modelling. The following has been achieved.-

- The open and grey literature has been critically reviewed and a number of gaps have been examined. In the literature, it is reported that the process of vapour formation and deposition is well understood. However, when modelling the coal/biomass co-firing using section 5.1 has shows that a solution to the underlining PDE's can be a challenging problem. As approaches used in CFD can perform inadequately because they become unstable (i.e. may diverge) when including more combusting compounds. Therefore do not have the capability of estimate the condensation of the matter problem. The reliance on the aerosol model (i.e. based on Stokes or Tomeczek approaches) in CFD has a major drawback as it does not explore the importance of physical scale between condensing molecules and solid masses.
- The mesh-free method has enabled an examination of the behaviour of particles or vapours at a precise location in a geometric domain. An equivalent geometric positional accuracy can be difficult to achieve with a meshed system. The mesh-free method adopted here is a rational model that maps to way particles behave, while the meshed or adaptive mesh methods are more abstract.
- The objective of improving the existing approach to modelling the movement of particles has been achieved by using Arrhenius equation to determine the rate that volatiles are burnt off. In advancing the Arrhenius equation to quantify the rate of burn-off and the movement of particles using numerical modelling, this thesis has shown the limitation of meshed CFD when applied to combustion models and when attempting to model vapour phase movement. If TDMA is used to solve the PDE's that predict the rate that volatiles are burnt off, this can restrict the choice of initial start values. This restriction in the initial start values is due to a division by zero error.
- A new mathematical approach, which uses mesh-free methods to solve Hamilton's equations with a consideration of the total energy of the system, has been developed. The initial objective set earlier in this thesis as 'extending the particles and vapour phase movement' has been achieved by adapting statistical molecular mechanics to

predict the vapour phase pathways. Subsequently, this thesis meets the object of 'modelling the state of matter around the superheater tube and around the particles in motion' because models have been chosen that predict the quantity of gas transformed to vapour through the application of the Peng-Robinson equation of state. The approach of Peng-Robinson is physical scale independent unlike Stokes or Tomeczek approaches and can model changes in gas-vapour phase due to changes ambient temperature.

- A model has been developed which can simulate the mass accumulation process based on graph and combinatorics theory. The complex particle and molecular interaction physics within fireside combustion gas particle fields have been simplified using graphs and combinatorics models that are based on 'many particle physics'. Simplifying the complex mathematics of particle and molecular interaction within gas flow has improved the modelling of predicting the path those particles. An improve understanding of the mass accumulation process from vapour onto ash particles and vapour onto tubes is a key over-arching goal.
- This thesis has fulfilled the objective of 'investigating the feasibility of using mesh-free solution to solve partial differential equations for predicting particle motion and thermodynamic properties'. The thesis has brought forward and extended 'Least Squares Finite Difference' mesh-free method by using Mayer's functions. The extended the LSFD mesh-free method has successfully predicted the intensive thermodynamic properties of pressure and temperature and the non-intensive thermodynamic property of the velocity of particle motions. The performance of the mesh-free methods has been validated with exact solutions based on the theory of potential flow. The performance of the mesh-free solver has shown that it has 'graceful degradation' and provides the user of with a clear indication of inadequate performance, while being tolerant of the typical chaotic and unpredictable behaviour those other types of meshed solvers exhibit.

9 Future Work

This thesis has developed original concepts for the solution of a specific problem in applied science. These problems have evolved from the study of deposition environment around superheater tubes. This includes in this study of the motion of particles, gas and vapours and also the phase changes of gases to vapours. While preparing this thesis, additional areas where this research work could be developed further and that were not foreseen at the start of the task, have come to mind.

The following points could therefore be taken further:-

- For a specific fuel mixture of biomass and coal the mass deposition rate for each fuel mixture should be ascertained.
- The modelling of the condensation of vapour onto particles has been has up to now been based on the 'body centre cubic crystal' (bcc) structure model, but 'face centre cubic' (fcc), 'hexagonal close-packed' (hcp) and amorphous structures should be investigated using the Mayer functions and based on statistical quantum mechanics. This would open up capability to model the aspects of solidification, phase changes and particle motion in fields other than combustion particle and gas/vapour deposition.
- A scheme to allow a less rigid array of stencils nodes would permit the more complex geometries to be model. Expanding this idea the user would place a stencil anywhere in the geometric domain and the thermodynamic information would pass to and from the nearest neighbouring stencils.
- Developing a method of locating a group of stencils circumferential around a tube for modelling the intensive thermodynamic properties close to the tubes surface in more detail.
- To develop a vortex/wake model using the graph theory approach as outlined in chapter 7.
- Finally, fuel/temperature/particle/vapour data produced in the model should be calibrated and validated based on real datasets from real PF Combustion process.

10 References

1. Abimael, F. D. & Fernandes, D. T., 2009. A quasi optimal petrov-galerkin method for helmholtz problem. *International Journal for Numerical Methods in Engineering,* 80(12), p. 1595–1622.
2. Adanez, J. et al., 2003. Combustion of wood chips in a CFBC: modelling and validation. *Ind. Eng. Chem. Res,* Volume 42 No. 5, p. 987–999.
3. Albina, D. O., Millrath, K. & Themelis, N., 2004. *Effects of Feed Composition on Boiler Corrosion in Waste-to-Energy Plants.* s.l., 12th North American conference Waste to Energy Conference (NAMTEC).
4. Åmand, L.-E., Leckne, B., Eskilsson, D. & Tullin, C., 2006. Deposits on heat transfer tubes during co-combustion of biofuels and sewage sludge. *Fuel,* Volume 85, No.1, pp. 1313-1322.
5. Andersen, K. W. et al., 2000. Deposit Formation in a 150 MW Utility PF-Boiler during Co-combustion of Coal and Straw. *Energy Fuels,* Volume 14, p. 765–780.
6. Andrews, M. J. & O'Rourke, P. J., 1996. The multiphase particle-in-cell (MP-PIC) method for dense particulate flows.. *International Journal of Multiphase Flow,* Volume 22, No. 2, pp. 379-402.
7. ANSYS, 2001. *Fluent Handbook.* s.l.:ANSYS, Inc.
8. Atkins, P. & De Paula, J., 2003. *Physical Chemistry.* s.l.:Oxford University Press.
9. Atluri, S. N., Liu, H. T. & Han, D. Z., 2006. Meshless Local Petrov-Galerkin (MLPG) Mixed Finite Difference Method for Solid Mechanics. Volume 15, no.1, pp. 1-16..
10. Babuška, I. & Melenk, J., 1997. The Partition of Unity method. *International Journal for numerical methods in Engineering,* Volume 40, pp. 727-758..
11. Backman, R., Hupa, M. & Skrifvars, B. J., 1999. *Predicting superheater deposit formation in boiler burning biomass.* Kona, Hawaii, Proceeding of an engineering foundation conference on mineral matter in fuel.
12. Baik, J., Deift, P. & Johansson, K., 1999. On the distribution of the length of the longest increasing subsequence of random permutation. *Journal of AMS,* Volume 12, pp. 1119-1178.
13. Basttisa, J. J., Hughes, E. E. & Tillman, D., 2000. Biomass co-firing at Seward Station. *Biomass and Bioenergy.,* Volume 19, pp. pp. 419-427.
14. Baxter, L. L., 1998. Influence of ash deposit chemistry and structure on physical and transport properties. Volume 56, No. 1-2, pp. 81-88,.
15. Baxter, L. L., 2004. *Biomass Co-firing. An overview.* Rome, Italy, Second World conference on biomass for energy industry and world climate.
16. Becidan, M., Sørum, L., Frandsen, F. & Pedersen, A. J., 2009. Corrosion in waste-fired boilers: A thermodynamic study. *Fuel,* Volume 88, p. pp. 595–604.
17. Berge, C., 1962. *The Theory of Graphs and its Application.* s.l.:Greenwood Press.
18. Berry, M. W., Mezher, D., Philippe, B. & Sameh, A., 2005. Parallel Algorithms for the Singular Value Decomposition. In: *Handbook of Parallel Computing and Statistics.* s.l.:Chapman and Hall.
19. Bieneke, W., 1979. *Application of Graph Theory.* s.l.:Academic Press.

20. Bouteville, A., 2005. Numerical simulation applied to chemical vapour deposition process. Rapid thermal cvd and spray cvd. *Journal of Optoelectronics and Advanced Materials,* Volume 7, No. 2, pp. 99 - 606.
21. Brink, A., Kilpinen, P. & Hupa, M., 2001. A simplified kinetic rate expression for describing the oxidation of volatile fuel-N in biomass combustion. *Energy Fuels.,* Volume 15, p. 1094–1099.
22. Buhre, B. J. et al., 2007. Oxy-fuel combustion technology for coal-fired power generation. Volume 31, pp. 32-47.
23. Chen, S. & Doolen, G. D., 1998. Lattice Boltzmann method for fluid flow. *Annu. Rev. Fluid Mech.,* Volume 30, p. 329–64.
24. Chow, T. Y., 1999. What Is a Closed-Form Number?. *The American Mathematical Monthly,* pp. 440-448..
25. Cocks, D., 2005. *Mathematical Modelling of Dune Formation,* Oxford: Trinty College, University of Oxford.
26. Davidsson, K. O. K. J. G. P. J. B. C. J. U., 2002. The effects of fuel washing techniques on alkali release from biomass'. Volume Vol. 81, No. 1, pp. 137-142..
27. Demirbaş, A., 2005. Biomass Co-Firing for Boilers Associated with Environmental Impacts. *Energy Sources, Part A: Recovery, Utilization, and Environmental Effects,* Volume 27 No. 14, p. 1385 – 1396.
28. De, S. & Assadib, M., 2009. Impact of co-firing biomass with coal in power plants – A techno-economic assement. *Biomass and Bioenergy,* Volume 33, p. 283–293.
29. Di Mare, F., Jones, W. P. & Menzies, K. P., 2004. Large eddy simulation of a model gas turbine combustor. *Combustion and Flame,* Volume 137, p. 278–294.
30. Dobkin, D. M. & Zuraw, M. K., 2003. *Principles of Chemical Vapor Deposition.* s.l.:Kluwer.
31. Dudek, S. A., Wessel, R. A. & Strempek, R. A., 1991. *Three dimensional numerical modelling of stoker fired power boilers.* s.l., ASME International Mechanical Engineering Congress and Exposition, Nashville, Tennessee USA.
32. Durbin, P. A. & Pettersson, B. A., 2001. *Statistical Theory and Modeling for Turbulent Flows.* s.l.:Johns Wiley & Sons.
33. Energy Technologies Unit, 2007. *DTI UK Biomass Strategy.* s.l.:Department of Trade and Industry.
34. Frandsen, F. J. et al., 1997. *Deposition and Corrosion in straw and coal-straw co-fired utility boilers.* s.l., Proceedings of an Engineering Foundation Conference on Mineral Matter in Fuels, Kona, Hawaii.
35. Frank, P., 2001. *Fundamentals of heat and mass transfer.* s.l.:John Wiley and Sons.
36. Frey, S., Martins-Costa, M. L. & Saldanha Da Gama, ,. R. M., 2008. Petrov-Galerkin approximation for advective-diffusive heat transfer in saturated porous media. *Latin American Applied Research,* Volume 38, pp. 169-178..
37. Fuchs, N. A., 1963. *The mechanics of aerosols.* s.l.:Pergamon Press.
38. Geiser, J. & Röhle, R., 2008. Modeling and Simulation for Physical Vapor Deposition: Multiscale Model. *Int Journal of Comp Sci,* Volume 2. No. 4, pp. 177- 186.

39. Germann, L., 1996. Mathematical modelling of straw bale combustion in cigar burners. *Energy Fuels.,* Volume 10 No. 2, p. 276–283.
40. Glazier, J. A. & Libchaber, A., 1988. Quasi-periodicity and dynamics systems: An experientialist view. *IEEE Transactions On Circuits And Systems,,* Volume Vol. 35, no. 7, pp. 790 - 809.
41. Goldberg, D. E., 1989. *Genetic Algorithms in Search Optimisation and Machine Learning.* s.l.:Addison and Wesley.
42. Golub, G. H. & Van Loan, C. F., 1998. *Matrix Computation.* s.l.:John Hopkins Press.
43. Gross, E. K. U., Runge, E. & Heinonen, O., 1994. *Many Particle Theory.* s.l.:IOP English Edition.
44. Gu, M., Demmel, J. & Dhillon, I., 1994. *Efficient Computation of Singular Value Decomposition with Application to Least Value Problems,* Department of Computer Science, University of Tennessee, Knoxville, TN USA: s.n.
45. Haray, F., 1967. *Graph Theory and Theoretical Physics.* London: Academic Press.
46. Hein, K. R. G. & Bemtgen, J. M., 1998. EU clean coal technology—co-combustion of coal and biomass. *Fuel Processing Technology,* Volume 54, No. 1-3, pp. 159-169.
47. Heinzel, T. et al., 1998. *'Slagging and fouling in dry and molten ash',* s.l.: PFC JOULE III – OPTEB Contract JOR3-CT95-0057 Final Report 1998.
48. Hill, T. L., 1987. *'Statistical Mechanics: Principles and Selected Applications'.* s.l.:Pub. Dover.
49. Hirota, K. & Kimura, O., 1943. A Theory of the Ludwig-Soret Effect. *Bulletin of the Chemical Society of Japan,* Volume 18 , No.3, pp. 111-116..
50. Huang, Y., Wu, W. & Zhang, H., 2004. Numerical model of particle dispersion in the wake of gas particle flows past a cylinder using discrete vortex method'.. *Powder technology,* Volume 162., pp. 73- 81.
51. Husimi, K., 1950. Note on Mayers' Theory of Cluster Integrals. *Journal of Chemical Physics,* Volume 12, pp. 682 - 684.
52. IEEE 754, 2008. *IEEE Standard for Floating-Point Arithmetic,* s.l.: IEEE.
53. Jensen, P. A., Stenholm, M. & Hald, P., 1997. Deposition investigation in straw-fired boilers. *Energy & Fuels,* Volume 11,, pp. 1048-1055.
54. Johnson, W. R., 1998. *'The Handbook of Fluid Dynamics'.* s.l.:CRC Press.
55. Jöller, M., Brunner, T. & Obernberger, I., 2007. Modelling of aerosol formation during biomass combustion for various combustor and boiler types. *Fuel Processing Technology,* Volume 88, p. 1136 – 1147.
56. Kær, S. K. & Rosendah, L., 2003. *Extending the modelling capacity of cfd codes applied to biomass-fired boilers.* Copenhangen, Denmark, Proc. ECOS, p. 251–264.
57. Kaer, S. K., Rosendahl, L. A. & Baxter, L. L., 2006. Towards a CFD-based mechanistic deposit formation. *Fuel,* Volume 85, No. 5-6,, pp. 833-843.
58. Kajitani, S., Suzuki, N., Ashizawa, M. & Hara, M., 2006. CO2 gasification rate analysis of coal char in entrained flow coal gasifier. Fuel, Volume 85, Issue 2, pp. 163-169.

59. Kansa, E. J., Aldredge, R. C. & Ling, L., 2009. Numerical simulation of two-dimensional combustion using mesh-free methods. *Engineering Analysis with Boundary Elements,* Volume 33, Issue 7, pp. 940-950.
60. Kaufmann, H., Nussbaumer, T., Baxter, L. & Yang, N., 2000. Deposit formation on a single cylinder during combustion of herbaceous biomass. *Fuel,* Volume 79, p. 141.
61. Khan, A. A., de Jong, W., Jansens, P. J. & Spliethoff, H., 2009. Biomass combustion in fluidized bed boilers: Potential problems and remidies. *Fuel Processing Technolgy,* Volume 90, pp. 21-50.
62. Kosinski, P. L. & Hoffmanna, A. C., 2005. An Eulerian–Lagrangian model for dense particle clouds. *Computers & Fluids,* Volume 36, Issue 4,, pp. pp. 714-723.
63. Kreyszig, E., 2006. *'Advanced Engineering Mathematics'.*. s.l.:J. Wiley and Son.
64. Kuppan, T., 2000. *Heat Exchanger Design Handbook.* s.l.:CRC Press.
65. Latva-Somppi, J. et al., 1997. Ultrafine ash particle formation during waste sludge incineration in fluidized bed reactors. *Combustion Science. Technology,* Volume 134,, pp. 433 - 455..
66. Le Bellac, M., Mortessagne, F. & Batrouni, G. G., 2004. *'Equilibrium and Non-Equilibrium Statistical Thermodynamics'.* s.l.:Cambridge University Press..
67. Leckner, B., Åmanda, L. E., Lücke, K. & Wertherb, J., 2004. Gaseous emissions from co-combustion of sewage sludge and coal/wood in a fluidized bed. *Fuel,* Volume 83, No. 4-5, pp. 477-486.
68. Lewy, H., 1957. An example of a smooth linear partial differential equation without solution. *Annals of Mathematics,* Issue 2nd Series 66 (1):, p. 155–158.
69. Lin, C., Peng, T. & Wang, W., 2010. Effect of particle size distribution on agglomeration/defluidization during fluidized bed combustion. *Powder Technology,* Volume Article in Press.
70. Lind, T. et al., 1997. *Fly ash deposition onto the convection heat exchangers during combustion of willow a circulating fluidized bed boiler.* s.l., Proceedings of an Engineering Foundation Conference on Mineral Matter in Fuels, Kona, Hawaii.
71. Lin, L., Gustafsson, E. & Stand, M., 2010. *High-Temperature Kinetics of Fine Biomass Char Particles in Air and CO2.* Florence, s.n., pp. 797 - 801.
72. Li, S. & Liu, W., 2004. *'Meshfree Particle Methods'.* s.l.:Springer.
73. Li, S. & Liu, W. K., 2002. Meshfree and particle methods and their applications. *Appl. Mech. Rev.,* Volume 55, Issue 1.
74. Li, S., Wu, A., Deng, S. & Pan, W., 2008. Effect of co-combustion of chicken litter and coal on emissions in a laboratory-scale fluidized bed combustor fuel. *Processing technology,* Volume 89, p. 7 – 12.
75. Liszka, T., 1984. An Interpolation method for an irregular net of nodes. *International Journal for the Numerical Methods in Engineering,* Volume 20, pp. 1599-1612.
76. Liszka, T. & Orkisz, J., 1980. 'The Finite difference method at arbitrary irregular grids and its application in applied mechanics'.. *Comp. Struct.,* Volume 11, pp. 83-95..

77. Liu, W. K. et al., 2000. Multi-scale methods. *International Journal for numerical methods in Engineering,* Volume 47, pp. 1343 - 1361.
78. Liu, Y. F., Mcelwain, D. L. S. & Donskoi, E., 1998. The Use Of A Modied Petrov-Galerkin Method For Gas-Solid Reaction Modelling. *IMA Journal of Applied Mathematics,* Volume 61 Issue 1, pp. 33-46..
79. Lockwood, F. C., Costen, P. G., Siddiqi, M. M. & Harrison, P. J., 2000. *Mineral Ash Transformation,* s.l.: Euro Clean Coal Net.
80. Lokare, S. S., 2006. *A mechanistic investigation of ash deposition in pulverized-coal and biomass combustion' PhD. Thesis.* s.l.:Brigham Young University.
81. Loo, S. v. & Koppejan, J., 2008. *The handbook of biomass combustion and co-firing.* s.l.:Earthscan.
82. Lorenz, E. N., 1962. Deterministic Non-periodic flow. *Journal of the Atmospheric Science,* Volume 30, p. 130 – 141.
83. Luo, K., Fan, J. & Cen, K., 2009. Transient Three dimensional simulation of particles dispersion in flows around a circle cylinder (Re= 140-200). *Fuel.,* Volume 80, pp. 1294-1301.
84. Lwin, Y., 2000. Chemical Equilibrium by Gibbs Energy Minimization on Spreadsheets. *Int. J. Engng Ed,* Volume 16, No. 4, pp. 335-339.
85. Magnussen, B. F. & Hjertager, B. H., 1976. *On mathematical modelling of turbulent combustion with special emphasis on soot formation and combustion.* Pittsburgh., In: 16th International symposium on combustion'. Cambridge. The Comb. Inst,, p. pp. 719–729.
86. Makkonen, P., 1999. *Artificially intelligent and adaptive methods for prediction and analysis of superheater fireside corrosion in fluidized bed boilers,* s.l.: University of Technology, Lappeenranta..
87. Matsumoto, A., 2000. Thermodynamic Quantities of the Frost-Kalkwarf Vapour-Pressure Equation. *Fluid Phase Equilibria,* Volume 172, Issue 2, pp. 105-110.
88. Mayer, J. E. & Mayer, M. G., 1940. *'Statistical Mechanics'.* s.l.:John Whiley and Sons.
89. McComb, W. D., 1994. *'The Physics of Fiulds Turbulence'.* Oxford UK: Oxford University Press.
90. Melenk, J. E. & Babuška, I., 1996. The partition of unity finite element method: Basic theory and applications. *Nuklearmedizin Nuclear Medicine ,* 139(1-4), pp. 198-204.
91. Meneveau, C., Poinsot, T. & Etssa, E., 1998. Simple Stochastic Model Particle Dispersion Including Intetia, Trajectory-Crossing and Continuity Effects. *Trans. of ASME,* Volume 120,, pp. 187-192.
92. Mile, J. T. R. et al., 1994. *Alkali Deposits Found in Biomass Power Plants,* s.l.: National Renewable Energy Laboratory, USA.
93. Miltner, M., Makaruk, A., Harasek., M. & Friedl, A., 2008. Computational fluid dynamic simulation of a solid biomass combustor: modelling approaches. *Clean Techn Environ Policy,* Volume 10, p. 165–174.
94. Mohanty, R. K. & Sigh, S., 2006. A new forth order discretization for single perturbed two dimensional non-linear elliptic boundary problems. *Applied Mathematics and Computation,* Volume 175, pp. 1400-1414.

95. Molintas, H. & Gupta, A. K., 2011. Kinetic study for the reduction of residual char particles using oxygen and air. *Applied Energy,* 88(1), pp. 306-315.
96. Mueller, C. et al., 2005. 'Deposition behaviour of molten alkali-rich fly ashes--development of a sub-model for CFD applications'. *Proceedings of the Combustion Institute,* 30(2), pp. 2991-2998 .
97. Mueller, C., Skrifvars, B., Backman, R. & Hupa, M., 2003. Ash Deposition prediction in biomass fired fluidised bed boiler –combustion of CFD and advance fuel analysis. *Progress in Computational Fluid Dynamics,* Volume Vol. 3, No. 2-4,, pp. 112-120..
98. Nielsen, H. et al., 2000. Deposition of potassium salts on heat transfer surfaces in straw-boilers: a pilot-scale study. *Fuel,* Volume 79, p. 131–139.
99. Nielsen, H. P., J., F. F., Dam-Johansena & K. Baxter, L. L., 2003. The implications of chlorine-associated corrosion on the operation of biomass-fired boilers. *Progress in Energy and Combustion Science,* 26(3), pp. 283-298.
100. Oakey, J. E. et al., 2003. *Review of status of advanced materials for power generation,* s.l.: DTI COAL R224 DTI/Pub URN 02/1509.
101. Obernbergera, I., Brunnera, T. & Bärnthaler, G., 2006. Chemical properties of solid biofuels—significance and impact. *Biomass and Bioenergy,* 30(11), pp. 973-982.
102. Olushola, A. S., Olaleka, F. S., Folahan, A. A. & Bhekumusa, X. J., 2012. Characterization of Fly Ash Generated from Matla Power Station in Mpumalanga, South Africa. *E-Journal of Chemistry,* 9(4), pp. 1788-1795.
103. Parsons Brinckerhoff Australia Pty Limited, 2005. *Tarong Northern Land Ash Emplacement project,* Brisbane, Australia: Tarong Energy Corporation Limited.
104. Patankar, S. V., 1980. *'Numerical Heat Transfer and Fluid Flow'.* Washington DC: Hemisphere.
105. Peng, D. Y. & Robinson, D. B., 1976. A new two parameters equation of state.' Industrial Engineering and Chemistry Fundamentals. *Industrial Engineering and Chemistry Fundamentals,* 15(1), pp. 59-64.
106. Pillow, A. F., 1970. Diffusion and conection in visous flows. *Bulletin of the Australian Mathematical Society,* Volume 2, pp. 145-164.
107. Press, H. W., Flannery, B. P., Teukosky, S. A. & Vetterling, W. T., 1989. *'Numerical Recipes The Art of Scientific Computing (Fortran Version)'.*. s.l.:Cambridge University Press.
108. Pyykőnen, J. & Jokiniemi, J., 2003. Modelling alkali chloride superheater deposition and its implications. *Fuel Processing Technology,* Volume 80, p. 225 – 262.
109. Richards, G. H., Harb, J. N. & Zygarlicke, C. J., 1984. *Inorganic transformations of ash deposition in combustion.* ASME, New York, Engineering foundation conference proceedings.
110. Robertson, D. et al., 2002. Electron Microscopy Characterization of Aluminum Alloy - Fly Ash Composites. *Microscopy and Microanalysis,* 8(Suppl. 2), pp. 1278 - 1279.
111. Robinson, A. et al., 1984. *Fireside Issues Associated with Coal-Biomass Co-Firing.* New York., Engineering foundation conference proceedings, ASME.

112. Salvetti, M. V., Marchioli, C. & Soldati, A., 2006. *Lagrangian tracking of particles in large- eddy simulation with fractal interpolation.* Porquerolles, France, Conference on Turbulence and Interactions TI2006,.
113. Scharler, R., Kuerten, J. G., Schulze, K. & Obernberge, I., 2007. *Numerical simulation of ash particle impaction in tube bundles - A case study as a basis for a CFD based ash deposit formation model in convective heat exchangers,* Berlin: VDI-Berichte.
114. Schreiber, F., Zanini, F. & Roosen-Runge, F., 2011. *Virial Expansion - A Brief Introduction,* Tubingen: Universitat Tubingen.
115. Segerdahl, K., Pettersson, J., Svensson, J. E. & Johansson, L. G., 2004. Is Kcl(g) Corrosive at Temperature Above its Dew Point? Influence of KCl(g) on Initial Stages of the High Temperature Corrosion of 11% at 600ºC. *Material Science Forum,* Volume 461-464,, pp. 109-116.
116. Skrifvars, B. J., Westen-Karlsson, M., Hupa, M. & Salmenoja, K., 2010. Corrosion of superheater steel materials under alkali salt deposits. Part 2: SEM analyses of different steel materials. *Corrosion Science,* 52(3), pp. 1011-1019,.
117. Smoot, L. D. & Smith, P. J., 1985. *Coal Combustion and Gasification (The Plenum Chemical Engineering Series).* s.l.:Springer.
118. Sobey, I. J., 1982. Oscillatory flows at intermediate Strouhal number in asymmetry channels. *Journal of Fluid Mechanics, Vol 125:,* p. 359–373.
119. Spalding, D. B., 1970. A Novel Finite-differnce Formulation for Differential Expressions Involving both First and Second Derivatives. Volume 4, p 551..
120. Spalding, D. B., 1972. A Novel Finite-difference Formulation for Differential Expression Involving both First and Second Derivation. *Int J. Numer. Methods Eng.,* Volume 4, pp. 551-559.
121. Spalding, D. B., 1976. Mathematical models of turbulent flames: a review. *Combustion and Flames,* Volume 13, pp. 3-25.
122. Srinivasachar, S., Helble, J. J. & Boni, A. A., 1990. *An experimental study of the inertial deposition of ash under coal combustion conditions.* 23rd Symposium (International) on Combustion, Pittsburgh, The Combustion Institute.
123. Srivastava, S. C., Godiwalla, K. M. & Banerjee, M. K., 1997. Fuel ash corrosion of boiler and superheater tubes. *Journal of Materials Science,* Volume 33 No. 4, p. 835 – 849.
124. Strandström, K., Mueller, C. & M., H., 2007. Development of ash particles deposition model considering build-up and removal mechanism. *Fuel Processing Technology,* 88(11-12), pp. 1053-1060.
125. Tomeczek, J., 1994. *Coal Combustion,.* s.l.:Krieger Publishing Company.
126. Tomeczek, J., Palugniok, H. & Ochman, J., 2004. Modelling of deposits formation on heating tubes in pulverized coal boilers. *Fuel,* 83(2), pp. 213-221.
127. Tomeczek, J. & Wacławiak, K., 2009. Two-dimensional modelling of deposits formation on platen superheater in pulverized coal boilers. *Fuel,* 88(8), p. 1466–1471.
128. Tosum, I., 2002. *Modelling in transport phenomena: a conceptual approach.* s.l.:Elsevier.

129. Tumuluru, J. S. et al., 2011. *A review on biomass torrefaction process and product properties.* Stillwater USA, Symposium on Thermochemical.
130. Vagonyte, E. & Minchener, A., 2007. *Status of co-firing technology within Europe.* s.l.:Report by European Biomass Association..
131. Valentine, J. R. & Smith, P. J., 2002. *Numerical predictions of deposition with a particle cloud tracking technique.* s.l.:Reaction Engineering.
132. Vepsalainen, B. M. K. H. T. L. T. T. A., 2009. *Development and Validation of a 3-Dimensional CFB Furnace Model.* Clearwater, Florida, 34th International Technical Conference on Coal Utilization & Fuel Systems.
133. Versteeg, H. K. & Malalasekera, W., 1995. *An Introduction to Computational Fluid Dynamics.* s.l.:Longmans.
134. Walas, S. M., 1994. *'Phase Equilibria in Chemical Engineering'.* s.l.:Butterworth..
135. Walsh, P. M. et al., 1990. Deposition of bituminous coal ash on an isolated heat exchanger tube: Effects of coal properties on deposit growth. *Prog. Energy Combust. Sci,* 16(4), pp. 327--345.
136. Wang, Y. Y. L., 2008. CFD Studies on Biomass Thermochemical Conversion. *Int. J. Mol. Sci,* 9,(1-2), pp. 1108-1130.
137. White, F. M., 2008. *Fluid mechanics.* s.l.:McGraw-Hill.
138. Wibberley, L. J. & Wall, T. F., 1982. Alkali-ash reactions and deposit formation in pulverized-coal-fired: experimental aspects of sodium silicate formation and the formation of deposits. *Fuel,* 61(1), pp. 93-99.
139. Wilson, R. J. & Beineke, L. W., 1979. *Application of Graph Thoery.* London: Achademic Press Inc (London) Ltd.
140. Witt, P. J., Perry, J. H. & Schwarz, M. P., 1997. *Application of CFD to Fluidised Bed System.* s.l., Inter Conf. on CFD in Mineral & Metal Processing and Power Generation..
141. Ye, D. P., Agnew, J. B. & Zhang, D. K., 1998. Gasification of a South Australian low-rank coal with carbon dioxide and steam: kinetics and reactivity studies. *Fuel,* 77(11), pp. 1209-1219.
142. Zdravkovich, M. M., 2003. *Flow around circular cylinders part 2.* s.l.:Oxford Science Publication.
143. Zhenga, Y., Jensena, P. A. J. A. D., Sander, B. & Junker, H., 2007. Ash transformation during co-firing coal and straw. *Fuel,* 86(7-8), pp. 1008-1020.
144. Zhou, H., Jensen, P. A. & Frandsen, F. J., 2007. Dynamic mechanistic model of superheater deposit growth and shedding in a biomass fired grate boiler. *Fuel,* 86(10-11), p. 1519–1533.
145. Ziada, S., 2006. Vorticity Shedding and Acoustic Resonance in Tube Bundles. *J. of the Braz. Soc. of Mech. Sci. & Eng,* XXVIII(2), pp. 186 - 199.

Appendixes

Appendix A. - Equations and Formula

Equations and formula used in this thesis and not explained are included here:

A1. - Gibbs Entropy Equation

$$S = -k \sum_i p_i \log p$$

Where

- k_B= Boltzmann Constant
- i = Energy state
- p_i = Probability of a energy state will occur during the system's fluctuations

A2. -Reynolds Number, Re

$$Re = \frac{VL}{\nu}$$

Where

- V is the mean fluid velocity (m/s)
- L is a length of the object that the flow is going through or around (m)
- ν is the kinematic viscosity ($\nu = \mu / \rho$) (m^2/s)

A3. - Raoult's Law

$$p = p_A^* x_A + p_B^* x_B + \cdots$$

Where

- p^*_i is the vapour pressure of the pure component.
- x_i is the mole fraction of the component in solution.
- p = saturation pressure

A4. – Sherwood number, Sh

$$Sh = \frac{\dot{\beta}\ \mathrm{D}}{L}$$

Where

- L is a characteristic length (m)
- D is mass diffusivity ($m^2.s^{-1}$)
- $\dot{\beta}$ is the mass transfer coefficient ($m.s^{-1}$)

A5. – Nusselt Number, Nu

$$Nu = \frac{h \cdot L}{k_f}$$

Where

- h = convective heat transfer coefficient
- k_f = thermal conductivity of the fluid
- L = characteristic length

A6. – Schmidt Number, Sc

$$Sc = \frac{\nu}{D} = \frac{\mu}{\rho D}$$

Where

- ν is the kinematic viscosity
- D is the mass diffusivity
- μ is the dynamic viscosity
- ρ is the density

A7.- Churchill–Bernstein (Mass transfer definition)

$$Sh = 0.3 + \frac{0.62\,\mathrm{Re}_D^{1/2}\,Sc^{1/3}}{\left[1+(0.4/SC)^{2/3}\right]^{1/4}}\left[1+\left(\frac{\mathrm{Re}_D}{282000}\right)^{5/8}\right]^{4/5} \quad Sc\,\mathrm{Re}_D \geq 0.2$$

Where

- Sh is Sherwood number
- Sc is Schmidt number
- Re is Reynolds

A8. – Boltzmann Entropy Equation

$$S = k \sum W$$

Where

- S is entropy
- k_B is Boltzmann Constant
- W is the number of microstates consistent with the given microstate.

A9. – Particle relaxation time constant in a fluid

$$\tau = \frac{\rho_p d_p^2}{18\mu}$$

where

- τ is the particle relation time
- ρ_p is density of particle
- d_d is particle diameter
- μ is viscosity

Appendix B. - Real and Potential Flows

For example a laminar flow around cylinder is defines by its streamlines by the potential flow function.

$$G(z) = z + \frac{1}{z} \tag{B-1}$$

Where z relates to a potential function that describes a streamlines or flow sheet passing diametrically around the cylinder.

This potential flow function only applies when the properties of the fluid are incompressible, inviscid and irrotational. With these properties this fluid will obey the laws of conservation of mass and conservation of momentum. The inviscid fluid is describes by Euler Laws as

- $\nabla \cdot \mathbf{u} = 0$ (Conservation law of mass) (B-2)
- $\frac{\partial}{\partial \mathrm{t}}\mathbf{u} + (\mathbf{u} \cdot \boldsymbol{\nabla})\mathbf{u} = -\frac{\mathbf{1}}{\boldsymbol{\rho}}\boldsymbol{\nabla}\rho$ (Conservation of momentum) (B-3)

where $\boldsymbol{u}$ is the flow velocity, ρ is the fluid density and $\boldsymbol{\nabla}$ the gradient operator. The irrotational property of a fluid is that which describes the characterised the flow to follow the geometric shape of the cylinder. In pure mathematical terms the irrotational property is defines using velocity field **v** and is said to be irrational if the curl operator is zero. These properties of 'irrotational' and 'inviscid' hold true except at point near to the buff object such as a cylinder. At this point a point close the cylinder surface this classical mathematics theory of fluid flow departs from the experimental observation.

In classical mathematics a body moving through a fluid at constant velocity **v** is assumed that the flow is at rest at point infinitely far away. Such a fluid flow will follow the body, such that the velocity field is of the form $\boldsymbol{u}(\boldsymbol{x}, t) = \boldsymbol{u}(\boldsymbol{x} - \mathbf{v}\, t, 0)$, and thus

$$\frac{\partial \boldsymbol{u}}{\partial t} + (\boldsymbol{v} \cdot \boldsymbol{\nabla})\boldsymbol{u} = \mathbf{0} \tag{B-4}$$

since there exists a velocity potential φ such that $\boldsymbol{u} = \nabla\varphi$, this can be integrated with respect to **x**

$$\frac{\partial \varphi}{\partial t} = -\mathbf{v} \cdot \boldsymbol{\nabla\varphi} + \boldsymbol{R}(\mathbf{t}) = -\boldsymbol{v} \cdot \boldsymbol{u} + \boldsymbol{R}(\boldsymbol{t}) \tag{B-5}$$

where R(t) is a function of time with respect to **x**. The force **F** that the fluid exerts on the body is given by the surface integral

$$F = -\int_A \rho \boldsymbol{n} dS \tag{B-6}$$

where A is body surface and n the normal vector on the body surface There it follows from eq. (B-6) that

$$\mathrm{p} = -\rho\left(\frac{\partial\varphi}{\partial \mathrm{t}} + \frac{1}{2}\mathbf{u}\cdot\mathbf{u}\right) = \rho\left(\mathbf{v}\cdot\mathbf{u} - \frac{1}{2}\mathbf{u}\cdot\mathbf{u} - \mathrm{R(t)}\right) \tag{B-7}$$

thus

$$\mathrm{F} = -\int_{\mathrm{A}} \mathrm{p}\mathbf{n}\mathrm{dS} = \mathrm{p}\int_{\mathrm{A}} \left(\frac{1}{2}\mathbf{u}\cdot\mathbf{u} - \mathbf{v}\cdot\mathbf{u}\right)\mathbf{n}\mathrm{dS} \tag{B-8}$$

with the contribution of R(t) to the integral being equal to zero.

Since velocity is a vector quantity, it's more convenient to work in vector components. The *k*th component of this eq. (B-9) reads

$$\mathrm{F_k} = \rho\int_{\mathrm{A}} \sum_{\mathrm{i}}\left(\frac{1}{2}\mathrm{u_i^2} - \mathrm{u_i v_i}\right)\mathrm{n_k dS}. \tag{B-9}$$

Let *V* be the volume occupied by the fluid. The divergence theorem says that

$$\frac{1}{2}\int_{\mathrm{A}} \sum_{\mathrm{i}} \mathrm{u_i^2 n_k dS} = -\frac{1}{2}\int_{\mathrm{V}} \frac{\partial}{\partial \mathrm{x_k}}\left(\sum_{\mathrm{i}} \mathrm{e_i^2}\right)\mathrm{dV} \tag{B-10}$$

The right-hand side is an integral over a finite volume, so this needs some justification, which can be provided by applying the potential theory (Kreyszig, 2006) to show that the velocity ***u*** must fall off as r^{-} – corresponding to velocity potential field dipole function z in this case of 3-dimensional finite body - since for a cylinder the complex potential function in polar coordinates is

$$z = re^{I\theta} \tag{B-11}$$

By substituting (B-1) into (B-11) will results in

$$z = re^{I\theta} + \frac{1}{re^{I\theta}} \tag{B-12}$$

The imaginary part of the function G represents the streamline function of flow around the cylinder φ(r, θ) in polar coordinates.

$$\varphi = \frac{(-1+r^2)\sin(\theta)}{r} \tag{B-13}$$

If a unit circle radius (i.e. r=1) then far enough away from the cylinder the effect of 1/z will be small compared to z and therefore the streamlines will be parallel. Hence with the streamline function φ and the cylinder radius r the path of the fluid around the cylinder can be plotted for fixed points from the cylinder's surface. This theoretical behaviour of fluid flow pass smoothly around a cylinder is not normally found in real fluid flows as will be discussed next. The effect of the reaction to the force applied to the cylinder from the flow of fluid is called drag and can be introduced by integrating the pressure p_s over the surface of the cylinder.

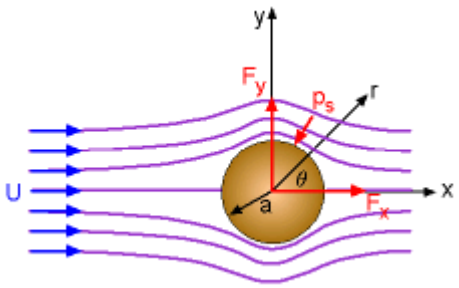

Figure B-1. Velocity and Lift force vectors derive from the fluid flow around a cylinder

$$F_x = -\int_0^{2\pi} P_s \cos\theta a \, d\theta$$

$$= -\int_0^{2\pi} \left[P_0 + \frac{1}{2}\rho U^2(1 - 4\sin^2\theta)\right]\cos\theta \, a \, d\theta$$

$$= 0 \tag{B-14}$$

While lift is the resulting force acting perpendicular to the uniform flow direction and can be obtained by

$$F_y = -\int_0^{2\pi} P_s \sin\theta a \, d\theta$$

$$= -\int_0^{2\pi} \left[P_0 + \frac{1}{2}\rho U^2(1 - 4\sin^2\theta)\right]\sin\theta \, a \, d\theta$$

$$F_y = 0 \tag{B-15}$$

Since the assumption and boundary conditions of potential flow is that flow is incompressible and inviscid then the upstream dynamic pressure at the upstream stagnation point has value of

$$p_d = \rho U^2 \,/\, 2 \tag{B-16}$$

where ρ is density, U is velocity and P_d is the dynamic pressure. Therefore P_d represents the pressure value needed to decelerate the free stream flow of speed U. This flow pattern is symmetrical both upwind and downwind of the tube. Therefore the same pressure value will appear at the downstream stagnation point. This symmetry arises only because the flow is completely frictionless and a mathematical defined theoretical flow.

The low pressure on sides on the cylinder will be expected to provide the centripetal acceleration of the flow. Integrating the centripetal acceleration over the radius 'a' in Figure B.1 yields minimum pressure $p_{s,}$ for the velocity U of gas density ρ as.

$$p_s - p_\infty \approx -\rho U^2 \tag{B-17}$$

The exact solution for the lowest pressure is

$$p_s - p_\infty = -\frac{3}{2}\rho U^2 \tag{B-18}$$

In the low pressure side of the tube the maximum velocity V at P_s will be V=2U. This increase in velocity on the low pressure side is accounted because of the centripetal acceleration needed to maintain the conservation of volume of the fluid passing over the tube.

With potential flow solution develop in this chapter based on the assumption of inviscid flow and implies that drag tends to vanish. In real fluid flow the viscous effects are important and will cause the flow to separate away from the cylinder and drag is always non zero in actual flows. This discrepancy is called d'Alembert paradox.

In real fluid flows the separation from cylinder caused by a mixture of pressure drag and skin friction drag. Skin friction drag is the result of the interaction of the fluid with the surface and the effect of fluid viscosity boundary layers. In general, for stationary bluff bodies such as cylinders then pressure drag is much greater than skin friction drag.

A potential flow or real fluids flow described by Euler's law are scale variant and are therefore not applicable to the study of particles motion in the size that ranges from sub micro to millimetre size. It's not possible to determine the exact position of particles in respect to time in a fluid flow using Euler's law because the fluid is assumed to be a continuum.

Appendix C. - Graph Theory

C1 Fundamental definitions

This chapter is not a full text on graph theory, but a brief introduction into the principle properties of plane and planer graphs. The text will outline the basic properties of a class of graph and then extent the application of these basic properties to the solution of equation in a geometric space. While general statements and discussion will be written in the third person (i.e. 'it', 'its' or 'it is'), mathematical statements and proofs in graph theory are written in the first person using the term 'we'. The reader should be aware of the change in personage within this text and the reason for this.

Graph Theory is a branch of mathematics is connected to the study of planer graphs and their properties. A planer graph is best described as a graph that can be embedded in a plane

The following two graphs are examples of planer graphs

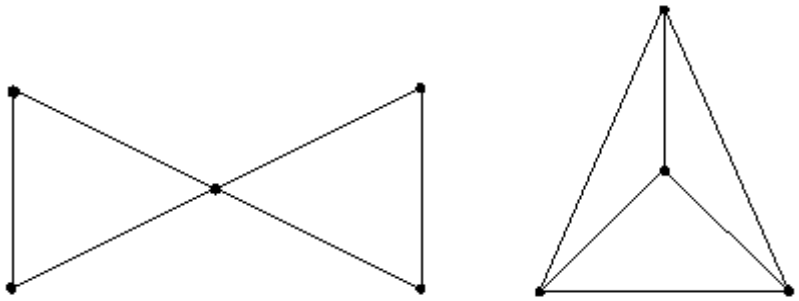

(C-1)

The following graphs are examples of non-planner graphs, within the graph some lines cross and are not joined.

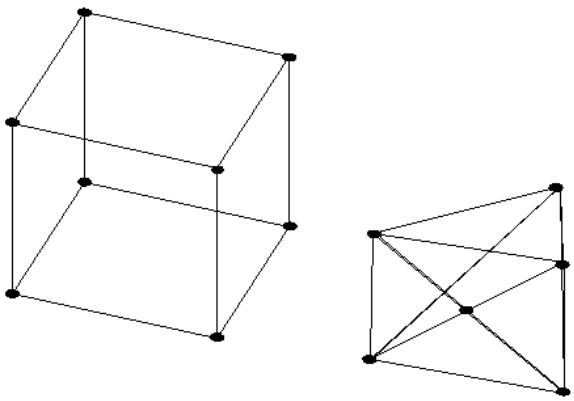

(C-2)

A planer graph can be non-planer graph, in which case it becomes a plane graph, for example a square prism end on is a plane graph. Since the face of a square prism can be orientated so that it is embedded in a flat plane, it's obvious that it is a plane graph.

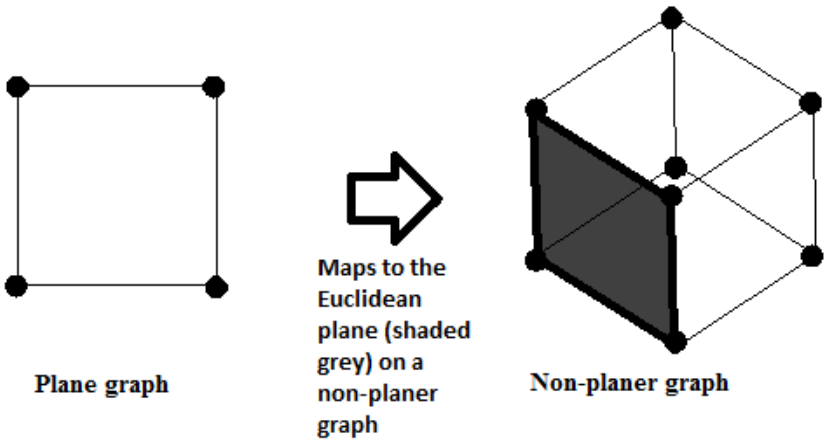

(C-3)

A precise definition of plane graphs can be abstracted to a series of vertices and edges. Vertices can also be called nodes or points and edges can also be called lines, in the following example there are 6 vertices and 7 edges.

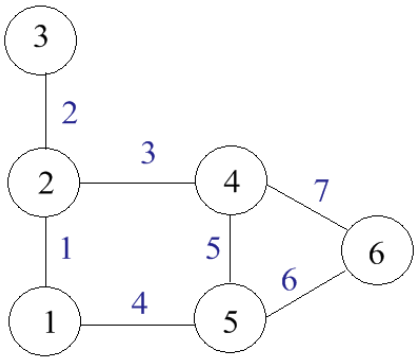

(C-4)

C2. Plane Graph

A plane graph can be replicated as abstract functions as a finite set of vertices (V) and edges (E) as (V, E). In the Euclidean plane $\mathbb{R}^2$, a *plane graph* has the following properties

i. $V \subseteq \mathbb{R}^2$;
ii. every edge is an arc between two vertices;
iii. different edges have different end points;

iv. The interior of an edge contains no vertex and no point of any other edge.

For a plane graph to be defined with the symbol *G* in this natural way, it will have vectors *V* and is therefore expressed as the linkage of vectors and graph as *G* on *V*. This definition of *G* on *V* will also extend to sub-graphs within the principle graph *G*, for example *H* is a sub-graph of *G*, therefore the vectors associated with the sub-graph is expressed as *H* on *V*.

When *G* is a plane graph the region $\mathbb{R}^2 \backslash G$ is define as a face of *G*, all faces of plane graphs are open subset of the Euclidean plane $\mathbb{R}^2$ and hence are bounded by *G*. This bounding of the faces within the graph *G* is described as the frontiers in *G*. These frontiers are held within a large disc *D* than includes all the frontiers of *G*. Since *G* is bounded by the frontiers faces, one of its faces inside the disc *D* will be unbounded and the remaining faces inside G will be bounded. The faces of *G* are denoted by *F(G).*

Isomorphism

Within the subject of graph theory isomorphism of the graph is the direct one relationship to one relationship (or a bijection) between vertex sets of *G* and *H*

$$f: V(G) \rightarrow V(H)$$

such that two vertices *u* and *v* in *G* are adjacent in *G* if and only if *u* and *v* are adjacent in *H.*

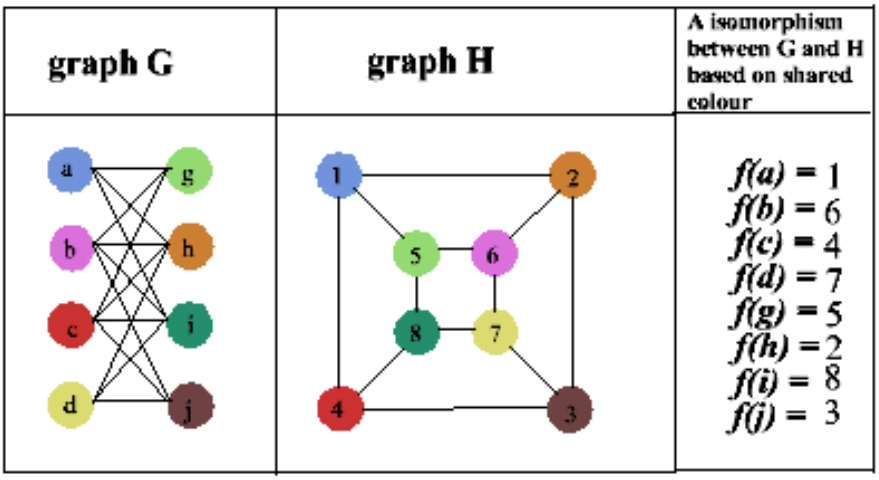

(C-5)

For an undirected graph *G* between two vertices *u* and *v* the edges are reference as e_1. A subdivision vertex *w* on *G* produces two edges e_1 and e_2 and sub-graphs labelled *G'*, within the undirected graph H.

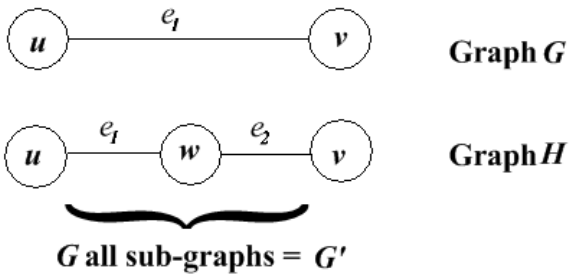

(C-6)

The graph *G* is homomorphism with *G'* if *G* can be mapped to *G'* and the graphs of *G* and *G'* respect their structures on the graph of H. In the abstract a graph homomorphism *f* from graph *G= (V, E)* to *G'= (V, E)*, is written as $f = G \rightarrow G'$, is a mapping between $f: V \rightarrow V'$ from the vertex set *G* to the vertex set *G'* such that $\{u, v\} \in E$ implies that $\{f(u), f(v)\} \in E'$.

Up to now we have applied graph homomorphism to undirected graph. To complete the study of graph isomorphism then it's important to include directed graph. A directed graph or digraph is a pair *G= (V, A)* of

- a set *V*, called vertices or nodes
- a set *A* of ordered pairs of vertices called arcs, directed edges, arrows

Given a directed graph G then in abstract the graph homomorphism *f*: *G= (V, E)* to *G'= (f(u), f(v))*, is an arc of *G'* if *G= (f(u), f(v))* is an arc of *G*.

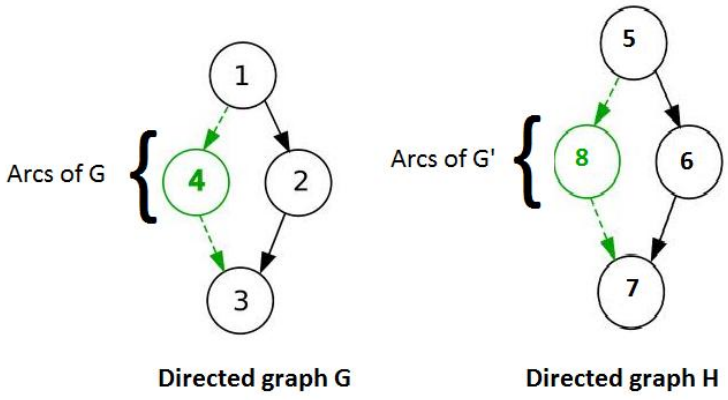

(C-7)

If there exist a homomorphism $f: G \rightarrow H$ then we write $G \rightarrow H$, else if there is not then we write $G \nrightarrow$H. An isomorphism is a bijective homomorphism between a vertices set.

Appendix D. - Perturbation, Probability Density and Graph Theory

Perturbation theory consists of mathematical methods that are used to find approximations to problems that cannot be solve exactly. The mathematical method seeks to find an approximated solution by computing a series expansion from an exact solution of a similar problem. The solution of the position change of many-bodies in a fluid is one problems that is solvable using permutations theory.

For a single particle of mass *m* at a point X the motion of the particle to X' is independent of time boundary but is expressed in terms of the conservation of energy.

$$\mathbf{H} = \mathbf{T} + \mathbf{U} + \mathbf{V} \tag{D-1}$$

Where H is the Hamiltonian Interaction, T is the Kinetic Energy, U is the internal energy and V is the Potential Energy.

To apply the Hamiltonian Interactions to the motion of particles then a system of generalised coordinates is applied adopting Lagrangian mechanics. The Hamilton equations are rearranged as a Lagrangian interaction.

$$\mathrm{L} = \mathrm{T} + \mathrm{V} \tag{D-2}$$

For a series of coordinate points

$$\{q_i | i = 1, \dots, N\} \tag{D-3}$$

Then the kinetic energy of body a time t is defined by the Lagrangian L, when V=0, as

$$\mathrm{L} = \frac{d}{dt}\left(\frac{\partial T}{\partial \dot{q}}\right) - \left(\frac{\partial T}{\partial q_i}\right) + 0 \tag{D-4}$$

It's assumed that a body moves from an initial start position to the next coordinate point as

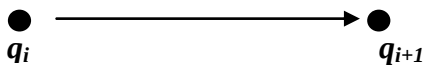

Then for such event of a particle to move from q_i to q_{i+1}, independent of time *t*, is a function of a probability density function P. For any particle q_i will have a probability of being in the vicinity of coordinate q_{i+1} is therefore P_i. The general form of the Lagrangian time independent motion of a particle is

$$\mathrm{P}_i\left(q_i, \dot{q}_{i,} t\right) = \frac{\partial L}{\partial q} \tag{D-5}$$

Rewriting eq. (D-6) in terms of velocity then

$$\mathrm{H} = \sum \dot{q}_i \frac{\partial L}{\partial \dot{q}_i} - \mathrm{L} = \sum \dot{q}_i \mathrm{P}_i - \mathrm{L} \tag{D-6}$$

This is the Legendre transformation of the Lagrangian L.

For any particle to exist at point q_{i+1} its initial position q_i has to be known. The change in position of q_i to q_{i+1} in time t when the initial and final position of particles are unknown are a key element of tracking the path of particles in turbulent flow. The positional uncertainty in this problem has a solution that is resolved by adopting an evolution equation of a many-body system. Consider a simple dynamic system, characterized by a variable X(t), which satisfies the Hamilton equation.

$$\frac{d\mathrm{X}}{dt} = [\mathrm{X}, \mathrm{H}] \tag{D-7}$$

where the Poisson's bracketed terms [ ] are define in eq. (D:7) and H is the Hamiltonian of the system. If eq. (D-8) represents a one dimensional oscillator, where X is the displacement from the equilibrium at any time *t* and H is the sum of the kinetic and potential energies

In a general case when using eq. (D-8) it's likely that X(*t*) will be found given X(0). Assuming that derivatives of X exists to all orders, then X(*t*) can be written in terms of X and its derivatives at *t* = 0 by means of a Taylor series

$$\mathrm{X}(t) = \mathrm{X}(0) + t\dot{\mathrm{X}}(0) + \frac{t^2}{2}\ddot{\mathrm{X}}(0) + \cdots$$

$$[\mathrm{H}]\mathrm{X} = [\mathrm{X}, \mathrm{H}] \tag{D-8}$$

where a dot over a character represents the derivative with respect to time. The derivative of X to any order *n* can be denoted by eq. (D-10). Appling the Poisson brackets operation to eq. (D-8)

$$\dot{\mathrm{X}} = [\mathrm{X}, \mathrm{H}] = [\mathrm{H}]\mathrm{X} \tag{D-9}$$

It follows that the derivatives of X can be written as

$$\ddot{\mathrm{X}} = \left[\ddot{\mathrm{X}}\mathrm{H}\right] = \left[[\mathrm{X},\mathrm{H}],\mathrm{H}\right] = [\mathrm{H}^2]\mathrm{X} \tag{D-10}$$

and so on for any order *n*.

$$\mathrm{X}(t) = \mathrm{G}(t - t')\mathrm{X}(t') \tag{D-11}$$

With the appropriate substitution from eq. (D-9), eq. (D-10) and eq. (D-11) into eq. (D-14) can easily obtain X(*t*) through using the form

$$\mathrm{X}(t) = \sum_{n=0}^{\infty} \frac{t^n[\mathrm{H}^n]\mathrm{X}(0)}{n!} \tag{D-12}$$

The function G(*t*) is known as the propagator, and is defined as

$$G(t) = \exp\{[H]t\} \tag{D-13}$$

For stationary systems, which depend only on the difference between times and not their absolute value, then eq. (D-13) can be generalized as.

$$\mathrm{X}(t) = \mathrm{G}(t)\mathrm{X}(0) \tag{D-14}$$

The idea of a propagator comes from quantum field theory where its significance defines the probability amplitude that corresponds to the propagation of a particle from a wave. The quantum field theory approach is applied here as a solution to a many-body problem that is scale independent in terms of individual particle dimensions or an individual particle mass.

When quantum field theory is applied to sub-atomic particles the probability amplitude becomes the propagator and is defined as

$g(\mathbf{X}, \mathbf{X}' : t, t')$ = probability amplitude that, if at time t' a particle appears at **X**' to a system in its ground state, the particle will be found at X for some time t > t', with the system still in its ground state

$g(\mathbf{X}, \mathbf{X}' : t, t') = 0,$ if $t < t'$

The associated probability density $P(\mathbf{X}, \mathbf{X}' : t, t')$ is given by

$$P(\mathbf{X}, \mathbf{X}' : t, t') = g(\mathbf{X}, \mathbf{X}' : t, t')g^*(\mathbf{X}, \mathbf{X}' : t, t') \tag{D-15}$$

where g is the Green function of the Schrödinger equation and g* is the complex conjugate. This use of quantum field theory is applied to the many-body problem by interpreting the propagator operation directly in terms of the probability density. The quantum propagator *P* is

denoted as *G* and replaces the classical propagator as $G(\mathbf{X}, \mathbf{X}': t, t')$. The original definition of a quantum field theory propagator in eq. (D-19) can now be modified to fit the many- body problem, as

$G(\mathbf{X}, \mathbf{X}': t, t') =$ probability density that, if at time t' a particle is at rest at a point at X' at a time t', then at a later time t it will be found at point X

$$G(\mathbf{X}, \mathbf{X}': t, t') = 0, \text{ if } t < t' \qquad \text{(D-16)}$$

If there is no interaction with the existing particles of the many-body system, then a single particle of interest (called a test particle) moves from **X**' at a time *t*' to **X** at time *t* in a purely deterministic way. In such a case the propagator G = G_0 and is called the free propagator.

D1 Perturbation and Feynman diagrams

The propagator of the many-body theory can be applied to both strong interaction such as collision and weak interaction such as an applied force or forces. The test particle in this classical (non-quantum) problem will move from a point **X'** at time *t'* in a medium containing other particles or scattering centres. If there is no interaction the test particle will arrive at point **X** at time *t.* It's likely though that the test particle will interact with other particle or external forces. Therefore if the test particle undergoes an interaction there will be a delayed or its path will be altered. If such an event occurs what is its probability of the test particle reaching **X** at time *t.*

Consider the case of a series of fixed scattered centres labelled {A, B, C, …}, that are located a spatial positions {$\mathbf{x_A}$, $\mathbf{x_B}$, $\mathbf{x_C}$, …}, and that they have the probability of scattering the test particle {P(A), P(B), P(C), …}. The total probability of the test particle going from a point X' to a point X is found by adding up the all the probabilities of all the possible paths the test particle could move through the system. The overall probability (i.e. the propagator) will be the expansion of the order of each term that the test particle has interaction with the scattering centres. This expression would have the form such as

$$G(\boldsymbol{x}, \boldsymbol{x}') = G_0(\boldsymbol{x}, \boldsymbol{x}') + G_1(\boldsymbol{x}, \boldsymbol{x}') + G_2(\boldsymbol{x}, \boldsymbol{x}') \cdots \qquad \text{(D-18)}$$

where G_o(**x, x'**) is the free propagator corresponding to the case where the test particle travels from **x**' to **x** without being scatter by any interaction with the system.

The term $G_1(\mathbf{x}, \mathbf{x'})$ is a first order term, the result of a test particle being scattered once only while travelling between $\mathbf{x}$' to $\mathbf{x}$. The term $G_2(\mathbf{x}, \mathbf{x'})$ is a second order term, again the result of a test particle being scattered twice. This pattern of expression is repeated such that $G_n(\mathbf{x}, \mathbf{x'})$ is the nth term of the test particle being scattered n times while travelling between $\mathbf{x}$' to $\mathbf{x}$.

If the probability of scattering is applied to the expression in eq. (D-21) for the first scattering centres A as an example. Then there arises a series of events of which determine the path of the test particles these are;

- the probability of the particle moving between $\mathbf{x}$' to $\mathbf{x_A}$ (i.e. $G_o(\mathbf{x'}, \mathbf{x_A})$),
- the probability of the particle is scattered by A (i.e. P(A))
- and the subsequent probability that the test particle moves from $\mathbf{x_A}$ to $\mathbf{x}$ (i.e. $G_o(\mathbf{x}, \mathbf{x_A})$).

The resulting probability for the process of a test particle moving from $\mathbf{x}$' to $\mathbf{x}$ is the product of the probability of three separate scattering events just specified. Therefore combining the contribution of each of the probabilities for the three separate scattering events in to right hand side of eq. (D-17), results in a first order equation in terms of A as follows;

$$G_1(\boldsymbol{x}, \boldsymbol{x'}) = G_0(\boldsymbol{x}, \boldsymbol{x'})P(A)G_0(\boldsymbol{x}, \boldsymbol{x'}) \qquad \text{(D-19)}$$

Including all first order terms for B, C, etc, will expand eq. (D-17) so that it can be written as

$$G_1(\mathbf{x}, \mathbf{x'}) = G_0(\mathbf{x}, \mathbf{x_A})P(A)G_0(\mathbf{x_A}, \mathbf{x'}) + G_0(\mathbf{x}, \mathbf{x_B})P(B)G_0(\mathbf{x_B}, \mathbf{x'}) + G_0(\mathbf{x}, \mathbf{x_C})P(C)G_0(\mathbf{x_C}, \mathbf{x'}) \ldots \qquad \text{(D-20)}$$

The second order terms are more complicated since they are now the probability of two types of interactions. In the first interaction type results in a first order expression of a test particle being scattered once from an interaction either centre A or B only. In the second interaction, the second order form is an outcome of a test particle being effect twice by the two scattered centres A and B. This second order on the right hand side of eq. (D-18) can be written as

$$G_2(\mathbf{x}, \mathbf{x'}) = G_0(\mathbf{x}, \mathbf{x_A})P(A)G_0(\mathbf{x_A}, \mathbf{x_A})P(A)G_0(\mathbf{x_A}, \mathbf{x'}) + G_0(\mathbf{x}, \mathbf{x_B})P(A)G_0(\mathbf{x_A}, \mathbf{x_B})P(B)G_0(\mathbf{x_B}, \mathbf{x'}) \ldots \qquad \text{(D-21)}$$

the series can be completed by writing down all possible parings from {A, B, C, …}, including repetitions.

In this way all the expansion of the power series $G(\boldsymbol{x}, \boldsymbol{x'})$ can be obtained to all orders *n* with elements using the propagator G_0. However, as the left hand side of the combinatorial

equation G(***x, x'***) is expanded on the right hand side in powers to order *n*, then the complexity of the calculation will increase. At some stage the combinatorial equation G(***x, x'***) will becomes too complex to write down and hence it's easier to use graph (or diagrams) to replace the algebraic symbols. From now on the term diagram will be used extensively instead of graphs when discussing the expansion of a perturbation series.

The diagram uses a symbol which is the topological equivalent of the combinatorial equation G(***x, x'***). The expansion of eq. (D-20) that is associated with the perturbation series is constructed from terms that substituting the diagrams for mathematical symbols.

Table D-1. Equivalence of mathematical symbol to diagram part

Mathematical symbol	Diagram part
$G_o(\mathbf{x}, \mathbf{x'})$	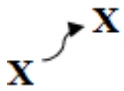
G(***x, x'***)	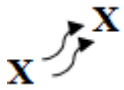
P(A)	

In Table D-1 the scattering probability P references scattering centre A, but the scattering centre could also be any member from the set {A, B, C, …}. If such an alternative scattering centre other than A is referenced then the diagram part changes from A to another member of the set, for example B.

Illustrated in Figure D-1 is a second order configuration eq. (D20) as a diagram. It is possible to build Figure D-1 with the combination of all the diagrams in Table D-1 (which are called diagram parts). Some very elaborate picture representation of the perturbation series can be constructed as shown in Figure D-2.

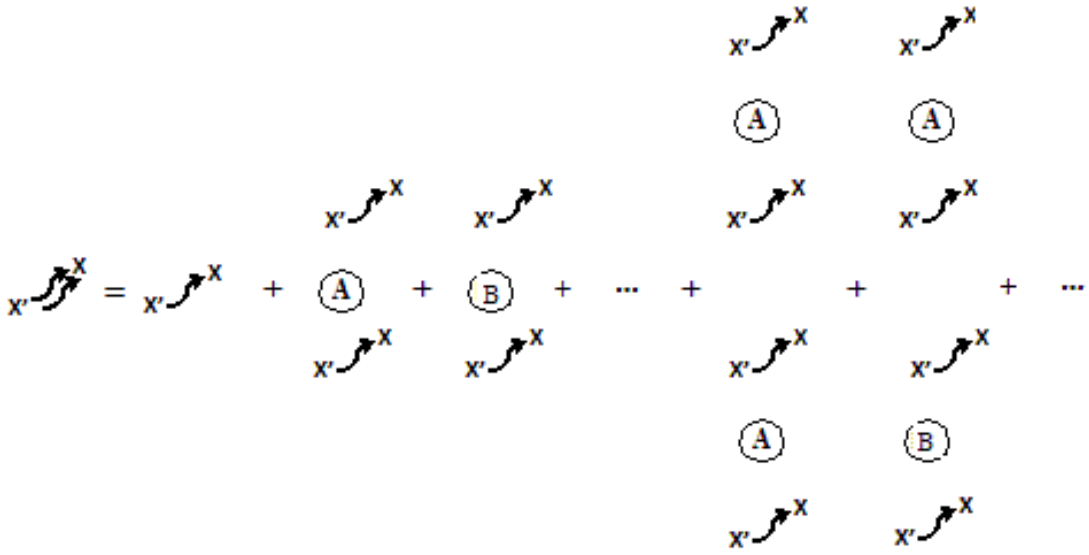

Figure D-1. A Perturbation series of a complex track of a particle of second order with two scatter centres A and B.

The perturbation series shown in Figure D.2 is the probability of a scattering event happening as the test particle tracks from **x'** to **x** passing the scattering centres A and B. Where

-  is the total probability the test particle will complete the track G(***x, x'***)
-  is the probability the test particle will pass without scattering G(***x, x'***)

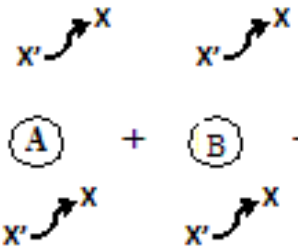

- is the probability a test particle will be scattered by either scattering centre A or B while tracking the function G(***x, x'***).

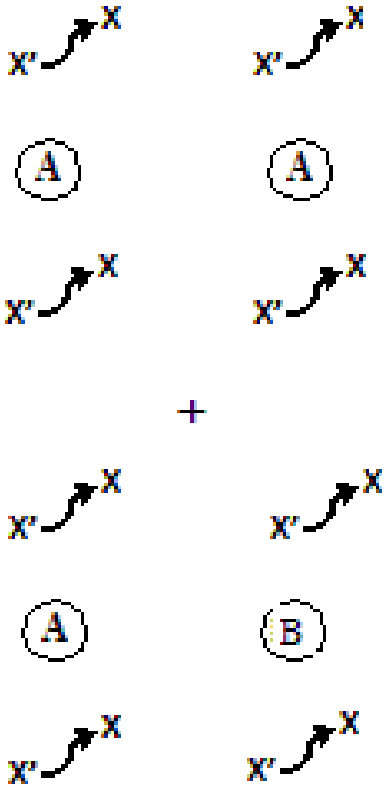

- is the probability a test particle will be scattered by both scattering centre A and B while tracking the function G(***x, x'***)

An assumption is that the probabilities of G_0 and P will take values between zero and unity. Suppose that all free propagators are at or near unity in magnitude. Then, if all P factors are very much smaller than unity, the perturbation will converge very rapidly after which a rational approximation will be obtained. In such a calculation the using the first or higher order terms will help obtain the required accuracy. This is the standard classical application of perturbation theory.

If in the case of scattering probabilities P summed to a value greater than unity and all the other factors where very much smaller than unity, then P would be dominate. Let's assume that P(A) is dominate and the perturbation series is approximated by Figure D-2 to the third order. In general the series would only converge very slowly or even diverge. This type problem is widely known as the 'general problem of strong interaction'.

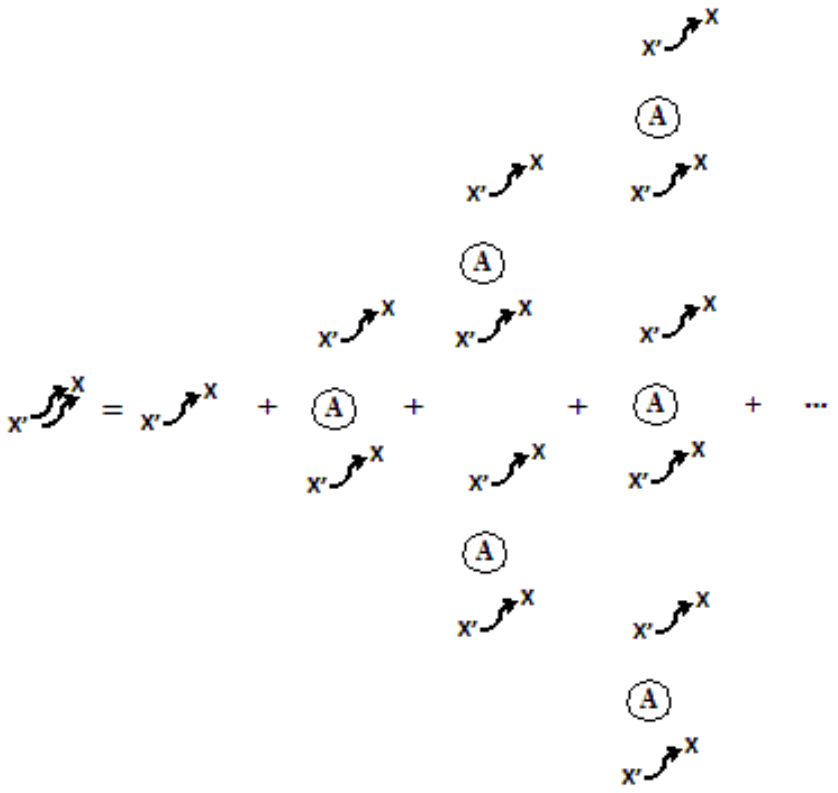

Figure D-2. Perturbation series for the case where P(A) is large, and all the other scattering probabilities are negligible in comparison.

The common solution to a general problem of strong interaction is returning to the analytical form of the perturbation series and applying a geometric progression. It's clear from Figure D-2 that there is a regular progression, so the perturbation series can be decompose to the analytic form and factorised on the right hand side to obtain

$$G(\mathbf{x},\mathbf{x}') = G_0(\mathbf{x},\mathbf{x}') + G_0(\mathbf{x},\mathbf{x}')P(A)G_0(\mathbf{x},\mathbf{x}') \times \{1 + P(A)G_0(\mathbf{x},\mathbf{x}') + [P(A)G_0(\mathbf{x},\mathbf{x}')]^2 + \cdots\} \quad \text{(D-22)}$$

and summing the geometric progression series.

$$G(\mathbf{x},\mathbf{x}') = G_0(\mathbf{x},\mathbf{x}') + G_0(\mathbf{x},\mathbf{x}')P(A)G_0(\mathbf{x},\mathbf{x}')\frac{1}{1-P(A)G_0(\mathbf{x}_A,\mathbf{x}_A')} \quad \text{(D-23)}$$

This technique is known as 'partial summation' and important is widely approach to many practical problems that involve perturbation series such as in the treatment of Brownian motion.

This method of using diagrams and partial summation constitutes a general mathematical method. The general principles of this graphical method are as follows

1. Use the rules above to draw the unlabelled graphs for each order. For each action, then a graph must be topologically distinct. For example the action of a strong interaction (i.e. impact), weak interaction (applied force) and free energy change must have a different diagram shape as illustrated in Figure D.1.
2. Perform the integration necessary to obtain a numerical value for each unlabelled diagram.
3. Label each diagram in all possible ways as illustrated in Figure D.1
4. Multiply the result of (3) with that of (2) and add up over all topologically distinct graphs for a particular order

To conclude this chapter the rules governing how to make good topological classifications of perturbation diagrams. This can be achieved by grouping all perturbation diagrams into three types, based on the second order or type G_2 in Table D-2

Disconnected graphs: these have two or more bonds with no particle in common as Type 1 in Table D-1

Reducibly connected graphs: these have two or more bonds with only one particle in common, so cutting the diagram at the vertex corresponds to particle in two or more disconnected diagram as Type 2 in Table D-2.

Irreducibly connected graphs: all bonds with two or more particles in common and hence cannot be reduced to disconnected diagrams with only one cut as Type 3 in Table D-2. This approach to modelling complete functions was developed by Dr. Richard Feynman as a tool to the solution of perturbation of reactions between elementary particles and is called generically Feynman Diagrams. The approach has been modified in this thesis to a multi-scale approach of modelling the behaviour of particles in combustion gas flow

Table D-2. Relating the action the particle undergoes with the perturbation progression as the result of increasing number of scattering centres or order of the problem.

Type	*Action*	*Diagram Part*				
		$G(\boldsymbol{x}, \boldsymbol{x}')$	*Order n*			
			G_0	G_1	G_2	G_3
1	Particle track with strong interaction (i.e. impaction with a solid body)			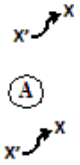	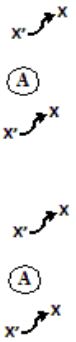	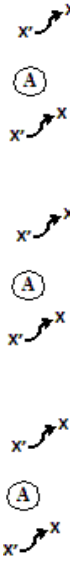
2	Particle track with weak interaction (i.e. path diverted by an applied force)				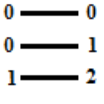	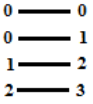
3	Particle track free energy change (i.e. particle undergoing a condensate state change)	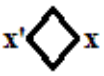			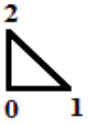	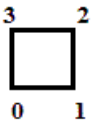
Notes: Different actions on a particle must adopt different diagrams shapes to differentiate one action class from other (i.e. they must be topologically distinct).						

Appendix E. - Mayer Functions (theory)

Mayer's Function are named after Joseph Edward Mayer and Maria Goeppert Mayer who investigated real gases and there molecular interactions.

In an Ideal gas molecular interactions between molecules do not occur, but in a real gas there do. Mayer and Mayer developed a theoretical treatment of the virial coefficients in terms of cluster integrals. virial coefficients are how far the real gas departs from the ideal gas and simplest model are two hard spheres molecules not bonded together.

To illustrate Mayer functions take three molecules bonded together form one of four ways

Figure E-1. Cluster Graph of three molecules and possible bonding pairs.

For molecular unions of 1, 2 and 3 molecular pairs the cluster integrals are N1 – N3

$$b_1 = \frac{1}{!V}\int d\Gamma = 1 \qquad \text{(E-1)}$$

$$b_2 = \frac{1}{2!V}\iint f(r_{12})\mathrm{d}\Gamma_2\mathrm{d}\Gamma_1 = \frac{1}{2}\int_0^{\infty} 4\pi r^2 \qquad \text{(E-2)}$$

by using Mayer f-cluster notation. For more than 3 chain clusters it becomes more complex so it is advisable to use a cluster diagram. The key definition for forming a cluster diagram is the irreducible cluster, for any cut vertex b_l, has a factorised corresponding integral similar to that of N-1 to N-3 but denoted as β_i. More generally,

$$b_3 = \frac{1}{3!V}\iiint (f_{31}f_{21} + f_{32}f_{21} + f_{32}f_{31}f_{21})\mathrm{d}\Gamma_3\,\mathrm{d}\Gamma_2\mathrm{d}\Gamma_1 \qquad \text{(E-3)}$$

Whenever there is a graph with a cut vertex, each 'irreducible sub-graph' contributed to a factor to the integral. Hence, a graph b_l in eq. (E-2) has an irreducible cluster integral defined as for Cartesian coordinates as

$$\beta_1 = \frac{1}{V}\int_2^{\cdots}\int f_{12}\; dx_1 dy_1 dz_1 dx_2 dy_2 dz_2 \qquad \text{(E-4)}$$

In general terms the cut vertex β_i is defined in terms of volume V and separation between molecular pairs k_n, as

$$\beta_i = \frac{1}{k!V}\int \overset{\cdots}{(3k+1)} \int \begin{pmatrix} \text{All irreducible} \\ \text{graphs of order } l+1 \end{pmatrix} dx_1 dx_1 dx_1 \ldots dx_{k+1} dx_{k+1} dx_{k+1} \qquad \text{(E-5)}$$

where k+1 is the nth virial coefficient represented in 3-dimensional Cartesian space as (3k+1). The term l is related to k_n as

$$\sum_{k=1}^{k=l-1} k_n = l - 1 \qquad \text{(E-6)}$$

It is simpler to define the these molecular configurations networks in terms of 'Husimi trees' which are formed by joining together polygons and edges in this manner, using in this particular case, the cluster graphs in Figure E-1.

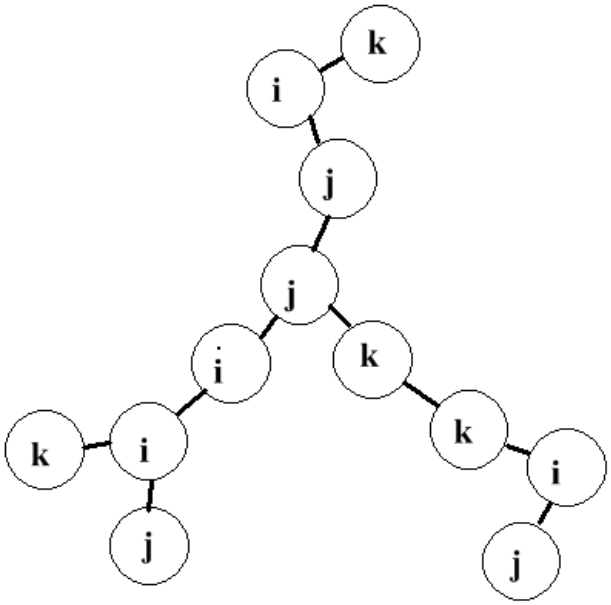

Figure E-2. Custer graph 'cacti' product from the irreducible cluster in Figure E-1

A potential output shown in Figure E-2, so from a root simple polygon a complex structure can be form. An alternative name of 'Husimi Trees' is 'cacti'.

The development of the cacti of Figure E-2 is the expansion of the function g(r), where r is the minimum space which two molecules can occupy. The expansion is continued over 5 molecules, which is normally shown as a pentangle.

The expansion of the interconnection between molecular groups and the virial expansion is summarised as setting f_{12} as the cacti joins itself for example i joins i, j joins j or k joins k in Figure E-2. Using the same logical approach then f_{23} represents the joining of one cacti to a

different cacti with a single link such as i to k, i to j, Where 3 links are made then setting f_{34} represents the combined joining of cacti i, k and j by two or three links. Thus the combinatory progression, based eq. (E-1) to eq. (E-3) for Figure E 2, is

- First order

$f_{12} =$ 

Second order

$f_{23} = \frac{1}{V}$ ()

- Third order

$f_{23} = \frac{1}{V^2}$ () (E-7)

These graphs in eq. (E-4) represent the first, second and third order terms of the cacti of Figure E2. There are clear advantages of this approach in that similar topological groups can be clearly identified. Its easer to manipulate topological groups than algebraic equation and there is a one-to-one relationship between molecular position and topological form. The formation of algebraic solutions above third order is very demanding but using virial cluster diagrams its relatively easy. Where an integration operation is applied to a graph the counterpart is coloured black.

- Integration operation

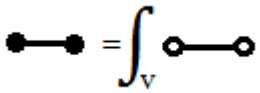

(E-8)

For all the microstates within thermodynamics system are statistically represented by the partial function Z. To calculate thermodynamic properties at a point within the system boundaries, for example reduce pressure, the graph approach can simplify the procedure. In the canonical formalism P[T,V,N] at Temperature T, in Volume V, containing N number of particles and a second order partial function $Z_{Q,}$ then using the integral graph form; the reduce pressure at a point is defined by the integral operation as

$$\begin{aligned} \mathrm{P[T,V,N]} &= \mathrm{kT}\,\partial_{\mathrm{V}} \log \mathrm{Z(T,V,N)} \\ &= \mathrm{kT}\,\partial_{\mathrm{V}} \log \mathrm{Z_Q(T,V,N)} \end{aligned}$$

$$P[T,V,N] = \mathrm{k}T\,\partial_{\mathrm{V}}\left[-\log\mathrm{N}! + \mathrm{N}\log\mathrm{V} + \log\left\{1 + \frac{\mathrm{N}(\mathrm{N}-1)}{2\mathrm{V}}\right\}\right]$$

$$\approx \mathrm{k}T\,\partial_{\mathrm{V}}\left[-\log\mathrm{N}! + \mathrm{N}\log\mathrm{V} + \log\mathrm{V}\frac{\mathrm{N}(\mathrm{N}-1)}{2\mathrm{V}}\right]$$

$$\approx \mathrm{k}T\,\partial_{\mathrm{V}}\frac{N}{V} - \frac{\mathrm{k}T}{2}\left(\frac{N}{V}\right)^2 \qquad \text{(E-9)}$$

where the approximation $\log(1+x) \approx x$ for small densities and $N(N-1) \approx N^2$ (Schreiber, Zanini & Roosen-Runge 2011) and k_B is Boltzmann constant.

It's a simple process to extend the combinatory progression to include molecular formations of different orders. If another molecule call 'l' is included into Figure E-2 this will produce a forth order expansion f_{45}

- Fourth order

$f_{45} = \frac{1}{V^4}$ (

Where $\frac{1}{V^4}$ is formed of fourth order canonical terms connected into cacti in Figure E-2 and the curved connected is the minimum distance that two particles or two particle pairs can occupy the same space.

Appendix F. - Uncertainty Analysis of Case studies.

Node Error

For any particle element the node error is based on the number of the thermodynamic properties that converge in any run. The properties are Pressure, Volume and Temperature at each node on each element, where appropriate these include vector components in x, y, z Cartesian coordinates such as velocity in u, v, w coordinates.

$$Node\ error = \frac{Number\ of\ thermodynamic\ properties\ failed\ to\ converge}{Total\ number\ of\ thermodynamic\ properties}\ \%$$

Convergence

Convergence is defined as when the last value fits within the present margin of error and within the limit of the number iteration permitted. For example, if the margin of error is permit to be +/- 0.0005 and the number iterations are set to achieve this limit are 10 then, a failure is recorded if these criteria is not meet.

Hence, the table below summarises when the pressure limit from last iteration is 10125 Pa and the iteration limit is 10

Convergence test	
Pass	**Fail**
Pressure limit from current iteration is 10125 Pa	Pressure limit from current iteration is 10133 Pa
Number of iteration so far is 8	Number of iteration so far is 11

Appendix G. - Pipe Furnace Drawing and mesh-free node configuration

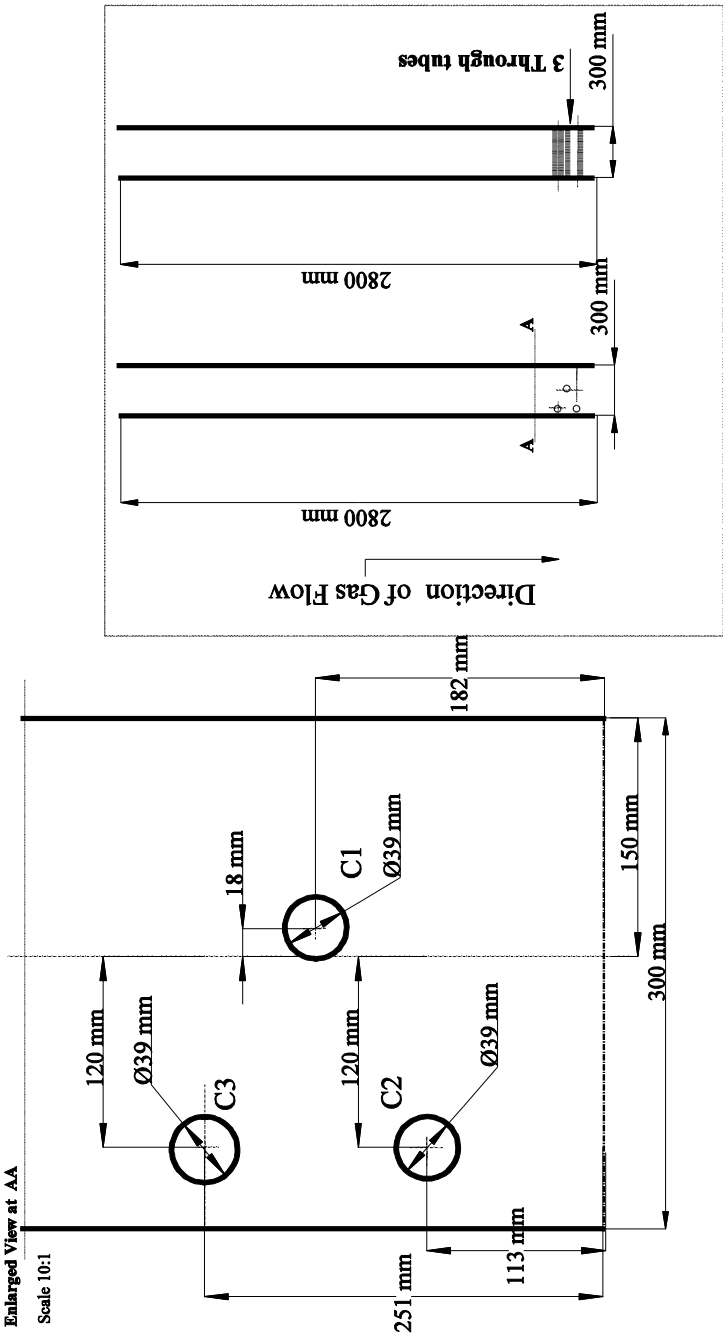

Figure G-1. General arrangement of tube layout for case study 2

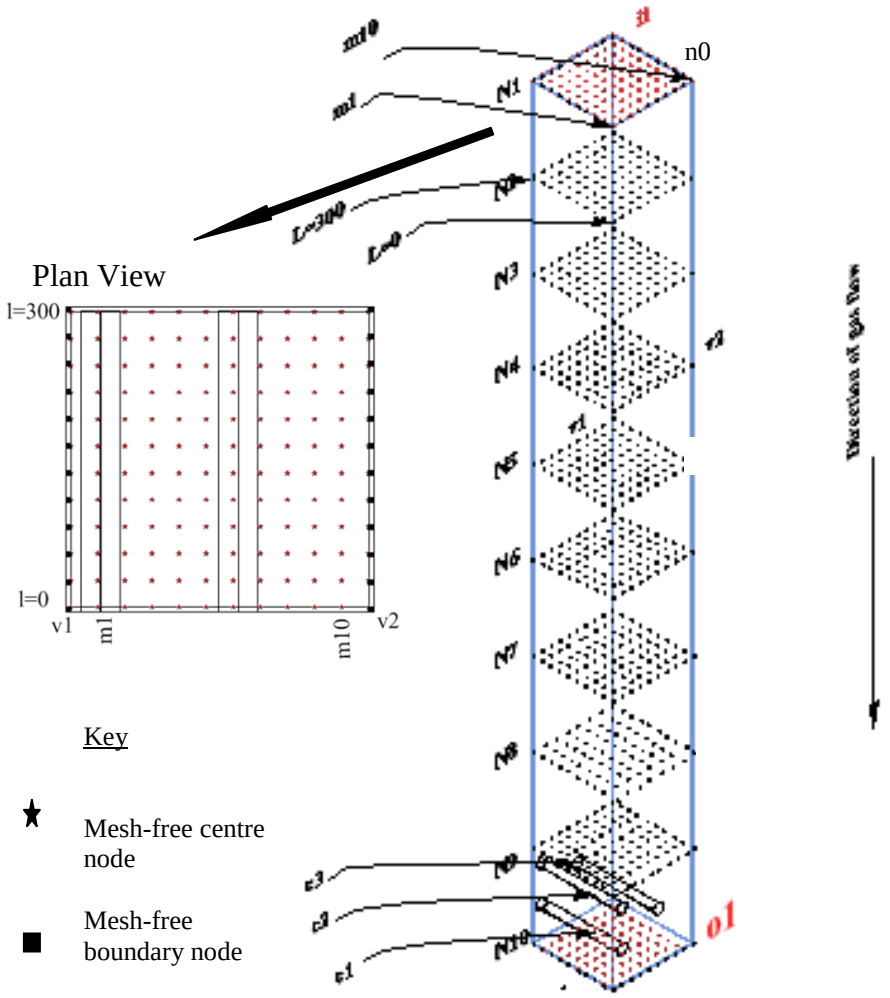

Figure G-2. Mesh-free centre node distribution for the test combustor

The nodes are distributed in a equal space patten, depth has 10 centre nodes number l0 to l10; width has 10 centre nodes labelled m0 to m10; hieght has 10 centre nodes labelled n0 to n10. The boundary centre nodes are the interfaces between the free gas and the surface of the tubes or combustor walls. Ten nodes are place radial around the tube labelled n1 to n10 and 10 nodes are place circumferentially labelled l1 to l10 in Figure G-3.

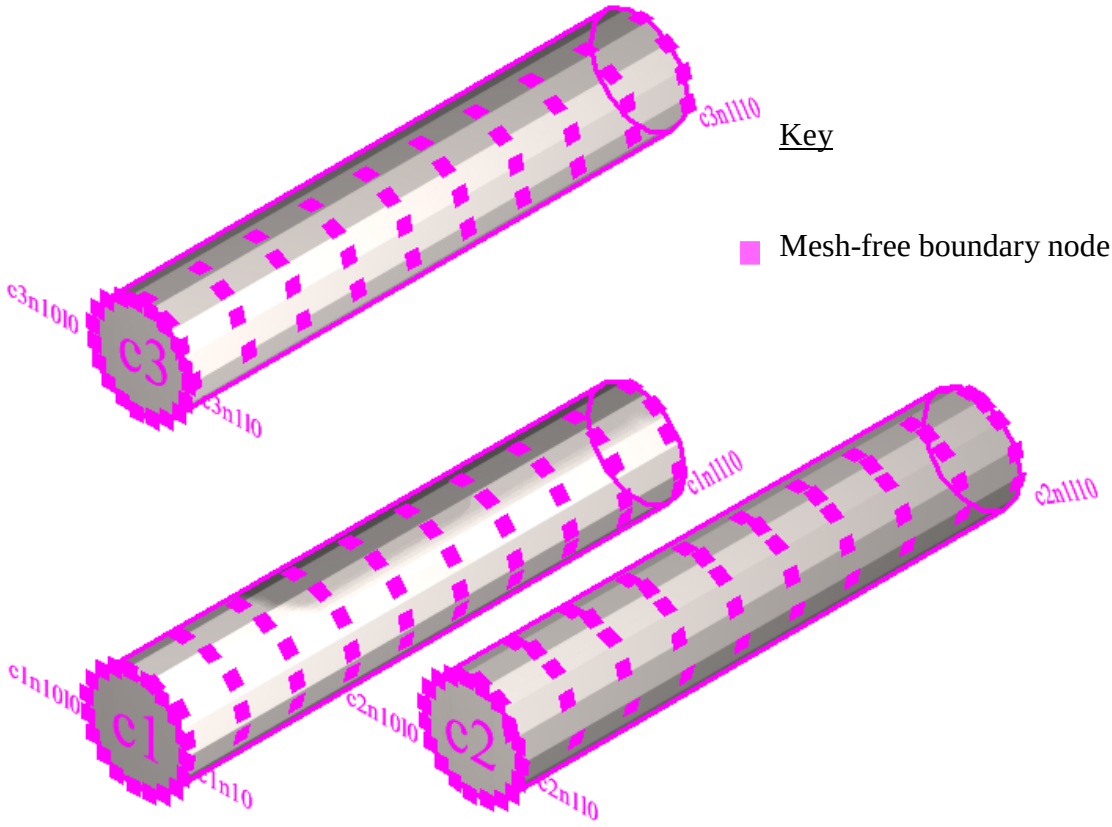

Figure G-3. Mesh-free centre node distribution for the test combustor with the arrangement of the centre nodes on the tubes c1, c2 and c3.

Appendix H. - Modelling initial values for case studies

Table H-1. Summary of the initial properties required for Chapter 6, case study 1 simulating coal combustion

Initial Properties	Values
Wall roughness	0.2
Viscosity	4.152e-5 Pa·s
Density	0.34 kg/m^3
Diffusion	0.9
Pressure	101325 Pa
Temperature	1073 K
Velocity	40 m/s
Turbulence Energy k	0
Turbulence dispersion ε	0
Fuel Reaction Rate	-0.000130046
Oxygen reaction rate	-6.69059E-06
Products reaction rate	-0.005597682
Fuel Mixture Density	0.5 kg/m^3
Oxygen Mixture Density	0.91 kg/m^3
Inert Mixture Density	1.02 kg/m^3
Fuel Gas Constant	1
Oxygen Gas Constant	0.26
Inert Gas Constant	0.294
Fuel Relative Volumes	0.6
Oxygen Relative Volumes	0.12
Inert Relative Volumes	0.34
Fuel Arrhenius Constant	30
Oxygen Arrhenius Constant	30
Inert Arrhenius Constant	1327
A Kinetic Constant	0.002
B Kinetic Constant	0.01
C Kinetic Constant	0.01
Universal Gas Constant	8.314472 J K^{-1} mol^{-1}
Stoichiometric Ratio	2.5
Heat Capacity Ratio	1.195
Alpha Pressure U	0.55
Alpha Pressure V	0.55

Alpha Pressure W	0.55
Alpha Velocity X	0.55
Alpha Velocity Y	0.55
Alpha Velocity Z	0.55
Alpha Combustion S	0.55
margin (maximum solver error)	0.05
Mean Particle Size	0.000005 m
Mean Particle Mass	1.963495×10^{-08} kg

Table H-2. A Summary of the initial properties required for Chapter 6, case study 2 simulating coal/biomass combustion.

Initial Properties	**Values**
Wall roughness	0.2
Viscosity	4.152×10^{-5} Pa·s
Density	0.34 kg/m^3
Diffusion	0.9
Pressure	101325 Pa
Temperature	1073 K
Velocity	30 m/s
Turbulence Energy k	2
Turbulence dispersion ε	0.2
Fuel Reaction Rate	-0.000130046
Oxygen reaction rate	-6.69059×10^{-06}
Products reaction rate	-0.005597682
Fuel Mixture Density	0.5 kg/m^3
Oxygen Mixture Density	0.91 kg/m^3
Inert Mixture Density	1.02 kg/m^3
Fuel Gas Constant	1
Oxygen Gas Constant	0.26
Inert Gas Constant	0.294
Fuel Relative Volumes	0.6
Oxygen Relative Volumes	0.12
Inert Relative Volumes	0.34
Fuel Arrhenius Constant	30
Oxygen Arrhenius Constant	30
Inert Arrhenius Constant	1327

A Kinetic Constant	0.002
B Kinetic Constant	0.01
C Kinetic Constant	0.01
Universal Gas Constant	8.314472 $J K^{-1} mol^{-1}$
Stoichiometric Ratio	2.5
Heat Capacity Ratio	1.195
Alpha Pressure U	0.56
Alpha Pressure V	0.56
Alpha Pressure W	0.56
Alpha Velocity X	0.56
Alpha Velocity Y	0.56
Alpha Velocity Z	0.56
Alpha Combustion S	0.56
Margin (maximum solver error)	0.1
Mean Particle Size	0.00001
Mean Particle Mass	4.90748×10^{-08}

The following figure shows the simulation build up of deposits by mass at in Chapter 6 case study 2 by mass at 25mm section. The position is of each section is shown in Figure G.2

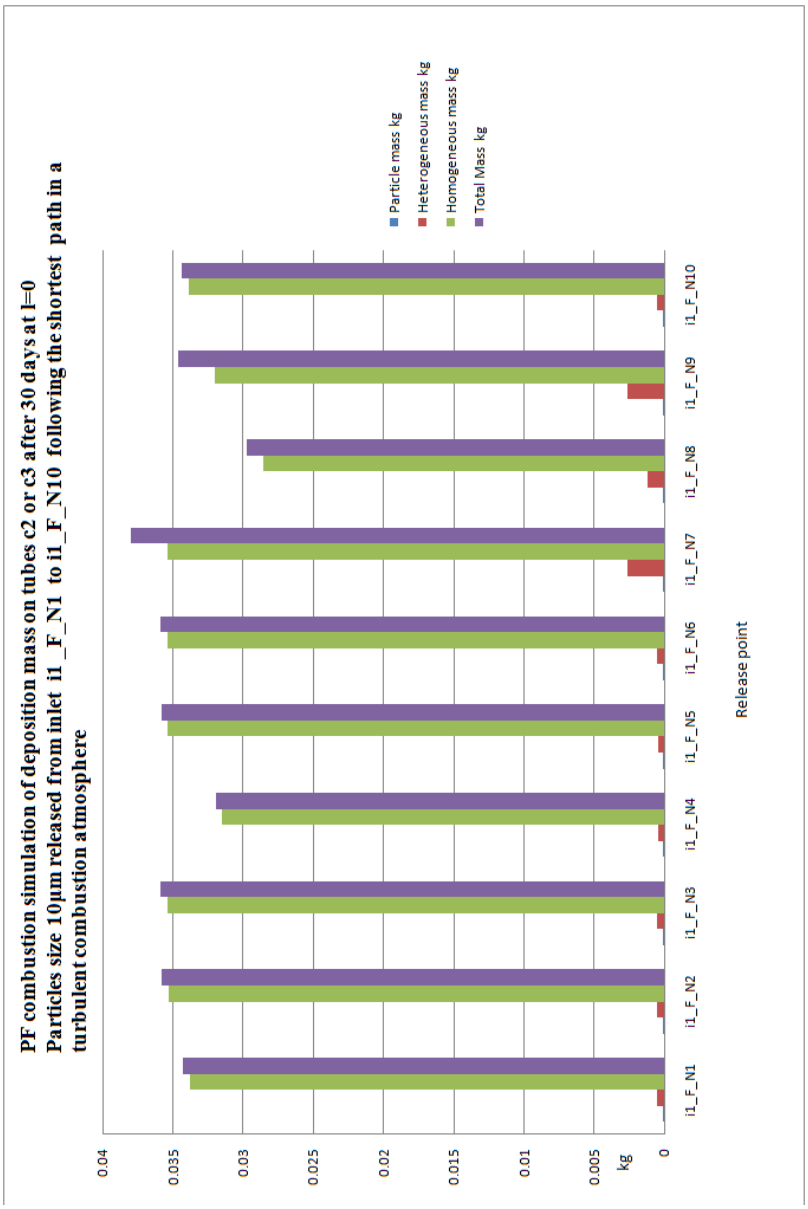

Figure H-1. Particles/vapour mass impacting on tubes c2 and c3 for Chapter 6 case study 2 at l=0.

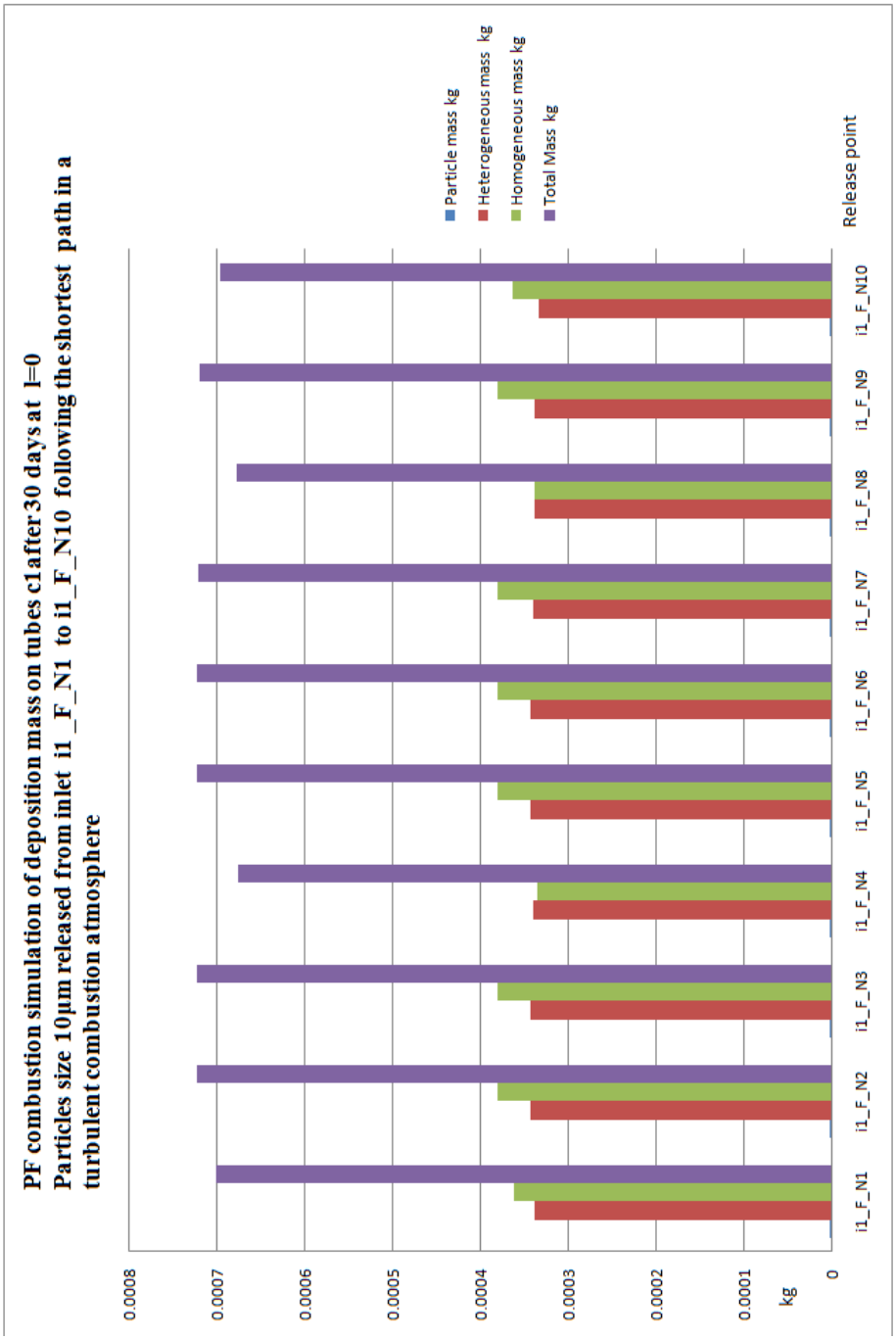

Figure H-2. Particles/vapour mass impacting on tubes c1 for Chapter 6 case study 2 at l=0.

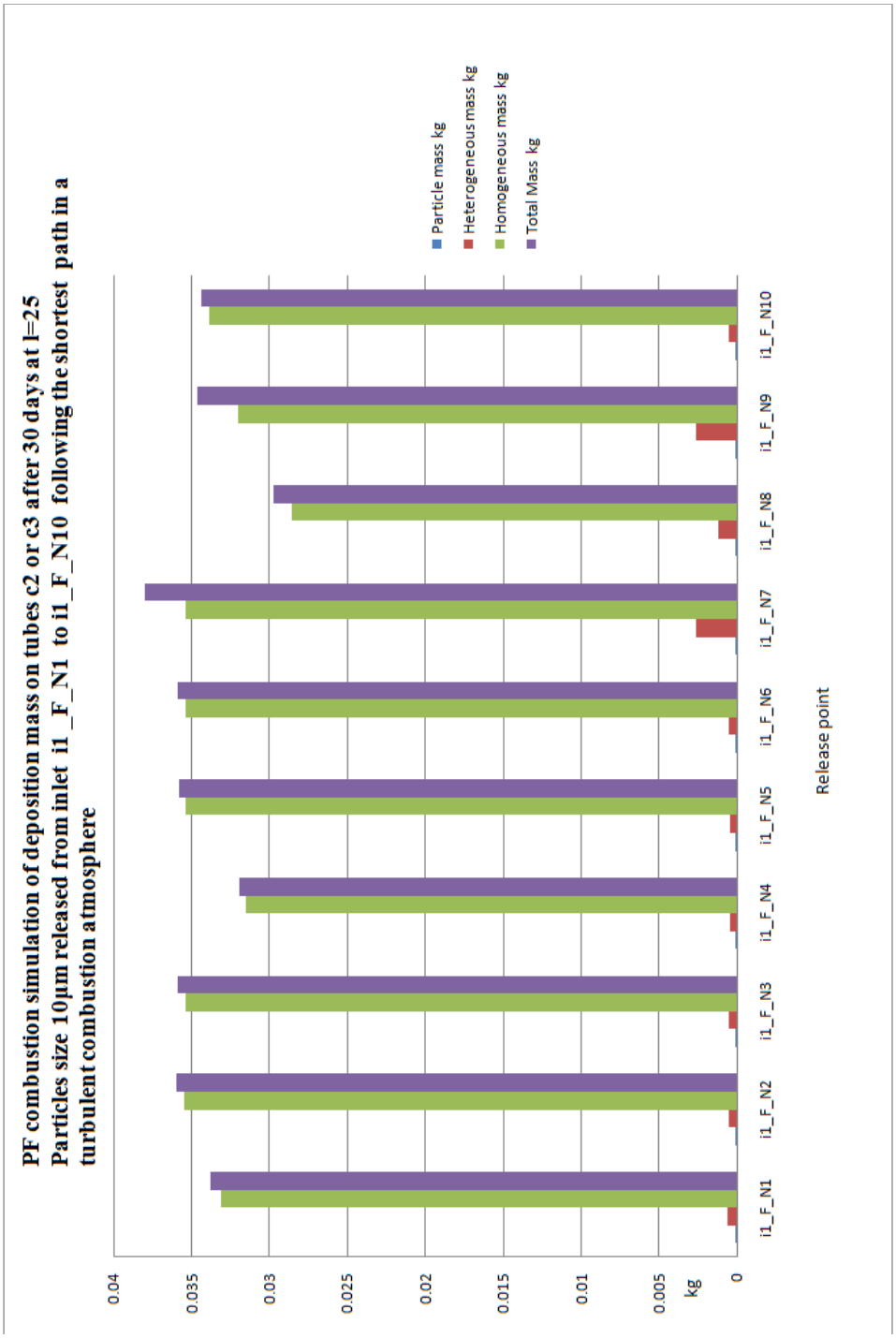

Figure H-3. Particles/vapour mass impacting on tubes c2 and c3 for Chapter 6 case study 2 at l=25.

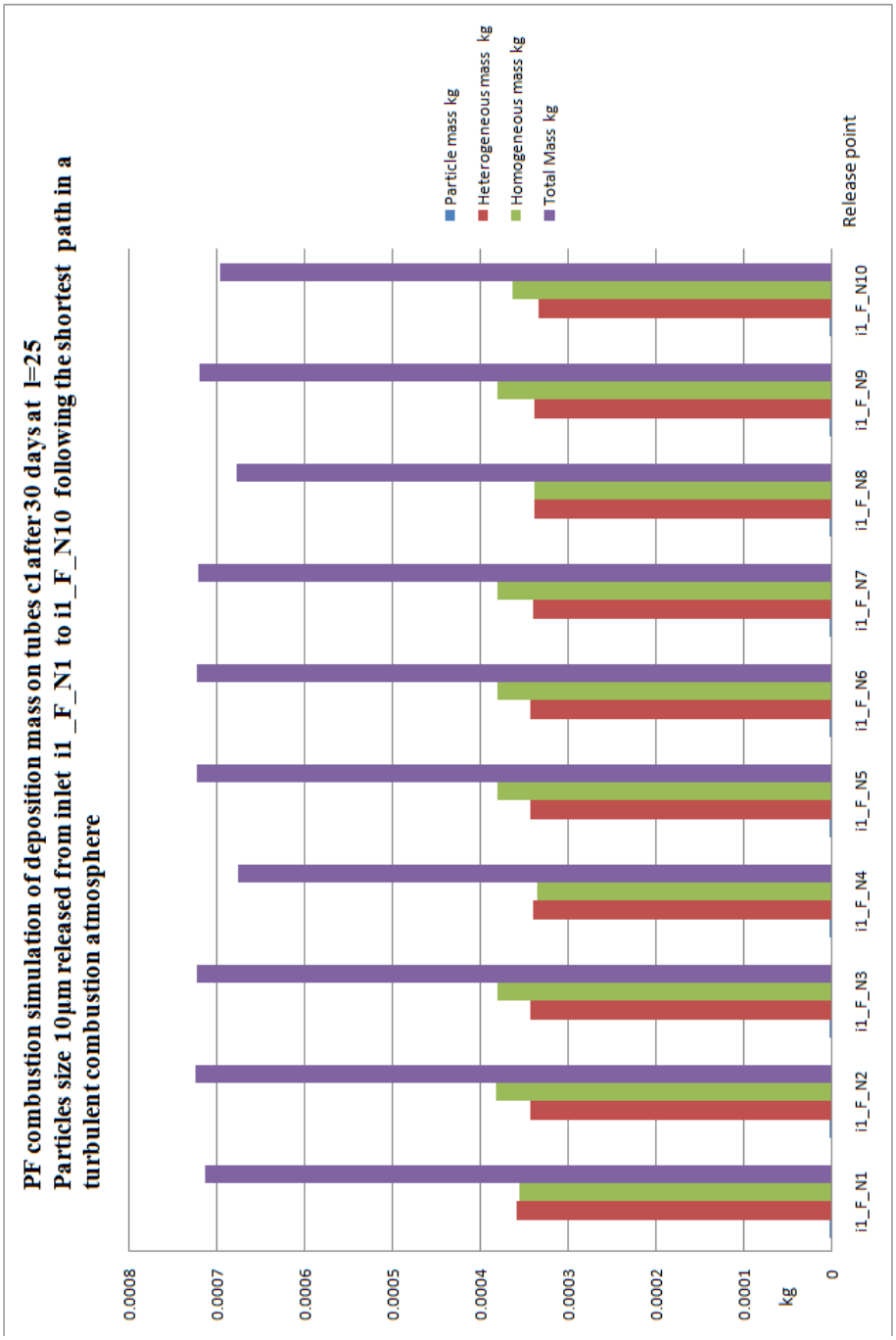

Figure H-4. Particles/vapour mass impacting on tubes c1 for Chapter 6 case study 2 at l=25.

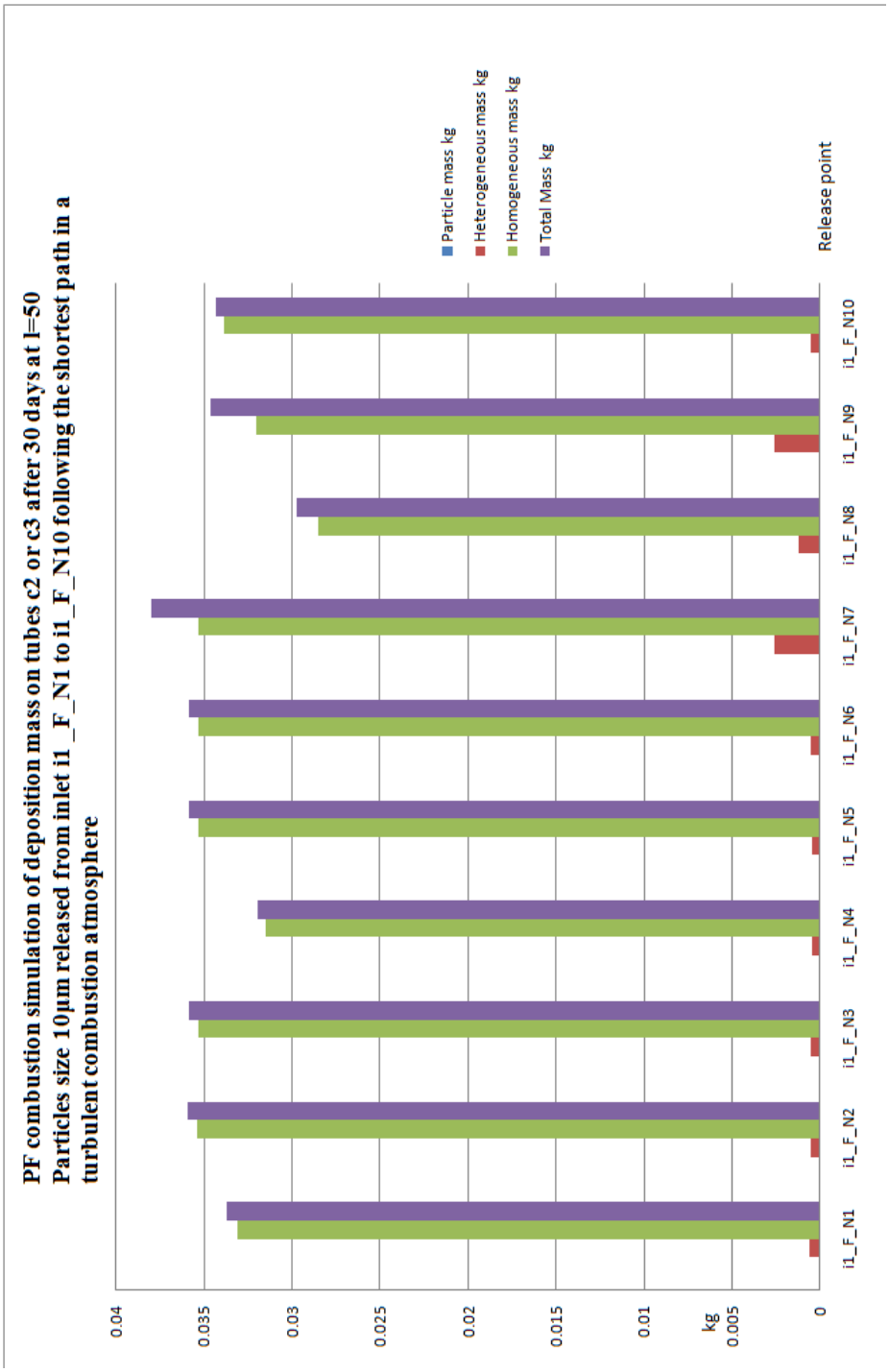

Figure H-5. Particles/vapour mass impacting on tubes c2 and c3 for Chapter 6 case study 2 at l=50.

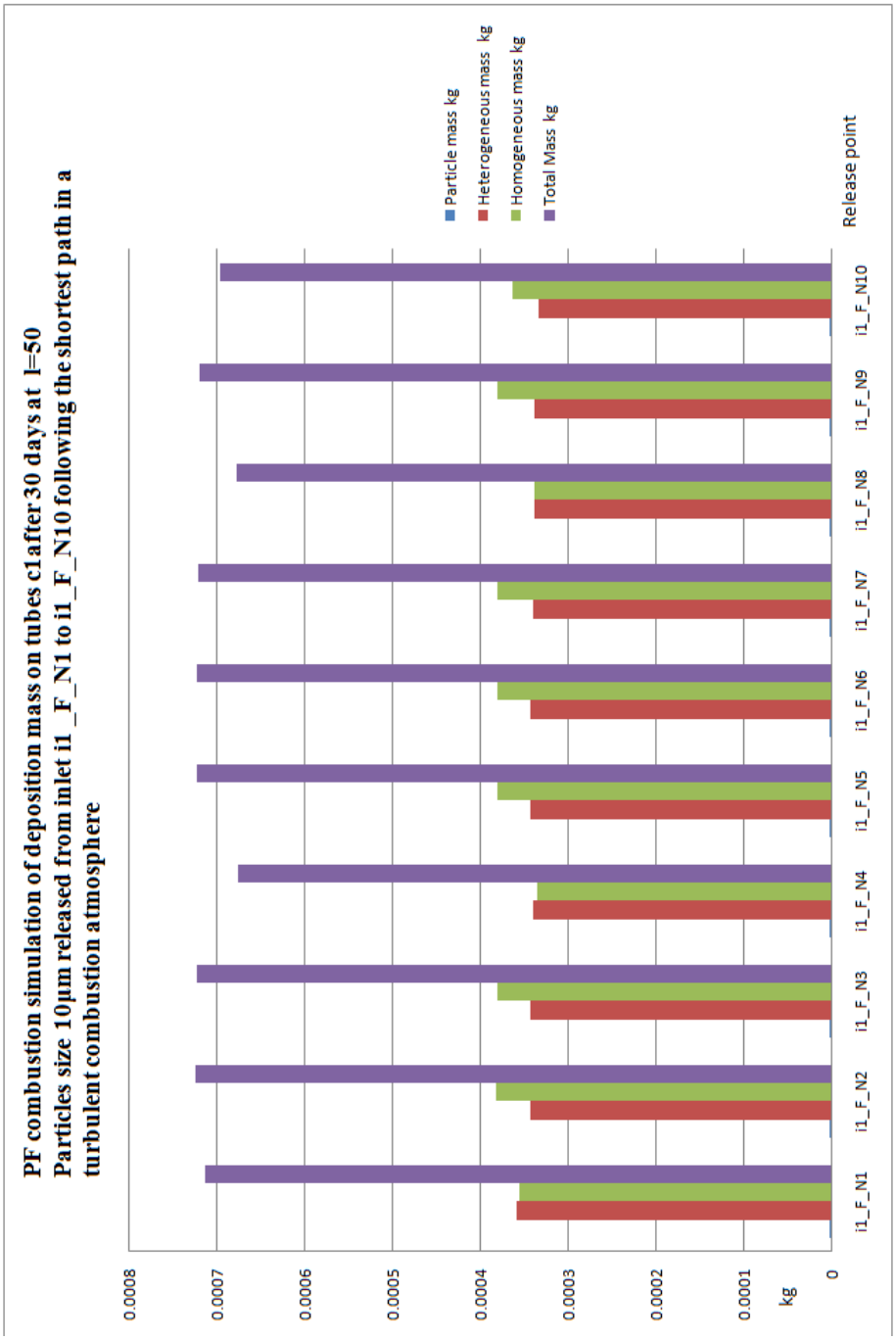

Figure H-6. Particles/vapour mass impacting on tubes c1 for Chapter 6 case study 2 at l=50.

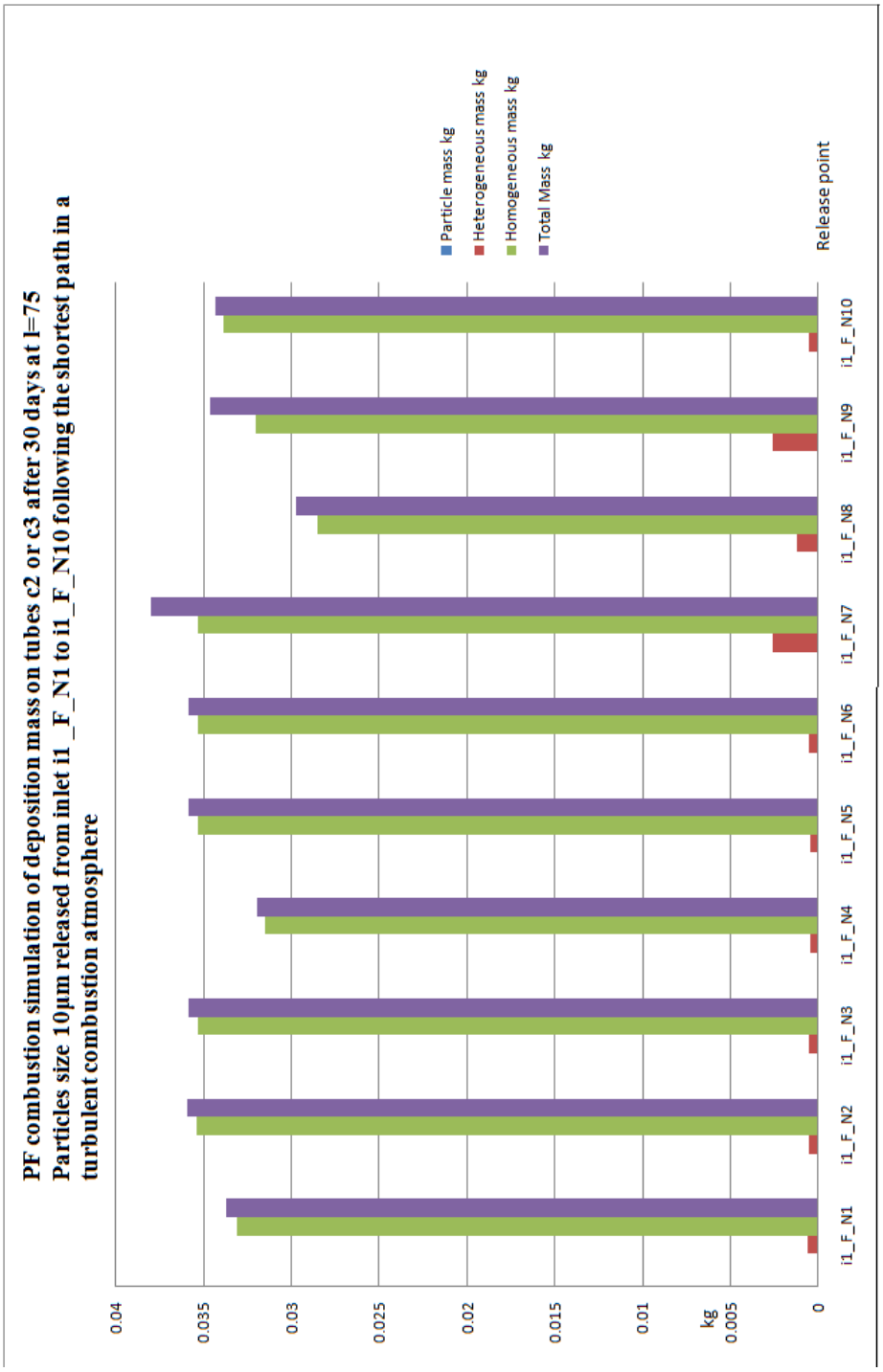

Figure H-7. Particles/vapour mass impacting on tubes c2 and c3 for Chapter 6 case study 2 at l=75.

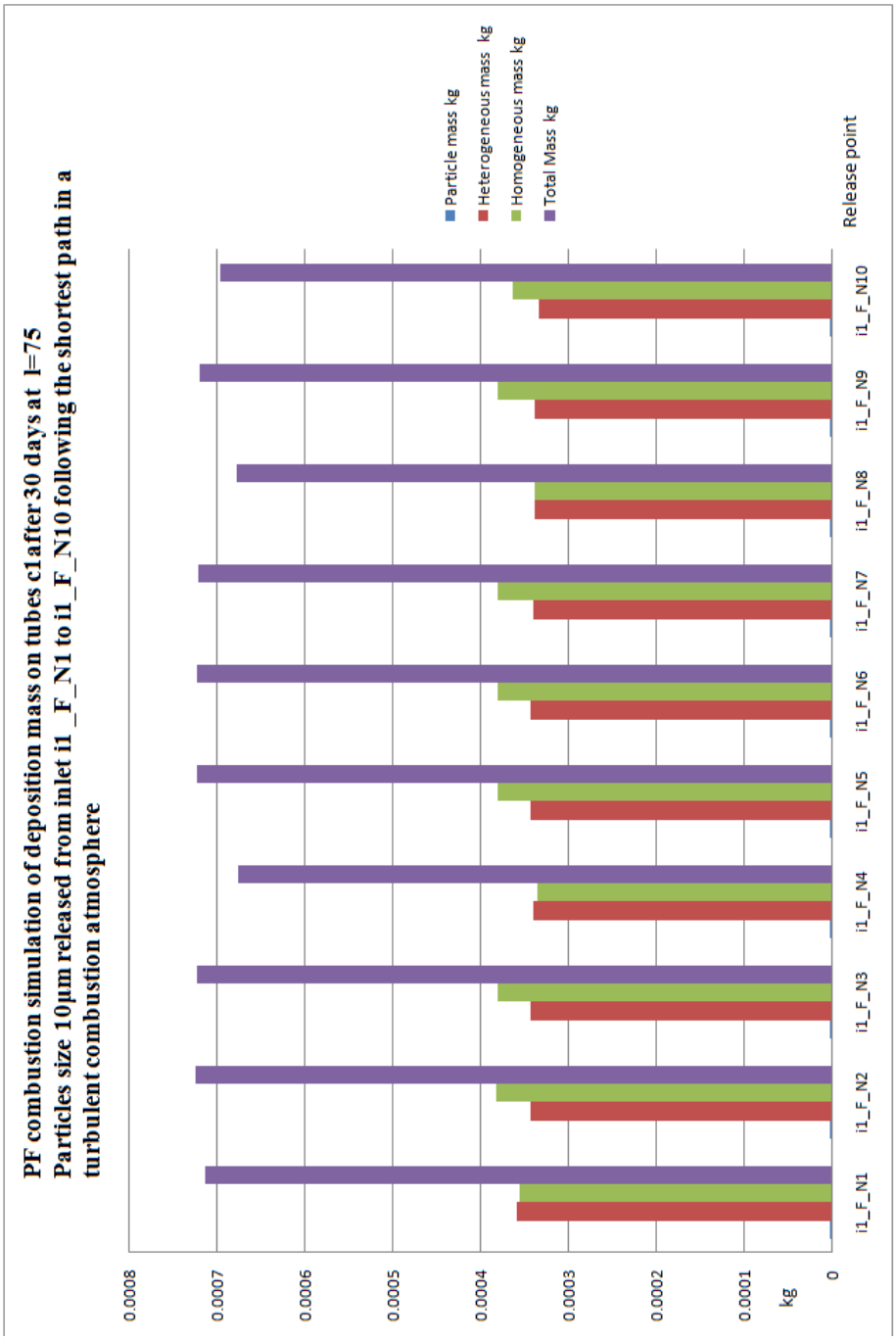

Figure H-8. Particles/vapour mass impacting on tubes c1 for Chapter 6 case study 2 at l=75.

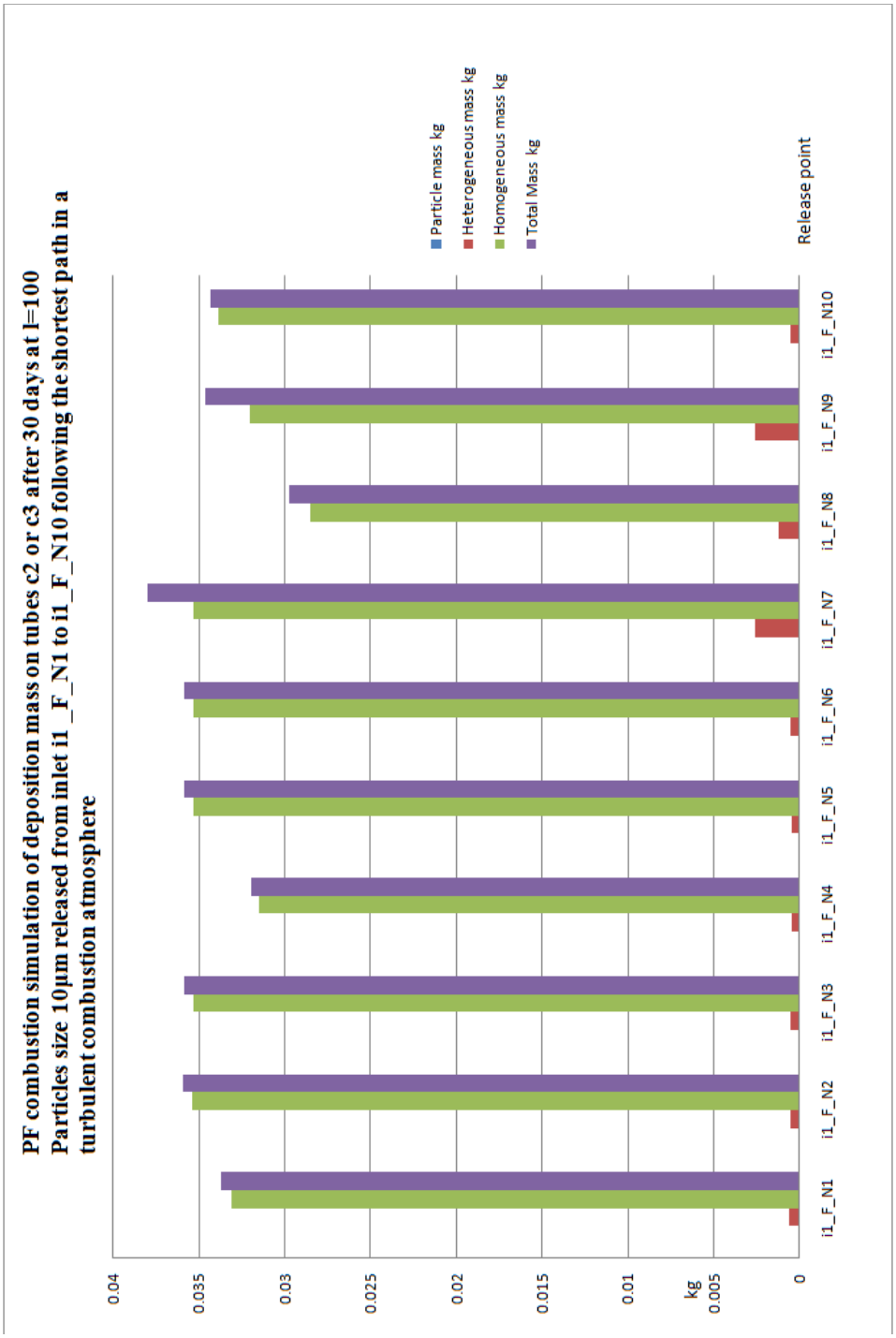

Figure H-9. Particles/vapour mass impacting on tubes c2 and c3 for Chapter 6 case study 2 at l=100.

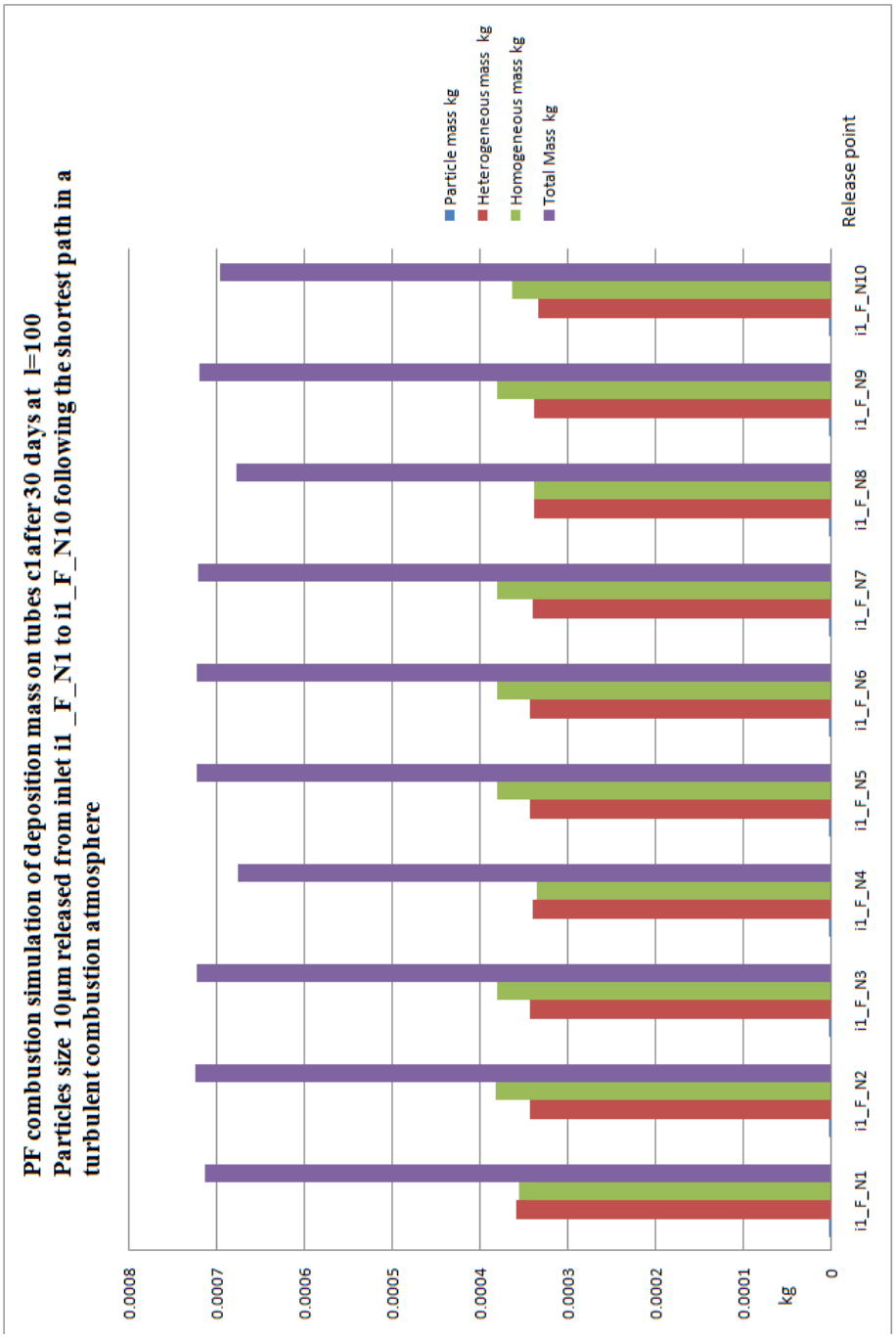

Figure H-10. Particles/vapour mass impacting on tubes c1 for Chapter 6 case study 2 at l=100.

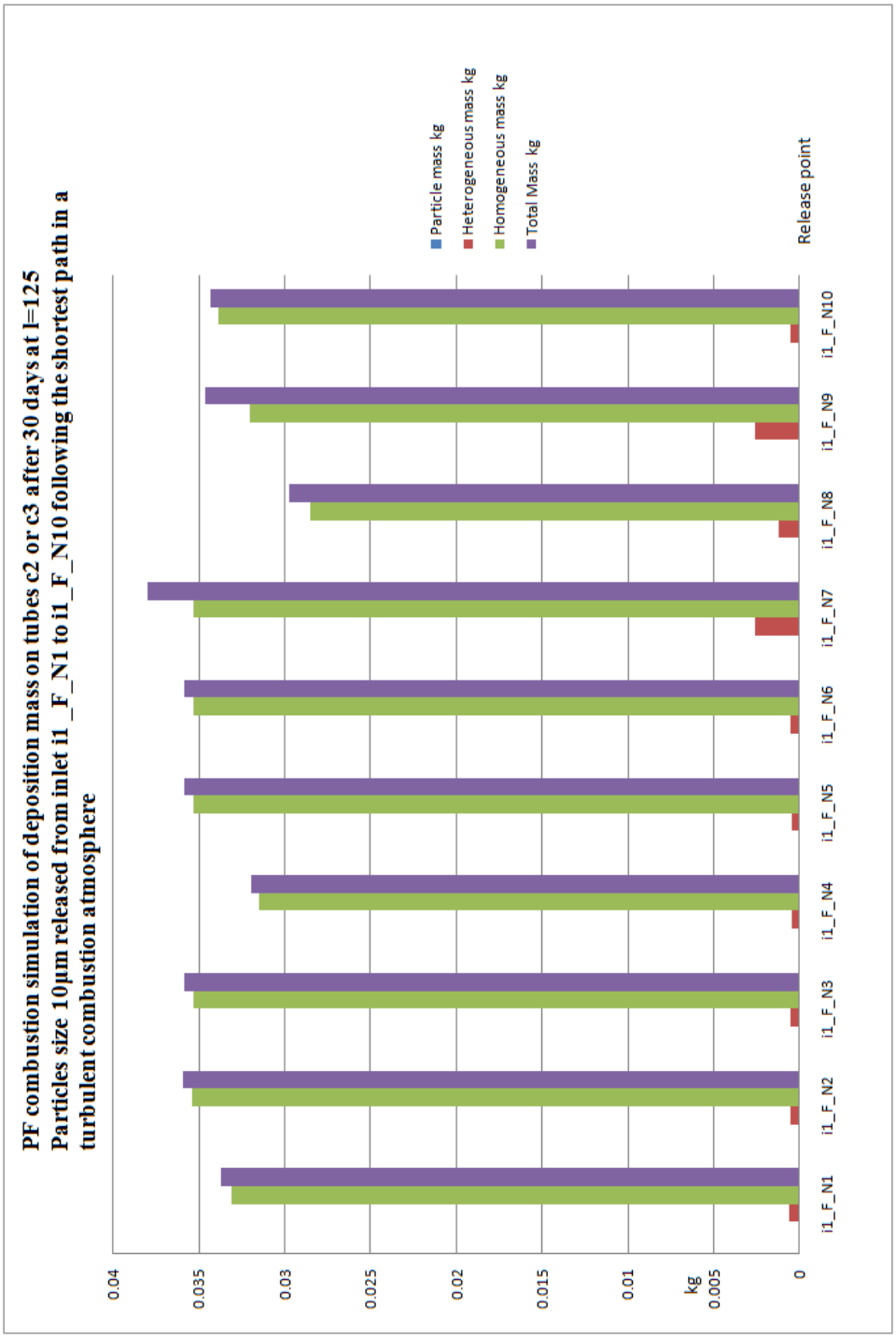

Figure H-11. Particles/vapour mass impacting on tubes c2 and c3 for Chapter 6 case study 2 at l=125.

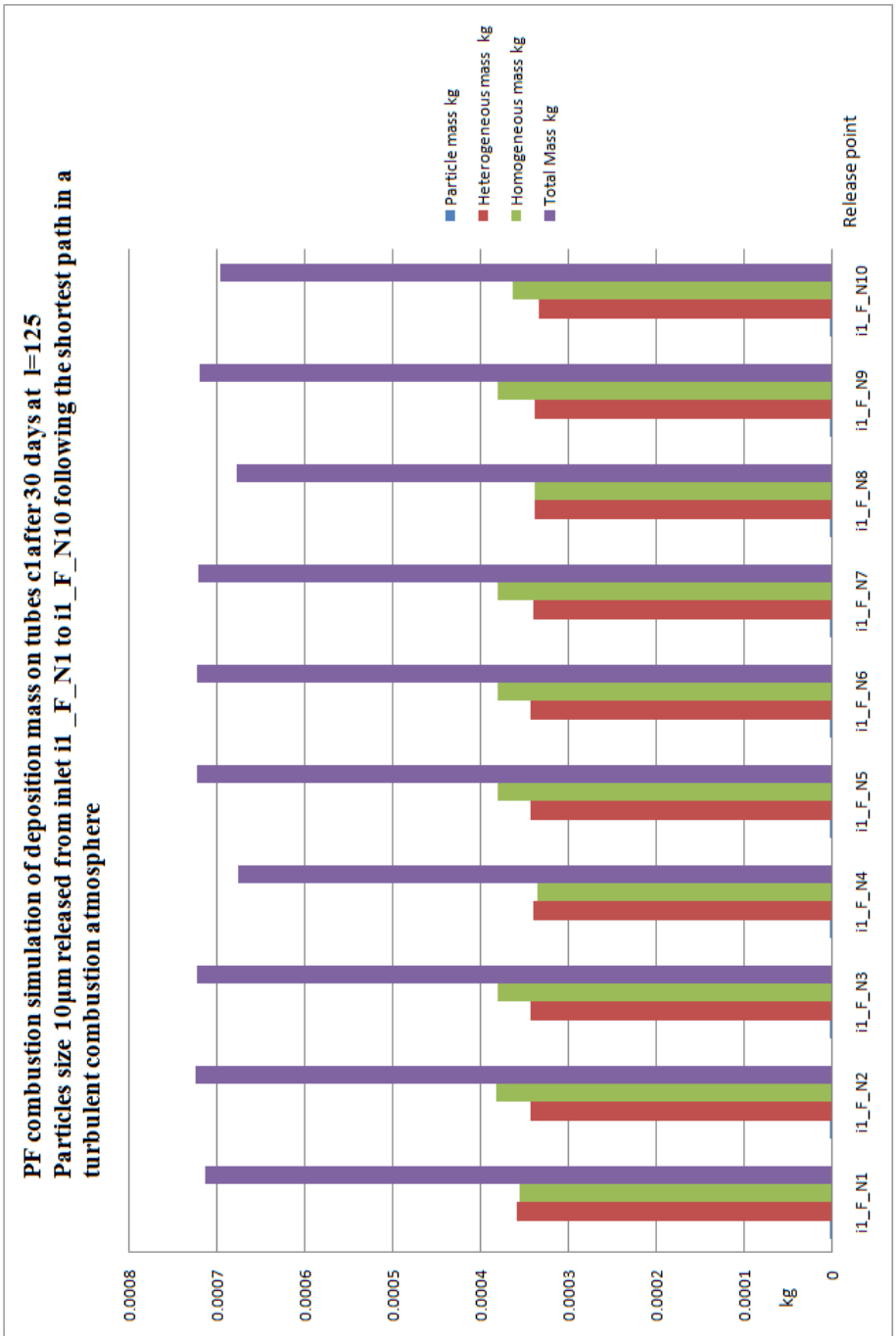

Figure H-12. Particles/vapour mass impacting on tubes c1 for Chapter 6 case study 2 at l=125.

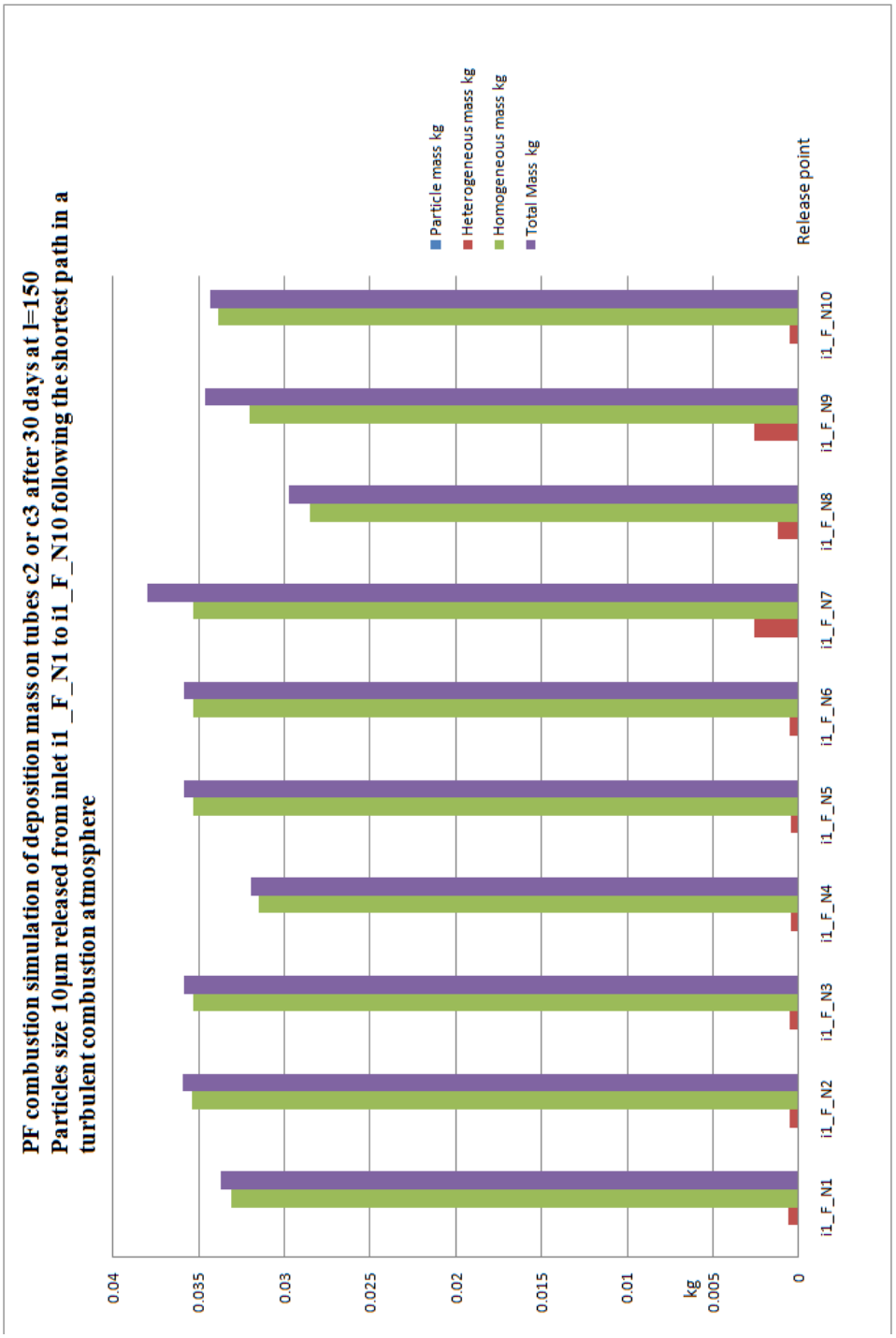

Figure H-13. Particles/vapour mass impacting on tubes c2 and c3 for Chapter 6 case study 2 at l=150.

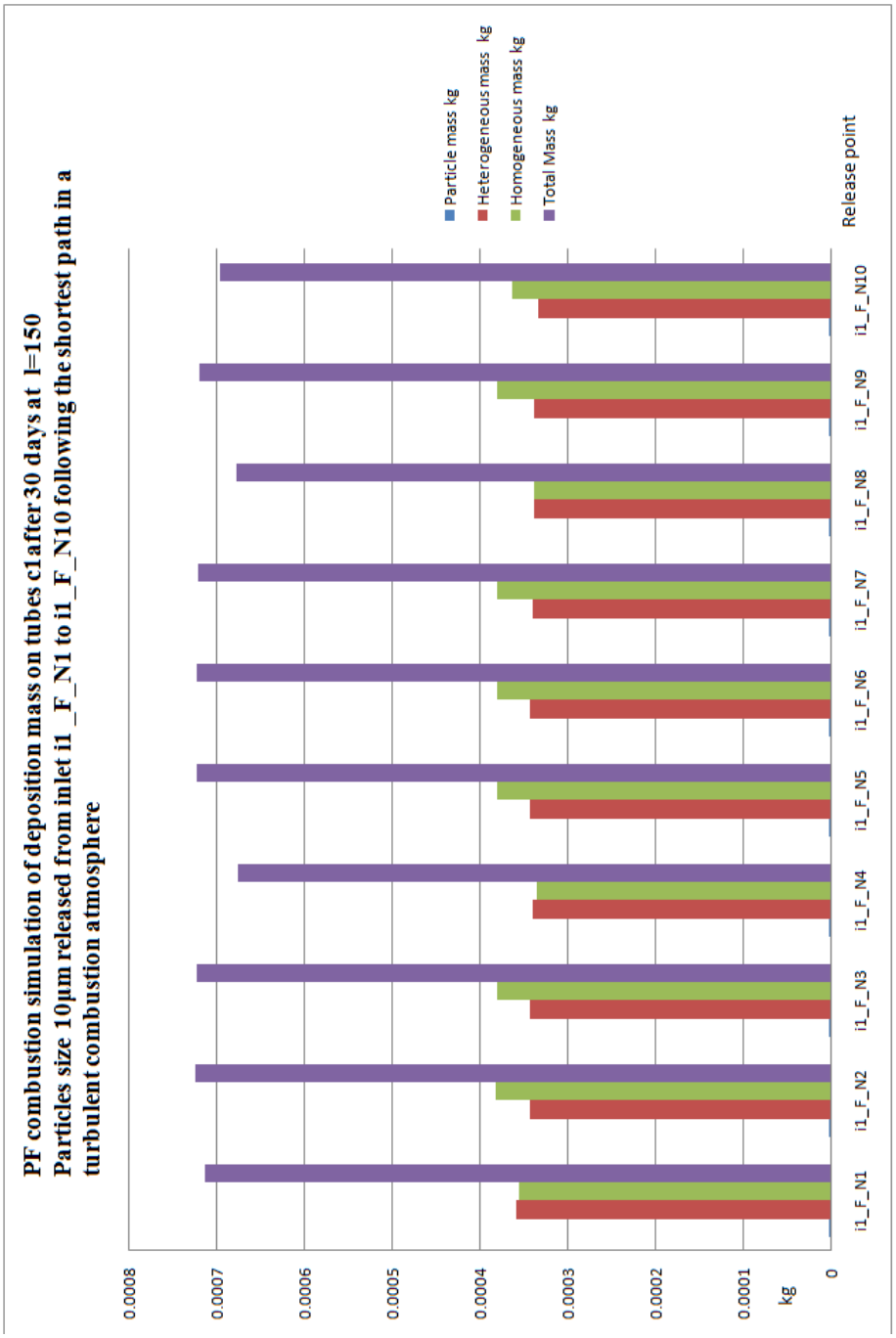

Figure H-14. Particles/vapour mass impacting on tubes c1 for Chapter 6 case study 2 at l=150.

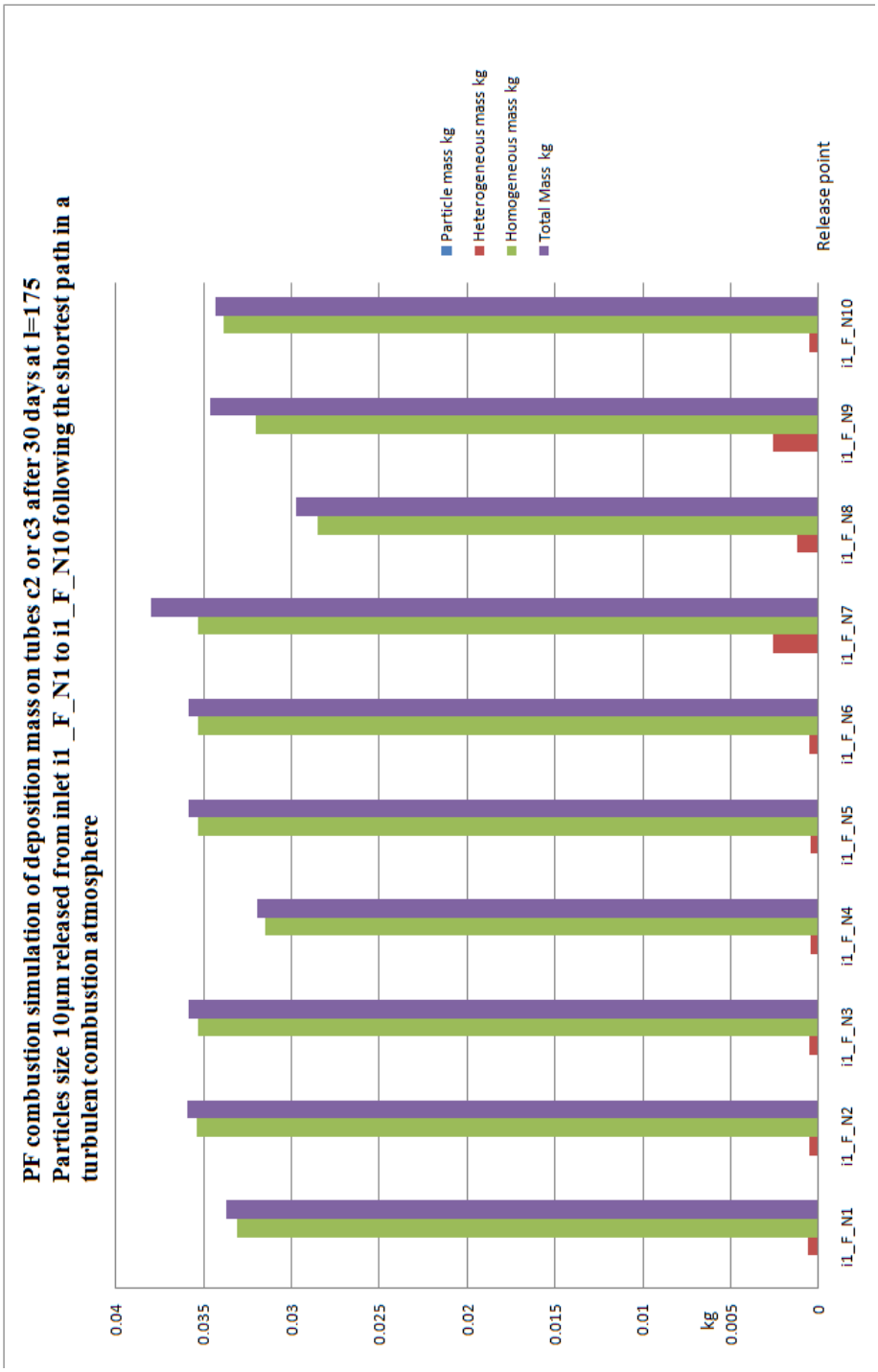

Figure H-15. Particles/vapour mass impacting on tubes c2 and c3 for Chapter 6 case study 2 at l=175.

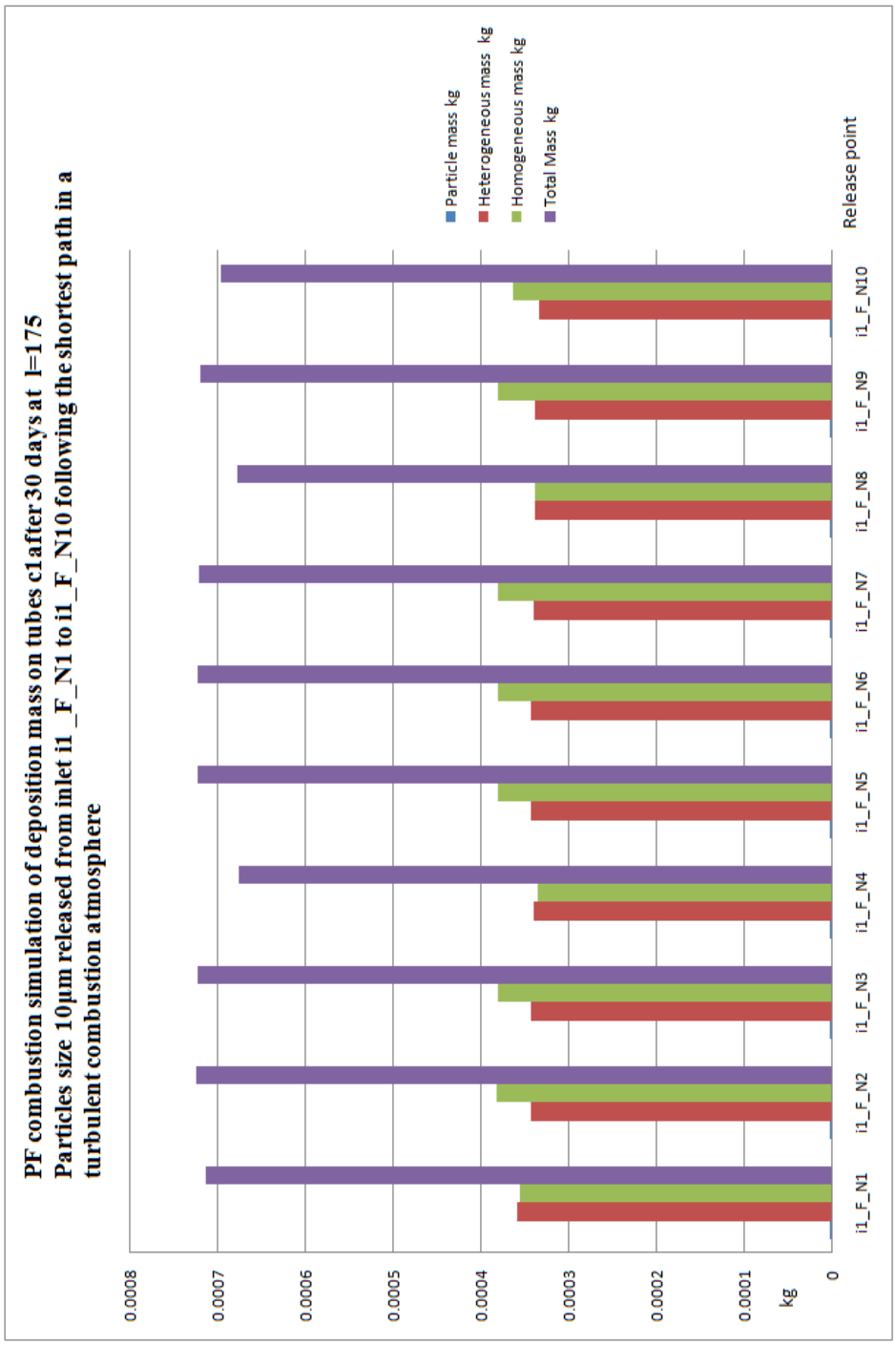

Figure H-16. Particles/vapour mass impacting on tubes c1 for Chapter 6 case study 2 at l=175

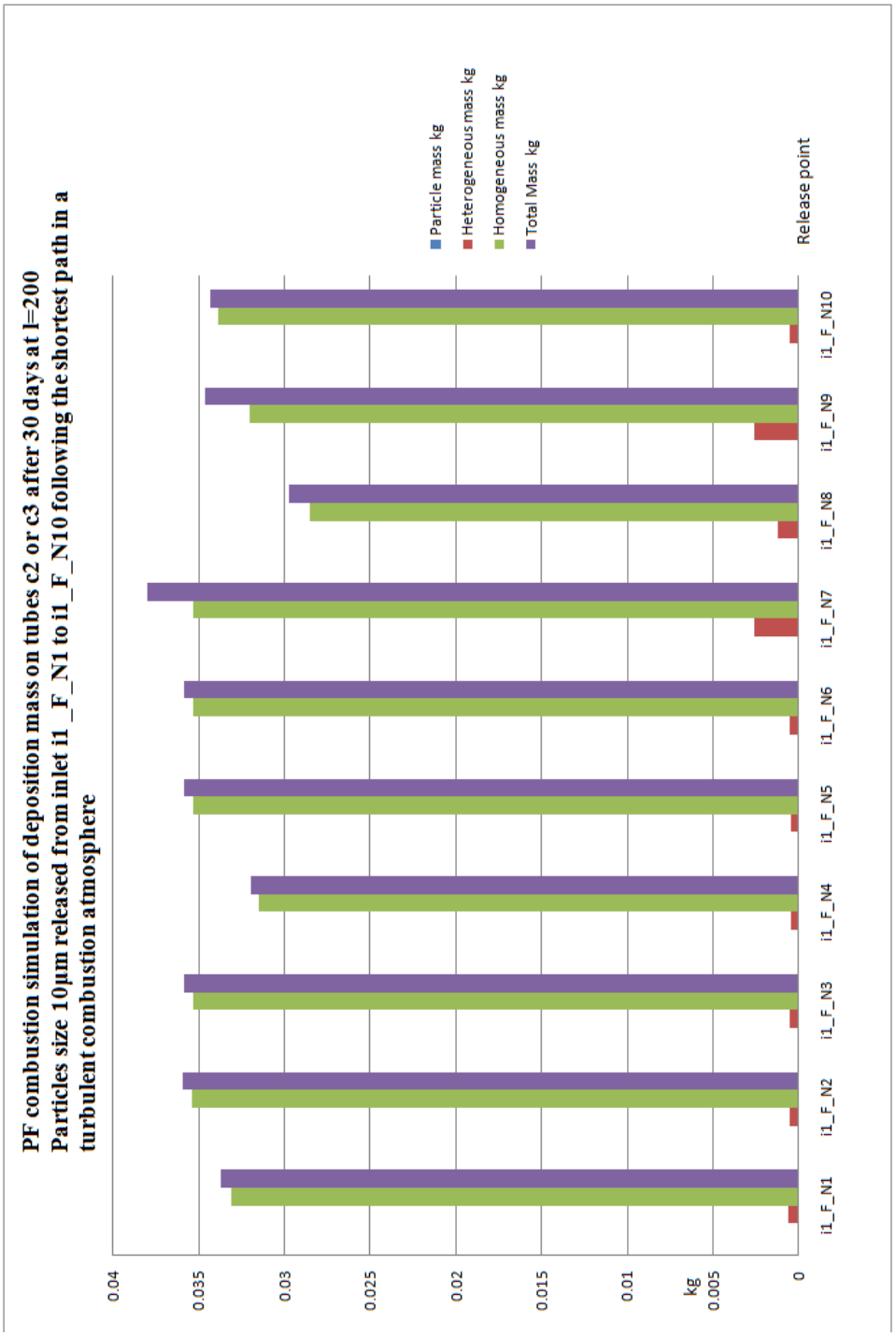

Figure H-17 Particles/vapour mass impacting on tubes c2 and c3 for Chapter 6 case study 2 at l=225.

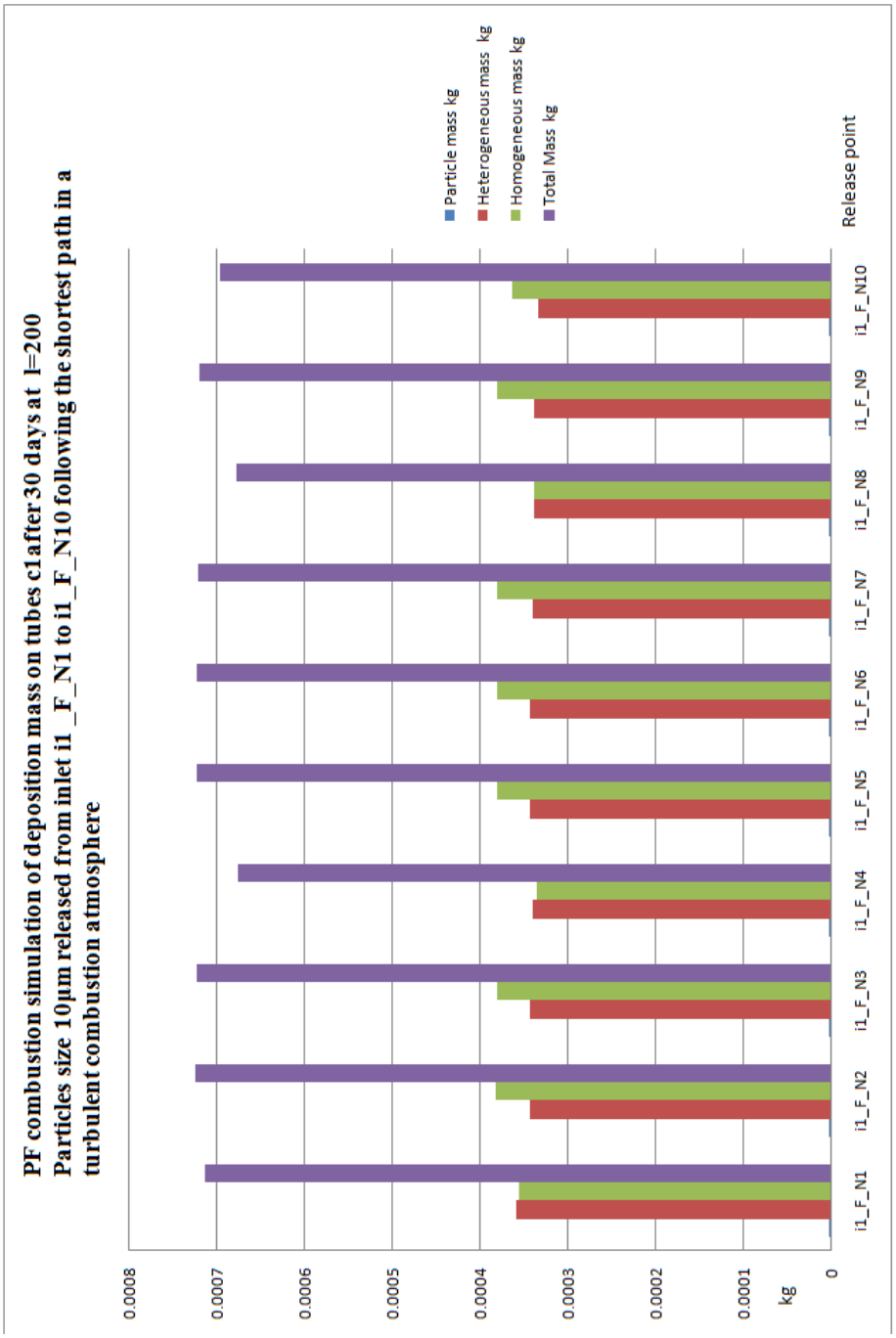

Figure H-18. Particles/vapour mass impacting on tubes c1 for Chapter 6 case study 2 at l=200.

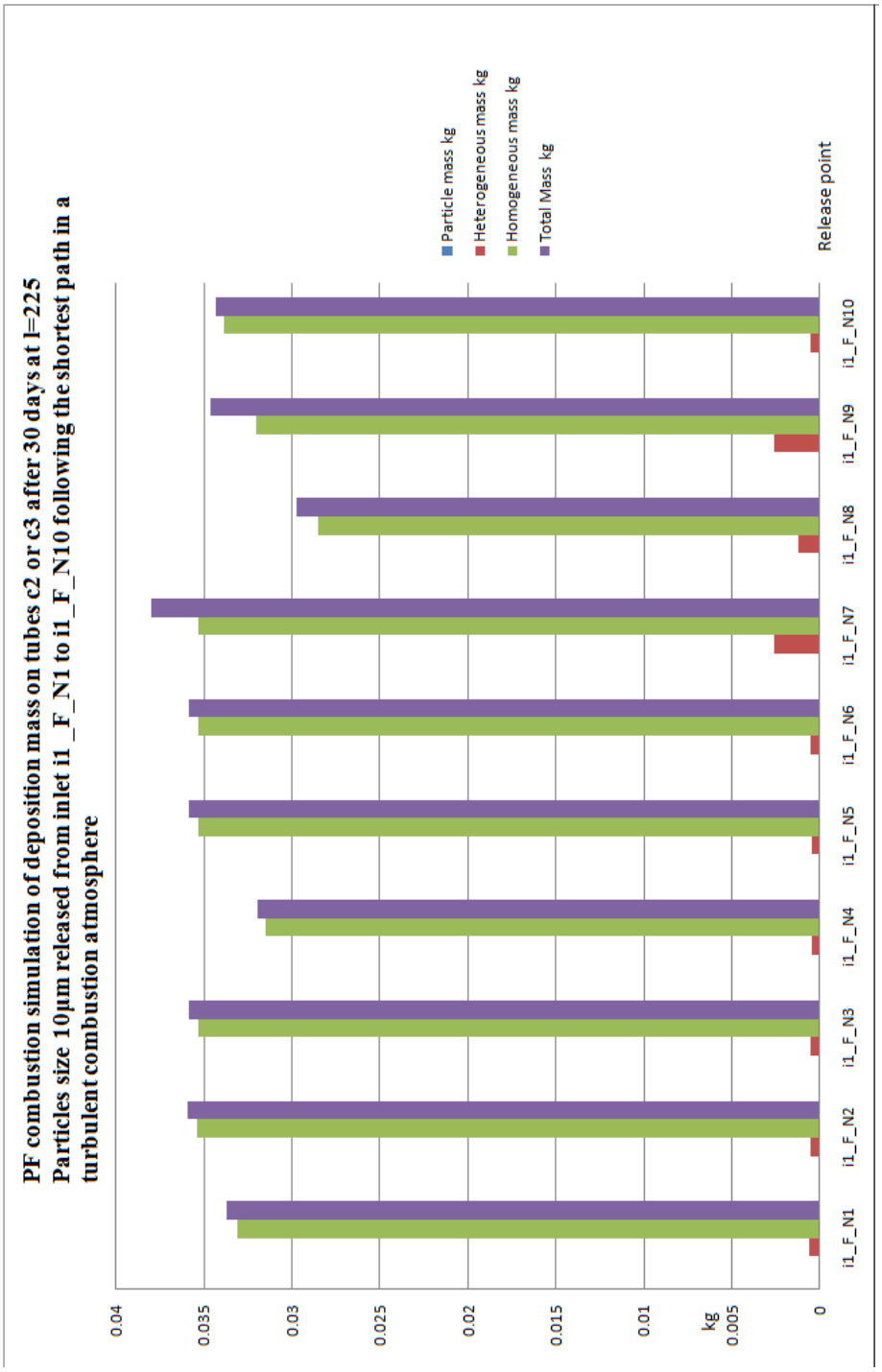

Figure H-19. Particles/vapour mass impacting on tubes c2 and c3 for Chapter 6 case study 2 at l=225.

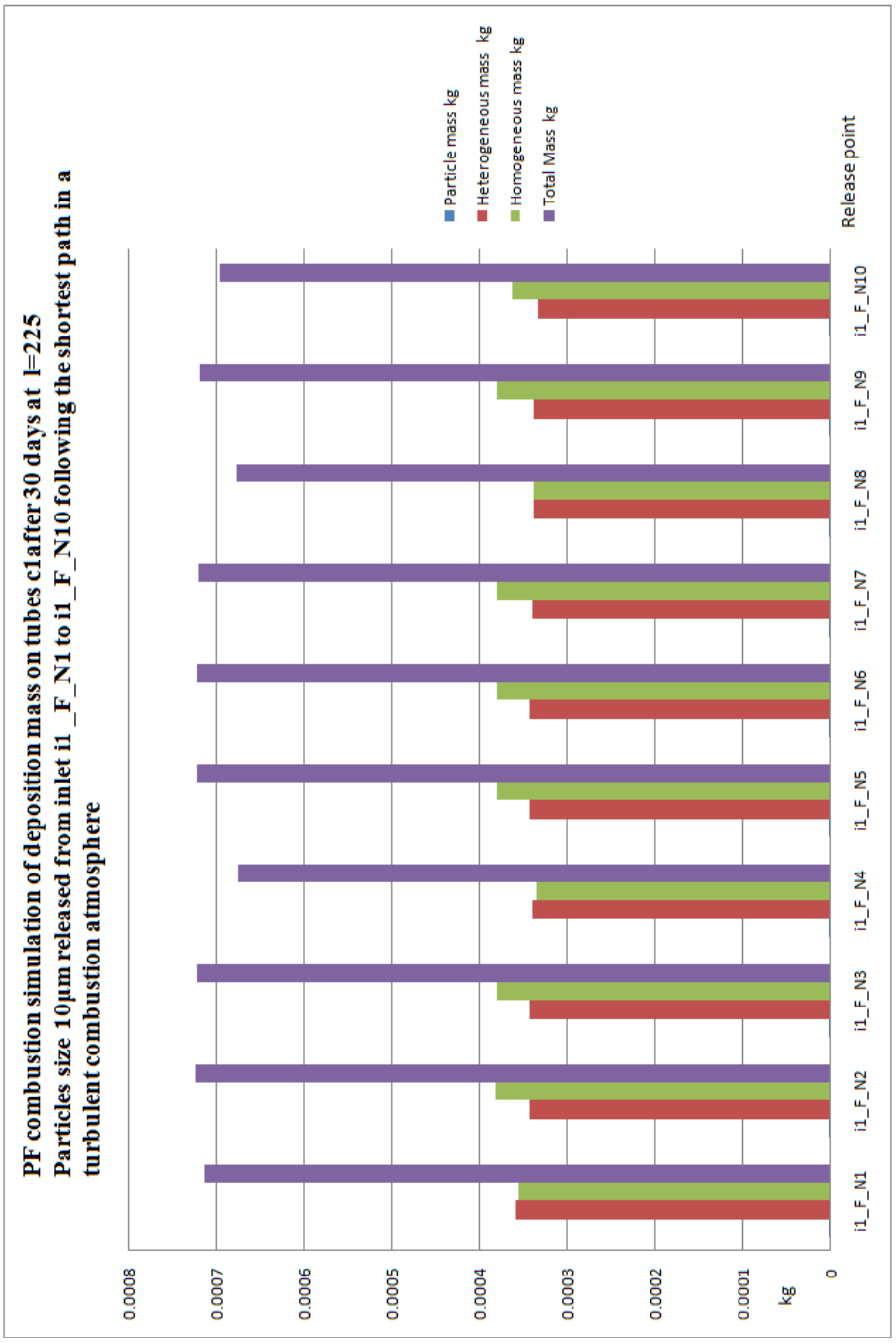

Figure H-20. Particles/vapour mass impacting on tubes c1 for Chapter 6 case study 2 at l=225.

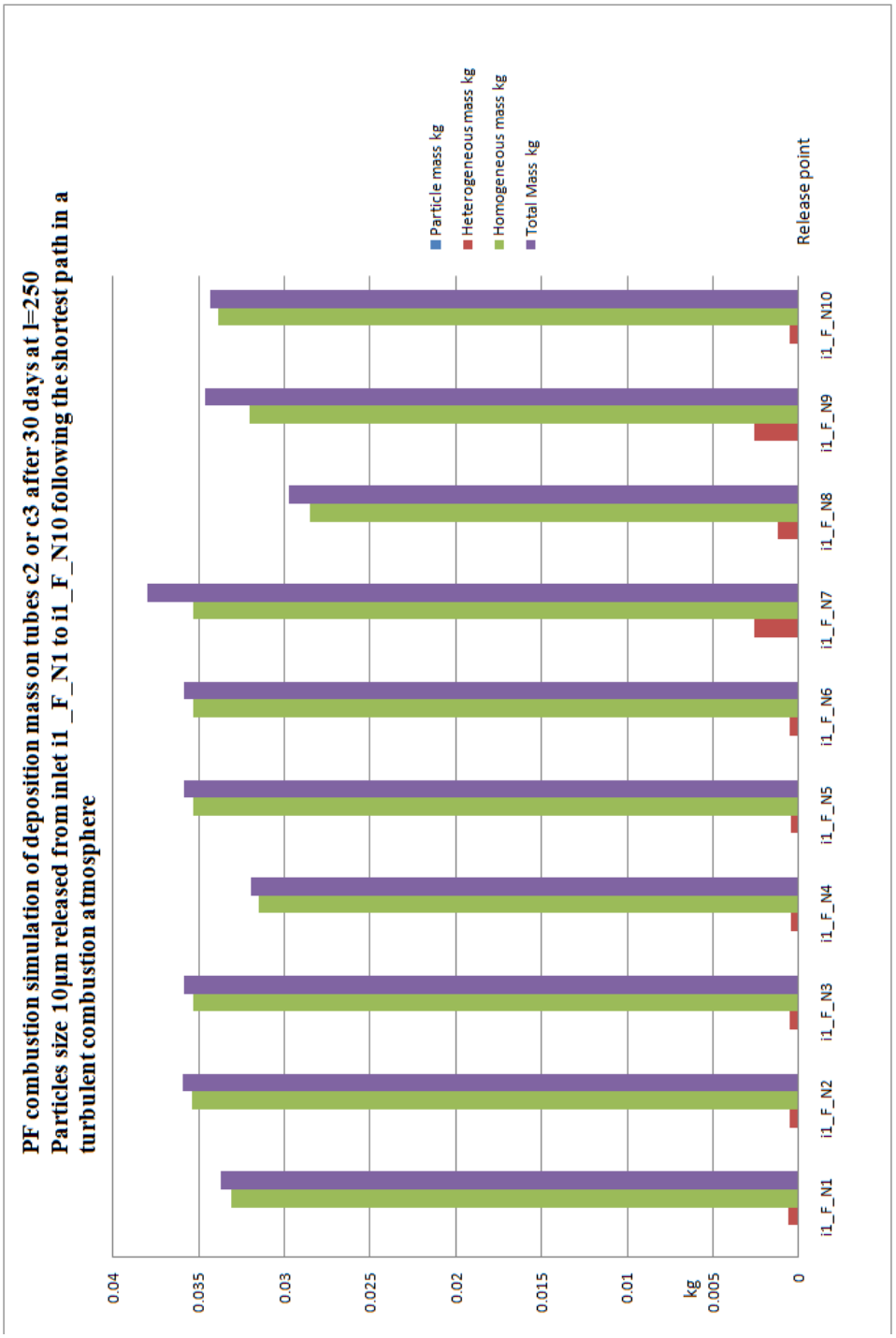

Figure H-21. Particles/vapour mass impacting on tubes c2 and c3 for Chapter 6 case study 2 at l=250

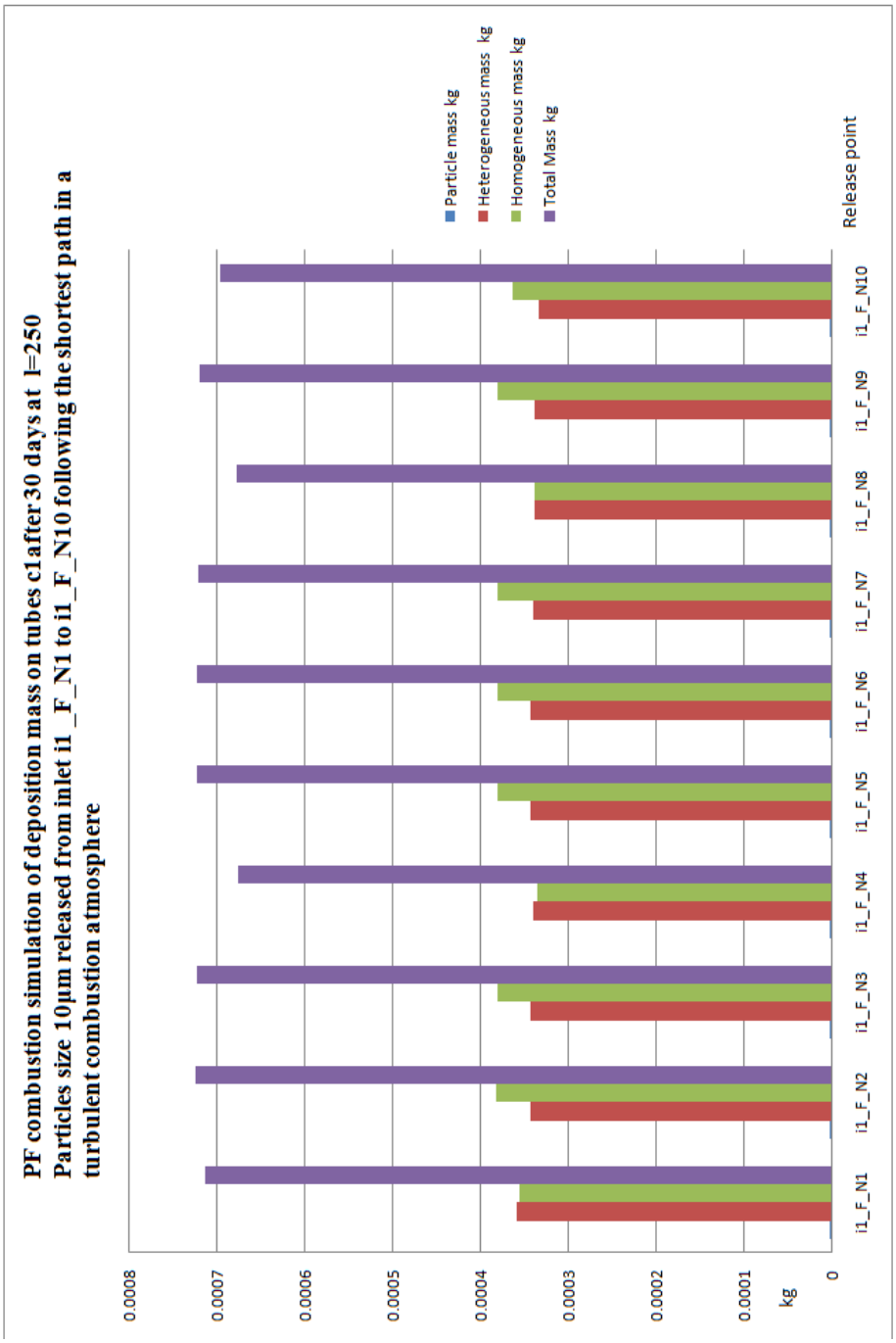

Figure H-22. Particles/vapour mass impacting on tubes c1 for Chapter 6 case study 2 at l=250

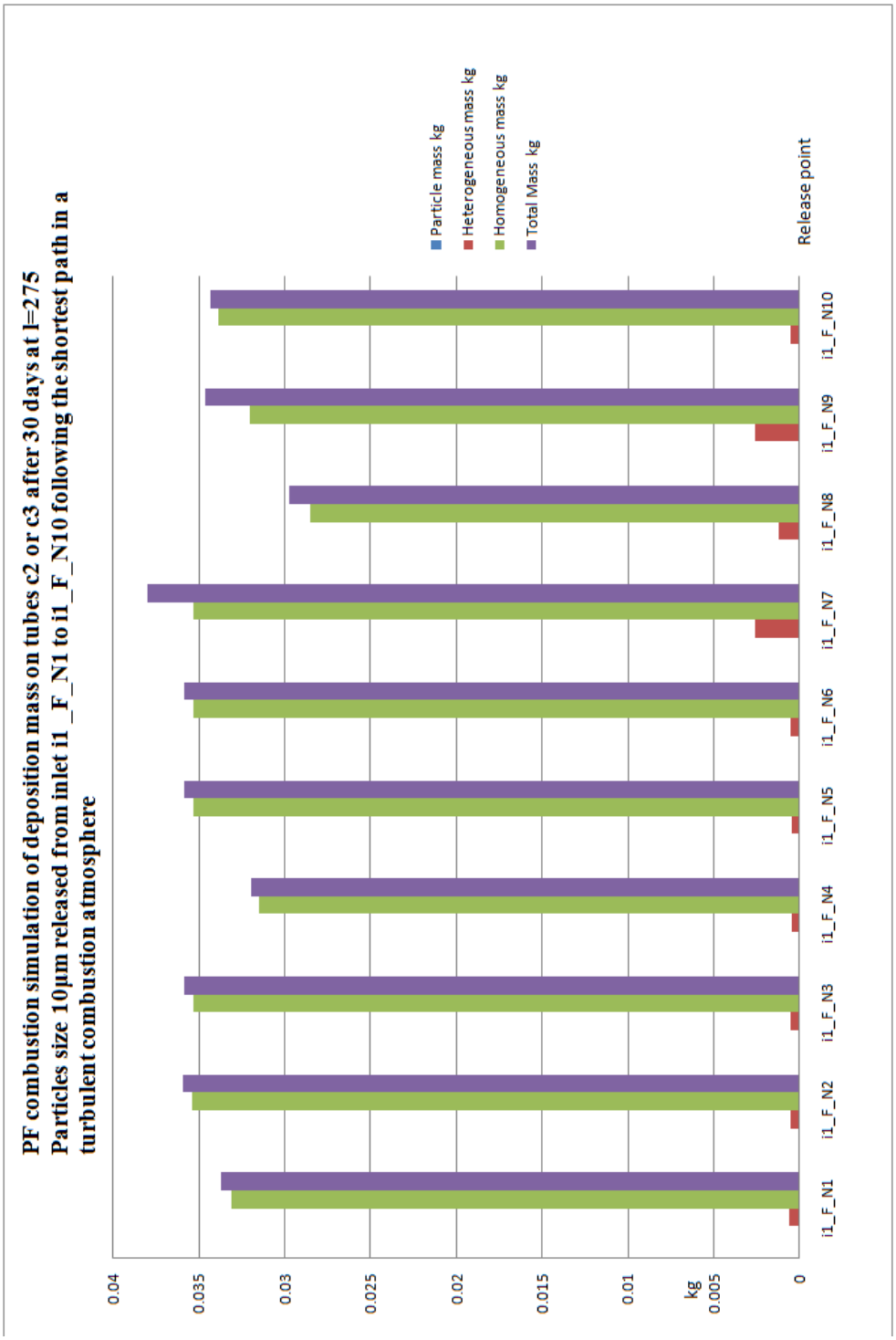

Figure H-23. Particles/vapour mass impacting on tubes c2 and c3 for Chapter 6 case study 2 at l=275

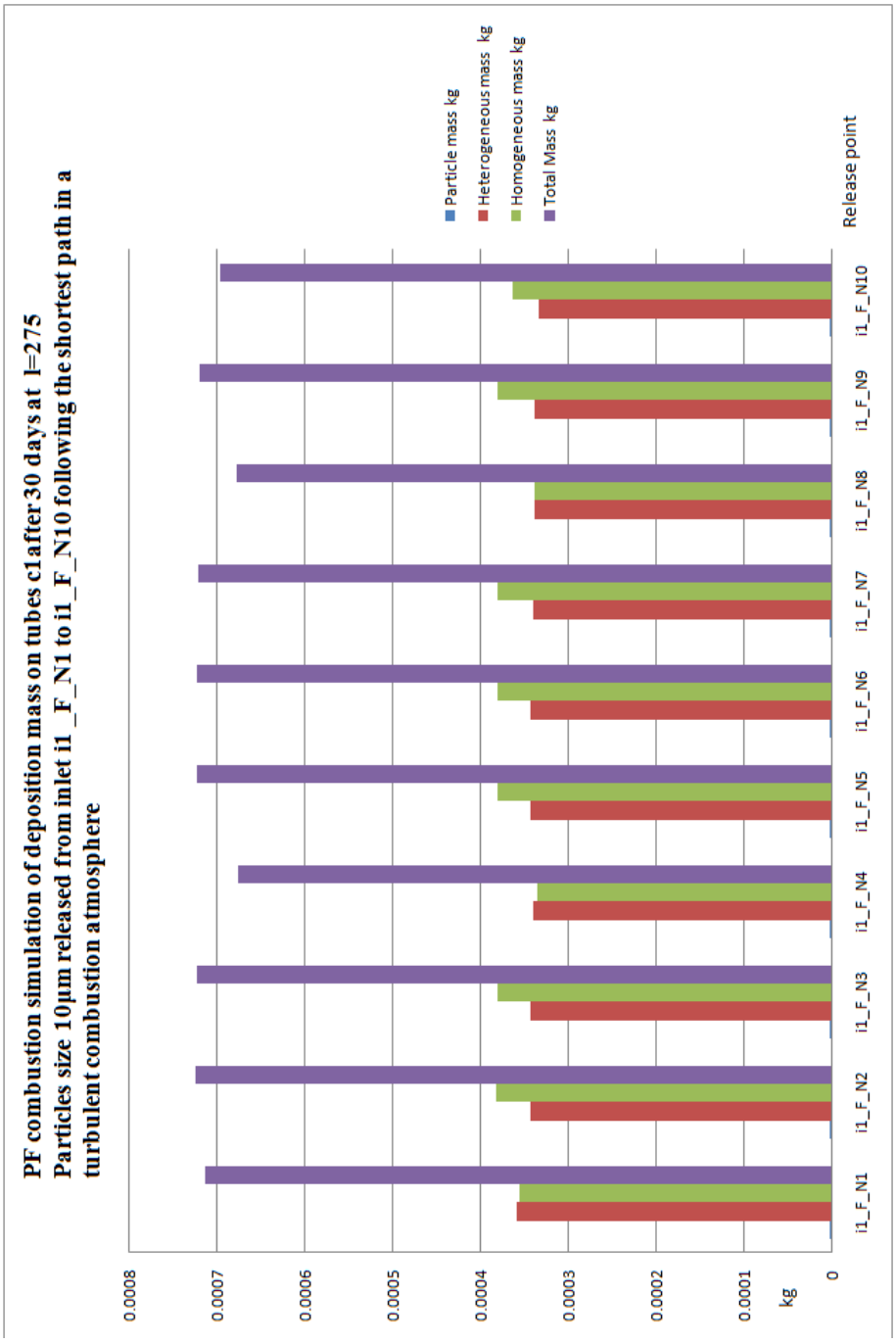

Figure H-24. Particles/vapour mass impacting on tubes c1 for Chapter 6 case study 2 at l=275

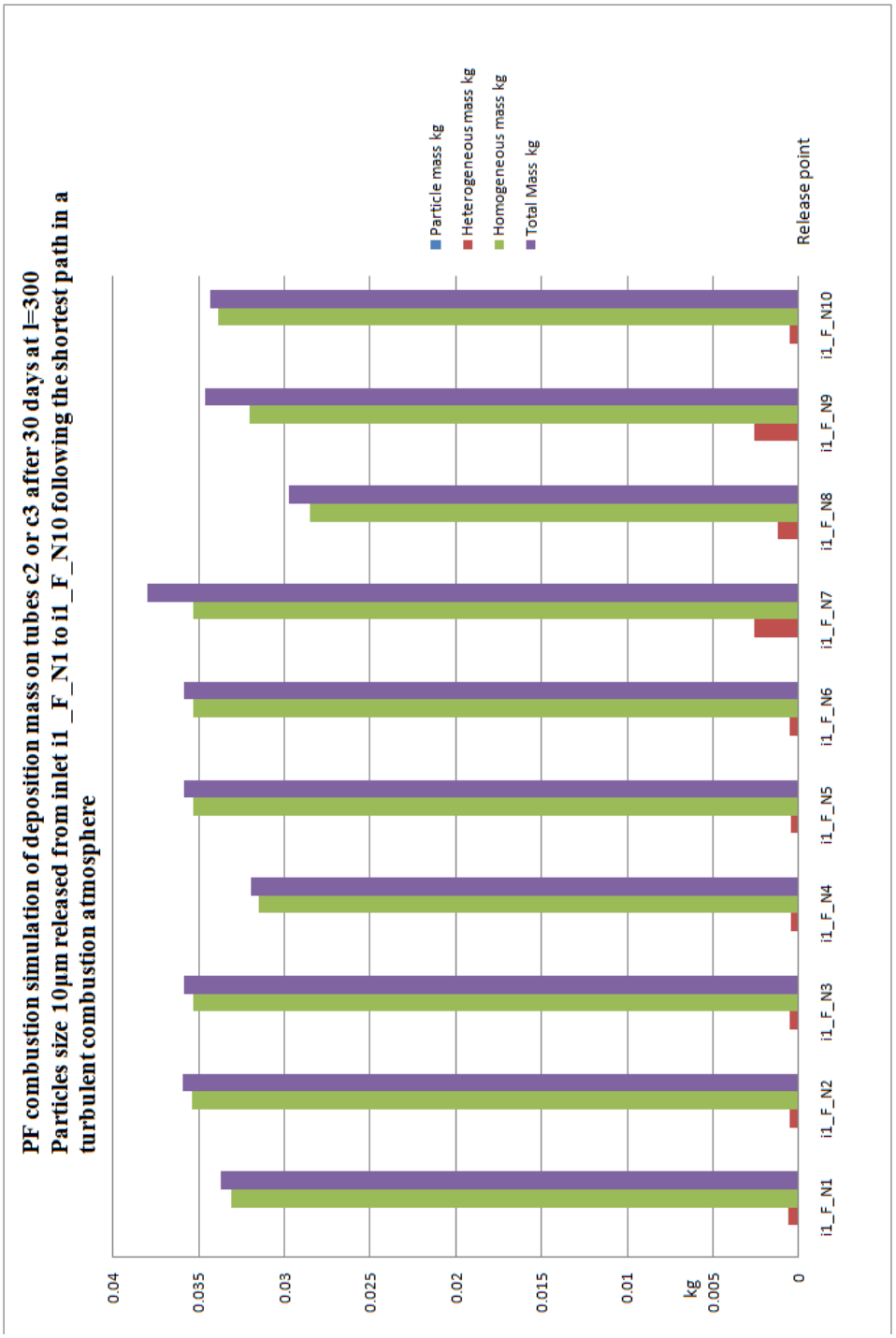

Figure H-25. Particles/vapour mass impacting on tubes c2 and c3 for Chapter 6 case study 2 at l=300

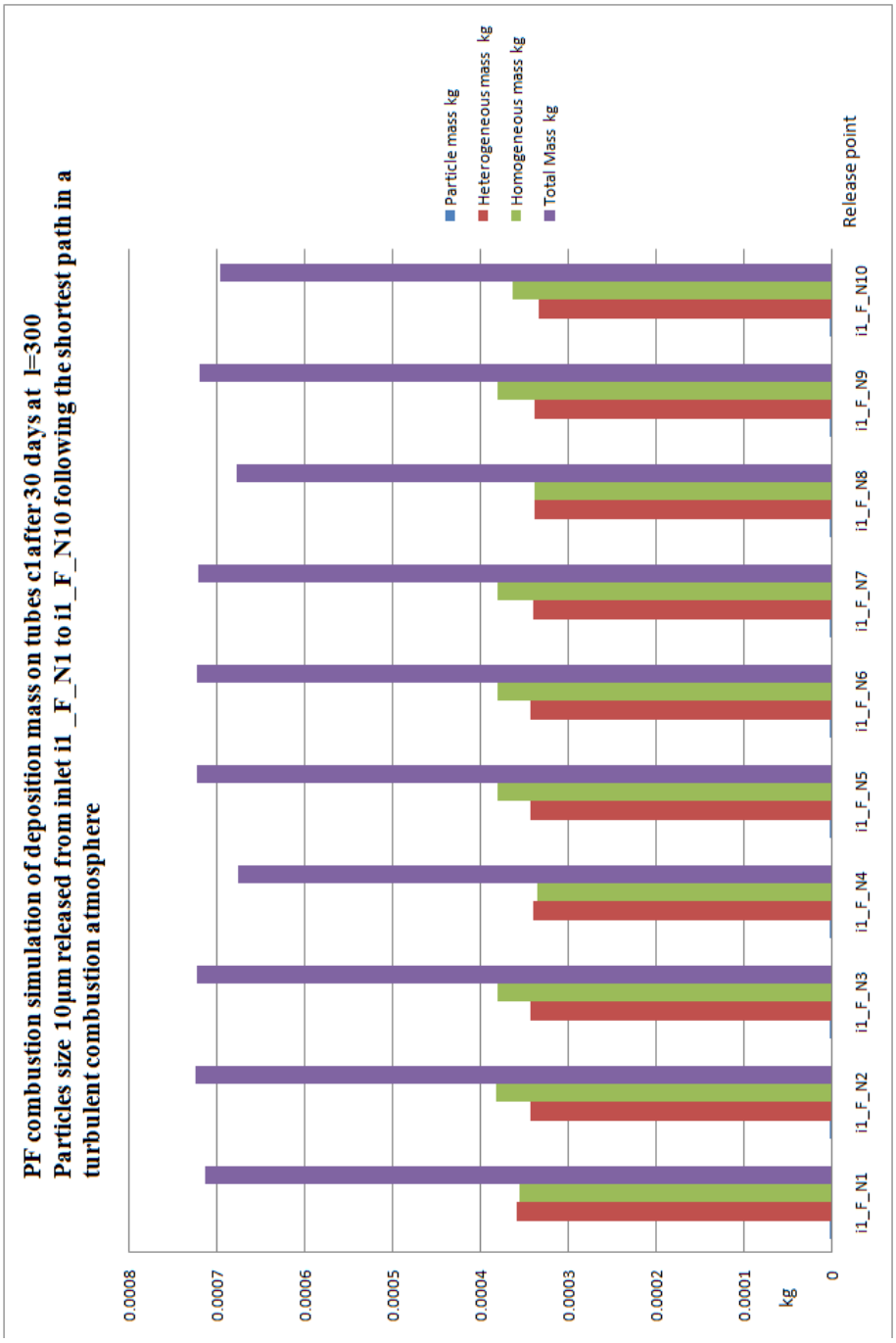

Figure H-26. Particles/vapour mass impacting on tubes c1 for Chapter 6 case study 2 at l=300